UNIVERSITÀ DEGLI STUDI DI MILANO

Ph.D. course in Industrial Chemistry – XXXIII Cycle

FACOLTÀ DI SCIENZE E TECNOLOGIE

Hydroxyapatite-based materials for environmental processes

Michele Ferri
R11863

Supervisor: Professor Antonella GERVASINI

Co- supervisor: Prof. Stefano TRASATTI

Dr. Pierangela CRISTIANI

Ph.D course coordinator: Prof. Dominique Roberto

A.Y. 2019/2020

SUMMARY

Abstract

In the present dissertation, hydroxyapatite-based and composite materials have been rationally designed, synthesized, characterized and applied to processes of environmental concern, namely wastewater remediation (as sorbents) and electrochemical CO_2 reduction reaction (as electrocatalysts).

Hydroxyapatite (HAP, $Ca_{10}(PO_4)_6(OH)_2$) belongs to the family of calcium phosphates. It is characterized by biocompatibility, marked water insolubility, thermal and chemical stability, and structural flexibility; in addition, the surface of the material is highly functionalized, with co-presence of acid and basic moieties conferring to HAP surface amphoteric properties. The combination of the unique features herein listed have led scientists to investigate on the application of HAP in several fields, from biomedical to catalytical uses, with promising results.

In this PhD project, pristine and composite HAP materials have been synthesized according to an optimized wet co-precipitation route. The structural and morphological features of the obtained samples have been investigated by a wide set of proper physical-chemical techniques: elemental analyses, N_2 adsorption/desorption isotherms, XRD, TEM (and STEM) imaging, TEM/EDX mapping, transmittance FT-IR and Raman spectroscopies, and XPS. Since adsorption onto materials' surface is crucial in both sorption and catalytic applications, a special attention has been devoted to surface properties. Indeed, the number and interaction strength of the acid/basic surface sites of the samples have been thoroughly determined by combining zeta potential measurements, gas-solid calorimetric/volumetric titrations, and liquid-solid volumetric titrations, thus assessing the amphoteric nature of HAP-based surfaces.

At first, pristine stoichiometric HAP has been studied as sorbent for the remediation of inorganic pollution in wastewater. Five different sites of the HAP surface may be involved in the metal ion trapping process: two inequivalent Ca sites by ion exchange mechanisms and some surface groups (mainly phosphate and hydroxyl groups) by adsorption. The ability of HAP in removing from aqueous solutions five target heavy metal cations (namely Pb(II), Cu(II), Cr(III), Co(II) and Ni(II)), alone or in combination, has been assessed performing batch sorption tests (industrial-like set-up) and by means of the collection of adsorption isotherms in a broad concentration range. The modelling of experimental data obtained from sorption tests allowed to quantitatively assess HAP sorption capacity and to disclose a specific trend of affinity of HAP towards target cations, namely Pb(II) > Cu(II) > Cr(III) > Co(II) > Ni(II). Leaching test, performed contacting metal-loaded samples with freshwater, confirmed the almost total retention of these pollutants by HAP (Ni(II) being the sole exception), therefore ensuring no secondary pollution issues.

An insight on the adsorption mechanisms of these cations onto HAP surface have been gained by the further physical/chemical investigations carried out on metal-loaded samples. Liquid-phase microcalorimetric experiments allowed to directly measure the energetics of cations' adsorption phenomena onto HAP. The application of a microcalorimetric approach to cations' adsorption onto HAP does not only corroborate the information collected from the characterization of metal-loaded samples. Indeed, comparing the energetic contributions of several cations, it has been possible to demonstrate, for instance, that the metal ionic radius was not the only parameter directing the adsorption mechanism onto HAP. Indeed, several other parameters such as the cation speciation, the pH of the solution, and the solubility of the phosphate salts of the metal under study all partake in directing the adsorption process.

Finally, two case studies assessed the applicability of stoichiometric HAP as sorbent in the remediation of simulated wastewaters from mining and electrical industries in which several hazardous metal species (Ni and Co) may be present at different ratio and under different conditions (e.g. pH).

Since wastewater pollution is usually a complex issue and inorganic pollutants like heavy metal cations may be found in co-presence with organic hazardous species (e.g. dyes, pesticides…), the design of proper sorbents for the simultaneous removal of both classes of compounds is of paramount importance for

environmental protection. Although HAP is an ideal sorbent for inorganic cations, it does not display the same affinity towards organic species; carbon-based materials (e.g. activated carbons) are instead the benchmark sorbents in this field. With the aim of developing novel dual-nature sorbent, HAP/C composites have been designed and tested in the simultaneous remediation of organic and inorganic pollution.

After screening diverse carbonaceous scaffolds, the choice fell on a biomass derived mesoporous carbon, which ensured an eco-friendly nature and a large surface area of the resulting composites. HAP/C composites demonstrated to effectively possess a dual nature, combining both HAP and activated carbon adsorption capacities and therefore simultaneously removing benchmark organic and inorganic pollutants (methylene blue and Cu(II), respectively) from simulated wastewaters. Consistently with structural and morphological characterization, experimental results indicate that a carbon content of *ca*. 8 wt.% in composites guarantees optimal removal performances. Moreover, leaching tests demonstrated that retention features of both moieties are retained as well: HAP/C composites do not suffer from secondary pollution problems.

Beyond being exploited as sorbent, an exploratory study has been performed with the aim to benefit from HAP peculiar sorption properties in the field of electrochemical detection of hazardous species: in this specific case, the detection of trace amounts of heavy metal cations in waterbodies by square wave anodic stripping voltammetry (SWASV). HAP/C composites have been implemented as modifiers in self-standing and mechanically stable electrodes. After optimizing the electrochemical setup, operative conditions and electroanalytical parameters, best sensing performances were delivered by HAP/C-modified electrodes where composite's carbon content was *ca*. 8 wt.%, achieving linear response ranges and limits of detection in the range of units of μM (i.e. ppb) for benchmark pollutants like Cu(II) and Pb(II).

However, as to allow the hydroxyapatitic moiety of the composite to exert its preconcentration assist, the typical SWASV analytical procedure had to be modified, with the addition of a preconcentration step prior to the reductive one. Despite the beneficial effect exerted by HAP towards cations adsorption and thus electrode sensitivity, the incorporation of HAP in the electrodes resulted in a strict dependence of the analytical signal on their exposure time to the polluted solution. Moreover, the permanent modification of the electrode surface (i.e. permanent retention of pollutants by the HAP moiety of the composite) cannot be excluded when electrodes are contacted for long time with solutions containing high concentration of heavy metal species. These shortcomings may limit the applicability of the HAP/C-modified electrodes to moderately polluted effluents where long "acquisition" time can be afforded, and a continuous in-line monitoring is not mandatory.

At last, during my 6 months stay at University of California Irvine (UCI), hosted by Prof. Plamen Atanassov group, HAP has been applied as dopant in CO_2RR electrocatalysts. The rationale behind HAP doping of Cu-based electrocatalysts stems from the peculiar ability of HAP phosphate (basic) surface groups to adsorb CO_2 in a bent configuration, thus destabilizing the molecule (i.e. breaking its linearity). Since CO_2 configurational stability is deemed to be the main contributor to the large overpotential associated with CO_2 electrochemical reduction, HAP doping aims to ease the process by acting as a reservoir of destabilized CO_2 molecules, ideally maximizing the production of high added-value C_{2+} compounds under moderate cathodic potentials.

Composite electrocatalysts, composed by a carbonaceous support (a N-doped 3D assembly of graphene nanosheets), an active phase (copper nanoparticles, $\varnothing \approx 25$ nm) and HAP (as dopant) have been synthesized. Structural and morphological characterizations indicate that both doped and undoped catalysts exhibited large surface area and pore volume, ensuring optimal mass diffusion and reagents/products transfer under reaction conditions. On the other hand, TEM/EDX mapping and XPS analyses disclosed that a satisfactory dispersion of both copper nanoparticles and HAP onto the support have been achieved, realizing the close contact between active phase and dopant that was envisaged by design.

When tested in a lab scale CO_2 electrolyzer (i.e. an electrochemical flow-cell), doped and undoped catalysts achieved promising performances. First of all, both electrocatalysts displayed a faradic efficiency (FE) towards CO_2RR ≥ 80% throughout the whole potential range under investigation (from *ca*. 0 to *ca*. -1 V vs RHE – IR corrected), minimizing parasitic Hydrogen Evolution Reaction (HER).

The undoped catalyst generated almost selectively ethylene under moderate cathodic potential (FE ≈ 92% at ≈ -0.1 V vs RHE) while, applying increasingly cathodic potentials, ethylene faradic efficiency decreases (FE ≈ 20% at ≈ -0.8 V vs RHE) in favor of formate (FE ≈ 55% at ≈ -0.8 V vs RHE). On the other hand, the results obtained testing doped electrocatalysts demonstrate that HAP doping actually altered CO_2RR product distribution. HAP doped catalysts yielded small quantities of C_{2+} products (acetone and acetate, total FE ≈ 30% at ≈ -0.1 V vs RHE) under the application of slightly cathodic potentials while boosting formate production at large cathodic potentials (FE ≈ 70% at ≈ -0.8 V vs RHE) at the expenses of ethylene, which completely disappears at E ≈ -0.8 V vs RHE. This peculiar behavior of the doped electrocatalyst has been attributed to HAP sorption properties as well: in particular, the presence of acid sites (Ca^{2+} and hydroxyl group vacancies δ_{OH-}) onto HAP surface has been deemed to stabilize the first reaction intermediate (the radical anion $CO_2^{\bullet-}$) in O-bound configuration, thus favoring the reaction pathway leading to formate at the expenses of ethylene and all C_{2+} products in general.

Although the doped electrocatalyst was designed aiming to increment the production of C_{2+} compound through the exploitation of HAP surface basic sites, the experimental results suggest that acid sites are instead playing an active role in the process. Despite this unexpected outcome, acid/base doping was proven to be a useful tool in directing the selectivity of electrochemical CO_2RR processes.

Overall, the present study demonstrates that the unique features of HAP make it a versatile material which may be applied for the protection of the environment at 360 degrees, from water to air remediation, as pristine and/or composite material, as sorbent and/or catalysts' dopant.

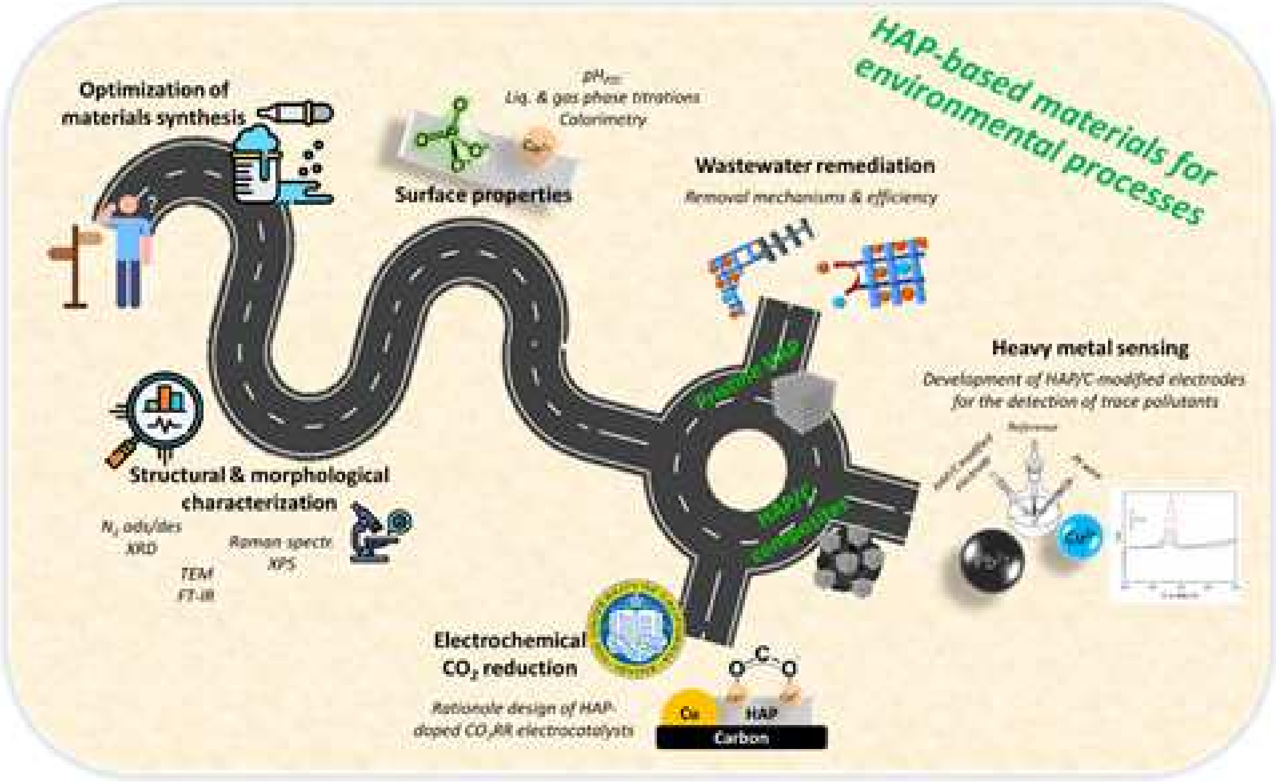

Graphical abstract

Chapter 1: Introduction to hydroxyapatite: chemical and physical properties

The family of apatites is composed by minerals characterized by the general formula $Me_{10}(XO_4)_6Y_2$, where generally:

- "Me" represents a divalent cation (Ca^{2+}, Mg^{2+}, Sr^{2+}, Pb^{2+}…), which could, with a slight variation of the material stoichiometry, be replaced by mono- (Na^+, Li^+, K^+…) and/or trivalent (Cr^{3+}, La^{3+}, Al^{3+}…) cations;
- "XO_4" is usually a trivalent anionic tetrahedron, such as PO_4^{3-}, VO_4^{3-} or AsO_4^{3-}. As for cations, substitution with different valence anions is possible, especially in the case of bivalent (SO_4^{2-} and CO_3^{2-}, among others);
- "Y" is a monovalent anion, like OH^-, Cl^- or F^-. Even in this case, replacement with divalent anions (O^{2-}, CO_3^{2}) is possible as well.

Amid apatites, calcium phosphates (Me = Ca; X = P) form a specific subgroup characterized by biocompatibility, biodegradability and relative natural abundance [1]. Calcium phosphates family itself exhibits a broad variety of compounds, characterized by different stoichiometries and, therefore, chemical-physical properties [2,3]. In the subgroup of calcium orthophosphates, the most common and naturally occurring phases are classified according to their Ca/P atomic ratio: pyrophosphate ($Ca_2P_2O_7$, CPP, Ca/P = 1), octa-calcium phosphate ($Ca_8H_2(PO_4)_6$, OCP, Ca/P = 1.33), tricalcium phosphate ($Ca_3(PO_4)_2$, TCP, Ca/P = 1.5), hydroxyapatite ($Ca_{10}(PO_4)_6(OH)_2$, HAP, Ca/P = 1.67) and tetra-calcium phosphate ($Ca_4(PO_4)_2O$, TTCP, Ca/P = 2).

Hydroxyapatite (HAP), the calcium dibasic phosphate with chemical formula $Ca_{10}(PO_4)_6(OH)_2$, spikes among all these compounds thanks to its importance as biomaterial, chemical properties and natural availability and/or easy and cheap synthesis. As a matter of fact, HAP is the principal inorganic component of mammals' hard tissue [1–3], namely bones and teeth, conferring them (in combination with collagen) peculiar hardness and strength. Because of optimal biocompatibility and bioavailability, it finds large application in the biomedical field [4], from bone filling/repair applications [5] to the coating processes of metal prothesis [6]. Moreover, the unique and tunable composition and physical/chemical features of HAP stimulated a growing interest by the scientific community towards the material, resulting in its application in heterogeneous and environmental catalysis [7–11], wastewater remediation [11–17], sensing devices [18–21], chromatography [22], protein delivery medium [23] and drug releasing agent [24].

1.1 Synthesis, structure and physical properties of HAP

1.1.1 HAP synthesis

Literature presents a wide variety of HAP synthetic routes [8,11,25]. Interestingly, HAP can be obtained from low cost and readily available biological resources (mainly Ca-based minerals [26]) and even from mineral wastes, such as eggshells, mussel shells and animal bones [11,27,28]. Despite this possibility, a big share of the literature reports on the use of low-cost pure chemicals and of wastes of industrial activity [29] as precursors of HAP; the reasons behind this choice lie in the differences between natural resources-derived HAP and proper synthetic HAP. Indeed, because of the precursors' nature, HAP obtained from waste exhibit lower atomic purity, higher structural defectiveness and lower surface area/porosity [11], thus impacting on the material performances.

However, pure chemicals employed in HAP synthesis are characterized by natural abundancy and cheapness as well, branding even synthetic HAP as an environment-friendly material. Typically, $Ca(NO_3)_2$,

$Ca(OH)_2$, CaO and other calcium phosphates are used as Ca^{2+} precursors, whilst P_2O_5, H_3PO_4, $(NH_4)_2HPO_4$ and $(NH_4)H_2PO_4$ are generally employed as PO_4^{3-} precursors [8].

Starting from pure chemicals, three different methods can be identified for the synthesis of HAP powders: (*i*) dry methods, (*ii*) wet methods, (*iii*) alternative energy input methods. Table 1 briefly summarize the most common variants of such methods, also presenting specific strengths and weaknesses.

1.1.2 HAP composition

Due to a unique compositional and structural flexibility, HAP can bare a remarkable number of defects and/or cationic/anionic substitutions without substantially altering its lattice. Physical and chemical properties are on the other hand affected by such modifications, making HAP a tunable material in terms of experimental performances.

Standing to its chemical formula, HAP presents a Ca/P atomic ratio equal to *ca*. 1.67. However, HAP exhibits a peculiar compositional flexibility, which allows to obtain highly non-stoichiometric HAP compounds without significant alteration of the pristine crystallographic structure. In such structures, electrical charges balance is guaranteed by defects like (*i*) Ca^{2+} and/or OH^- vacancies and (*ii*) introduction of protons. These defect bearing ability and intrinsic compositional flexibility make more accurate to denote HAP with the chemical formula $Ca_{10-x}(HPO_4)_x(PO_4)_{6-x}(OH)_{2-x}$ [30] with $0 < x < 1$.

Literature demonstrate that it is possible to synthesize monophasic HAP with Ca/P ratio ranging from 1.5 to *ca*. 1.7 [31,32]. Interestingly, Ca/P ratio has been proven to determine bulk and especially surface [11,15,33,34] properties of HAP.

Apart from alterations of Ca/P ratio caused by Ca^{2+} defectiveness, replacement of the former cations and/or anions of HAP can take place under specific synthetic conditions or by means of ion-exchange processes (see paragraph 1.2.2.1), thus altering surface and bulk properties of the material as well.

Among all the possible substitutions, insertion of carbonate CO_3^{2-} groups into the lattice is surely the most commonly observed compositional variation. Such anionic substitution yield compounds belonging to the family of carboapatites, exhibiting the general chemical formula $Ca_{10}[(PO_4)_{6-x-y}(HPO_4)_x(CO_3)_y][(OH)_{2-(x+y)}(CO_3)_{x+y}]$ [33]. Since HAP possessed two distinct anionic sites, CO_3^{2-} ions can locate in two different positions, substituting PO_4^{3-} groups (B-type carbonate) or OH^- ones (A-type carbonate). The different valence of the anions normally implies contemporary substitution on both sites but Ca^{2+} defects as well as proton insertion (as presented in the paragraph above) could act as charge balancing agents, thus yielding HAPs with preferential A or B-type carbonatation [15,33].

Further details about HAP compositional flexibility will be discussed in paragraph 1.2.

1.1.3 HAP structure and morphology

HAP crystallizes in the hexagonal system, according to the space group $P6_3/m$ geometry [35,36], and presents the following crystallographic parameters: a, b = 9.418 Å, c = 6.881 Å, $\alpha,\beta = 90°$, $\gamma = 120°$ (JCPDS No. 9-432) [35]. It is noteworthy that HAP unit cell comprises 10 Ca atoms in two crystallographically different Ca sites, namely Ca(I) (4 atoms) and Ca(II) (6 atoms). HAP formula could be rearranged as $Ca(I)_4Ca(II)_6(PO_4)_6(OH)_2$, to take into account this crystallographic feature. The presence of two nonequivalent sites plays an important role in terms of ion-exchange capability, with consequences on material functionality and catalytic performance of Me-doped HAPs.

HAP structure can be described as a three-dimensional network of hexagonally packed tetrahedral PO_4^{3-} ions, where P^{5+} ions stand in the center of the polygon, whose top corners are occupied by oxygen atoms. These anions are ordered in columns in the HAP lattice, delimiting two types of unconnected channels (Figure 1, from reference [37]). The first channel is characterized by a diameter of *ca*. 2.5 Å. It is surrounded by Ca^{2+}

ions in coordination with 9 oxygen atoms belonging to tetrahedral PO_4^{3-} ions; the lattice position of such Ca^{2+} ions is referred to as columnar Ca(I) site. The second channel presents a larger diameter (*ca*. 3.5 to 4 Å). It is bordered by Ca^{2+} ions, arranged in a triangular configuration in coordination 7 (six oxygen atoms from phosphate groups, one from hydroxyl group). These sites are usually referred to as screw-axis Ca(II) sites. Charge balance in the lattice is guaranteed by OH^- groups, hosted in the channels with alternating orientations. Hydroxyl ions are located in the center of type II channels (almost on the triangle plane of calcium), packed in columns perpendicular to the unit cell face, thus oriented along the c-axis. The large dimension of these channels, together with the slight mobility of OH^- groups (at high temperature) and the possibility of H hopping (at RT), accounts for the uniaxial ionic conductivity exhibited by HAP; the topic is discussed in detail in paragraph 1.1.4.

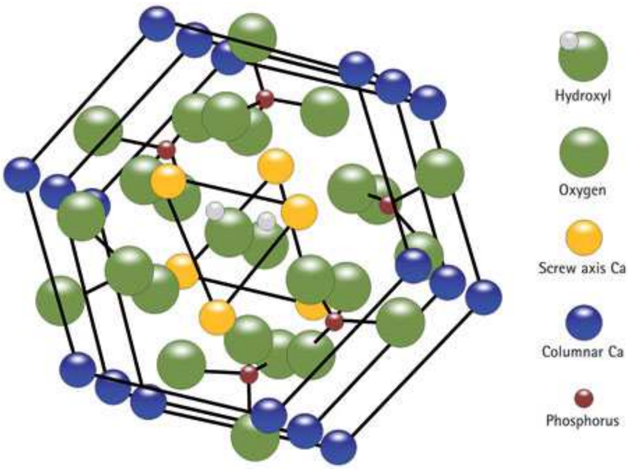

Figure 1: Schematic depiction of HAP unit cell structure. From reference (Brunton et. al, 2013)

From a morphological point of view, HAP tends to crystallize in needle/rod-like shape in absence of specific synthetic conditions [1,38]. Needles/rods obtained are elongated along the c-axis, thus evidencing natural epitaxial growth on 00z crystal planes [8,17]. However, by means of hydrothermal, emulsion and template-based synthetic routes, HAP can be shaped into conventional/hollow spheres [39], platelets [40] and flower-like [28] morphologies among others.

Depending on synthetic procedure and thermal history, HAP powders exhibit specific surface area ranging from 5 to 100 m^2g^{-1} [1,38]. Porosity is likewise influenced; HAP are moderately mesoporous materials [1,38], with a negligible microporous contribution unless when very specific synthetic procedures are adopted to develop microporosity [41].

1.1.4 HAP physical properties

From the physical point of view, water insolubility and thermal/chemical stability justify academic and industrial interest towards liquid and gas phase catalytic/environmental applications of HAP even if, to date, its exploitation in such processes are still limited. At the same time, together with biological features, mechanical properties of HAP-based composites underpin the material implementation in the medical field. Utilization of HAP in electrical/electrochemical applications is a relatively recent field of research: the electrical insulating properties and mono-axial ionic conductivity of HAP are being exploited in energy storage, delivery and generation and electro/photocatalytic processes.

HAP is characterized by a marked water insolubility [42] at ambient temperature and in neutral pH ($K_{ps} \approx 4.7 \cdot 10^{-59}$). However, the solubility of the material depends upon solution ionic strength [42], temperature (HAP indeed presents inverse solubility [43]) as well as solution pH. Indeed, according to Le Châtelier principle, acid/base neutralization between PO_4^{3-} and OH^- with H^+ could drive the dissolution reaction (Equation 1) towards the products:

$$Ca_{10}(PO_4)_6(OH)_2 \leftrightarrow 10Ca^{2+} + 6{PO_4}^{3-} + 2OH^- \qquad K_{ps} \approx 4.7 \times 10^{-59}$$

$$OH^- + H^+ \leftrightarrow H_2O \qquad pK_W = 14$$

$${PO_4}^{3-} + H^+ \leftrightarrow {HPO_4}^{2-} + H^+ \leftrightarrow H_2{PO_4}^- + H^+ \leftrightarrow H_3PO_4 + H^+ \qquad pK_{b1} = 1.65; pK_{b2} = 6.80; pK_{b3} = 9.85$$

Equation 1

The peculiar dissolution equilibria of HAP with the associated release of phosphate species impart to HAP unique solid-state buffering features. As a result of its surface flexibility and partial dissolution, the pH at the liquid interface of HAP is buffered at the pH_{PZC} of the material, reported in literature to range from *ca*. 4 to *ca*. 6 [44–46]. The difficulties in determining an exact pH_{PZC} for HAP are addressable to the amphoteric nature of its surface (further discussed in section 1.2), which generally impacts on the reliability of these measures.

Besides being stable under a wide pH range, HAP shows remarkable thermal stability. Such stability is dependent upon several factors, mainly synthetic conditions, thermal history and Ca/P ratio, with the latter being the most important. Literature reports indeed that stoichiometric HAP preserves its lattice structure, without decomposition phenomena and/or segregation of new phases when thermally treated up to 1450°C for 3 h [47]. In the case of non-stoichiometric HAP, segregation of CaO (for over-stoichiometric materials, i.e. $Ca/P > 1.67$) or $Ca_3(PO_4)_2$ (for sub-stoichiometric materials, i.e. $1.5 < Ca/P < 1.67$) takes place in the temperature range between 700 and 1100°C [31,48]. Influence of synthetic conditions and thermal history on HAP thermal stability reflect on mass losses associated to thermal treatment. Removal of chemisorbed water and/or decomposition of carbonates [49,50] are the main contribution to the phenomenon.

Despite unavoidable thermal sintering, HAP has proven to be able to undergo both temperature cycles and long-lasting high temperature treatments, thus resulting an effective heterogeneous catalyst and/or active phase support [11]. For example, HAP have been exploited as acid-base catalyst in biodiesel production, exhibiting good catalytic activity and recyclability while producing a fuel which completely fulfill the ASTM standards required for biodiesel [51]. In the same field of application, HAP has even been employed as active phase support for CaO-CeO_2 nanoparticles, giving a yield of biodiesel production above 80% [52]. Another successful application of HAP as heterogenous catalyst falls in the field of VOCs oxidation: indeed, Sun et al. [53] demonstrated that HAP is active in formaldehyde oxidation at room temperature, indicating the material as a candidate for replacing the precious metal-based catalyst currently in use for this process. Moreover, HAP was proven to oxidize other common VOCs, such as toluene, ethyl acetate and iso-propanol, in a relatively low temperature range (400 to 500°C) [54].

Mechanical properties of HAP monoliths and/or thin layers are strictly dependent on porosity and especially on the nature of the organic/inorganic binder added to the material. Relatively high bending and compression strengths could be obtained for HAP-based composites [55,56].

Due to its ceramic nature, HAP is an electrical insulator ($\sigma \approx 10^{-9}$ S m^{-1} at RT [57]) and, as previously anticipated, a modest monoaxial ionic conductor. Whilst mechanism of conduction in HAP is still unclear, literature univocally agrees on an ionic conduction based on ions hopping along the c-axis channels [57]. Ca(II) and PO_4^{3-} ions are not thought to contribute to conduction: protons (at $T < 200°C$, activation energy in the range of ≈ 0.4 eV) and OH^- ions (at $T > 700°C$, activation energy in the range of ≈ 2 eV) determine the conductivity of the material [57], together with synthetic method and thermal history (i.e. content of surface and bulk water molecules). Such thermal activated ionic conductivity and electrical insulating properties at RT are paving the way for new and innovative applications of HAP-based and/or doped materials in electrochemical field, i.e. as ionic conductor in solid oxide fuel cells [58–61] as well as dopant/charge separator in electro/photocatalysis [62,63].

Table 1: Common synthetic routes to HAP powders (adapted from [25]*)*

	Method	Synthesis temperature	Particle size	Degree of crystallinity	Phase purity	Particle morphology	Size distribution	Cost	References
(*i*) Dry methods	Solid state	1000 to 1250°C	> 2 µm	High	Low	Diverse	Wide	Low	[25]
	Ball milling	RT	15-150 nm	Low	High	Diverse	Wide	Low	[64–68]
(*ii*) Wet methods	Co-precipitation	RT to ≈ 100°C	> 0.1 µm	Variable	Variable	Diverse	Variable	Low	[25]
	Hydrothermal	150 to 400°C	> 50 nm	High	High	Needle-like	Wide	High	[25]
	Emulsion	RT	5 nm to 1 µm	Low	Variable	Needle-like	Narrow	High	[25]
	Sol-Gel	300 to 900°C	10-200 nm	High	High	Diverse	Wide	Variable	[69–75]
	Hydrolysis	RT to 90°C	0.1 x 5 µm	Variable	High	Needle-like	Wide	Low	[76–78]
(*iii*) Alternative energy input methods	Microwave-assisted	-	100x25 nm	High	High	Diverse	Narrow	Variable	[25]
	Electrospinning	-	75x40 nm	-	-	-	-	Low	[25]
	Flux cooling	500°C	20x2 µm	High	-	Hexagonal	-	Variable	[25]
	Combustion	170 to 500°C	0.450 µm	Variable	High	Diverse	Wide	Low	[25]
	Electrospraying	-	10x30 µm	-	-	Fibers	Variable	Variable	[25]

1.2 Chemical features and surface properties of HAP

HAP exhibits a complex and highly functionalized surface, imparting to the material most of its peculiar properties, namely amphoteric nature and connected surface reactivity [11,33]. Moreover, thanks to the marked structural and compositional flexibility, the material presents a unique chemical reactivity. Indeed, adsorption processes efficiently take place at its surface according not only to a single but several mechanisms [11,79], according to the adsorbate nature and operational conditions (i.e. chemical environment) [15,17,79,80]. The same structural flexibility, together with the development of finely controlled synthetic routes, allows to tune HAP surface properties simply modifying the Ca/P ratio [15,34,81]. As example, when considering a wet co-precipitation synthetic route, fine tuning of Ca/P ratio of the resulting HAP is achieved varying precipitation pH, Ca/P ratio of precursors' solutions and/or synthesis temperature [31,34].

Herein the origin and nature of HAP surface reactivity will be discussed and a brief introduction to its enhanced adsorption properties will be reported.

1.2.1 Surface acidity-basicity

Since containing both acid and basic sites in a single crystal lattice unit, HAP surface exhibits several different functional groups to whom the peculiar amphoteric nature of the material is ascribable. Moreover, these sites display a great variety in terms of nature and interaction strength. Summing to these feature the high surface functionalization degree and heterogeneous distribution of acid/basic moieties, HAP possesses a noticeable potential for reactions requiring bifunctional solid catalysts containing both antagonist functionalities [33] (for example, Guerbet reaction [33,34]).

Depending on their nature, HAP surface functional groups (Figure 2) can be classified as [33]:

- Lewis acid sites: Ca^{2+} and OH^- vacancies (v_{OH}, δ^+)
- Lewis basic sites: Ca^{2+} vacancies (v_{Ca}, δ^-)
- Brønsted acid sites: HPO_4^{2-}
- Brønsted basic sites: O^{2-} (PO_4^{3-}), OH^-

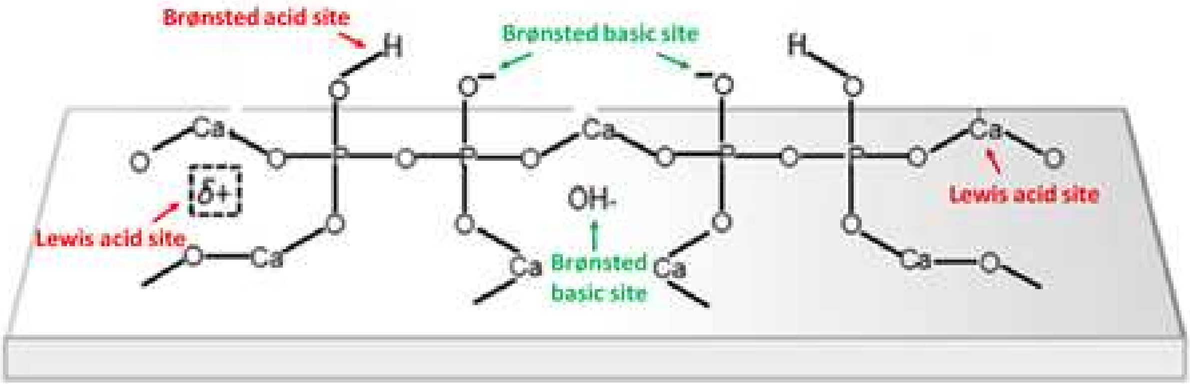

Figure 2: Model of HAP surface and identification of acid/basic functional groups. Adapted from reference (Silvester et al. 2014)

As discussed in the previous section, stoichiometry tunability (in terms of Ca/P ratio) and compositional flexibility are typical of HAP and are strictly connected with its surface acid/basic behavior. Deficient HAP (x > 0, Ca/P down to 1.50, paragraph 1.1.2) act as solid acid catalyst while for stoichiometric HAP (x = 0, Ca/P *ca*. 1.67) basic features are dominating [8,11,33,81]. Apart from the variations of the Ca/P ratio, surface acid/basic properties are also affected by cation (Ca(II) replacement with other alkaline earth species like Sr^{2+}, Mg^{2+}, Na^+, K^+, etc) or anion (OH^- and/or PO_4^{3-} replacement with F^-, Cl^-, CO_3^{2-}, etc) substitution.

Moreover, natural or induced HAP defectiveness could imply the insertion of protons in the lattice, with the formation of HPO_4^{2-} or (postulated) $-OH_2^+$ functionalities, altering the surface reactivity as well. The plethora of possible Ca/P ratio, composition and synthetic route (affecting other fundamental parameters such as specific surface area and morphology) accounts for the variety of acid/base titration results reported in literature [8,33] as well as for the wide range of the disclosed pH_{PZC} of HAP powders [44–46,82].

Carbonatation is by far the most common ionic substitution detected in both natural and synthetic HAPs and its effect on both stoichiometry, morphology and surface reactivity has been deeply studied [33], applying surface screening techniques such as NH_3-TPD, CO_2-TPD and probe molecule assisted XPS.

Further studies focused on strength and nature of basic sites [83], by gas-phase titrations with CO_2 and C_2H_2 coupled with in-situ FT-IR and DRIFT spectroscopy. Often, acid/base surface characterization has been corroborated by test reactions like Guerbet one or isopropanol decomposition [33,34], confirming both the amphoteric nature and the tunability of HAP's surface properties.

It must be pointed out that the majority of literature report on the determination of both number, nature and interaction strength of acid/basic sites using gas-solid techniques, while no liquid-solid characterizations are available to date. This lack of data does not allow to correlate performances of HAP in liquid phase (as catalyst or as sorbent) to the effective number of effective surface sites.

1.2.2 Adsorption capacity

Considering the importance of adsorption properties for candidate materials in the fields of environmental remediation and heterogeous catalysis, this brief insight on HAP adsorption capacity will fully justify both academic and industrial interest towards calcium apatite-based compounds.

1.2.2.1 Removal of inorganic species from aqueous solution

Thanks to its structural/compositional flexibility and surface reactivity, HAP has proven to efficiently adsorb and retain both cations and anions from aqueous solutions [11].

Literature reports HAP to be able to trap several metal cationic species, such as Cr, Pb, Cd, Ni, Zn, Al, Cu, Fe, Co, Mn and Fe [12,14–17,79,80,84,85], which are present in water in the form of cations. Different yields of removal are associated with different cations, according (*i*) the specific features of the HAP reported in the study and (*ii*) the affinity of the specific cation to HAP surface.

Considerations about point (*i*) stem from the plethora of synthetic methods available to obtain HAP. As a matter of fact, literature reports HAP materials with extremely variable surface area, porosity, degree of crystallinity, compositional purity and Ca/P ratio, thus making it difficult to compare results obtained by different research groups. All the above mentioned structural/morphological parameters are indeed proven to play a major role on metal removal performances [11]. In particular, higher surface area (and porosity) results to positively impact on HAP performance, whereas degree of crystallinity presents an inverse relationship with the cations removal efficiency [86]. It is important to stress that crystallinity and surface area are strictly connected, presenting nonetheless an inverse proportionality.

On the other hand, compositional purity effects on cations trapping efficiency are more complex to rationalize. Taking as example carbonated HAP (most common compositional modification in synthetic HAP, as previously discussed in paragraph 1.1.2), such anionic substitution alter Ca/P ratio while causing a modification of the surface properties at the same time. In this specific case, it has been reported [15] that carbonates functional groups affect the metal removing efficiency depending on the affinity of the adsorbate towards the latter and/or hydroxyl and phosphate groups. To date, no systematic study on how Ca/P ratio of pure HAP influence metal adsorption properties has been reported.

Focusing on studies in which a single batch of synthetic HAP has been tested for the removal of different cations, in single or multi-metal aqueous solutions [15–17,79,80,87], it is possible to shed light on point (*ii*).

In several studies, HAP exhibited preferential adsorption towards some cations over other, highlighting the fact that affinity between these species and HAP surface should be dictated by cations' valence and ionic radius (thus, charge density), electronegativity and speciation [11]. Obviously, operational parameters such as temperature, concentration, ionic strength and pH of the metal containing solution, stirring and contact time are not less important in determining the yield (and mechanism) of removal of metal species [16,17,46,79,80].

As discussed above, the pronounced heterogeneity of HAP surface allows the material to interact with adsorbates through several and distinct mechanisms. Thus, depending on the specific features of HAP surface and on the metal cation under study, adsorption can be exerted according to three main mechanisms: (*i*) ion-exchange, (*ii*) dissolution-precipitation and (*iii*) surface complexation.

(i) *Ion-exchange:*

Allowed by the compositional flexibility of HAP, this mechanism assume the replacement of a Ca^{2+} ion with a divalent cation, according to Equation 2 [86].

$$Ca_{10}(PO_4)_6(OH)_2 + x\,Me^{2+} \rightarrow Ca_{10-x}Me_x(PO_4)_6(OH)_2$$

Equation 2

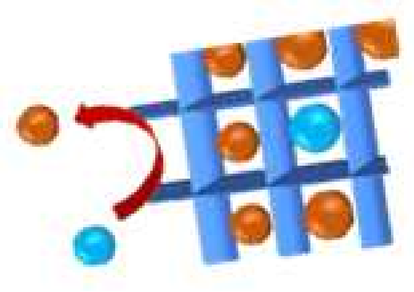

Figure 3: Schematic of ion-exchange mechanism (Ca^{2+} orange, Me^{n+} blue). From reference (Campisi et. al, 2018)

Ion-exchange mechanisms occur for metal cations with an ionic radius similar to that of Ca^{2+} (*ca*. 0.99 nm) [79]. Solution pH also plays a role in defining the mechanism's efficiency. Indeed, several studies reported that acidic pH hinder ion-exchange processes [84], inasmuch pH values lower than pH_{PZC} of HAP (generally ranging from 4 to 6) will cause electrostatic repulsion between sorbent surface and adsorbate [46].

It has to be stressed that, since adsorption is a phenomenon taking place at the surface, only surface exposed Ca^{2+} sites are supposed to be reactive in this kind of process. Moreover, due to the defect-bearing nature of HAP, the ion-exchange mechanism has proven to be effective even towards mono- and trivalent cations [79], with the lattice rearranging as to achieve a new charge-balanced configuration.

The presence of nonequivalent Ca(I) and Ca(II) sites complicates a thorough determination of sites' occupation [11] which is fundamental in assessing the coordination of the newly-entered metallic species. Since Me-doped HAP are often exploited in catalytic processes [8,9,11], ascertain the sitting of metal species if fundamental to correlate catalyst structure to catalytic performances.

(ii) *Dissolution-precipitation:*

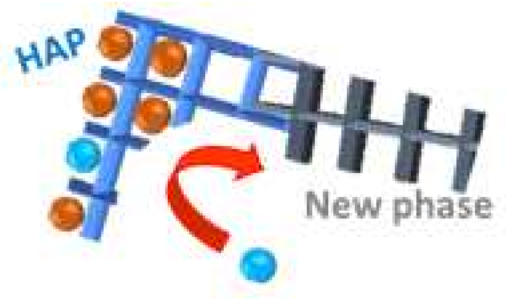

Figure 4: Schematic of dissolution-precipitation mechanism. From reference (Campisi et. al, 2018).

This mechanism takes place for metal cations which are able to form phosphate-based salts that result more stable than HAP itself (i.e. less soluble). In this case, HAP behaves more like a reactant than a sorbent: its dissolution supplies the media with phosphate ions which allows for the precipitation of metal cations present in the solution. The process is coupled with the formation of a new phase, normally with an apatitic structure.

The phenomenon can be described by the following equations:

$$Ca_{10}(PO_4)_6(OH)_2 + 14\,H^+ \rightarrow 10\,Ca^{2+} + 6\,H_2PO_4^- + 2H_2O$$

$$(10-x)\,Me^{2+} + (10-y)\,Ca^{2+} + 6\,H_2PO_4^- + 2H_2O \rightarrow Ca_{10-x}Me_{10-y}(PO_4)_6(OH)_2 + 14\,H^+$$

Equation 3

Among all the metal species trapped by HAP, Pb^{2+} distinguished itself for being trapped according to the present mechanism, with the formation of a crystalline lead-phosphate phase, namely hydroxyl pyromorphite, $Pb_{10}(PO_4)_6(OH)_2$ [15–17,79,80].

(iii) *Surface complexation:*

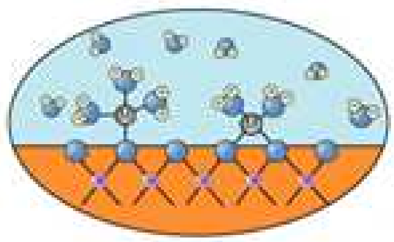

Figure 5: Schematic of surface complexation onto HAP surface.

The high degree of functionalization render HAP surface complexation one of the main trapping mechanisms exerted by the material toward metal cations. As reviewed in paragraph 1.2.1, HAP presents an amphoteric surface, which exposes Lewis and Brønsted basic features, such as Ca^{2+} vacancies and O^{2-} (from PO_4^{3-} functionalities) and OH^-, respectively. In the case of carboapatites, PO_4^{3-} and/or OH^- are partially replaced by CO_3^{2-}. In both situations, basic groups exert a complexing action towards the cations present in the contacting solution, thus immobilizing them onto HAP surface. As a matter of fact, surface complexation can be regarded as the first step of any adsorption process, thus playing a key role in both catalytic and sorption performance of the material.

1.2.2.2 Removal of organic pollutants from aqueous solution

Thanks to the possibility to participate in hydrogen bonds and the natural complexing ability of its surface functional groups, HAP has been reported to adsorb a long list of organic pollutants among which are counted dyes [88], benzene nitro-derivatives [89] and phenolic compounds [90]. Mechanisms of trapping of such molecules are primary surface complexation, hydrogen bonding and physical adsorption.

However, in the field of organic pollution remediation HAP-based materials are outperformed by carbonaceous materials, with the latter benefitting of higher surface area and π-π interaction ability, coming on top of large availability and low-cost [91]. From the point of view of environmental remediation of water streams, HAP-based and carbonaceous material can be actually considered complementary sorbent materials, both displaying low-cost, large natural availability and eco-friendly nature.

1.2.2.3 CO_2 adsorption onto HAP surface

CO_2 is the major contributor to global warming, being release in huge daily amount from fossil fuel consuming anthropogenic activities. Concurrently with the strive for the development of renewable energy technologies, CO_2 storage and conversion became a relevant topic in the last decades.

Various sorbent materials have been tested for CO_2 storage, with high surface area and basic ones (i.e. CaO, Li_4SiO_4 and Li_2ZrO_3) standing out as the most promising [92]. CO_2 molecule is indeed a Lewis acid, exhibiting a partial δ^+ at the carbon atom and partial δ^- on both O atoms, thus able to be strongly chemisorbed by basic functionalities.

Calcium phosphates compounds, including HAP, have been reported to effectively adsorb and retain CO_2 [93] when implemented as filter in a chimney-like configuration, where simulated combustion gas is continuously flowed. In such experiments, amorphous calcium phosphate was able to achieve complete removal of CO_2 in the stream after 2 hours and then maintaining a 100% process efficiency for long operation time. However, XRPD analyses revealed the presence of crystalline $CaCO_3$ on the exhaust material, thus highlighting a structural modification. On the other hand, HAP exhibited slightly lower but still outstanding performances, immobilizing *ca*. 15.9 $g_{CO2}\ g_{HAP}^{-1}$ while retaining its crystalline structure and notwithstanding the *ca*. 16-fold lower surface area in comparison with its amorphous counterpart.

Cheng et al. [94] were among the first to evaluate CO_2 adsorption capacity of HAP, reporting quantitative results from CO_2 adsorption isotherms. Cycling multiple CO_2 adsorption and desorption stages, reversibility of CO_2 adsorption was assessed to correlate with Ca/P ratio of HAP, i.e. with the acid/basic surface sites ratio. More specifically, the reversibility of the adsorption processes resulted to be strictly connected with the number of surface PO_4^{3-} groups (quantitatively determined by FT-IR), which were then supposed to act as reversible CO_2 adsorption sites. Ca-OH surface groups were instead deemed to cause irreversible CO_2 adsorption, with the formation of type A surface carbonates and physisorbed water (Figure 6).

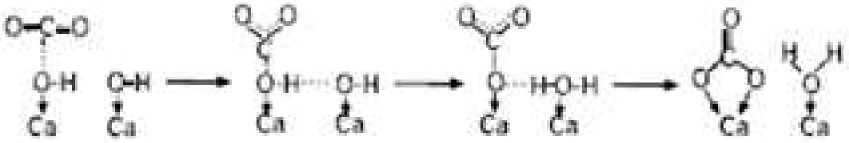

Figure 6: Mechanism of irreversible CO_2 adsorption on Ca-OH surface group of HAP. From reference (Cheng et. al, 1998)

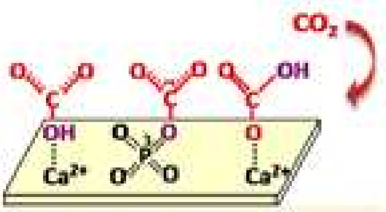

Figure 7: Schematics of CO_2 adsorption on HAP surface. From reference (Diallo-Garcia et. al, 2014)

A thorough study of CO_2 adsorption sites present on HAP surface was performed by Diallo-Garcia et al. [95]. The authors used CO_2 as Lewis acid probe molecule to shed light on the nature of HAP surface basic groups, following the adsorption process by in-situ FT-IR. The investigation revealed the presence of three possible CO_2 adsorption sites on HAP surface, namely the PO_4^{3-} and Ca-OH basic moieties and Ca^{2+} acidic functionalities (Figure 7).

As reported in Figure 8, CO_2 adsorption onto HAP surface generates peculiar FT-IR signals, related to physisorbed (2352 cm^{-1}) and chemisorbed CO_2. The two basic moieties present on HAP surface, phosphate and hydroxyl groups, give raise to two distinct surface features: $(PO_x)_s$-carbonates (1485-1385 and 1370-1345 cm^{-1}) and hydrogencarbonates (HCO groups, ranging from 1758 to 1180 cm^{-1}, stretching/bending modes), respectively. As indicated in Figure 6, hydrogencarbonates are formed upon CO_2 adsorption onto Ca-OH groups and has to be referred to as an unstable intermediate towards type A surface carbonates. Indeed, with increasing contact time, physisorbed CO_2 signal decrease in correlation with an increase in surface type A carbonates and physisorbed water, thus confirming the irreversible nature of CO_2 adsorption on Ca-OH sites (Figure 6). It is noteworthy that even Ca^{2+} acidic sites can collaborate in hydrogencarbonates formation and stabilization, by means of Lewis acid-type interaction with the partial δ^- of CO_2 oxygen atoms (Figure 7).

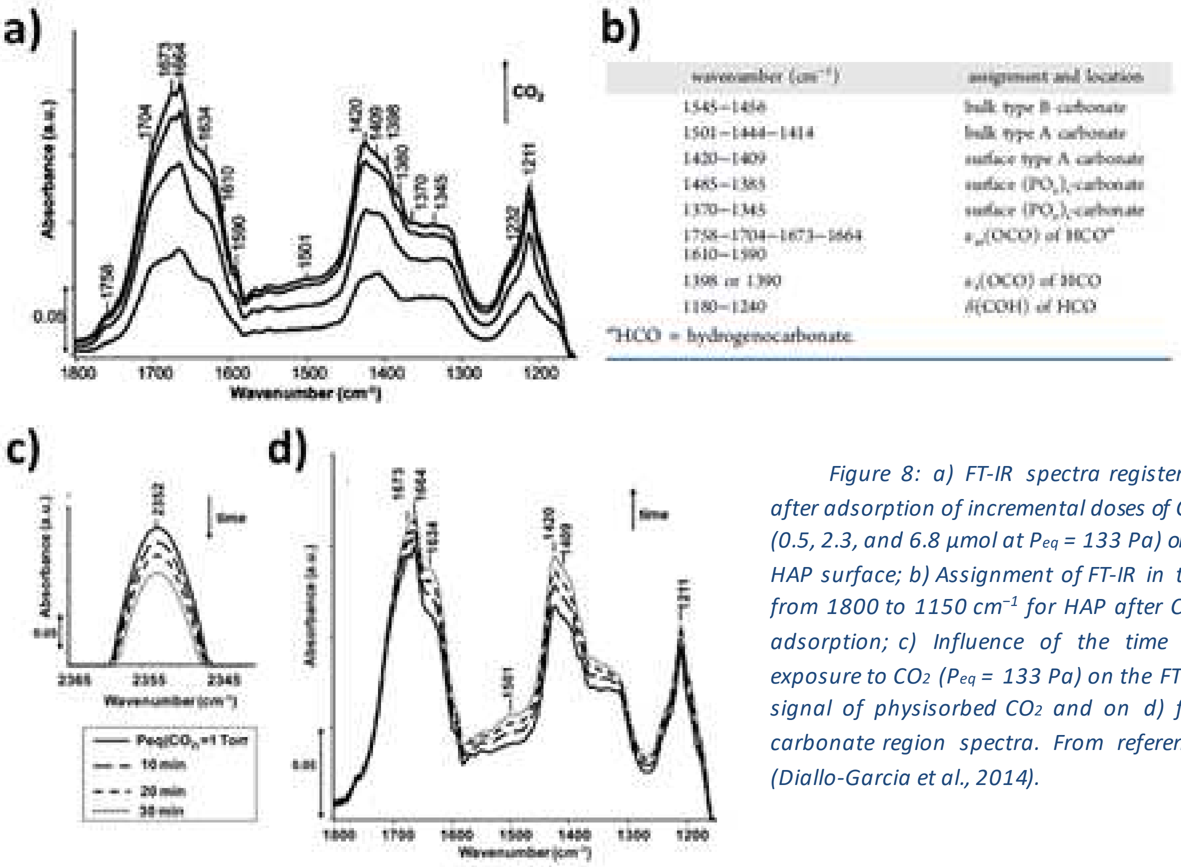

wavenumber (cm^{-1})	assignment and location
1545–1456	bulk type B carbonate
1501–1444–1414	bulk type A carbonate
1420–1409	surface type A carbonate
1465–1385	surface $(PO_x)_s$-carbonate
1370–1345	surface $(PO_x)_s$-carbonate
1758–1704–1673–1664 1610–1590	ν_{as}(OCO) of HCO^a
1398 or 1390	ν_s(OCO) of HCO
1180–1240	δ(COH) of HCO

^{a}HCO = hydrogenocarbonate.

Figure 8: a) FT-IR spectra registered after adsorption of incremental doses of CO_2 (0.5, 2.3, and 6.8 µmol at P_{eq} = 133 Pa) onto HAP surface; b) Assignment of FT-IR in the from 1800 to 1150 cm^{-1} for HAP after CO_2 adsorption; c) Influence of the time of exposure to CO_2 (P_{eq} = 133 Pa) on the FT-IR signal of physisorbed CO_2 and on d) full carbonate region spectra. From reference (Diallo-Garcia et al., 2014).

On the other hand, $(PO_x)_s$-carbonates signal seems to be altered only by CO_2 partial pressure and upon degassing it disappears first, confirming both interaction weakness and reversibility of CO_2 adsorption on phosphate sites. Dissociation of phosphate groups and formation of stable carbonates result impossible on such sites, confining CO_2 to a relatively stable surface-bond and bent configuration.

If CO_2 storage capacity of HAP is interesting to limit CO_2 emissions, way larger interest stems from the possibility to implement HAP (and phosphate chemistry in general) as dopant/active phase supports in catalysts performing CO_2 valorization processes. Indeed, the selective and reversible adsorption of CO_2 in bent configuration operated by phosphate groups could boost such processes, lowering interphase diffusion limitations and the overall activation energy of the process, that is normally penalized by the extreme stability of the linear configuration of CO_2 itself [96].

To date, the only application of HAP as co-catalyst/dopant has been reported by Chong et al., where HAP has been successfully employed on Pt/TiO_2 photocatalysts for photo/electrochemical CO_2 reduction, leading to satisfactory results in terms of lowering of the activation energy of the process [63].

Chapter 2: Synthesis and characterization of HAP for the removal of polluting metal species from wastewater

2.1 Metal pollution in waterbodies and its remediation: state of art

Water is a key factor for human, animal and plant life and it is regarded as one of the most important resources even from an industrial and economical point of view. Notwithstanding the wide abundancy at the earth's surface (estimated volume of 1.4 billion of km^3), less than 1% of such water can be classified as ready for use freshwater [97]. Population growth, in concomitancy with industrialization and gentrification, calls for an increase in freshwater demand and, at the same time, to a ramping pollution of water streams. Municipal and industrial waste discharges often suffer from low capacity, outdated and inefficient wastewater treatment units, behaving as bottlenecks in the anthropogenically modified water cycle. Indeed, time consuming processes for wastewater remediation lead to water scarcity. On the other hand, faster processes generally lack efficiency in removing polluting species, thus may cause the release of harmful compounds in the environment. Such pollution impacts on plants, animal and human health by means of pollutants' bioaccumulation through the food chain.

Among the polluting species that can be found in industrial and municipal water streams, heavy metals are an unavoidable issue that modern society must face. The main pollution sources are related to anthropogenic activities such as mining, smelters, cement/metal/electrical/chemical industries, fossil fuel combustion and pesticide/antibiotic use [98,99]; amid these pollution sources, metal processing and mining are the main contributors (concurring to *ca*. the 48% of the total release of contaminants in Europe [98]).

Although the definition is still under debate, the term "heavy metals" applies to the group of elements with a density higher than 4 g cm^{-3} and/or an atomic molar mass comprised between 63.5 and 200.6 g mol^{-1}, including both metals and metalloids [98–101]. According to this definition, species like As, Cd, Co, Cr, Cu, Hg, Mn, Ni, Pb, Sn, V, and Zn fall into the heavy metals group.

The vast majority of heavy metal species is naturally present on the earth's crust in detectable concentration, both in water and soil. Some of these species, in determined speciation and oxidation states, are even biologically essential (i.e. Cu(II) and Cr(III), as micronutrients [102]). However, increased concentration of these elements, caused by pollution emission from anthropogenic activities, has been proven to impact on human health [103]. Non-essential species (for example Pb(II) and Hg(II)) are instead toxic to living organisms even at concentrations as low as $\mu g\ L^{-1}$ (so, in the range of ppb). Heavy metals usually dispose of a rich speciation, reactivity and enhanced tendency to form complexes/coordination compounds, features imparted by their electronic shell. So, mobile forms of these elements can easily form in nature and spread to the environment through several media [98,99]. Moreover, heavy metals are bioavailable but non-biodegradable [98,99]. Thus, after entering in a living organism, they persist without being metabolized. So, they propagate through the food chain and, when ingested, they give rise to the phenomenon of bioaccumulation, which could cause several diseases. As a matter of fact, acute poisoning from heavy metals is rarely detected while chronic assumption of small doses of heavy metals generally results in bone degeneration and damage of both soft tissues, organs and blood [99].

Since this dissertation will focus on principally five heavy metal species (Cr(III), Cu(II), Ni(II), Co(II) and Pb(II)), Table 2 shows their anthropogenic sources, legislation limits in drinking and irrigation water, lethal doses and diseases arising from their long-term assumption. Table 3 reports instead on pollution of such species in some industrialized zones, highlighting the issue of concomitant presence of multiple harmful elements.

Table 2: Anthropogenic sources, maximum concentration levels, human assumptions and correlated diseases for selected heavy metal species (adapted from references Vareda et al. 2019, Burakov et al. 2018 and Wadhawan et al. 2020).

Heavy metal species	**Pollution sources**	**MCL**[a]		**PTWI**[d]	**Diseases correlated with chronic assumption**
		Drinking water[b]	*Irrigation water*[c]		
Co	Primary metallurgical processes Electroplating industries Paint industries Nuclear power plants Battery manufacturing Mining	N.S.	N.S.	N.S.	Skeletal deformities Diarrhea Hypertension Pulmonary issues Paralysis
Cr	Primary metallurgical processes Electroplating & coating industries Mining	50 $\mu g\ L^{-1}$	100 $\mu g\ L^{-1}$	-	Headache Nausea Diarrhea Carcinogenic
Cu	Battery manufacturing Corrosion of household plumbing Electrical industry Fertilizers Mining	2000 $\mu g\ L^{-1}$	200 $\mu g\ L^{-1}$	0.5 $mg\ kg^{-1}{}_{BW}$	Liver damage Wilson's disease Insomnia
Ni	Nickel plating industries Primary metallurgical processes Battery manufacturing	7 $\mu g\ L^{-1}$	200 $\mu g\ L^{-1}$	-	Dermatitis Chronic asthma Carcinogenic
Pb	Plumbing fixtures Cable coverings Ceramics & glasses Battery manufacturing Paint industries Oil (additive) Mining	10 $\mu g\ L^{-1}$	5000 $\mu g\ L^{-1}$	0.025 $mg\ kg^{-1}{}_{BW}$	Cerebral disorder (Saturnism) Renal, circulatory and nervous disorders

[a] *Maximum Concentration Limit;*

[b] *From reference* [104]

[c] *From reference* [105]

[d] *Provisional Tolerable Weekly Intake for humans* [106]

As it can be seen from Table 2, legal limits for Co(II) pollution are still not defined by WHO, FAO and/or national organization since its presence in wastewater is a quite recent issue, mainly correlated to its novel and large application in the energy storage field (e.g. as lithium battery dopant [107,108]). Relatively high concentrations of Pb(II) in irrigation water are instead allowed on the basis of its scarce mobility, solubility and bioavailability in soils, where it tends to bind with organic and colloidal matter [98].

Table 3: Relative water concentration of selected heavy metals in polluted sites exhibiting different pollution sources (adapted from reference Vareda et al. 2019).

Source nature	**Specific site**	**Relative water concentration**[a]				
		Co	*Cr*	*Cu*	*Ni*	*Pb*
Mines	Iberian Pyrite Belt, Spain	-	7.78	111.35	1955	160.70
	Yiyang, China	-	13.20	0.05	85.71	3.00
Industrial sites	Electroplating wastewater, XXX	-	35.9	3.2	1.3	8.6
	Dehli industrial area, India	-	Up to 319	Up to 48	Up to 40	Up to 326
Rivers in industrial area	Khoshk river, Iran	-	11.00	0.03	28.57	13.00
	Yamuna river, India	-	39.66	8.82	392.59	111.21

[a] *Expressed as ratio between metal species in waterbodies and the same metal legal limit in drinking water.*

Probably because of the absence of strict legal limits, Co(II) species concentration in wastewaters is not reported in the vast majority of up to date review papers (Table 3), notwithstanding extensively research has been recently conducted on the topic [109]. However, since its increasing exploitation as dopant in Li-based batteries and other electrical applications, Co(II) concentration is expected to raise in battery manufacturing and electrical industries effluents, probably in combination with another common dopant as Ni [107].

Data reported in Table 2 and Table 3 underline (*i*) the strict legislation that industrial and municipal water remediation facilities are subjected to, (*ii*) the hazardousness of chronic heavy metal species assumption, even at low concentration and (*iii*) the widespread nature of the problem, exacerbated by the remarkable mobility of these pollutants and their persistency in living organisms.

To preserve environment equilibria and human and animal health, wastewater must be treated before being discharged. Several methods for heavy metal remediation have been proposed, studied and applied in the last decade [98,101]. Their suitability depends on a plethora of factors, with efficiency of removal, operation time and cost, industrial feasibility/scalability and secondary pollution issues being the most important.

The most common physical-chemical technologies applied to wastewater remediation are chemical precipitation, flocculation/coagulation, membrane filtration (category including reverse osmosis, nanofiltration and ultrafiltration, in decreasing order of performances), ion-exchange, electrochemical methods (electrodialysis and electrodeposition) and adsorption [98,99,101]. The main advantages and drawbacks of all these techniques are briefly summarized in Table 4.

Table 4: Comparison of strengths and weaknesses of the most common techniques employed in heavy metal remediation of wastewaters (adapted from reference Vareda et al. 2019).

Process	Advantages	Drawbacks
Chemical precipitation	Low cost Zero energy consumption Simple design and operation Safe operation	High consumption of precipitant agent Production of high volume of sludge with high disposal cost Stringent disposal standards for sludge itself
Flocculation/coagulation	Fast settling of suspensions Improved sludge settling	Sludge production with related disposal expenses
Membrane filtration	Small space requirement High efficiency Tunable selectivity	High operation cost Membrane fouling High pressures and energy consumption required to achieve high efficiencies
Ion-exchange	No sludge production High removal capacity Fast kinetics Selectivity	All-purpose resins do not exist High cost of the resins Resins regeneration Treatment of regeneration solution (secondary pollution risk)
Electrochemical methods	Selectivity High efficiency No sludge production	High costs in terms of electrical power consumption Not cost effective for non-precious metals
Adsorption	Simple design and operation Low operational cost High efficiency Low-cost adsorbents available Can be selective	Efficient sorbents could be expensive Disposal/regeneration of the “exhausted” sorbent

A thorough analysis of the pros and cons of the processes highlight that low-cost unit operations (i.e. chemical precipitation, flocculation/coagulation) are prone to generate remarkable quantity of sludges, whose disposal costs hinder the economical sustainability of the process, besides opening to the possibility of secondary pollution. Faster, cleaner and more efficient and selective techniques (based on filtration and or electrochemical techniques) are on the other hand expensive in terms of energy consumption and/or installation costs.

Adsorption stands out among all remediation methods since it is characterized by low capital and operational costs, limited space occupation, flexibility, high volume treatment capability and an overall simple design of process. In the adsorption process, pollutant dissolved in the aqueous phase are confined on a solid (sorbent) surface by means of physisorption (Van der Waals and coulombic forces) and/or chemisorption (creation of a new chemical bond, covalent or ionic). The efficiency of the process is tightly related to the sorbent properties, in addition to operational conditions (i.e. pH, solution’s ionic strength, stirring, temperature, concentration of polluting agent, volume to solid ratio, co-presence of pollutants, etc.). With the appropriate adsorbent, efficient removal of heavy metal species with fast kinetics can be achieved.

More than 3000 papers on heavy metal removal by different sorbents have been published in 2018 [98]; several materials of both natural and synthetic origin proved to be potentially adequate for industrial remediation applications [98,99,101,110,111]. Despite differences in testing conditions, literature agrees on some physical/chemical properties as fundamental for a sorbent to be efficient: high surface area, high degree of surface functionalization and thermal and chemical stability. In addition to these "technical" features, economical and industrial evaluations ask for low-cost, availability, non-toxicity and reusability/recyclability of the spent sorbent [98,99].

For the above mentioned reasons, the main conventional sorbents such as activated carbon and metal oxides/hydroxides (expensive, difficult to reuse/recycle and often subjected to secondary pollution issues) have been gradually put aside in favor to novel low-cost nanostructured materials, derived from renewable resources: zeolites, nanostructured allotropes of carbon clays/inorganics, chitosan and bio-derived polymers [99].

Hydroxyapatite belongs to the family of these emerging and environmentally sustainable materials. It possesses all the common physical/chemical features requested for an optimal sorbent, as previously reported in paragraph 1.2.2.1, together with the possibility to be synthesized from Ca-rich wastes from the food industry. HAP performances in wastewater remediation are outstanding: HAP can adsorb some hazardous cationic species like Cr, Pb, Cd, Ni, Zn, Al, Cu, Fe, Co, Mn, and Fe [16,79,80], with efficiencies that depend on both HAP characteristics and operational conditions. Some authors reported an almost total retention of pollutants by metal-loaded HAP when tested for leaching in water and/or more aggressive solutions [79]. Although this permanent confinement of hazardous species could be seen as optimal in terms of secondary pollution risks, it hinders the regeneration of the sorbent, posing serious threat to its application at industrial level. Exploitation of the metal-loaded HAP as catalyst in reaction of environmental concern [9,11] could overcome the problem, creating the HAP valorization cycle that our group has been working to validate in the last years and that will be illustrated in the Final Summary of this dissertation (Section 5).

Interestingly, when studying multi-metal polluted solutions, some authors reported preferential adsorption onto HAP surface of some cations over other. Several factors affect removal efficiency and competitive effects: (*i*) higher affinity of specific species towards HAP surface [16,79,80], (*ii*) HAP degree of crystallinity [86] and (*iii*) elemental composition (both in terms of Ca/P atomic ratio and carbonate substitution [15]). Besides efficiencies of removal, adsorption mechanisms are determined by sorbent-sorbate interaction as well. Cations' electronegativity and especially charge density (i.e. ionic radius and valence) are reported in literature to address the metal uptake towards a specific mechanism [11,79]. However, literature is not consistent in pairing metal species and uptake mechanism onto HAP surface, highlighting that the underpinnings of the phenomena are complex and not fully understood. No proper volumetric and thermodynamic studies, respectively aimed to a full comprehension of the removal efficiency and the energetics of cations trapping, are reported to date.

In this chapter the synthesis and structural, morphological, compositional and surface characterization of stoichiometric HAP will be reported. Then, efficiencies, competitive effects and mechanism of uptake of target heavy metals onto HAP surface have been investigated by means of both volumetric (i.e. batch adsorption tests and collection of adsorption isotherms) and thermodynamic (i.e. liquid phase microcalorimetry) techniques, shedding light on the adsorption phenomena, mainly in terms of uptake mechanism, energetics and overall sorption performance. Leaching tests results are presented as well. Then, two specific case studies, in which stoichiometric HAP will be applied to the remediation of complex simulated industrial effluents will be presented and discussed. Finally, HAP performances in heavy metal remediation and the new insights provided by this multi-disciplinary approach to the topic will be wrapped up in the conclusion section.

2.2 Physical-chemical characterization of synthetic hydroxyapatite

Stoichiometric HAP has been synthesized according to a wet co-precipitation method, starting from $Ca(NO_3)_2 \cdot 4H_2O$ and $(NH_4)_2HPO_4$ solutions as Ca(II) and PO_4^{3-} precursors, respectively. Details of the synthetic route are reported in section 8.1.1. This optimized synthesis returns *ca.* 4.19 g of stoichiometric HAP per batch, with an almost quantitatively reaction yield (> 99%).

Synthetic HAP has been structurally, morphologically and compositionally characterized by means of ICP/AES for Ca/P atomic ratio determination, nitrogen adsorption-desorption isotherms (N_2 ads/des), scanning transmission electron microscopy coupled with energy-dispersive X-ray probe (STEM/EDX), synchrotron X-ray powder diffraction (XRPD), Fourier Transform Infrared Spectroscopy (FT-IR) and zeta-potential measurements (for the determination of HAP's point of zero charge, pH_{PZC}). Since chemical stability is paramount for a material to be considered a reliable sorbent, synthetic HAP (hereinafter referred to as pristine or as prepared HAP) has been subjected to harsh conditions (immerged in an aqueous solution at pH 3 by HNO_3 for 24 h) and then comparatively investigated.

Surface features of as prepared HAP (i.e. acid and basic sites) were investigated by means of state-of-art gas-solid techniques (collection of calorimetric/volumetric adsorption isotherms) and novel liquid-solid titrations (according to the Liquid Recirculation Chromatographic Method [112]).

Instrumental and procedural details of these analyses can be found in the Experimental Section, paragraphs 8.2.1 and 8.2.4, respectively.

2.2.1 Structural, morphological and compositional characterization

Ca/P ratio of synthetic HAP has been measured by ICP/AES on solutions of mineralized sample. HAP exhibited stoichiometric Ca/P ratio (Table 5), which is consistent with the ratio of the synthetic conditions (i.e. concentration ratio between precursors' solutions).

N_2 adsorption/desorption isotherms of synthetic HAP are presented in Figure 9a. According to IUPAC classification, HAP exhibits a type IV isotherm, which is typical of mesoporous materials. Limited uptake of N_2 at high p/p^0 indicates scarce macroporosity. The presence of a hysteresis loop is associated with capillary condensation in mesopores; always according to IUPAC classification, its shape belongs to type H2. Such loop is particularly difficult to interpret and generally attributed, rather over-simplifying, to condensation/evaporation processes occurring in bottle-shaped pores [113]. Specific surface area of HAP has been evaluated applying the 3-parameters BET model equation (Figure 9b) to the low-pressure region of the adsorption branch and stood around 85 $m^2\ g^{-1}$ (Table 5). Mean pore radius, pore volume (Table 5) and pore size distribution (Figure 9c) have been calculated by means of B.J.H. model. HAP confirmed its mesoporous nature, showing a mean pore radius of *ca.* 4 nm with a pore size distribution almost fully centered in the 2 to 10 nm region.

After exposure to acidic environment, Ca/P atomic ratio of HAP increases to an over-stoichiometric value of *ca.* 1.72 (Table 5). Such a variation could be ascribable to (*i*) preferential dissolution, inducing Ca and PO_4^{3-} defectiveness and/or ionic substitutions or (*ii*) decomposition of HAP with formation of new phases and/or highly defective amorphous segregation. On the other hand, morphological features of the material appear not to be altered; the surface area value is indeed comparable to that of pristine HAP while only a small decrease in mean pore radius and pore volume are detected (Table 5), probably ascribable to a moderate pore collapse. N_2 adsorption/desorption isotherms, BET interpolation and pore size distribution for HAP after exposure to acidic environment are available in the Supplementary Material (paragraph 10.1.1, Figure 78).

Table 5: Compositional and morphological features of HAP: as prepared and after the exposure to an acidic aqueous solution.

Sample	**Ca/P ratio**	**Surface area**[b]	**Mean pore radius**[c]	**Pore volume**[c]
	atom/atom	*m^2 g^{-1}*	*nm*	*cm^3 g^{-1}*
As prepared HAP	1.662 [d] ± 0.039	85.05[d] ± 1.49	4.26[d] ± 0.06	0.219[d] ± 0.004
Post-stability test HAP[a]	1.715	84.98	3.99	0.190

[a] *Sample exposed to acidic conditions (pH 3) by HNO_3 for 24 h*

[b] *Evaluated according to 3-parameter BET model.*

[c] *Evaluated according to B.J.H. model.*

[d] *Average values from different HAP batches.*

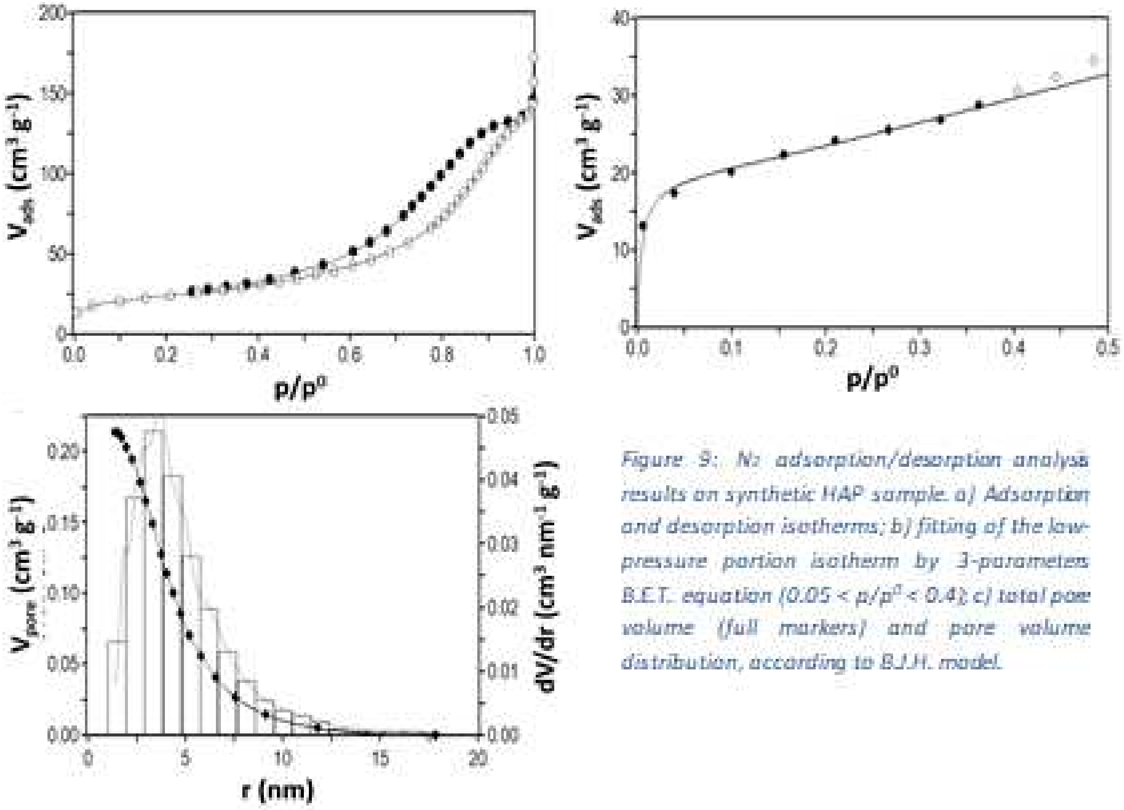

Figure 9: N_2 adsorption/desorption analysis results on synthetic HAP sample. a) Adsorption and desorption isotherms; b) fitting of the low-pressure portion isotherm by 3-parameters B.E.T. equation (0.05 < p/p^0 < 0.4); c) total pore volume (full markers) and pore volume distribution, according to B.J.H. model.

TEM micrographs of HAP disclose a needle-shape morphology (Figure 10a), with crystallites dimension ranging from 40 to 200 nm in length and from 6 to 8 nm in width. Crystallite domains appear to be stacked one upon another along their length, following a head-to-tail arrangement. Further investigation by high resolution TEM (Figure 10b) reveal that crystallites elongated along the c-axis: indeed, the 0.81 nm spacing between crystal lattices can be address to (100) planes of hexagonal HAP. The diffraction pattern reported in Figure 10c proves the polycrystalline nature of the material: several diffraction rings are displayed, all indexed as crystallographic planes of HAP. EDX analysis (available in the Supplementary Material, Figure 79), performed on selected area, indicates the presence of solely Ca, P and O, thus confirming the phase purity of synthetic HAP. Ca/P ratio from EDX analysis has not been reported since the method does not qualify as quantitative.

In Figure 10d, the synchrotron radiation XRPD pattern of HAP is reported together with the final Rietveld refinement, calculated according to the $P6_3/m$ space groups structure of HAP. The refinement confirmed the phase purity of the sample. Moreover, the absence (within the experimental resolution) of amorphous material has been checked by analyzing mechanical mixtures of TiO_2 (with known rutile/anatase ratio) + HAP, applying the principles of PDF analysis (patterns reported in the Supplementary Material, Figure

80b). In fact, PDF/G(r) (analysis of diffraction data in the actual interatomic distances space) allows to detect possible positional disorder [114] as well as symmetry decreases in respect to the average structure [115], both contributions determined by the presence of amorphous phases. Data have been fitted against the hexagonal model of HAP and results in the 1–10 Å ranges are graphically reported in Figure 10e. Fits at higher r values is graphically reported in the Supplementary Material (Figure 80d). Most important contributions to the PDF peaks in the 1.5–5 Å range are indicated in the figure. Only a small peak around 2 Å was not assigned (labelled with an asterisk). To sum up, the correspondence between collected and fitted pattern extended down to very low r values points to the absence (or negligible presence) of amorphous phases, which would cause discrepancies between experimental and fitted peaks [116]. HAP crystallographic structure is not affected by exposure to acidic environment: no alterations in cell constants, atomic positions, and apd values (Supplementary Material, Figure 80a and c) are evidenced.

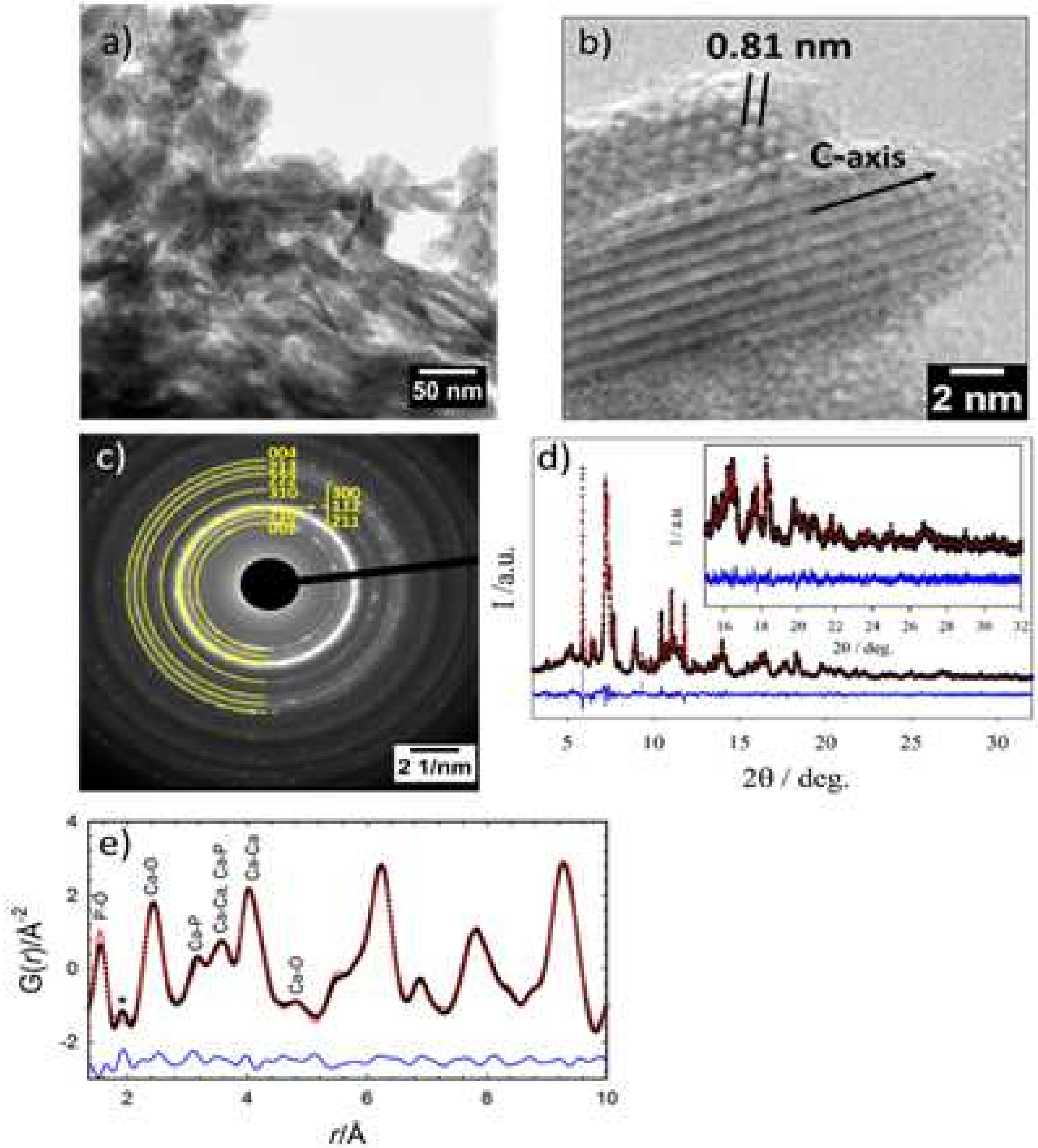

Figure 10: Morphology and structure of synthetic HAP sample. a) Representative TEM micrograph of HAP; b) high resolution TEM micrograph of two nanocrystal domains with the c-axis parallel and perpendicular to the image plane, respectively; c) Selected Area Electron Diffraction (SAED) pattern indexed to the hexagonal HAP phase; d) Synchrotron XRPD pattern, measured (black crosses) and calculated (red line) profiles with residuals (blue line); inset highlights the high angle (2ϑ) regions patterns of the sample; e) G(r) refinement using the real space Rietveld method, observed (black crosses), calculated (red line), and residual (blue line).

Further confirmation comes from refinement of cell parameters, performed on both pristine and acid environment exposed HAP. Refined parameters are reported in the Supporting Material, Table 32. Synthetic HAP exhibits slightly smaller unit cell's dimensions and volume in respect to theoretical calculations for hexagonal ($P6_3/m$) HAP. After exposure to acidic environment, cell parameters are slightly increased, slightly overcoming theoretical values. The minimal discrepancy (*ca.* 0.3%) from theoretical and calculated unit cell's dimension can be accounted as intrinsic computational error.

Transmission FT-IR spectra of pristine HAP and after exposure to acidic conditions are reported in Figure 11a. As typical of apatites, IR spectra presents contributions in three main regions. The broad band with maximum between 3300 and 3500 cm^{-1} is generated by O-H stretching modes of water molecules, both adsorbed on surface and constitutive. The sharp band at *ca.* 3570 cm^{-1} is instead assigned to the O-H stretching mode of structural hydroxyl groups. Contributions in the low energy region (from 500 to *ca.* 1100 cm^{-1}) are addressed to phosphate groups fundamental vibrational modes. The bands in the region comprised between 1350 and 1600 cm^{-1} are ascribable to partial carbonatation, the most common compositional impurity found in synthetic HAP. As prepared HAP exhibits minima and negligible contributions for both A-type and B-type carbonates, suggesting that the material can be considered compositionally pure, as indicated by Ca/P atomic ratio, TEM/EDX analyses and XRPD refinements. Conversely, exposure to acidic environment causes an increase in the carbonatation degree of HAP, as clearly detectable from Figure 11a. This carbonatation effect could be due to partial dissolution of HAP under acidic conditions and partial replacement of structural phosphate and hydroxyl groups by carbonates originated by the CO_2 dissolved in solution. Magnification in Figure 11b highlights an almost equivalent intensity of contribution from both bulk A and B-type carbonates species [83], thus suggesting simultaneous substitution of phosphate and hydroxyl groups. PO_4^{3-} replacement by CO_3^{2-} could explain the increase in Ca/P ratio in HAP subjected to acidic treatment.

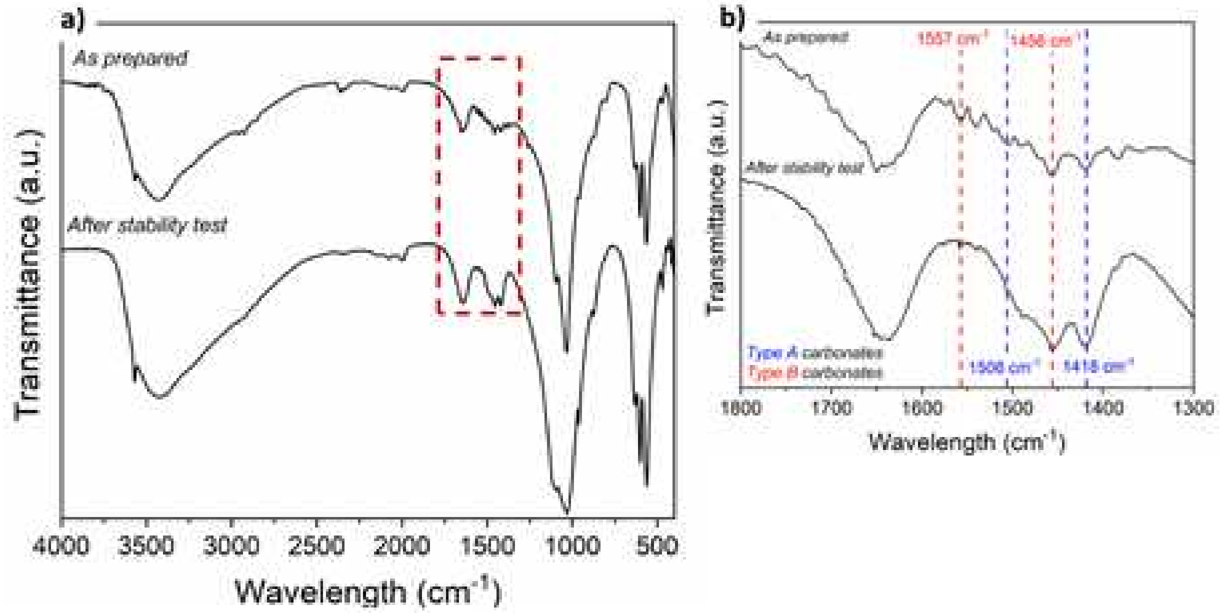

Figure 11: a) FT-IR spectra comparison between as prepared HAP and post-acid solution exposure; b) carbonate region (1600 to 1350 cm^{-1}) magnification.

Finally, zeta-potential measurement of pristine HAP allowed to assess the pH_{PZC} of the material. As reported in Figure 12, pH_{PZC} of synthetic stoichiometric HAP is *ca.* 5, in accordance with the values reported in literature for synthetic stoichiometric HAP [44,46]. However, the determination of pH_{PZC} of an amphoteric material is always associated with a relevant error, stemming from the dual nature of the material's surface.

The pH_{PZC} here reported can thus be considered a first and rough evaluation of the surface properties/reactivity in aqueous solution, while more rigorous approaches for the proper quantification of the number and interaction strength of acid/basic HAP surface sites will be carried out by ad-hoc techniques (paragraph 2.2.2).

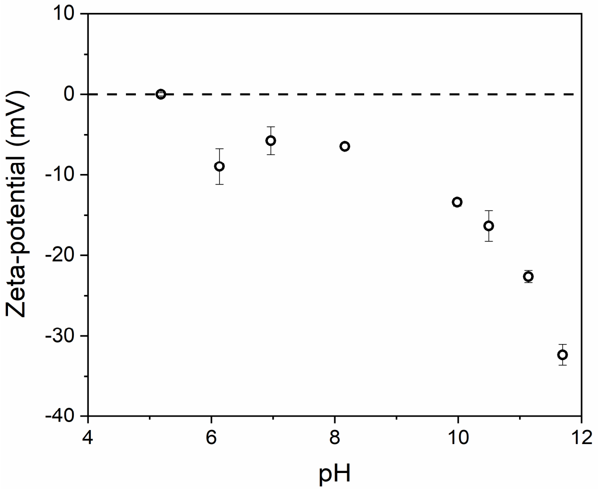

Figure 12: Zeta-potential determination vs. pH for pristine HAP

In conclusion, the material obtained by co-precipitation is a strictly stoichiometric HAP and it presents phase and compositional purity. The material is nanostructured (nano-needles elongated along the c-axis), thus exhibiting high surface area despite the high crystallinity degree. HAP resulted structurally and morphologically stable under harsh conditions (aqueous solution at pH 3 by HNO_3) for relatively long exposure time (24 h); slight increase in Ca/P atomic ratio in the post-treated material could be ascribed to an increased carbonatation degree.

2.2.2 Investigation of surface acid and basic sites

Since adsorption takes place at solids' interface, identification, quantification and determination of the strength of surface acid/basic groups of HAP are of paramount importance. Indeed, such evaluations allow to correlate sorption ability with material's properties.

A thorough investigation of sites' strength distribution is achievable only by coupling an isothermal titration of acid/basic surface sites with an in-situ monitoring of the evolved adsorption heat. Such technique falls under the name of gas-solid acid/basic calorimetric/volumetric titration. In collaboration with Institute of Research on Catalysis and the Environment of Lyon (IRCELYON), surface acidity and basicity of HAP have been titrated in gas phase at 80°C, using NH_3 and SO_2 as acidity and basicity probes, respectively. Details about used instruments and experimental procedure can be found in paragraph 8.2.4.3.

The choice of ammonia has been straightforward: indeed, NH_3 has been widely reported in literature as gas phase basic probe for surfaces titration [117]. Typical ammonia interactions with a reactive surface are: (*i*) H-bonding to surface oxygen atoms, (*ii*) proton transfer from surface O-H groups and (*iii*) coordination to electron-deficient metal atoms (i.e. metal centers exhibiting a partial δ^+). Thus, NH_3 is a reliable probe for both Brønsted and Lewis acid sites.

Sulphur dioxide is a less common but effective probe molecule as well. The reason behind the choice of SO_2 instead of more common CO_2 was dictated by the risk of reactive formation of stable surface carbonates onto HAP surface [83], thus misrepresenting the effective number of basic sites. SO_2 can coordinate to O^{2-} and -OH groups forming sulfite and hydrogen sulfite species, respectively. Strong acidic character allows SO_2 to probe almost all basic sites present on a surface, regardless their strength.

The collection of two consecutive adsorption isotherms separated by a desorption step allows not only the measurement of total acid/basic sites (I adsorption run) but even the absolute and percentage quantification of weak and strong sites (II adsorption run and difference between runs, respectively). Number of acid/basic sites where calculated from experimental data interpolation at P_{eq} = 0.2 torr. Numerical results of gas phase titrations are reported in Table 6, while the probes' adsorption isotherms are shown in Figure 13a. The whole data registered by the instrument are available in the Supporting Material (Figure 81 and Figure 82).

Table 6: Gas phase quantification of surface acid and basic sites of synthetic HAP. Acidity probe: NH_3, basicity probe: SO_2. Isotherms collected at 80°C.

Sample	**Site type**	**Acidic sites**	**Basic sites**	**Acid/Basic**
		meq g^{-1}	*meq g^{-1}*	*Ratio*
HAP	Total	0.290	0.221	1.31
	Strong[a]	0.099 (34%)[b]	0.174 (78%)[b]	0.57

[a] *Obtained by I and II run difference between n_{Ads} values at P_{eq} = 0.2 torr.*

[b] *Percentage of strong sites on total.*

Simultaneous presence of both acid and basic sites proves the amphoteric nature of HAP surface (Figure 13a). Acid to basic sites ratio (last column in Table 6) indicates that a major number of total acidic sites than basic, which contrast with what expected for a stoichiometric HAP [11,33]. On the other hand, when considering strong sites (i.e. the number of sites obtained from the difference between those titrated in the first and second adsorption run), the ratio is reversed, indicating that the percentage of strongly interacting basic sites is larger than the acidic one (second entry in Table 6). It is however important to stress out that the number of surface sites volumetrically determined by gas-solid techniques can be affected by relevant errors in the fact that the extent of the surface which is actually investigable is limited by probe molecules condensation issues. Moreover, condensation of the two probes, NH_3 and SO_2, occurs at way different partial pressure, heavily affecting the acid/basic ratio previously discussed.

The most reliable and interesting results we can obtain from this gas-solid technique is instead associated with the calorimetric analysis, which allows to have an insight on surface sites' interaction strength.

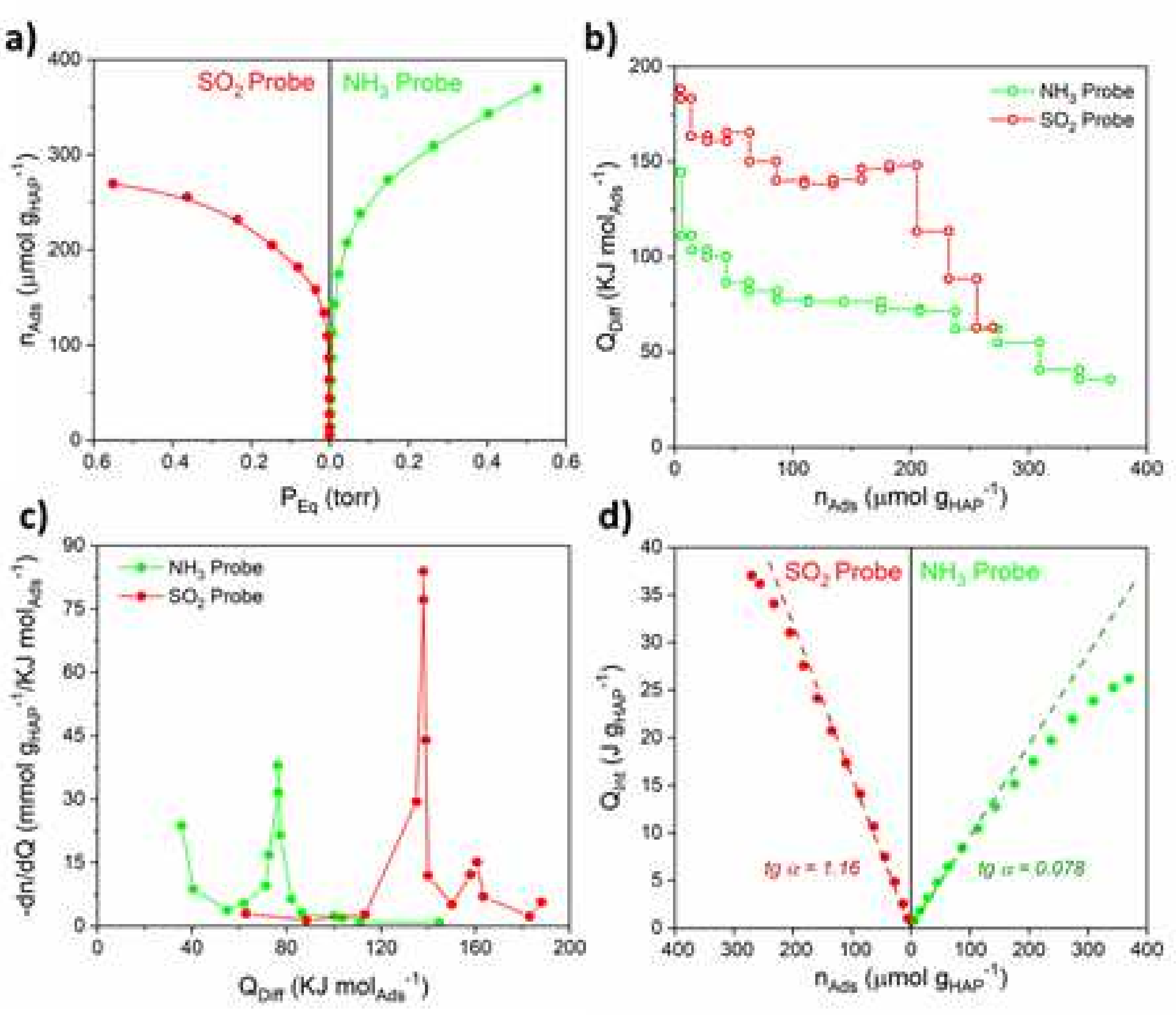

Figure 13: a) Adsorption isotherm, collected at 80°C, of NH_3 and SO_2 probe molecules onto HAP surface; b) Trends of differential heat of adsorption (Q_{Diff}) versus amount of probe molecule adsorbed (n_{Ads}); c) Acid/basic sites' energy distribution; d) Integral heat of adsorption (Q_{Int}) as a function of n_{Ads}.

Figure 13b shows the differential heat of adsorption (Q_{DIff}) as function of the amount of adsorbed probe molecules. NH_3 adsorption at zero coverage (n_{Ads} = 0, bare HAP surface) returns an initial Q_{Diff} value of *ca*. 140 kJ mol^{-1}, which drops steeply, evidencing a small population of strong acid sites. An energetic plateau is reached around 80 kJ mol^{-1}, corresponding to the presence of homogeneous medium-strength acid site. After the plateau, the strength of the acid sites drops stepwise down to *ca*. 30 kJ mol^{-1}, indicating a heterogeneous distribution of low-energy acid sites. Conversely, SO_2 adsorption generates a higher initial Q_{Diff} value (*ca*. 180 kJ mol^{-1}). A first narrow plateau is displayed at 160 kJ mol^{-1}, followed by a more pronounced one at *ca*. 140 kJ mol^{-1}: such trend reveals the presence of detectable amounts of very strong and strong basic sites, respectively. For higher surface coverages (n_{Ads} > 200 μmol g_{HAP}^{-1}), heat released decreases stepwise (heterogeneous distribution of medium-strong interacting sites). The value of 60 kJ mol^{-1}, obtained at the end of titration, suggest that a wide number of weak basic sites have not been titrated (experimental limitations), impacting on acid to basic sites ratio as discussed above.

Derivative of curves represented in Figure 13b yields the energy spectra of HAP surface reported in Figure 13c. The spectra show that the HAP possesses a strong basic sites population (adsorption heats in the range between 120 and 140 kJ mol^{-1}) coupled with a smaller population of very strong basic sites (*ca*. 160 kJ mol^{-1}). Concerning the acid sites, the related spectrum reveals a medium-strength site population around 60-

80 kJ mol^{-1}. Increasing trend at the low energy endpoint suggest a second population of weak acid sites, exhibiting adsorption heats < 40 kJ mol^{-1}.

Summing up all the heat evolved from all the probe adsorbed to HAP surface at determined titration points, the integral heat of adsorption (Q_{Int}) can be plotted as a function of the probes adsorbed amount, n_{Ads} (Figure 13d). For extremely low surface coverages, HAP acid and basic sites could be considered homogenous, since Q_{Int} vs n_{Ads} curves result to be properly fitted by lines. The slope of such lines is representative of sites' interaction strength and indeed returns the same trend reported by Figure 13b and c.

Although the collection of gas-solid calorimetric/volumetric isotherms using acid/basic probe molecules is the state-of-art tool for assessing the surface properties of materials, the results obtained can be hardly correlated to the effective performance of sorbent and/or catalysts operating at the liquid-solid interface. Indeed, factors like solvent interaction with the materials' surface are generally not taken into account when the surface is characterized by gas-solid techniques.

In order to obtain quantitative data which could relate with the actual sorption performances of HAP when contacted with aqueous solutions containing pollutants, the quantification of surface acid and basic sites of HAP was performed by a close-to-operando liquid-phase titration, according to the Liquid Recirculation Chromatographic Method (LRCM) [112]. 2-phenylethylamine (PEA) and benzoic acid (BA) were used as basic and acid probe, respectively. Titrations were carried out in a non-polar and aprotic solvent like cyclohexane (i.e. mimicking gas-solid titration conditions) for a preliminary determination of *intrinsic* acidity and basicity (hereinafter referred to as I.A. and I.B.). Then, titrations were performed in water, the actual solvent in which HAP will be tested as sorbent: under these conditions, *effective* acidity and basicity (hereinafter referred to as E.A and E.B.) were assessed. Description of LRCM principles, of the modified HPLC line used for the titration and all the experimental details are reported in paragraph 8.2.4.1. Collected isotherms have been mathematically modeled and treated according to what reported in paragraph 10.1.1.

In Figure 14 the acid-base titrations of HAP are presented as adsorption isotherms of PEA and BA collected at 30°C in cyclohexane (a) and in water (b). Numerical results, derived from modelling of experimental data according to the Langmuir model equation, are reported in Table 7. Table 33 in the Supporting Materials reports all the Langmuir parameters (n_{max}, b_{ads} and R^2) regressed from the isotherm curves in Figure 14.

Table 7: Liquid phase quantification of surface acid and basic sites of synthetic HAP. Acidity probe: PEA, basicity probe: BA. Isotherms collected at 30°C.

Sample	**Site type**	**Acidic sites**		**Basic sites**		**I.A./I.B.**
		meq g^{-1}		*meq g^{-1}*		
		Intrinsic [a]	*Effective* [b]	*Intrinsic* [a]	*Effective* [b]	
HAP	Total	0.159	0.0297	0.199	-	0.80
	Strong	0.038 (24%)[c]	0.011 (36%)[c]	0.084 (42%)[c]	-	0.45

[a] *Determined in cyclohexane.*

[b] *Determined in water.*

[c] *Percentage of strong sites on total.*

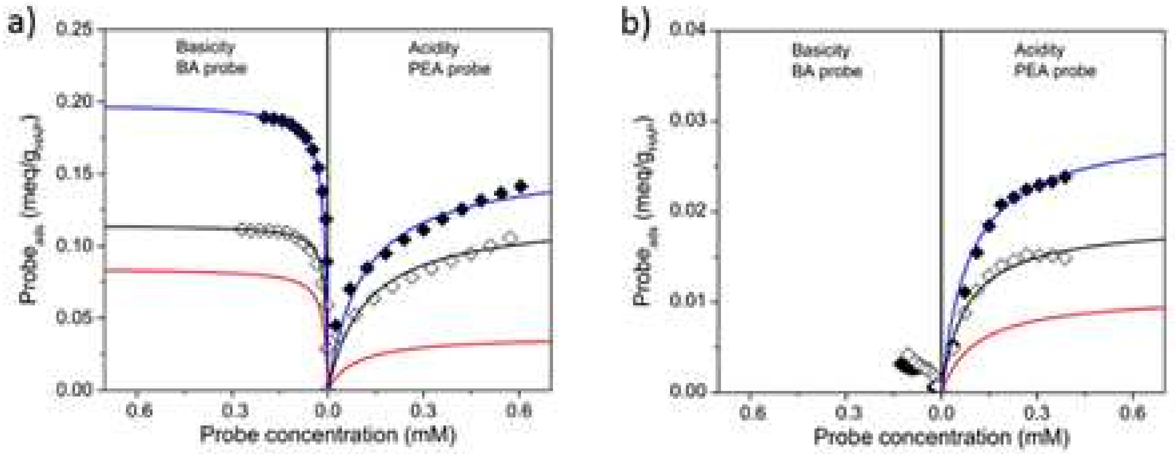

Figure 14: Adsorption isotherms of PEA (for acidity) and BA (for basicity) probes at 30°C on synthetic HAP sample evaluated in a) cyclohexane, for determining the intrinsic acidity and basicity, and in b) water, for determining the effective acidity and basicity. Full markers and empty markers represent I and II adsorption runs, respectively. Red lines represent the calculated Langmuir curves of PEA and BA adsorptions on strong acid and base sites; black lines represent the calculated Langmuir curves for II runs; blue lines represent the adsorption trends of I runs, obtained as sum of red and black lines (for details on data analysis, see paragraph 10.1.1).

Starting from intrinsic acidity/basicity: HAP surface demonstrate contemporary presence of both acidic and basic functionalities, in accordance with its postulated amphoteric features and consistently with the results obtained from gas-solid titrations (Figure 13a and Table 6). The overall lower number of sites assessed under liquid-solid conditions in respect with gas-solid ones stems from the different molecular dimension of probe molecules.However, under liquid-solid titration conditions, the analysis is not limited by the previously discussed condensation issues of probe molecules, therefore a full probing of the surface is possible. This ensure a more reliable determination of the number of acid/basic sites and especially of their ratio. Indeed, when titrated under liquid-solid conditions, the number of total surface basic sites results to be higher in respect with acidic ones, determining an I.A/I.B. ratio < 1 (Table 7). These results are consistent with the stoichiometric nature of the synthetic HAP under study [11,33]. As for gas-solid titrations, running two different adsorption runs interspersed with a desorption step allowed to discriminate between strongly and weakly interacting sites, although no quantitative information about interaction strength can be obtained under liquid-solid conditions. The percentage of basic strong sites stood around 42% whilst strongly interacting acidic sites are less than the 25% (Table 7). Thus, (I.A./I.B.)$_{strong}$ is even more favorable to basic moieties.

When titrated in the presence of a polar and protic solvent like water, HAP manifests only muffled acidic property (*ca*. 0.0297 meq g^{-1} of acid sites, *ca*. 1/10 of those titrated in cyclohexane). On the other hand, basic sites could not be titrated, likely because unable to interact with the probe molecule since engaged in strong interactions with water molecules. To date, no titration method has been reported for the determination of basic sites in aqueous solution.

Overall, liquid-solid titrations of HAP surface, performed according to LRCM principles, shows that in absence of any solvent competitive effect (i.e. in a condition that mimics gas-solid titrations), HAP is a basic rather than acidic material. The higher number of strong basic sites disclosed by LRCM is consistent with the energetic distribution obtained from gas-solid measures. In aqueous environment, strong interaction with water hinders the determination of the number of effective basic sites. It must however be stressed that this limitation in the titration stems mainly from the probe molecule (in terms of Lewis acidity) and do not necessarily implies the loss of basic properties of HAP under aqueous conditions.

To conclude, stoichiometric HAP exhibits an amphoteric surface, slightly more basic than acidic. Basic sites display a marked population of strong and very strong interacting functionalities, presumably O^{2-} (deprotonated phosphate groups) and Ca-OH species. In virtue of such marked interaction strength, basic sites are not titratable in aqueous media, probably because engaged in stable H-bonds with water molecules. This behavior evidences the retention of the strength of basic sites in aqueous environment. On the other hand, acidity, mainly developed on HAP surface by Ca^{2+} sites, PO_3OH, and vacancies (v_{OH}), is characterized by medium interaction strength of sites and therefore only slightly muffled by the presence of water.

2.3 Remediation of simulated polluted wastewaters by HAP: removal efficiencies and mechanisms

As previously discussed in paragraph 1.2.2.1, thanks to its unique adsorption properties, HAP has been tested and used as sorbent for heavy metal wastewater remediation and a large amount of papers can be found in literature in this regard [11,12,16,79,80]. However, a whole and clear visual of HAP removal efficiencies and inorganic cations uptake mechanisms onto its surface cannot be produced by a thorough review process and data gathering. As a matter of fact, the number of variables impacting on HAP sorption behavior is large. Since HAP morphological, structural and surface features are strictly dependent on its synthesis and thermal history, comparing performances of materials obtained through different routes is a difficult task. Moreover, HAP adsorption tests in literature display a clear inhomogeneity of employed operational conditions: fundamental parameters such as initial metal concentration, pH, temperature, stirring and solid to liquid ratio vary from study to study, impeding proper data comparison.

Regarding uptake mechanism of metal cations onto HAP surface, literature results to be inconsistent on the majority of metal species, with rare exceptions like Pb(II) [16,118]. Nonetheless, in no cases mechanisms can be considered as undoubtedly unraveled because of the process complexity stemming from HAP's surface heterogeneity. Often, inadequate characterization brought to unclear mechanistic claims, thus increasing literature uncertainty.

After reporting a thorough characterization of the synthetic HAP used in this study, the following section will present a systematic study on HAP removal efficiency and uptake mechanism of selected cations. Cations adsorption onto HAP surface has been investigated with complementary techniques, as to shed light on the underpinnings of the phenomenon.

2.3.1 Volumetric approach: static batch adsorption tests and adsorption isotherms

A first screening of the adsorption capacity of HAP towards five selected heavy metal species, namely Cu(II), Pb(II), Cr(III), Ni(II) and Co(II), has been carried out according to the static batch adsorption test procedure reported in paragraph 8.3.1.1. Such an experimental configuration has been chosen since similar to industrial decontamination processes, were stirring is rarely applied.

The results of preliminary screening tests are summarized in Figure 15 (conditions are reported in the caption) as percentage of metal removal. Numerical data can be found in the Supporting Material (Table 34).

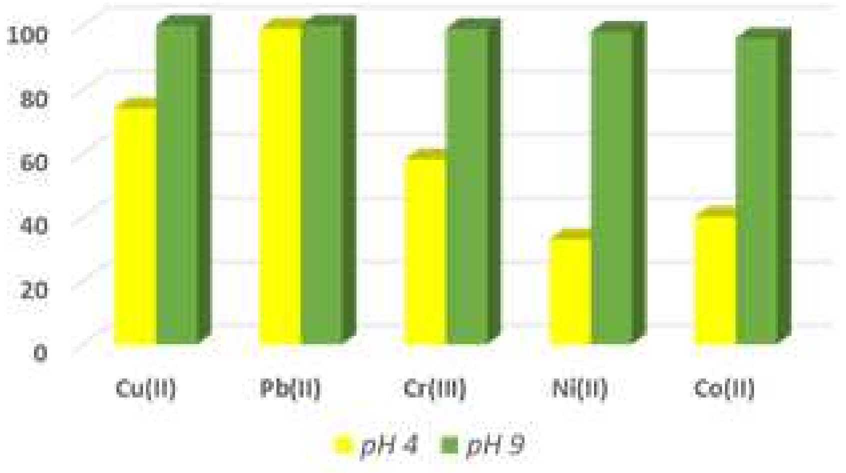

Figure 15: Me^{n+} removed (%) by HAP in static single metal batch adsorption test at different pH. $t_{contact}$ = 24 h, T = 30°C, solution volume to solid ratio ca. 100 mL g_{HAP}^{-1}, initial Me^{n+} conc. = 300 ppm.

Analyzing data obtained from tests performed under acidic conditions (pH 4, yellow bars in Figure 15), a clear trend of metal species affinity towards HAP surface can be detected: Pb(II) > Cu(II) > Cr(III) > Co(II) > Ni(II). Results agree with the majority of literature [79,80,119,120], even if, as written above, proper comparisons are hindered by different HAP features and testing conditions.

Under alkaline conditions (pH 9, green bars in Figure 15), removal efficiency approaches 100% for all metal species. An increase in sorption ability of HAP is expected under basic conditions: indeed, for pH > pH_{PZC}, HAP surface become negatively charged, thus interacting more favorably with metal cations. However, chemical precipitation, due to heavy metals speciation (Supplementary Material, Figure 83), surely partake to the trapping process.

From the outcome of these preliminary tests, gathering of adsorption isotherms of the five target species has been projected in terms of operational conditions (i.e. concentration ranges, pH, temperature, contact time).

Experimental adsorption isotherms for Cu(II), Pb(II), Cr(III), Ni(II) and Co(II) on stoichiometric synthetic HAP are reported in Figure 16, as amount of metal species loaded onto HAP surface (q_e, $mmol_{Me}$ g_{HAP}^{-1}) versus the residual metal concentration at the equilibrium (C_e, mmol L^{-1}). Isotherms have been collected at T = 30°C, according to the experimental procedure reported in paragraph 8.3.1.1. All tests were performed under acidic pH (*ca*. 4) since representative of polluted industrial effluents [98].

Experimental data, represented in Figure 16 by hollow black circles, have been fitted according to the most common isotherm model equations, namely Langmuir, Freundlich, Temkin, Toth (non-linear, 3-parameters equation), Fowler-Guggenheim and Flory-Huggins models. For each metal species all the regressed parameters for all isotherm models are reported in the Supporting Material (Table 37 to Table 41). Plots of linearly regressed experimental data for all metal species and all applied model isotherms are available in the Supporting Material as well (Figure 84).

Obviously, all model equations apply to gas-solid interfaces, thus their implementation in the interpretation of liquid-solid adsorption processes is subjected to intrinsic error [121]. Nonetheless, models have been extensively applied to adsorption phenomena taking place in condensed phase, returning good predications on sorbent-adsorbate interactions and overall helping data interpretation [14,89,122,123]. It should be noted that the failure to comply with some fundamental postulates of such model equations often causes the loss of physical meaning of determined equation parameters, limiting the information that could be gained from theoretical modelling. A brief review of the theoretical underpinnings of the model equations applied in this study can be found in the Supporting Material (paragraph 10.1.3).

In the study of metal species adsorption onto HAP surface, Langmuir and Freundlich models have proven to effectively describe most adsorbate-sorbent interactions [11,118–120]. However, before embarking on further discussion, a clarification is needed in the case of Cr(III) adsorption isotherm. As observable in Figure 16c, the quantity of Cr(III) adsorbed onto HAP surface reaches a first plateau at *ca*. 0.63 $mmol_{Cr(III)}$ g_{HAP}^{-1}; this portion of the isotherm, properly fitted by the Langmuir model equation, will be hereinafter referred to as the first branch of Cr(III) adsorption isotherm. Following the first branch, a further increase of the apparent adsorption capacity takes place when a specific critical C_e is overcome (*ca*. 8 mM) and a new plateau is reached at *ca*. 1.19 $mmol_{Cr(III)}$ g_{HAP}^{-1}, thus defining the second branch of the isotherm.

Langmuir model equation modelling (red full lines in Figure 16) resulted to be the most effective in describing the adsorption phenomena of all target species onto HAP surface. Regressed parameters, namely maximum monolayer coverage of the adsorbate on the sorbent (n_{max}, $mmol_{Me}$ g_{HAP}^{-1}) and Langmuir constant (b, L $mmol^{-1}$) are listed in Figure 16f together with the adjusted R^2 coefficient. Thus regressed n_{max} values represent the maximum adsorption capacity of HAP towards the studied heavy metal species: the obtained trend in terms of n_{max} is consistent with the one disclosed by the preliminary static adsorption tests, confirming the Pb(II) > Cu(II) > Cr(III) > Co(II) > Ni(II) affinity order. Converting n_{max} values in massive terms for an easier evaluation, HAP proved to be able to trap *ca*. 501.4 $mg_{Pb(II)}\ g_{HAP}^{-1}$, 79.4 $mg_{Cu(II)}\ g_{HAP}^{-1}$, 61.9 $mg_{Cr(III)}\ g_{HAP}^{-1}$ (total, first Langmuirian plateau of adsorption at 32.8 $mg_{Cr(III)}\ g_{HAP}^{-1}$), 22.5 $mg_{Co(II)}\ g_{HAP}^{-1}$ and 18.61 $mg_{Ni(II)}\ g_{HAP}^{-1}$ in single metal solutions and under acidic pH. These results candidate HAP as an effective sorbent for industrial wastewater remediation when compared to other low-cost materials presented in literature [124,125].

In the specific case of Cr(III), two n_{max} values reported in Figure 16f stem from the application of the Langmuir model equation on the first branch of the isotherm (red line in Figure 16c, up to C_e *ca*. 8 mM) and a polynomial fitting of the second branch, performed according to a logarithmic mathematical model. Indeed, as reported in Figure 16c and Table 39, no common model equation satisfactory interprets the second part of Cr(III) adsorption isotherm. The unusual presence of a steep increase of immobilized Cr(III) onto HAP at C_e equal to *ca*. 8 mM and the successful modeling of the latter by a logarithmic model (Dose-Response function) generally used in pharmacology to assess organisms' saturation suggest that the second branch of the Cr(III) adsorption isotherm may not be solely attributed to an HAP-driven adsorption mechanism. Evidences of a different immobilization of Cr(III) at high concentration will be provided by microcalorimetric studies (paragraph 2.3.2).

Besides n_{max}, the Langmuir constant (b) is obtained from regression. It is an energetic parameter, indicative of adsorbate-sorbent interaction. However, since Langmuir model equation postulates the homogeneity of adsorption sites, conditions absolutely not fulfilled by HAP surface, regressed b parameters cannot be considered physically accurate but at most as a mean value of the energetics of cations' interaction with all (diverse) HAP surface functionalities. For example, the case of Langmuir fitting on the first branch of Cr(III) adsorption isotherm returns unrealistic b values with an overall error exhibiting the same order of magnitude of the constant itself (Figure 16f). This highlights once more how the model may fail in the physical description of the phenomena when some of its fundamental postulates are not fulfilled by the system under study (in this case, the homogeneity of surface sites).

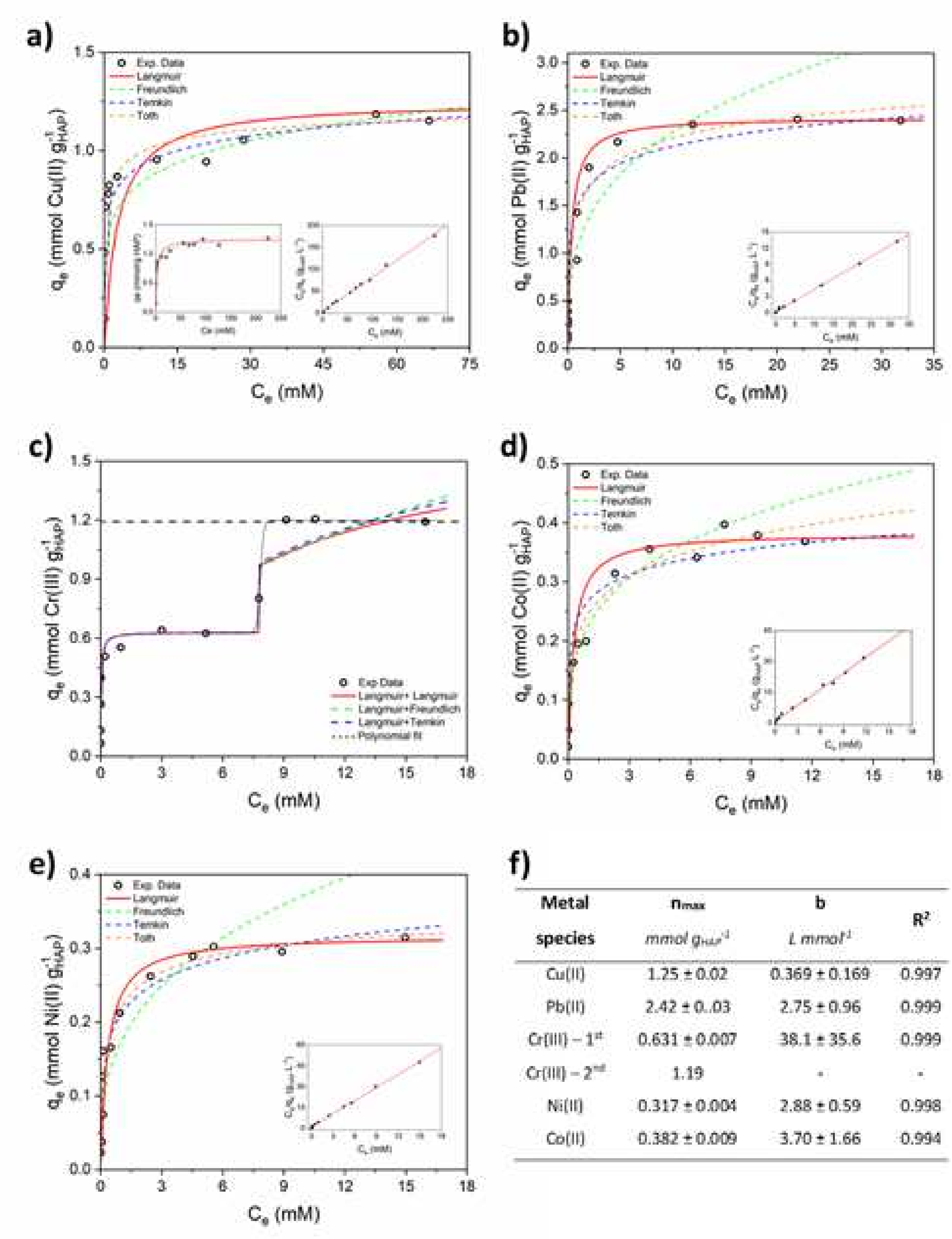

Metal species	n_{max} *mmol g_{HAP}^{-1}*	b *L $mmol^{-1}$*	R^2
Cu(II)	1.25 ± 0.02	0.369 ± 0.169	0.997
Pb(II)	2.42 ± 0..03	2.75 ± 0.96	0.999
Cr(III) – 1st	0.631 ± 0.007	38.1 ± 35.6	0.999
Cr(III) – 2nd	1.19	-	-
Ni(II)	0.317 ± 0.004	2.88 ± 0.59	0.998
Co(II)	0.382 ± 0.009	3.70 ± 1.66	0.994

Figure 16: Experimental data (black hollow circles) and model isotherms mathematical fitting for the adsorption of a) Cu(II), b) Pb(II), c) Cr(III), d) Ni(II) and e) Co(II). Insets in graphs from a to e report the linearization of experimental data according to the Langmuir model equation. In the case of Cu(II) (a), an additional inset reports the full C_e range in which the adsorption phenomenon has been studied, which is way larger than for other cations. Parameters regressed from the latter are listed in f). For Cr(III), n_{max} of the second branch of the isotherm has been extrapolated (black dotted line in Figure 16c) from the fitted logarithmic curve. Isotherms collected at 30°C.

Freundlich model equation is often reported to exhaustively describe the phenomenon of adsorption of several cations onto HAP surface [118,119]. As depicted in Figure 16, Freundlich model fails in interpreting the trend of experimental data collect at low and high q_e values. Thus, despite R^2 values approaching the unity, this empirical model does not represent the experimental trend of cations adsorption onto HAP. Moreover, Freundlich isotherm postulates an exponential energy distribution of the surface-active sites, a very different condition in respect with that of disclosed for HAP surface by calorimetric acid/base titrations (paragraph 2.2.2, Figure 13), that is likely the cause of the failing of the model for these systems.

Temkin model equation is commonly used to describe chemisorption processes in which lateral interaction (adsorbate-adsorbate) are not negligible. With the exception of Cu(II), this model equation fits experimental data with $R^2 > 0.920$, indicating a possible role of already adsorbed species in directing the phenomena. The regressed B parameter, indicative of the heat of adsorption of the process, results to be nearly zero for Ni(II), Co(II) and Cr(III) while it is slightly higher for Cu(II) (*ca*. 0.1 J $mmol^{-1}$) and Pb(II) (*ca*. 0.2 J $mmol^{-1}$). Such values could indicate an almost non-thermal uptake process, most likely ion-exchange or surface complexation, for all metal species. However, this would strongly contrast with the trapping mechanism of dissolution-precipitation that literature unanimously report for Pb(II) [11,16,26,118]. A more rigorous approach has to be thought to directly investigate the thermodynamics of cations adsorption onto HAP (i.e. isosteres approach and/or microcalorimetric studies). Further details about the heat of adsorption correlated with cations trapping will be presented in paragraph 2.3.2. It can be concluded that neither Temkin model equation can satisfactorily describe the physical nature of cations adsorption onto HAP.

Toth model equation is an empirical modification of Langmuir's one: it introduces a third parameter, *n*, that expresses the heterogeneity of the surface. *n* can range from 0, for a perfectly heterogenous surface, to 1, value at which Toth equation reduces to Langmuir model. Established that Langmuir equation properly fits experimental data and considering that surface heterogeneity of HAP surface is the main hindering to the correct application of such model, Toth equation should be the best choice to describe the phenomena. However, non-linear regression of experimental data according to Toth equation returns slightly overestimated n_{max} values, with Pb(II) and Co(II) giving unrealistic results (n_{max} 1.5x and 6x those obtained from linear Langmuir regression). On the other hand, Toth equation seems to model properly Cu(II) adsorption onto HAP, even from a graphical point of view (orange dotted line in Figure 16a): in this case indeed, the regressed n_{max} value is close to that obtained from Langmuir linear regression. *n* parameter is around 0.3, indicating marked heterogeneity of available surface sites towards Cu(II) adsorption. Nonetheless, the high value of the residual squares sum does not allow to fully rely on the Toth regressed parameters. Summarizing, Toth equation resulted less adequate than Langmuir model in fitting experimental data although the introduction of a parameter accounting for surface heterogeneity.

Fowler-Guggenheim model, a Langmuir modification that takes into account lateral interactions, resulted to be inadequate to fit all experimental data with the exception of Co(II) ones. It must be stressed that Temkin model, likewise based on the non-negligible nature of lateral interactions, gave best fitting results precisely for Co(II) data ($R^2 = 0.934$). Although there is a lack of experimental confirmations on this matter, it could be guessed that Co(II) adsortpion onto HAP is the process, amid the investigated metal species, that most suffer from lateral adsorbate-adsorbate interaction issues. The regressed parameter *w*, representing the interaction energy between adsorbed molecules, stood to a positive value of *ca*. 11 KJ mol^{-1}, suggesting repulsion forces between adsorbates.

Finally, Flory-Huggins model equation describes the characteristics of surface coverage of the solid by the adsorbate as a function of the number of available adsorption sites (*n* parameter) and thermodynamic spontaneity of the adsorption process itself (K_{FH}). Thus, regressing K_{FH} parameter and applying Van't Hoff equation (paragraph 10.1.3.6), it is possible to indirectly evaluate the Gibbs free energy (ΔG) of metal species adsorption onto HAP surface. The results indicate that all the studied cations adsorb spontaneously on HAP, with a driving force that follows the same order of removal efficiency and Langmuir regressed n_{max} values: Pb(II) > Cu(II) > Cr(III) > Co(II) > Ni(II). Since all tests were performed on the same material and in the same experimental conditions, the affinity scale here reported can be considered reliable in the limits of experimental error. It must be noticed that *n* parameter, descriptor of available adsorption sites, largely deviates from Langmuir n_{max} values only for Pb(II) and Cr(III) modeling; such result could stem from the unique nature of Pb(II) trapping process (dissolution-precipitation) that does not imply a strictly surface adsorption of the cation on HAP surface but rather a chemical reaction at the interface. Same considerations could be drawn for Cr(III) immobilization as well, since its mechanism of uptake seems to be not univocal.

After adsorption tests, the metal-loaded samples underwent structural characterization by XRPD. By means of these analyses, structural stability of the adsorbent was checked. Moreover, when possible, information on the adsorption mechanisms of target cations were gathered. XRPD patterns of metal-loaded samples are reported in Figure 17a.

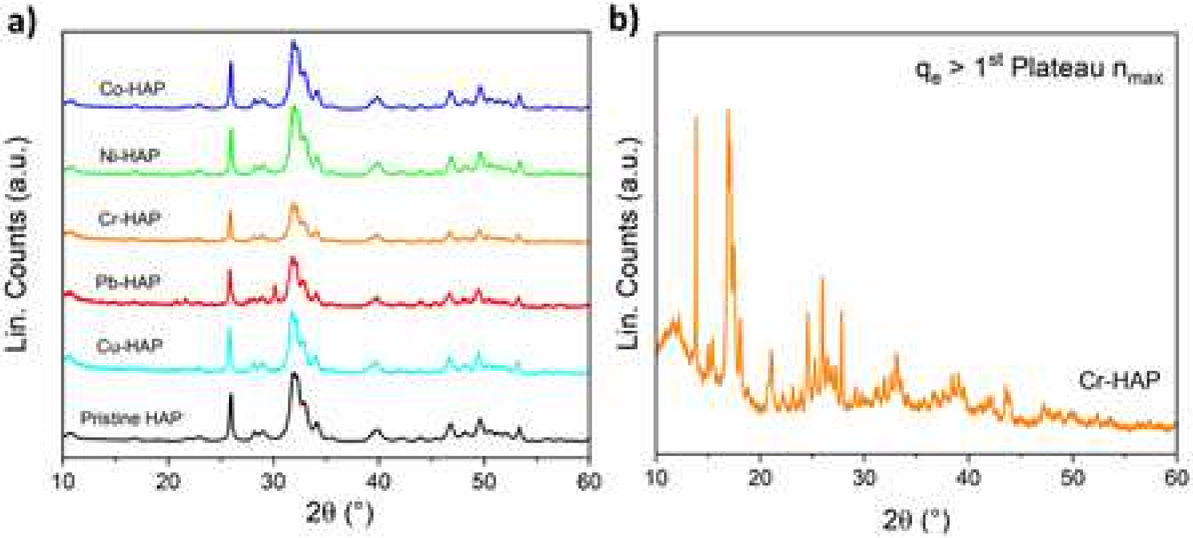

Figure 17: a) XRPD patterns collected on metal-loaded HAP samples. Diffractograms collected on samples exhibiting q_e values of ca. 80% n_{max} (see Figure 16f). When considering Cr(III), the n_{max} obtained from the Langmuirian fit on the first "branch" of the isotherm is considered; b) XRPD pattern collected onto Cr(III)-loaded HAP where $q_e \approx n_{max2}$ (Figure 16f).

For the five metal species under investigation, literature reports different uptake mechanisms: surface complexation/ion-exchange for Cu(II), Cr(III), Ni(II) and Co(II) [12,14,15,120,126,127] and dissolution-precipitation for Pb(II) [15,16,80,118].

XRPD patterns, collected on samples presenting $q_e \approx 80\%\ n_{max}$, are consistent with these claims: indeed, no alteration in the apatitic structure of HAP could be detected for Cu(II), Cr(III), Ni(II) and Co(II)-loaded HAPs while Pb(II) removal occurred with the formation of a new crystalline phase. The addition peak appearing around 30° in 2θ (red pattern in Figure 17a) unravel the formation of crystalline hydroxyl pyromorphite ($Pb_{10}(PO_4)_6(OH)_2$), confirming the dissolution-precipitation mechanism. Interestingly, XRPD patterns collected onto Cr(III)-loaded HAP samples with $q_e > n_{max1}$ (Figure 16f), presents a noticeable increment in the amorphous content, identified by the semicircular drifting of the background of the diffraction pattern at low diffraction angles (Figure 17b). This evidence is consistent with a possible change in the uptake mechanism of Cr(III), as suggested by the double plateau isotherm reported in Figure 16c. Further details will be discussed in paragraph 2.3.2, where microcalorimetric measures of Cr(III) adsorption onto HAP will disclose useful information to assess its uptake mechanism under these conditions.

Since ion-exchange processes for Cu(II), Cr(III) (up to C_e ca. 8 mM), Ni(II) and Co(II) should occur at the expenses of Ca(II), and considering the difference in ionic radii of these species (basically all smaller than the former), calculation of the unit cell parameters of metal-loaded samples could return information about the phenomena. A preliminary rough refinement of cell parameters carried out using CelRef V3 software (see paragraph 8.2.1 in the Experimental Section for details) have been performed. Main results are gathered and reported in the Supporting Material (Table 35 and Table 36).

Unit cell parameters did not vary according to a trend and moreover variations were deemed not significant. All metal-loaded samples presented almost the same increase in a and c parameters in respect with pristine HAP. The same increase was registered after exposure to acidic environment (paragraph 2.2.1, Table 32). Same conclusions could be drawn for unit cell refinement of hydroxyl pyromorphite phase (Table 36). At this point of the study it is not possible to state if (*i*) ion-exchange mechanism did not take place but rather a surface complexation (i.e. a process that do not alter HAP lattice) occurred or (*ii*) the limited beam intensity of a routine diffractometer, together with the low wt.% of loaded metal species, do not allow a robust analysis.

It is noteworthy that the affinity trend disclosed by both preliminary tests and adsorption isotherms directly relates to the complexation constants of the target metal species by the common functional groups exposed on HAP surface (Table 8). Surely, the association constants measured in liquid phase that are reported in Table 8 cannot be taken as a reliable absolute value for a liquid-solid interfacial system like the one under study. However, for an internal and relative comparison, they provide a rationale for the removal/affinity trend. This indicate that, as proposed in paragraph 1.2.2.1, surface complexation can be considered as the initial step of the adsorption phenomena for diverse metal species.

Table 8: Complexation constants of the target metal species with the functional groups representing the main basic surface moieties of HAP.

Metal species	**Log K_C [a]**					
	-OH		**-POH**		**-COH**	
	25°C	*$\mu = 0$*	*25°C*	*$\mu = 0.5$*	*25°C*	*$\mu = 0$*
Cu(II)	6.3		3.2		9.6	
Pb(II)	6.3		3.1[b]		13.1	
Cr(III)	10.1		N/A		N/A	
Ni(II)	4.1		2.1		6.9	
Co(II)	4.3		2.2		10.0	

[a] *K_C = Complex association constant, evaluated as [ML]/([M]·[L]), where ML is the metal-ligand complex, M the free metal cation and L the free anionic ligand.*

[b] *Measured at $\mu = 0$*

Considering the limited impact of carbonate groups because of their scarce presence on synthetic HAP surface (paragraph 2.2.1, Figure 11), a good correlation between percentage removal of Cu(II), Ni(II) and Co(II) and their complexing constant can be drawn.

Application of the same rationale to the case of Pb(II) is quite difficult, since the dissolution-precipitation mechanism does not necessarily implies an initial surface complexation step. Indeed, an interaction of Pb(II) with the phosphate groups present at the interphase (due to partial dissolution of HAP) can be supposed , thus bringing into play precipitation constants over complexation ones.

The case of Cr(III) is likewise complicated by several issues. First and foremost, complete data on complexation constants for Cr(III) are not reported in literature [128,129]. Moreover, its trivalent nature makes difficult and internal comparison when a fixed 1:1 stoichiometry between metal and ligand is postulated (Table 8). In addition, the alleged creation of new amorphous phases upon adsorption at high Cr(III) concentrations suggests that Cr(III) immobilization at $C_e > 8$ mM could be induced by phenomena that are not exclusively relatable to adsorption phenomena onto HAP surface but could relate to Cr(III) speciation. Indeed, further calorimetric studies, presented in next section, will evidence that Cr(III) peculiar speciation in aqueous phase (Figure 83 in Supporting Material) is supposed to determine the cation's behavior at HAP interface.

2.3.2 Thermodynamic approach: microcalorimetric study of the adsorption of Me^{n+} onto HAP surface

Investigate the thermodynamics and energetics of the adsorption of metal species onto HAP surface could return valuable information in terms of disclosure of the adsorption mechanisms and thus help the comprehension of the phenomenon. In this section, a volumetric approach, based on the calculation of isosteric heats ($\Delta_{st}H$) from experimental adsorption isotherms collected at different temperatures, will be presented. Then, data will then be complemented and corroborated by a direct measure of the heat evolved ($\Delta_{ads}H$) by the metal adsorption process by means of liquid-phase microcalorimetric experiments. Both experimental and instrumental details about isotherms collection and microcalorimetric titrations can be found in the dedicated section (paragraph 8.3.1.1 and 8.3.1.2, respectively).

The knowledge gained onto Cu(II), Pb(II), Cr(III), Ni(II) and Co(II) adsorption onto HAP surface in the previous section depicts two different mechanisms of capture: with the exception of Pb(II), whose uptake passes through a dissolution/precipitation mechanism, all the other species are adsorbed on HAP accordingly to a surface complexation/ion exchange process, with Cr(III) being an exception when a certain critical Cr(III) concentration is overcome. Thus, it can be expected that Pb(II) would exhibit a peculiar thermal pathway of removal. Indeed, due to its higher stability in aqueous solution ($K_{ps} < K_{ps\ HAP}$), the formation of hydroxyl-pyromorphite is supposed to be accompanied by heat release ($\Delta H < 0$, exothermal process), as a consequence of the creation of a new stable phase.

On the other hand, Cu(II), Cr(III) (for $C_e <$ *ca*. 8 mM), Ni(II) and Co(II) should all share a similar uptake mechanism and therefore a similar thermal pathway of adsorption. In line of principle, the $\Delta_{ads}H$ associated to whether surface complexation or ion-exchange is expected to be negligible in the fact that such mechanisms are almost non-thermal in nature.

Taking Cu(II) as representative of the species deemed to follow non-thermal adsorption pathways, the Pb(II) and Cu(II) $\Delta_{ads}H$ onto stoichiometric HAP has been investigated by gathering adsorption isotherms in a range of temperature comprised between 18 and 55 °C (291 to 328 K). Then, applying the Clausius-Clapeyron equation, the isosteric heat of the adsorption process ($\Delta_{st}H$) was calculated. In agreement with previous results, experimental data have been modelled according to the Langmuir isotherm equation. Moreover, Flory-Huggins model equation has been applied, in the effort to correlate spontaneity of the phenomena with temperature. Experimental data, fitted curves and regressed parameters are reported in Figure 18 and Table 9 for Cu(II) and Figure 19 and Table 10 for Pb(II). Linear regressions of experimental data are graphically reported in the Supporting Material (Figure 85 and Figure 86).

Cu(II) adsorption process onto HAP surface was satisfactorily fitted by the Langmuir model in the range of temperature studied (Figure 18). n_{max} values (Table 9) do not show a clear trend with temperature. However, the overall oscillation of n_{max} cannot be merely ascribed to experimental errors and a moderate endothermicity of the phenomena can be guessed by the slight increase in Cu(II) maximum loading comparing isotherms collected at the temperature endpoints. Despite not optimal correlation factors, modelling of the same experimental data according to Flory-Huggins equation seems to confirm the endothermicity of the phenomena. Indeed, overall $\Delta_{ads}G$ tends to more negative values when temperature increases (Table 9). Considering the moderate variations in both n_{max} and ΔG values, Cu(II) adsorption onto HAP seems to be a mildly endothermal process. Possible explanation to the phenomena could be the smaller ionic radius of Cu(II) in respect with Ca(II). Indeed, supposing Cu(II) is trapped onto HAP surface through an ion-exchange mechanism, differences in ionic radii between Cu(II) and Ca(II) (and thus charge densities) would result in a non-perfect balance of lattice ingress/egress and solvatation/desolvatation enthalpic contributions, generating mild thermal effects.

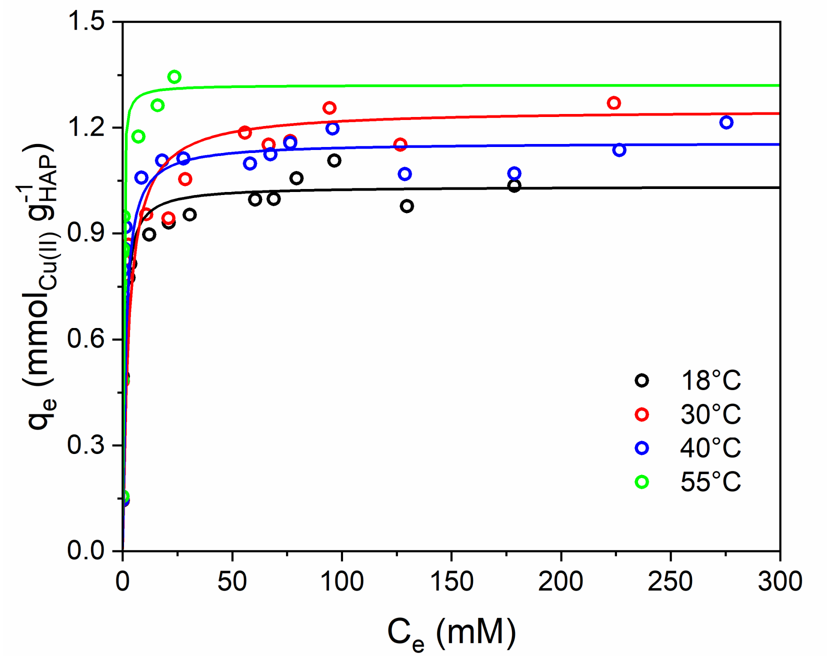

Figure 18: Experimental data and Langmuir fitted isotherms for Cu(II) adsorption onto HAP at different temperatures.

Table 9: Langmuir (top) and Flory-Huggins (down) model equations parameters regressed from experimental data of Cu(II) adsorption onto HAP at different temperatures.

Isotherm Model	**T**	**Parameter**	**Value**			**R^2**
Langmuir	291 K	n_{max} *(mmol* g_{HAP}^{-1}*)*	1.03	±	0.02	0.997
		b (L $mmol^{-1}$*)*	*(1.07*	±	*1.16)*	
	303 K	n_{max} *(mmol* g_{HAP}^{-1}*)*	1.25	±	0.02	0.997
		b (L $mmol^{-1}$*)*	*(0.369*	±	*0.169)*	
	313 K	n_{max} *(mmol* g_{HAP}^{-1}*)*	1.16	±	0.02	0.996
		b (L $mmol^{-1}$*)*	*(0.745*	±	*1.01)*	
	328 K	n_{max} *(mmol* g_{HAP}^{-1}*)*	1.32	±	0.02	0.998
		b (L $mmol^{-1}$*)*	*(5.30*	±	*4.76)*	
Flory-Huggins	291 K	n	0.514	±	0.058	0.898
		K_{FH} *(L* $mmol^{-1}$*)*	0.0724	±	0.0032	
		ΔG *(J* $mmol^{-1}$*)*	-6.62		0.11	
	303 K	n	0.745	±	0.092	0.867
		K_{FH} *(L* $mmol^{-1}$*)*	0.0634	±	0.0034	
		ΔG *(J* $mmol^{-1}$*)*	-6.95		0.14	
	313 K	n	0.379	±	0.073	0.749
		K_{FH} *(L* $mmol^{-1}$*)*	0.0581	±	0.0033	
		ΔG *(J* $mmol^{-1}$*)*	-7.17		0.14	
	328 K	n	0.167	±	0.002	0.922
		K_{FH} *(L* $mmol^{-1}$*)*	0.0422	±	0.0001	
		ΔG *(J* $mmol^{-1}$*)*	-7.97		0.002	

Even Pb(II) adsorption onto HAP surface was adequately described by the Langmuir model equation in the temperature range under study (Figure 19).

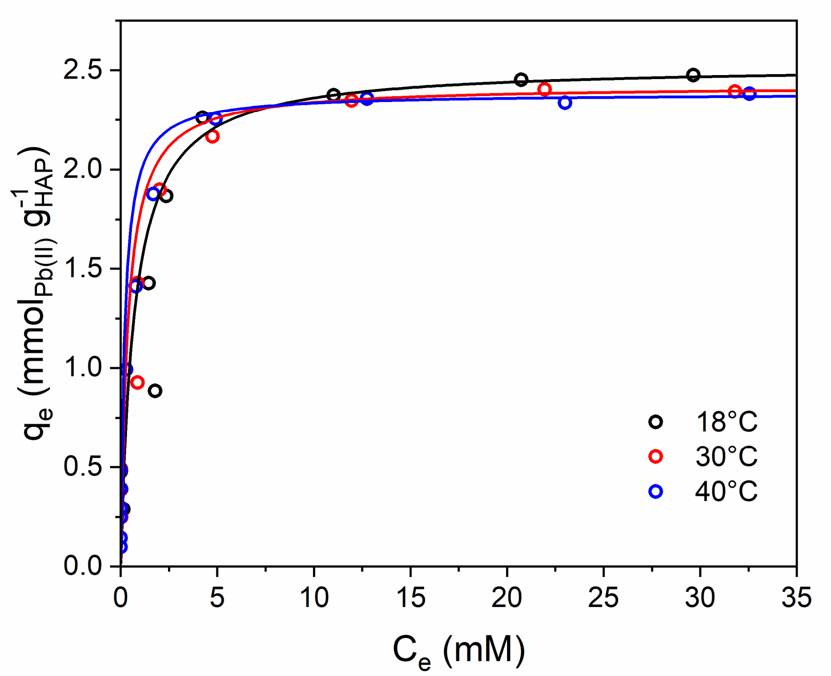

Figure 19: Experimental data and Langmuir fitted isotherms for Pb(II) adsorption onto HAP at different temperatures.

Table 10: Langmuir (top) and Flory-Huggins (down) model equations parameters regressed from experimental data of Cu(II) adsorption onto HAP at different temperatures.

Isotherm Model	**T**	**Parameter**	**Value**			**R²**
Langmuir	291 K	n_{max} *(mmol g_{HAP}^{-1})*	2.52	±	0.07	0.991
		b *(L mmol^{-1})*	1.44	±	0.62	
	303 K	n_{max} *(mmol g_{HAP}^{-1})*	2.42	±	0.03	0.999
		b *(L mmol^{-1})*	2.75	±	0.96	
	313 K	n_{max} *(mmol g_{HAP}^{-1})*	2.38	±	0.01	1.000
		b *(L mmol^{-1})*	4.83	±	1.49	
Flory-Huggins	291 K	n	0.0574	±	0.0126	0.697
		K_{FH} *(L mmol^{-1})*	0.0194	±	0.0001	
		ΔG *(J mmol^{-1})*	-9.93	±	0.01	
	303 K	n	0.0879	±	0.0096	0.895
		K_{FH} *(L mmol^{-1})*	0.0207	±	0.0001	
		ΔG *(J mmol^{-1})*	-9.77	±	0.01	
	313 K	n	0.0672	±	0.0183	0.731
		K_{FH} *(L mmol^{-1})*	0.0211	±	0.0003	
		ΔG *(J mmol^{-1})*	-9.72	±	0.03	

In this case, a monotonic decreasing trend of n_{max} values with temperature can be noticed (Table 10). Moreover, regression of experimental data according to the Flory-Huggins model equation returns increasing $\Delta_{ads}G$ values for increasing temperatures (Table 10), suggesting a lower spontaneity of Pb(II) uptake onto HAP at higher temperatures. These behaviors indicate an exothermal phenomenon that would be consistent with the previous assumption, foreseeing the formation of a new stable Pb-containing phase. Further considerations on the alleged exothermal effect of Pb(II) adsorption can be made recalling the peculiar HAP inverse solubility (paragraph 1.1.4): because of this behavior, higher temperature would cause a reduction of HAP dissolution, with a related decrease in concentration of free phosphate ions, thus hindering Pb(II) precipitation. However, the range of temperature under study ($\Delta T_{max} = 22°C$) is not wide enough to justify major variations in HAP dissolution and consequent PO_4^{3-} ions availability in the reaction media. Therefore, the decrease in $\Delta_{ads}G$ with increasing temperature cannot be assigned to "limiting reactant" issues; the exothermal nature of Pb(II) uptake onto HAP surface seems to be the only addressable factor concurring in the definition of $\Delta_{ads}G$ trend.

Further information on the energetics of adsorption phenomena can be provided by the determination of the isosteric heat of adsorption using the experimental adsorption isotherms collected at different temperatures. Isosteric heat of adsorption ($\Delta_{st}H$) at constant surface coverage can be computed adapting the Clausius Clapeyron equation to the adsorption phenomenon:

$$\frac{dln\,(C_e)}{dT} = -\frac{\Delta_{st}H}{RT^2}$$

$\Delta_{st}H$ can then be calculated from the slope of the so-called Clausius-Clapeyron-like plot, where ln (C_e) is plotted versus the inverse of the temperature (1/T). So, at each temperature, for fixed surface metal loading $q_e \leq n_{max}$, equilibrium concentration of residual metal species (C_e) has been calculated through the related Langmuir fitted isotherm. By reporting these data as a function of the reciprocal of the temperature, isosteres of adsorption are obtained, which describe ln (C_e) dependence on temperature at fixed surface Cu-coverages.

Isosteres of Cu(II) adsorption onto HAP are graphically reported in Figure 20, while their slopes and calculated $\Delta_{st}H$ values are listed in Table 11.

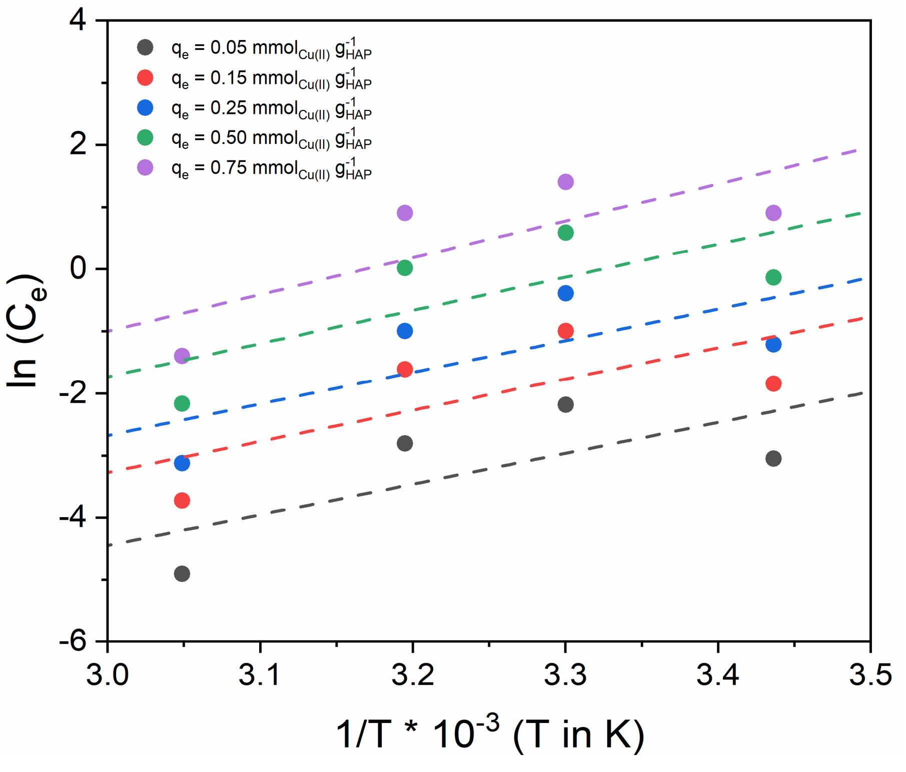

Figure 20: Adsorption isosteres for Cu(II) adsorption onto HAP at various Cu(II) loading (0.05 < q_e ($mmol_{Cu(II)}\ g_{HAP}^{-1}$) < 0.80).

Table 11: Isosteres slope and extrapolated $\Delta_{st}H$ for Cu(II) adsorption onto HAP surface.

q_e	Slope (regression)	$\Delta_{st}H$
$mmol_{Cu(II)}\ g_{HAP}^{-1}$	-	$J\ mol_{Cu(II)}^{-1}$
0.05	4.96	41.2 ± 30.2
0.15	5.01	41.7 ± 30.1
0.25	5.08	42.2 ± 30.0
0.50	5.34	44.4 ± 29.5
0.75	5.94	49.3 ± 28.4

In all cases, regression lines with a positive slope were obtained, implying an endothermal nature for Cu(II) adsorption onto HAP. However, the isosteric enthalpies shown in Table 11 indicate that Cu(II) uptake occurs with a very small heat absorption (around 40-50 J $mol_{Cu(II)}^{-1}$), with an computational error from the applied model that is in the same order of magnitude of the results themselves. Taking into account the amount of Cu(II) that can be effectively trapped onto HAP surface ($n_{max} \approx 1.2$ mmol g_{HAP}^{-1} in the temperature range under study) the phenomenon can be reasonably assumed to be non-thermal.

Pb(II) onto HAP isosteres are analogously reported in Figure 21 and numerical values displayed in Table 12.

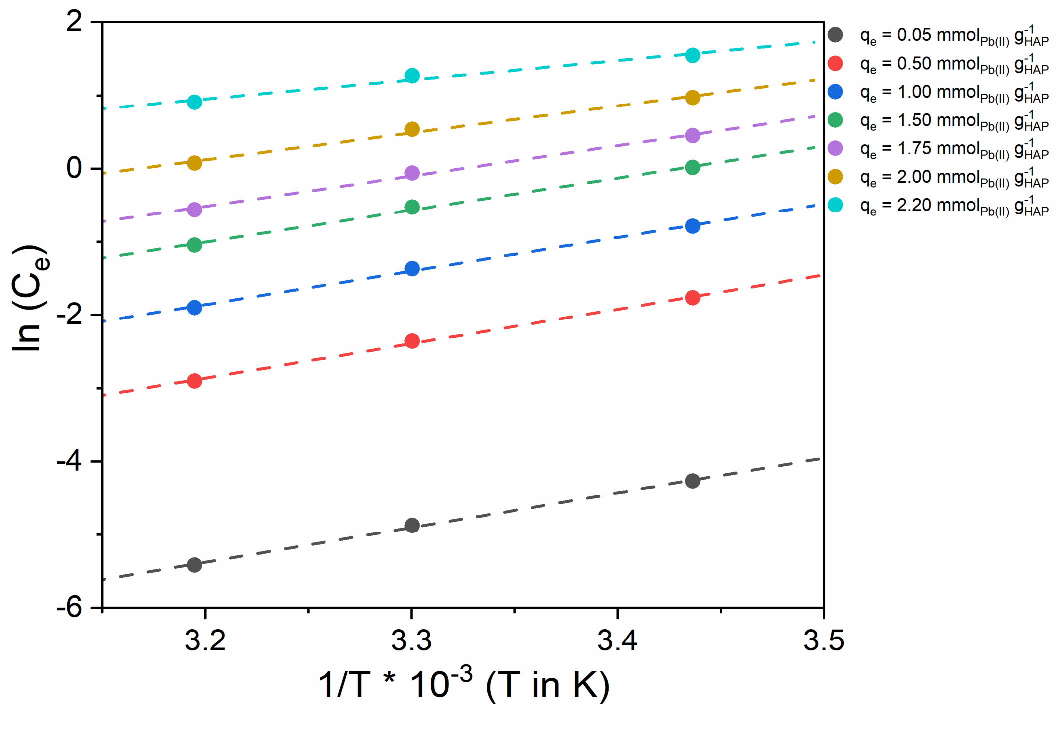

Figure 21: Adsorption isosteres for Pb(II) adsorption onto HAP at various Pb(II) loading (0.05 < q_e ($mmol_{Pb(II)}\ g_{HAP}^{-1}$) < 2.20).

Table 12: Isosteres slope and extrapolated ΔH_{st} for Pb(II) adsorption onto HAP surface.

q_e *$mmol_{Pb(II)}\ g_{HAP}^{-1}$*	**Slope (regression)** -	$\Delta_{st}H$ *$J\ mol_{Pb(II)}^{-1}$*
0.05	4.75	39.5 ± 1.71
0.50	4.70	39.0 ± 1.79
1.00	4.59	38.2 ± 1.92
1.50	4.38	36.4 ± 2.18
1.75	4.16	34.6 ± 2.42
2.00	3.69	30.7 ± 2.85
2.20	2.62	21.8 ± 3.41

Results are similar to those obtained for Cu(II) adsorption onto HAP surface, highlighting positive isosteres slopes, i.e. endothermal nature of the phenomena. $\Delta_{st}H$ calculated values are even lower than those registered for Cu(II), improbably depicting a non-thermal adsorption mechanism. Considering once again metal loading onto HAP (order of magnitude of units of mmol g_{HAP}^{-1}) and the $\Delta_{st}H$ extrapolated from isosteres, it becomes clear that this approach do not satisfy the sensitivity criteria for a thorough investigation of adsorption phenomena occurring in such extent.

Since measure of the heat absorption/release correlated with metal species adsorption cannot be determined with conventional indirect methods, a direct thermodynamic observation of the phenomena was pursued by means of liquid-phase microcalorimetry. Indeed, isothermal titration calorimetry allows to measure the heat evolution related to liquid-solid absorption phenomena when known aliquots of metal species are introduced into a sample cell containing an aqueous suspension of the sorbent. Information are obtained from the calorimetric profiles measured during such titration. Details about used instrument and experimental procedure of microcalorimetric titrations with metal solutions can be found in the Supporting Material (paragraph 8.3.1.2). This study was carried out in collaboration with IRCELYON.

Thanks to this method, the thermal effect of the target metal species adsorption onto HAP has been unraveled. In addition, other metal species, not listed among the target species investigated in the previous paragraph, have been tested in calorimetric titration, as to address ionic radius/mechanism correlations that literature still debate [11,79]. Even if to different extent, all the metal species studied were confirmed to be adsorbed by HAP by several studies [15,16,79,80,130].

First and foremost, a qualitative comparison of the calorimetric profile of several and diverse metal species is reported in Figure 22. The black profile in each graph was registered performing “blank” injections, namely injecting water in water (no metal species introduced, no HAP suspended in the measurement cell).

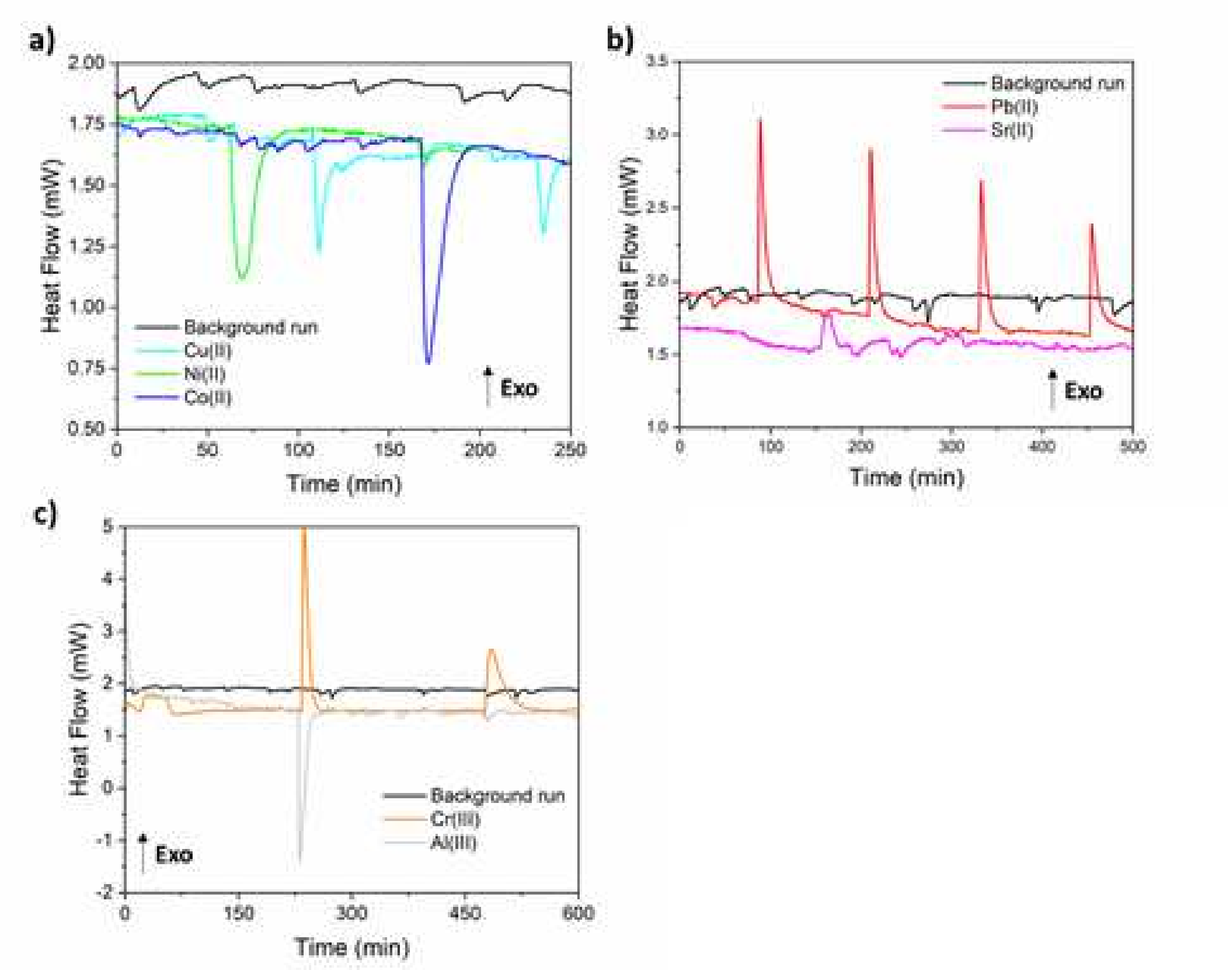

Figure 22: Comparison of calorimetric profiles of adsorption onto HAP for bivalent cations with a) smaller ionic radius and b) bigger ionic radius in respect with Ca(II). In c) calorimetric profiles of trivalent cations. According to the typical calorimetric convention, positive heat flow (i.e. positive peaks) indicate exothermal phenomena and vice versa for endothermal ones.

Table 13: Physical features of Ca(II) (reference) and of the cations under study together with their optimized conditions of microcalorimetric titration.

Metal species	Ionic radius[a]	Atomic number	Charge/radius	Optimized titration conditions		
	Å			*[Me]*	V_{Inj}	Δt_{Inj}
Ca(II)	1.00	20	0.0200	-	-	-
Cu(II)	0.73	29	0.0274	0.3 M	0.4 mL	2 h
Ni(II)	0.69	28	0.0290	0.5 M	1 mL to 0.2 mL	2 h
Co(II)	0.745	27	0.0268	0.5 M	0.2 mL	2 h
Pb(II)	1.19	84	0.0168	0.1 M	0.2 mL	2 h
Sr(II)	1.18	38	0.0169	0.3 M	1 mL to 0.2 mL	2 h
Cr(III)	0.615	24	0.0488	0.5 M	0.2 mL	4 h
Al(III)	0.535	13	0.0561	0.5 M	1 mL to 0.2 mL	3 h

[a] *From Shannon Ionic Radius Database.*

Despite major differences in concentration and volume of injected solutions (Table 13), Cu(II), Ni(II) and Co(II) all exhibited a quasi non-thermal (slightly endothermal) adsorption onto HAP surface (Figure 22a). This common behavior can be addressed to a similar adsorption process for these species onto HAP surface. Literature indeed suggests for them a surface complexation/ion exchange adsorption mechanism

[14,119,120]. Slight endothermicity could be caused by the difference in charge density among these bivalent cations and Ca(II): indeed, desolvatation of one among Cu(II), Ni(II) or Co(II) would require a positive enthalpic contribution which would be higher (in absolute value) than the exothermal counterpart represented by Ca(II) solvatation, since the charge density of “entering” species is slightly bigger than Ca(II) one. So, ionic radius and charge density seem in this specific case to direct the capture energetic and mechanism onto HAP surface.

However, in Figure 22b, such claim is readily denied by the calorimetric profile of two cations with a similar and bigger ionic radius (Table 13), namely Pb(II) and Sr(II). Notwithstanding the almost identical dimensions and charge density indeed, the two metal species exhibits different calorimetric behavior. Pb(II) adsorption onto HAP surface is accompanied by a net heat release ($\Delta_{abs}H < 0$, exothermal process), consistent with the formation of a new (more stable) phase through a dissolution/precipitation mechanism. The present result is not consistent with the $\Delta_{st}H$ calculated from the volumetric approach (Figure 21 and Table 12). Since microcalorimetry is by far the most reliable technique for the evaluation of the thermal effects associated to adsorption, it can be concluded that the adsorption isosteres (volumetric) approach do not fulfill the minimum sensitivity requirements to yield trustable $\Delta_{st}H$ values. Likely, the limited temperature range in which Pb(II) adsorption isotherms have been collected is the most limiting factor in terms of the analytical sensitivity.

Conversely, Sr(II) adsorption results to be basically a non-thermal process, with a minimal exothermicity that can be detected only for high concentration and injection volumes of Sr(II) solution (Table 13). As a matter of fact, Sr(II) is reported in literature to be ion-exchanged with Ca(II) in HAP lattice [46,130,131]; so, the rationale above exposed for Cu(II), Ni(II) and Co(II) stands for Sr(II) as well. The moderate exothermicity can be ascribed to an unbalanced enthalpic contribution from Sr(II) desolvatation/Ca(II) solvatation, this time in favor (in terms of absolute terms) of the latter (because of the lower charge density of Sr(II) in respect with Ca(II)). The comparison between Pb(II) and Sr(II) calorimetric profiles highlights that ionic radius and charge density are not the only parameters directing the mechanism of trapping onto HAP surface. Other factors, such as metal speciation and solubility of related phosphate salts, play a role in defining the pathway of the adsorption process.

Similar conclusions can be drawn when analyzing Figure 22c profiles.

Cr(III) and Al(III), two trivalent species with small ionic radius and high charge density, show indeed opposite behavior. Interestingly, Cr(III) seems to be adsorbed onto HAP surface with an initial strong exothermal contribution, following which moderate exothermicity is displayed. Marked thermal effect would be expected in the case of a dissolution/precipitation mechanism; however, no new crystalline phases were detected on Cr(III)-loaded HAP, although the generation of new amorphous phases was assessed upon adsorption of Cr(III) when $C_{e\ Cr(III)} > 8$ mM (Figure 17b). Considering Cr(III) speciation (Figure 83) and the HAP buffering ability to impose a nearly neutral pH at the liquid-solid interface (paragraph 1.1.4), this thermal phenomenon may can stem from the precipitation of amorphous Cr(III) oxy-hydroxides at the solid-liquid interface.

Cu(II) full calorimetric profile is shows in Figure 23a. Analyzing peak height, it can be noticed that after the first 2 injections the heat absorbed by the process becomes almost constant. Integration of peaks and plotting of differential heat (Q_{diff}, Figure 23b) versus the amount of injected Cu(II) confirms it. As a consequence, integral heat (Q_{Int}, Figure 23c) increases linearly with the amount of injected Cu(II). These trends originate because the amount of Cu(II) dosed (0.4 mL of a 0.3 M solution) is high enough to saturate HAP surface after only the two injections. As a matter of fact, the first two injections bring the system to a $q_e \approx 1.246$ $mmol_{Cu(II)}\ g_{HAP}^{-1}$, practically equal to the previously determined maximum Cu(II) adsorption capacity of HAP ($n_{max} \approx 1.25$ $mmol_{Cu(II)}\ g_{HAP}^{-1}$) under these operative conditions (T = 30°C). So, any other addition of

Cu(II) do not imply further adsorption of Cu(II) onto HAP surface and the heat measured henceforth is only ascribable to dilution effects and thermal noises of the injection itself. Therefore, considering the Q_{Int} evolved from the first two (meaningful) injections, *ca.* 1.5 J g_{HAP}^{-1}, adsorption of Cu(II) is confirmed to be an almost athermal phenomena. Summing up these calorimetric consideration with characterization of Cu(II)-loaded samples carried out above, a surface complexation/ion exchange mechanism appears plausible for Cu(II) as well as for Ni(II) and Co(II), which display similar behavior.

Cu(II) on HAP calorimetric isotherm, obtained correlating Q_{Int} (from microcalorimetric experiments) with the actual q_e (from volumetric experiments, Figure 87a in Supplementary Material), is reported in the Supplementary Materials (Figure 87a). Because of the modest $\Delta_{abs}H$ of the phenomenon and thus the necessity to inject large amounts of Cu(II) to detect slight thermal contributions, experimental data of the calorimetric isotherm were all collected in a narrow q_e range, too close to n_{max} to extrapolate meaningful information.

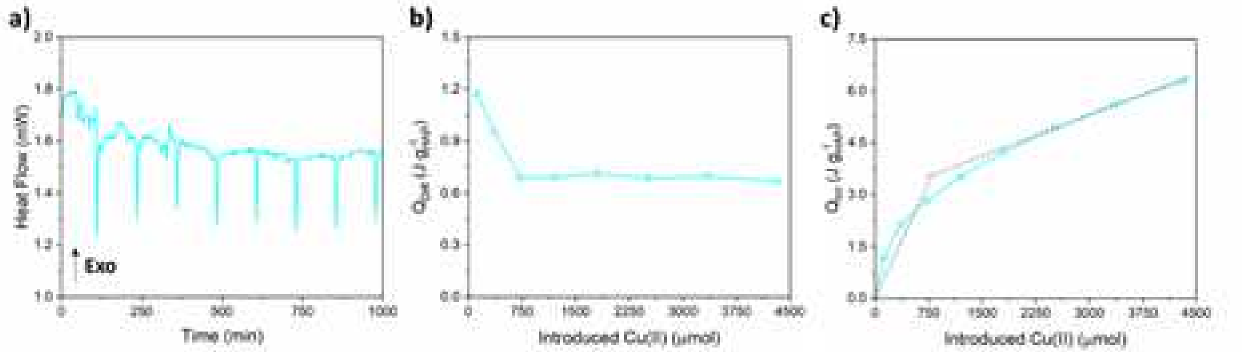

Figure 23: a) calorimetric profile, b) differential heat (Q_{Diff}) plot and c) integral heat (Q_{Int}) plot for Cu(II) adsorption onto HAP.

Pb(II) calorimetric titration returns a peculiar heat flow profile, made of a series of exothermal decreasing peaks (Figure 24a). Peak integration and plotting of Q_{diff} versus the amount of added Pb(II) (Figure 24b) reflect the diminishing trend guessed from the calorimetric profile. Likewise, Q_{Int} versus introduced Pb(II) (Figure 24c) implies the reaching of a plateau for a high quantity of injected Pb(II) moles.

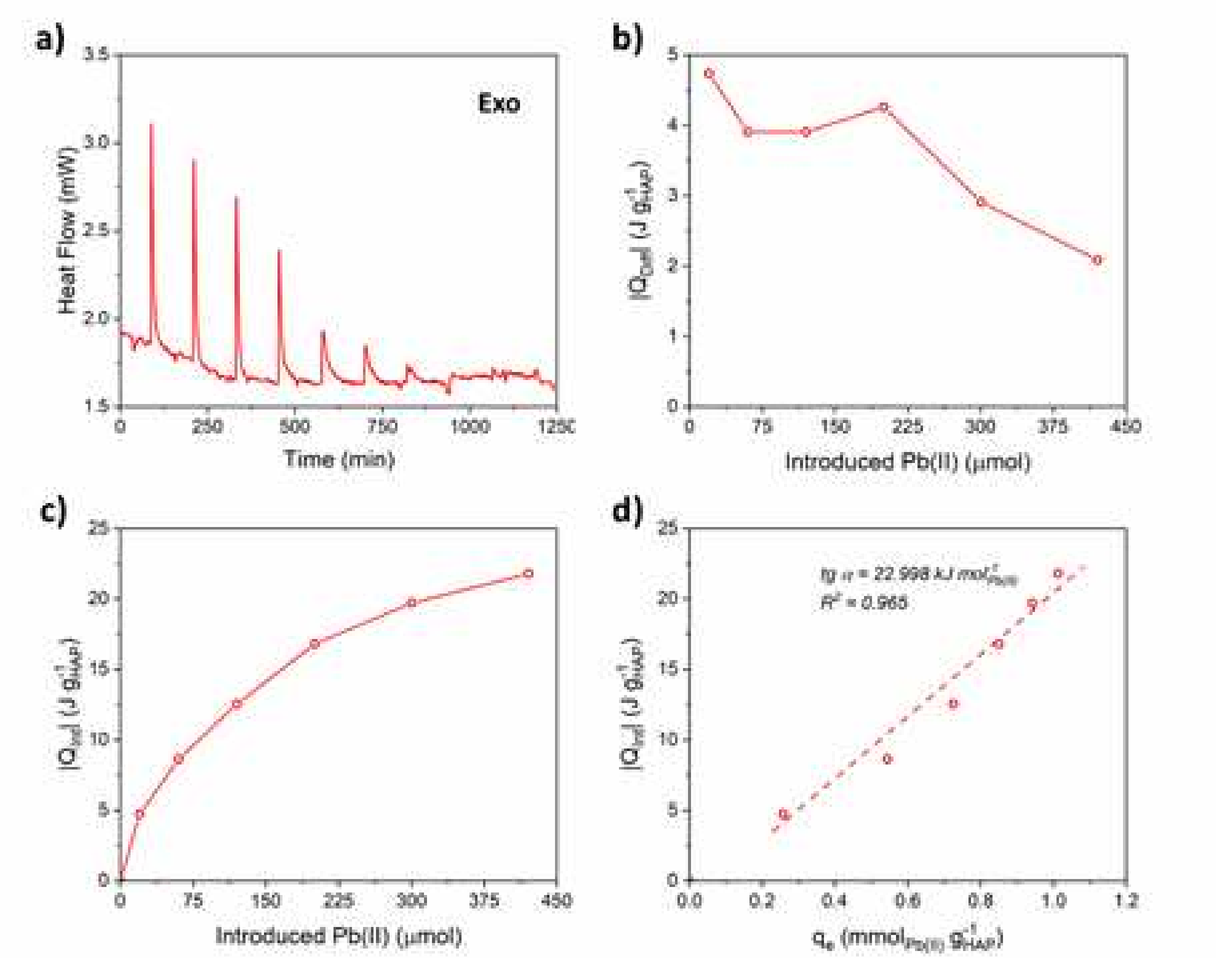

Figure 24: a) calorimetric profile, b) differential heat (Q_{Diff}) plot, c) integral heat (Q_{Int}) plot and d) calorimetric isotherm for Pb(II) adsorption onto HAP.

Thanks to the collection of Pb(II) adsorption isotherms and knowing the exact amount of Pb(II) introduced with each injection, the measured Q_{Int} can be related to a specific amount of adsorbed Pb(II) (q_e), thus obtaining the so-called calorimetric isotherm reported in Figure 24d. Experimental data show a linearly increase of Q_{Int} with q_e. A single regression line fits all data, indicating that one single mechanism is responsible for Pb(II) adsorption onto HAP surface (likely, dissolution/precipitation). From the slope of-this regression line (Figure 24d) the overall average $\Delta_{abs}H$ can be estimated. The formation of hydroxyl-pyromorphite is then assessed to be an exothermal process ($\Delta_{ads}H \approx -23$ kJ $mol_{Pb(II)}^{-1}$).

The calorimetric profile of Cr(III) adsorption onto HAP (Figure 25a) exhibits a series of exothermal and decreasing peaks like Pb(II) but, differently from the latter, peak height stabilizes and remain constant after the initial injections. This behavior influences the trend of both Q_{diff} and Q_{Int} curves (Figure 25b and c).

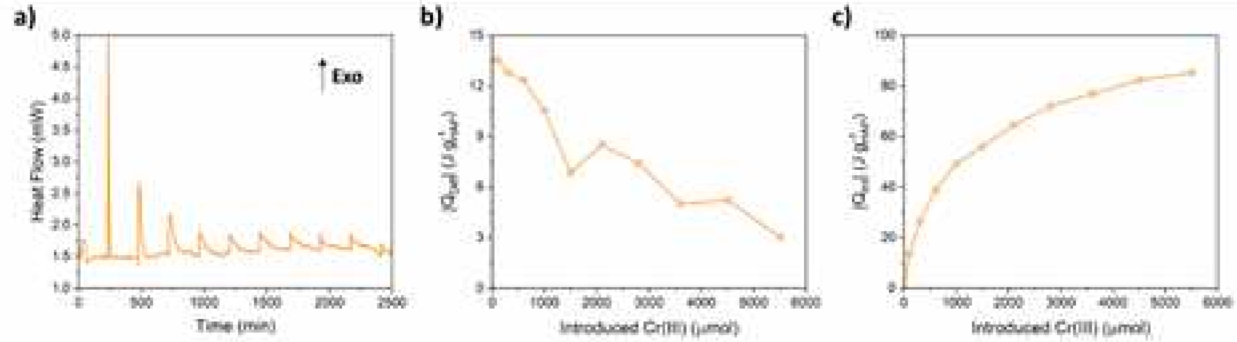

Figure 25: a) calorimetric profile, b) differential heat (Q_{Diff}) plot and c) integral heat (Q_{Int}) plot for Cr(III) adsorption onto HAP.

As for Cu(II) calorimetric studies, the comparative evaluation between volumetric and calorimetric data gives back a calorimetric isotherm (Supporting Material, Figure 87b) in which all experimental points are too close to n_{max} to derive any information about the $\Delta_{abs}H$ of the process. Even in this case, these results are due to the almost complete saturation of HAP surface sites available for Cr(III) immobilization (i.e. reaching of the second branch n_{max}, Figure 16f) during the very first injections. Conversely from Cu(II), Cr(III) adsorption is an exothermal process (first 3 injections) after which, because of HAP surface saturation, the thermal contribution may be addressed to dilution effects and thermal noise.

Considering the peculiarities of Cr(III) adsorption isotherm onto HAP (Figure 16c) and the fact that no significant thermal contributions could be detected when dosing small amounts of Cr(III) (i.e. reaching q_e values lower than the first branch n_{max}, Figure 16f), it may be supposed that the two isotherm branches represent two distinct Cr(III) uptake phenomena. At first, Cr(III) seems to be adsorbed onto HAP surface according to a surface complexation/ion-exchange mechanism. This conclusion is supported by (*i*) the almost null thermal effects detected when dosing Cr(III) as to obtain $q_e <$ first branch n_{max} (*ca*. 0.63 $mmol_{Cr(III)}\ g_{HAP}^{-1}$, Figure 16f) and (*ii*) the absence of any new crystalline and/or amorphous phase on Cr(III)-loaded samples in the same q_e range (Figure 17a). Then, the sudden increase in q_e at $C_e >$ *ca*. 8, which leads to a new plateau (second branch n_{max}, *ca*. 1.19 $mmol_{Cr(III)}\ g_{HAP}^{-1}$, Figure 16f) could be ascribed to a different (exothermal) phenomenon: dissolution-precipitation or (more likely) heterogenous precipitation of Cr(III) oxy/hydroxides at HAP interface, consistently with the appearance of an amorphous contribution as visualized in Figure 17b. Such process should be driven by the high Cr(III) concentration, HAP buffering ability (discussed in paragraph 1.1.4) and the consequent solubility issues of Cr(III) itself (see speciation graph in the Supporting Material, Figure 83). The achievement of the second plateau could then be ascribed to the massive coverage of HAP surface by the Cr(IIII)-based precipitate. The coverage of the HAP surface by the new Cr(III)-based phase results in the disappearance of a suitably buffered interface, therefore hindering further Cr(III) precipitation.

After this thorough physical/chemical characterization and the investigation of the underpinnings of metal cations adsorption onto HAP surface, synthetic stoichiometric HAP has been tested in the remediation of simulated wastewaters representative of some real industrial effluents and/or polluted regions (Table 3).

Two case studies will be presented. The first case study deals with Cr(III) pollution, in combination with Pb(II) and Ni(II) in a simulated effluent of a mining plant while the second is a predictive study for the application of HAP in the remediation of electrical industries effluents, where Ni(II) and Co(II) would be the main polluting species.

2.3.3 Case study n°1: Chromium pollution

A thorough study of HAP efficiency for Cr(III) removal in simulated polluted wastewater has been conducted in industrial-like setup (i.e. static batch adsorption tests). A vast screening of the effect of operational conditions and competitive effects (with Pb(II) and Ni(II), likely co-present in Cr(III) polluted streams, Table 3) has been carried out. All experimental details are reported in paragraph 8.3.1.1.

The effect of pH, contact time and initial metal concentration have all been evaluated. Specifically, Cr(III) uptake has been assessed in the pH range from 4 to 9, for different solution/solid contact times (up to 24 hours) and in the presence of initial Cr(III) concentrations ranging from *ca*. 0.3 to *ca*. 6 mM (i.e. *ca*. 15 to 300 ppm). Details about the actual experiments performed are reported graphically in the scheme inFigure 88 (Supporting Material). The choice of the three operative concentrations (*ca*. 0.3 – 1.4 – 5.8 mM, equal to *ca*. 15 – 75 – 300 ppm) was made to estimate HAP sorbent performance at low, medium and high pollutant concentration, standing to on-field sampling classification and WHO guidelines [106,132].

The main results obtained from Cr(III) adsorption tests on synthetic HAP are reported in Figure 26.

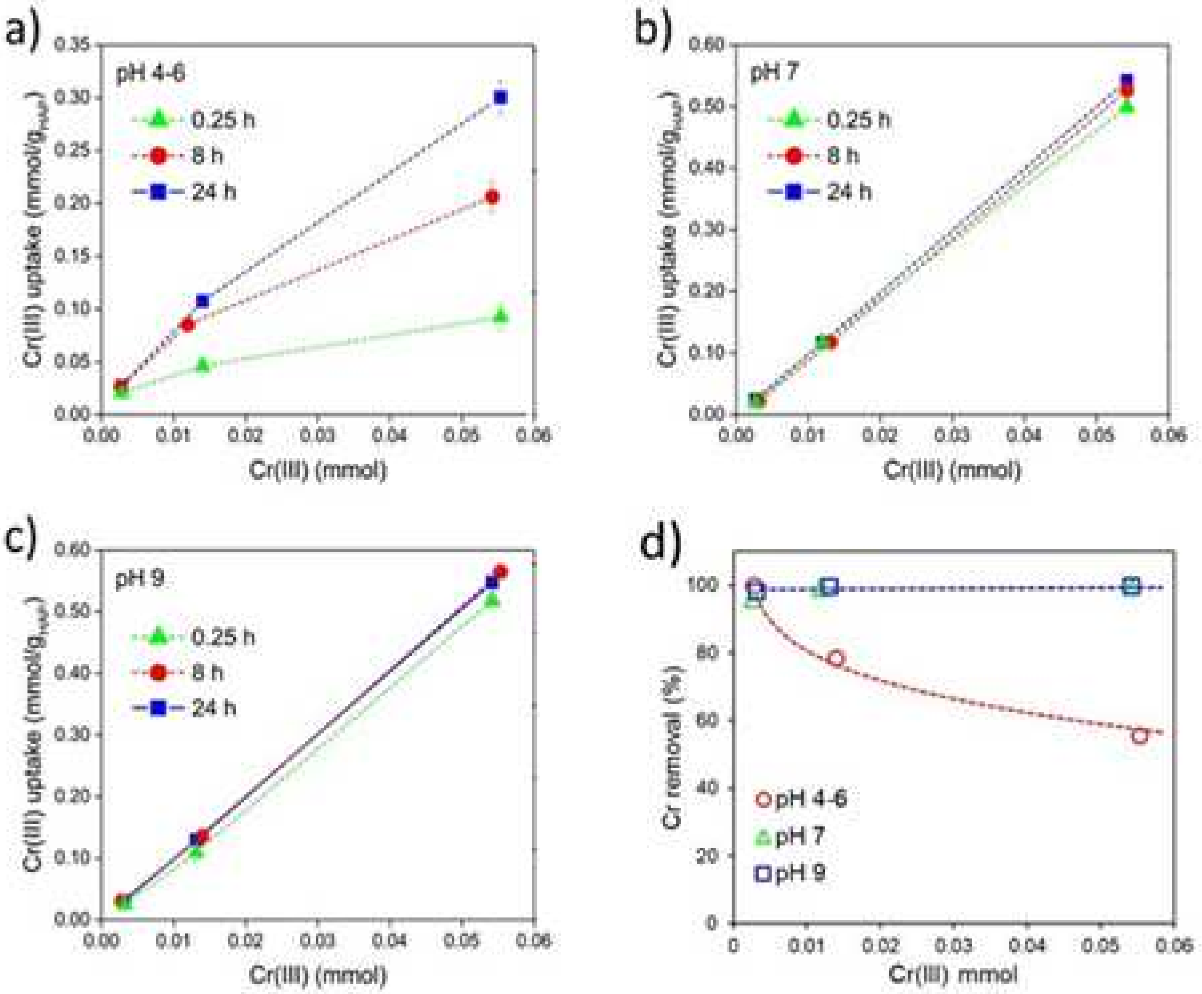

Figure 26: Results of the Cr(III) uptake experiments on synthetic HAP sample at different pH values as a function of initial moles of Cr(III) in solution at fixed volume (10 mL): a) natural pH (4 to 6); b) pH 7; and c) pH 9; d) percent Cr removal from solution for all the adsorption tests evaluated after 24 h. All batch tests were performed at 30°C with a solution volume to solid ratio of 100 mL g_{HAP}^{-1}. From reference (Ferri et al. 2019).

Cr(III) uptake by HAP increased with the initial amount of Cr(III) in solution with trends depending on the initial pH value of the solution. Only at pH 4-6 (i.e. natural pH of aqueous solutions containing from 15 to 300 ppm of Cr(III)), a clear effect of solid/solution contact time has been observed: three distinct curves, lying one over the other and with similar profiles, corresponding to analyses at 0.25 h, 8 h, and 24 h, are displayed in Figure 26a. Thus, Cr(III) trapping onto HAP surface increased with time. Moreover, percent Cr(III) removal decreased with initial Cr(III) amount in solution (Figure 26d), starting from almost 100% down to *ca*. 55% removal efficiency; in terms of Cr(III) uptake onto HAP surface, q_e ranges from *ca*. 0.03 $mmol_{Cr(III)}\ g_{HAP}^{-1}$ (pH 4, initial Cr(III) concentration equal to 15 ppm, removal efficiency *ca*. 100%) to *ca*. 0.30 $mmol_{Cr(III)}\ g_{HAP}^{-1}$ (pH 4, initial Cr(III) concentration equal to 300 ppm, removal efficiency *ca*. 55%). Comparing these q_e values to the n_{max} regressed from Cr(III) adsorption isotherm (Figure 16f), it is clear that the absence of stirring in an industrial-like setup would largely impact on the adsorption capacity of HAP.

Time dependency and diminishment of removal efficiencies for high Cr(III) amount suggest that, in this concentration range, Cr(III) should be trapped onto HAP surface by surface complexation/ion-exchange mechanism, as suggested by volumetric and calorimetric study presented in the previous sections. Dynamic competition with protons (exacerbated by the mild acidic pH) and static batch conditions could be addressed as the main causes of sluggish adsorption kinetics.

For neutral and basic pH values, similar trends in Cr(III) uptake versus initial Cr(III) amount were disclosed. Moles of removed Cr(III) increase in linear fashion with initial concentration (Figure 26b and c) and higher uptakes of Cr(III) occurred in comparison with natural pH conditions. From the viewpoint of percentage removal efficiencies, Cr(III) uptake was total at both neutral and basic pH (Figure 26d). In addition, no differences arose for different solid/solution contact times and the curves collected at 0.25 h, 8 h, and 24 h were quite superposed. This behavior suggest that removal kinetics are faster than under acid conditions and full remediation of Cr(III) pollution occurred in less than 15 minutes for all the investigated initial concentrations.

By considering the speciation diagram of Cr(III) species at pH 7 (Figure 83, supporting material), the uptake mechanism of Cr(III) onto HAP surface likely occurred by a cooperation of surface complexation/ion exchange (exerted by the sorbent in this concentration range) and precipitation of chromium oxy/hydroxides (exerted by the pH conditions and presumably taking place in the bulk of the solution rather than at solid/liquid interface, as in the case of high Cr(III) concentration). However, bulk precipitation of Cr(III) oxy/hydroxides can account only for *ca*. 10% of the total Cr(III) removal (roughly estimated from the speciation graph of Cr(III) reported in Figure 83). So, higher efficiency of the adsorption process can be postulated at pH 7 (in comparison with pH 4-5). In fact, the net overcoming of pH_{PZC} of HAP results in a more favored cationic adsorption [46].

Regarding tests carried out at pH 9 (Figure 26c), bulk precipitation of Cr(III) due to alkaline conditions could be assumed as the main Cr(III) immobilization pathway, as it can be deduced from Cr(III) speciation diagram (Figure 83).

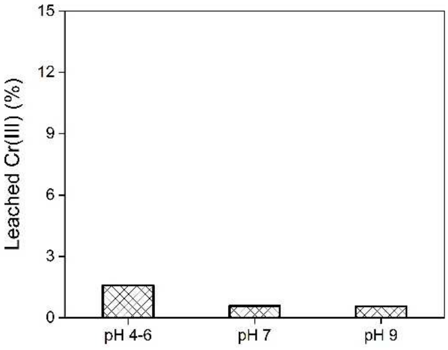

Figure 27: Percent of Cr(III) leached from Cr(III)-loaded HAP samples. Experimental details can be found in paragraph 8.3.1.1. From reference (Ferri et al. 2019).

To assess the risk of secondary pollution and check Cr(III) retention by HAP surface, leaching experiments have been performed on selected Cr(III)-loaded HAP samples. Results are graphically displayed as histograms in Figure 27.

Cr(III)-loaded HAP samples, obtained from the adsorption experiment under acidic pH, released *ca*. 2% of the total Cr(III) previously adsorbed by the material. Samples obtained from the experiments at neutral and basic pH released negligible amounts of Cr(III). These results indicate that (*i*) the highly functionalized HAP surface guarantee excellent Cr(III) retention, avoiding secondary pollution, (*ii*) a low percentage of Cr(III) trapped under acidic conditions is loosely anchored onto HAP surface (sluggish adsorption kinetics and charge repulsion could be responsible for such an unstable “intermediate” state of Cr(III) before a permanent accommodation onto HAP surface) and (*iii*) even if Cr(III) removal starts with chemical precipitation in bulk solution, HAP tightly retained the pollutant when it sits onto its surface, probably anchoring such oxy/hydroxide species as surface complexes.

To corroborate metal uptake tests, selected Cr(III)-loaded HAP samples have been morphologically and compositionally characterized by: ICP/AES analyses on mineralized samples, N_2 adsorption/desorption analyses and STEM/EDX (to have an insight on Cr(III) distribution onto HAP surface). XRPD analyses of Cr(III)-loaded HAP have already been presented in Figure 17 and as discussed above, in this range of concentration, no structural modifications occurred as function of Cr(III) uptake onto HAP surface (Table 35).

Table 14: Main properties of synthetic HAP and selected Cr(III)-loaded HAP samples. From reference (Ferri et al. 2019).

Sample	**Ca/P ratio**	**Surface area**[b]	**Mean pore radius**[c]	**Pore volume**[c]
	atom/atom	*$m^2\ g^{-1}$*	*nm*	*$cm^3\ g^{-1}$*
Pristine HAP	1.662	85.05	4.26	0.219
Post-stability test HAP[a]	1.715	84.98	3.99	0.190
Cr(III)-loaded HAP (natural pH)[d]	1.451	82.02	4.73	0.224
Cr(III)-loaded HAP (pH 7)[d]	1.393	102.45	4.52	0.220

[a] *Sample exposed to acidic conditions (pH 3) by HNO_3 for 24 h.*

[b] *Evaluated according to 3-parameter BET model.*

[c] *Evaluated according to B.J.H. model.*

[d] *Adsorption test performed at initial Cr(III) concentration ca. 5.8 mM (ca. 300 ppm), contact time = 24 h.*

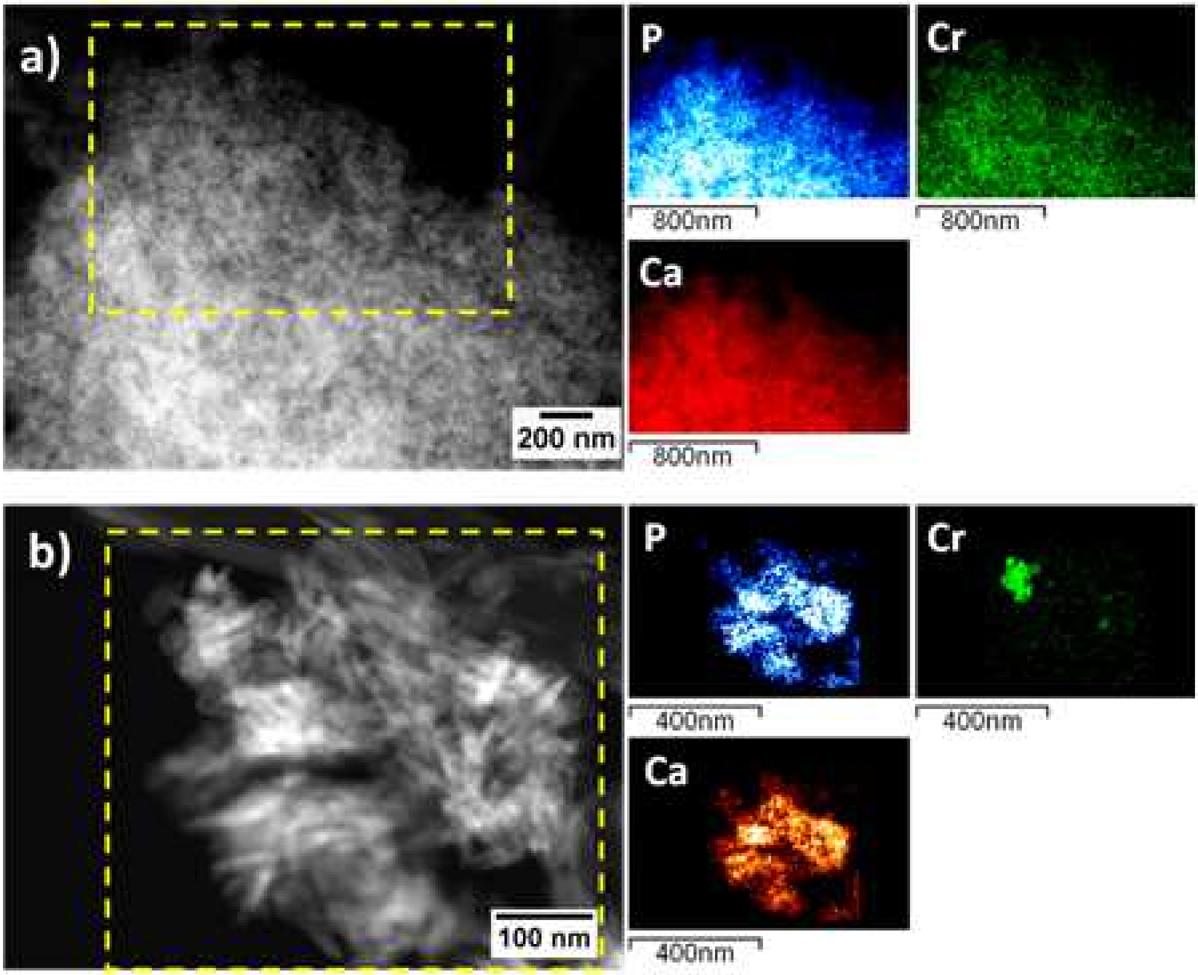

Figure 28: HAADF-STEM image of a sample grain (left side) and EDX element mapping of the selected area (right side) showing the phosphorous (blue), calcium (red) and chromium (green) of Cr/HAP sample after adsorption of Cr(III) at a) natural pH (4-6) and b) pH 7. From reference (Ferri et al. 2019).

Ca/P ratios (Table 11) of Cr(III)-loaded HAP samples decreased in comparison with pristine (stoichiometric) HAP. Such result could indicate partial substitution of lattice Ca(II) ions with Cr(III), despite preferential dissolution of HAP cannot be ruled out. Morphological integrity of the sorbent was confirmed by the results of N_2 adsorption/desorption analysis (Table 11). The increase in surface area of Cr(III)-loaded HAP obtained from adsorption test at pH 7 suggest the presence of high surface area amorphous chromium oxy/hydroxide phases onto HAP surface. Structural integrity after Cr(III) adsorption has already been assessed and discussed above (Figure 17 and Table 35).

When Cr(III) removal took place under natural pH (acidic conditions), a homogeneous dispersion of chromium onto HAP surface was revealed by STEM-EDX element mapping (Figure 28a). Conversely, Cr(III)-loaded HAP obtained at pH 7 presented a completely different structure, exhibiting large chromium-based aggregates (50 – 200 nm) segregated on HAP surface (Figure 28b). These observations seem to confirm the previous assumptions on Cr(III) adsorption mechanisms onto HAP: surface complexation/ion-exchange at acidic pH, predominant chemical precipitation under alkaline conditions and an intermediate situation at neutral pH.

Since in real industrial wastewater Cr(III) can be found in co-presence with other metal species, competitive effects have been evaluated as well. As presented in Table 3, Ni(II) and Pb(II) are common pollutants that tend to pair Cr(III) in industrial effluent streams. Thus, the ability of HAP to remediate heavy metal species pollution in ternary Cr(III) + Ni(II) + Pb(II) solutions has been investigated under conditions similar to those applied for single Cr(III) removal (see Figure 88 in Supporting Information for details). Batch adsorption tests have been performed following the same procedure reported for Cr(III) (Experimental Section, paragraph 8.3.1.1). Total initial moles in the simulated polluted solution have been kept constant at the concentration of *ca*. 6 mM. Metal species ratio was varied as to shed light on competitive effects. Moreover, pH effect on competition and overall capture performances has been assessed, carrying out adsorption experiments under both acidic (pH 4) and neutral (pH 7) environment.

Figure 29 displays the result of ternary-solution metal uptake tests onto HAP at pH 4 (Figure 29a and b) and 7 (Figure 29c and d). On the left, each metal species uptake is reported versus its own initial quantity while on the right the percentage uptake of each species is reported as a function of the metal species ratio in the initial solution.

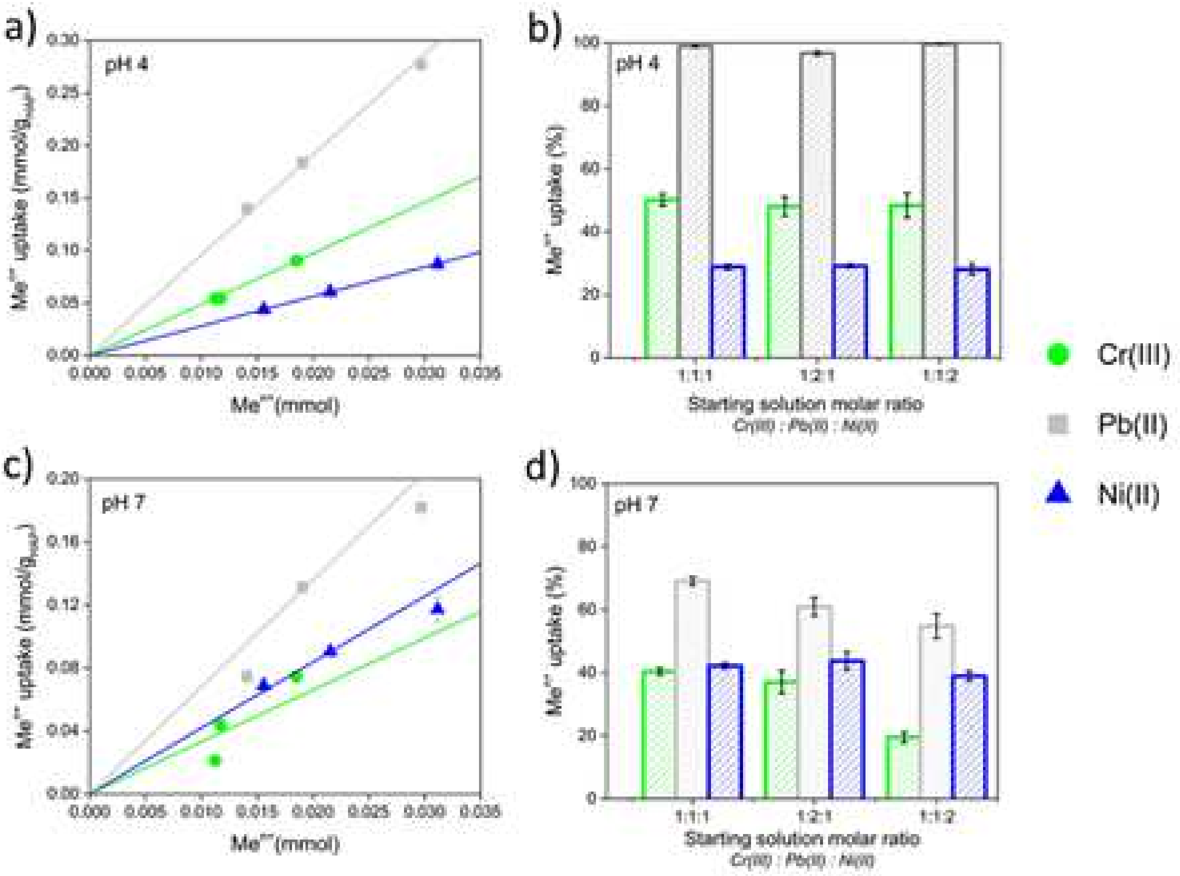

Figure 29: Results of the Cr(III), Ni(II), and Pb(II) uptake experiments on synthetic HAP sample as a function of total initial moles of metal ions in solution at a) pH 4; b) percent results; and at c) pH 7; d) percent results,. All batch tests were performed at 30°C for 24 h with ca. 6 mM initial total metal concentration with a solution volume to solid ratio of 100 mL g_{HAP}^{-1}. *From reference (Ferri et al. 2019).*

Linear trends of metal species uptake against own initial amount in solution characterized the experiments carried out at pH 4 (Figure 29a). Different slopes are displayed for different species, with Pb(II) exhibiting the highest one. Figure 29b indicates that Pb(II) was almost totally removed by HAP, independently from its initial moles in solution and the ratio between species. On the basis of these observations, of the literature on Pb(II) adsorption onto HAP [16,79,133] and the results obtained from the previously presented studies, it can be stated that Pb(II) adsorption onto HAP surface is not in competition with Cr(III) and Ni(II) since pursuing a completely different mechanism (dissolution-precipitation).

Focusing on Cr(III) uptake, it can be noticed that its capture trend is similar (in percentages) to that already discussed in Figure 26a. Indeed, *ca*. 50% of Cr(III) uptake on HAP occurred independently of the presence of the other metal species, Ni(II) and Pb(II), and of their relative ratio. Obviously, the absolute value of moles of Cr(III) on g_{HAP} decreased, indicating a competition with the other species.

Ni(II) resulted to be the least affine species to HAP surface: only a limited increase of Ni(II) removal (in terms of moles on g_{HAP}) has been observed doubling Ni(II) concentration in the initial solution. Thus, removal efficiency of Ni(II) stands around 30% at pH 4, regardless from metal species ratio, suggesting a generally hindered process in terms of affinity rather than a strict losing competitive effect. This observation is consistent with the above presented Ni(II) adsorption isotherms.

Different results were obtained from tests performed under neutral conditions. As verifiable from Figure 29c and d, the uptake of Cr(III) reduced in comparison with that of Ni(II). Although the metal uptake versus initial moles plot do not returns perfect linearity at pH 7, an inversion in species affinity can be guessed from Figure 29c, with Pb(II) maintaining the higher slope.

As above discussed, under neutral conditions HAP surface results negatively charged (since pH > $pH_{PZC\ HAP}$). Thus, the winning competitive effect of Ni(II) over Cr(III) must be sought in cations speciation at pH 7. Under neutral conditions, Cr(III) tends to form bulky oxy-hydroxy cations ($Cr(OH)^{2+}$, see Figure 83), with reduced charge density and mobility in solution. In contrast, Ni(II) still exists in solution as quasi-free ion (Figure 83). So, a consequent competitive advantage for the adsorption on HAP for Ni(II) occurs. The winning effect of Ni(II) adsorption by HAP over the Cr(III) is particularly clear for the experiment performed in the presence of a Ni(II) excess (Figure 29d, last group of histograms on the right).

Regarding Pb(II) results, the decrease of it removal, both in absolute and percentual terms, is consistent with the proposed dissolution-precipitation mechanism. Indeed, neutral pH (i.e. less acidic pH) means reduced HAP dissolution and therefore a lower amount of phosphate groups available in solution. In these conditions, fulfillment of the ideal conditions for hydroxyl-pyromorphite precipitation results hindered in comparison to tests performed in acidic environment [11,26].

Leaching tests have been carried out on multimetal-loaded HAP samples as well and the results are reported in Figure 30.

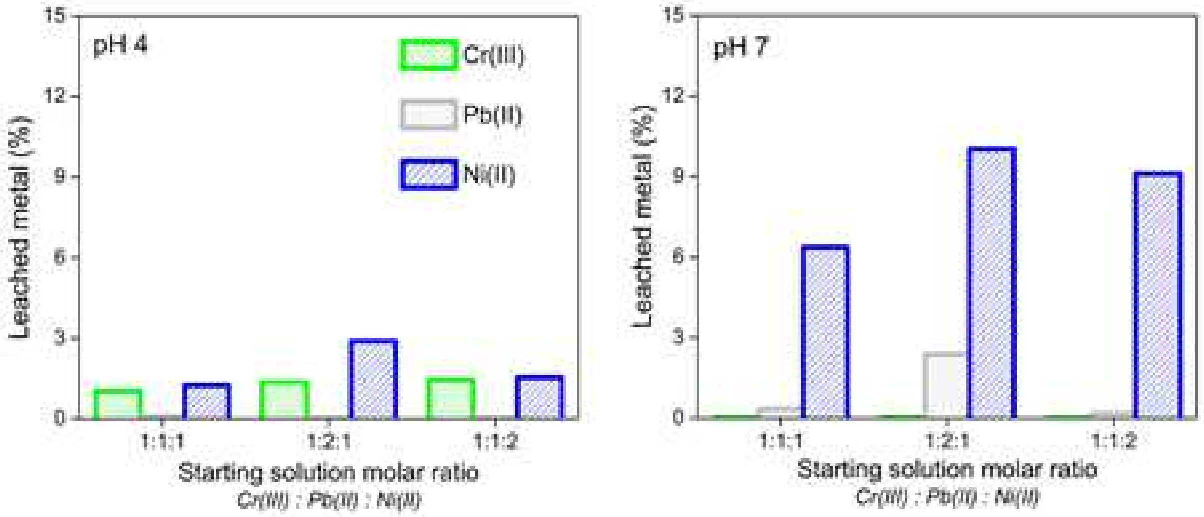

Figure 30: Percent of Me^{n+} leached from mulitmetal-loaded HAP samples at pH 4 (left side) and pH 7 (right side). From reference (Ferri et al. 2019).

Cr(III) almost permanent confinement onto HAP surface was confirmed, in particular when removed under neutral pH.

Opposite behavior was detected for Pb(II). No leaching phenomena occurred for this species when trapped under acidic pH while detectable release of Pb(II) was registered in multimetal-loaded samples obtained from adsorption test performed at pH 7. Maximum leaching, around 3% of total Pb(II) trapped, was measured for samples loaded in the presence of excess Pb(II). Pb(II) retention ability of HAP should be considered in function of the stability of the formed hydroxyl-pyromorphitic phase: acidic pH is surely beneficial for HAP dissolution and $Pb_{10}(PO_4)_6(OH)_2$ precipitation. On the other hand, neutral pH could hinder a correct nucleation and growth of the new phase, bringing to the formation of less stable $Pb_{10-z}Ca_z(PO_4)_6(OH)_2$ phases and/or amorphous (and thus more soluble) hydroxyl-pyromorphite.

The scarce affinity of Ni(II) towards HAP surface is further confirmed by leaching tests. As a matter of fact, Ni(II) suffers from major leaching in multimetal-loaded samples, with a release of *ca*. 9-10% of the previously adsorbed Ni(II) in the worst cases (i.e. when Ni(II) has been removed under neutral conditions). Such results demonstrate once again that Ni(II) weakly interacts with HAP surface and that its competitive advantage over Cr(III) in adsorption processes under neutral conditions does not guarantee a stable confinement of the species in the HAP structure.

Compositional, structural and morphological characterization of multimetal-loaded HAP samples was also carried out.

The sample obtained contacting HAP with an equimolar ratio of all metal species at pH 4 showed a lower Ca/P ratio in respect with pristine HAP (1.378 versus 1.662), likely due to Ca(II) replacement by adsorbed cations and especially Ca(II) release due to $Pb_{10}(PO_4)_6(OH)_2$ formation. Concerning morphologic parameters, surface area and pore volume of the sample were significantly lower than that of synthetic HAP (58.45 versus 85.05 $m^2\ g^{-1}$ and 0.128 versus 0.219 $cm^3\ g^{-1}$, respectively). Massive creation of crystalline hydroxyl-pyromorphite could explain these results. Moreover, pore clogging due to surface precipitation of such species could also account for the decrease in accessible pore volume, without altering mean pore radius (which keep constant at 4.26 nm for multimetal-loaded samples).

Surface sitting and eventual lattice position of Cr(III), Ni(II) and Pb(II) in multimetal-loaded samples have been investigated by means of HAADF-STEM coupled with EDX, FT-IR and XRPD analyses (Figure 31).

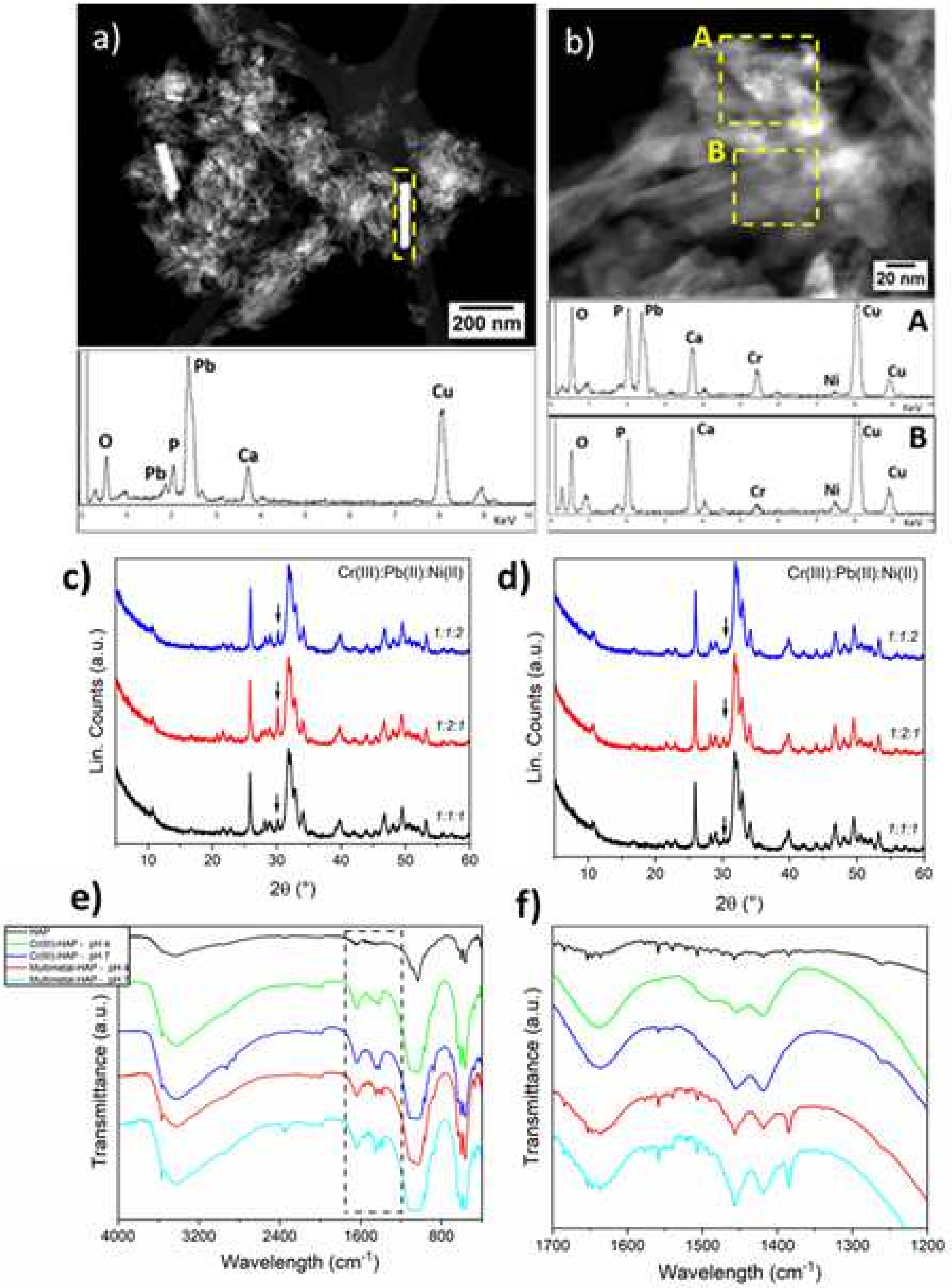

Figure 31: Characterization of multimetal-loaded samples. a) HAADF-STEM images at 69000X magnifications and b) 460000X of multimetal-loaded HAP samples (equimolar ratio, pH 4) and the corresponding EDX spectra of the selected areas. c) XRPD patterns of samples obtained after adsorption tests at pH 4 and d) pH 7. e) FT-IR spectra of multimetal-loaded HAP samples (equimolar ratio of metal species) and f) magnification of carbonates region.

Micrographs presented in Figure 31a and b, collected on multimetal-loaded samples obtained from adsorption tests at pH 4, showed bars of a segregated crystalline phase. EDX analyses confirmed the composition of such aggregates as hydroxyl-pyromorphite (Figure 31a, EDX spectra). Dissolution-precipitation mechanism is thus further assessed for the Pb(II) adsorption. However, STEM-EDX analysis at higher magnification revealed the presence of small Pb-rich segregated particles together with a high distribution of Ni and Cr atoms on the HAP surface (Figure 31b). Regarding Cr(III) and Ni(II), it is not possible to address a preferential capture onto hydroxyapatitic or hydroxyl-pyromorphitic phase; mechanism discrimination between surface complexation and ion-exchange can neither be stated.

XRPD patterns (Figure 31c and d) do not add specific information to the uptake mechanism apart from confirming the formation of crystalline hydroxyl-pyromorphite (additional peak at *ca*. 30° in 2θ). It is noteworthy that this peak intensity correlates with the amount of trapped Pb(II), resulting barely detectable on the multimetal-loaded sample obtained in excess of Ni(II) under neutral conditions (blue pattern in Figure 31d).

Finally, FT-IR spectra of metal-loaded HAPs are shown in Figure 31e. From the comparison with pristine HAP and Cr(III)-loaded HAPs, multimetal-loaded samples exhibits an extra-peak in the spectral region of carbonate groups (magnification in Figure 31f). Indeed, a new band centered at 1384 cm^{-1} appears in multimetal-loaded samples, regardless of the pH imposed during the adsorption process. This band might be associated with carbonatation of hydroxyl-pyromorphite, as reported in literature from studies on synthetic carbonate lead hydroxyapatite [134]. So, considering evidences of Ca(II) presence and possible carbonate substitution, the Pb-containing crystallographic phase formed upon dissolution-precipitation can be more accurately described as $Pb_{10-z}Ca_z[(PO_4)_{6-x-y}(HPO_4)_x(CO_3)_y][(OH)_2$.

2.3.4 Case study n°2: Nickel and cobalt pollution: a perspective on the treatment of electrical industries wastewater

As exposed in paragraph 2, Ni(II) and Co(II) are nowadays experiencing a marked increase in utilization in electrical applications. Indeed, with the global spreading of portable electronic devices and the automotive market moving towards electric power, the industry of electrical energy storage is exploring new solutions and incrementing the effectiveness of existing technologies. Nickel metal hydride batteries [135] and the promising $LiNi_{0.8}Co_{0.2}O_2$ cathodes for high-power lithium ion-cells [107,108] are only a couple of examples related to Ni(II) and Co(II) importance in the actual (and future) electrical market. Due to their forecasted larger use in electrical devices manufacture and the future creation of processes dedicated to spent batteries/cathodes recycling [136], Ni(II) and Co(II) wastewater pollution is going to become a future challenge for environmental protection.

The same approach applied in case study #1 was followed separately for the assessment of sorption ability of HAP towards Ni(II) and Co(II) in an industrial-like setup. Static batch adsorption tests have been performed for single metal containing solutions. Effects of initial concentration of both Ni(II) and Co(II) (from *ca*. 0.25 to *ca*. 4.2 mM, i.e. from *ca.* 15 to *ca*. 300 ppm), pH (acidic to alkaline) and contact time (from 15 min to 24 h) have been evaluated. Main results are displayed in form of removal efficiency histograms in Figure 32a for Ni(II) and Figure 33a for Co(II). Numerical data are listed in Table 42, Supporting Material. Ni(II) and Co(II) onto HAP adsorption isotherms have been already reported in Figure 16d and e, paragraph 2.3.1.

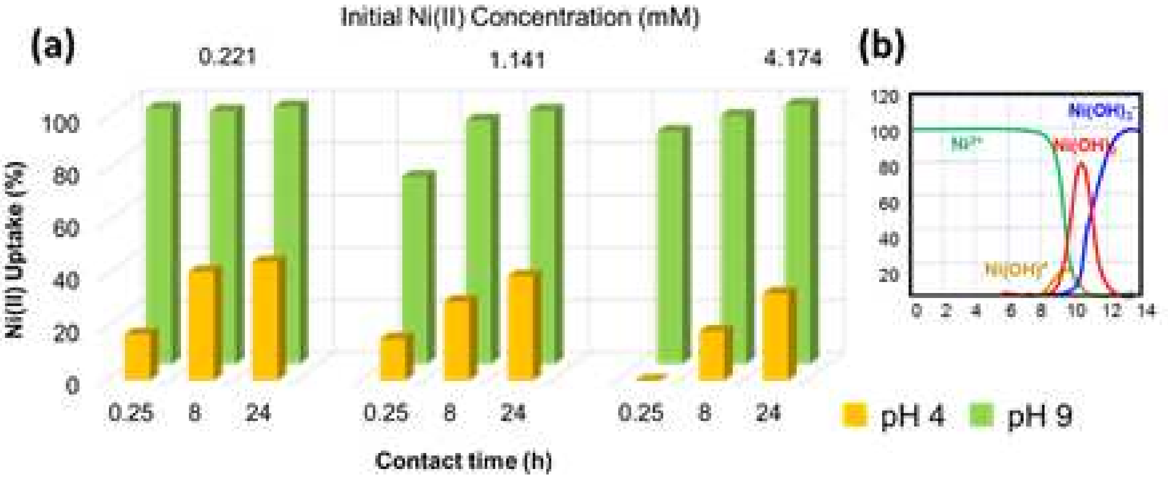

Figure 32: a) Ni(II) uptake (%) on synthetic HAP from static batch adsorption tests, carried out at 30°C, solution volume to solid ratio ca. 100 mL g_{HAP}^{-1}. b) Ni(II) speciation in aqueous solution.

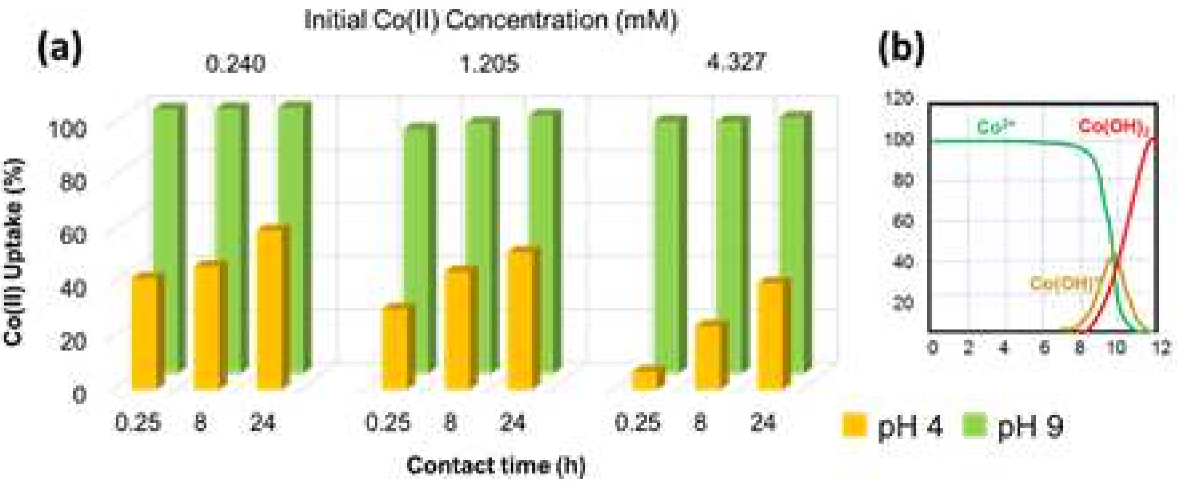

Figure 33: a) Co(II) uptake (%) on synthetic HAP from static batch adsorption tests, carried out at 30°C, solution volume to solid ratio ca. 100 mL g_{HAP}^{-1}. b) Co(II) speciation in aqueous solution.

Under acidic conditions (yellow bars in Figure 32 and Figure 33), the adsorption processes resulted to be strongly affected by the contact time. The effect is more pronounced for higher initial metal concentrations. Limited mass transfer kinetics (due to the static conditions) and the already discussed electrostatic issues connected with acidic pH ($pH < pH_{PZC}$ HAP) could be addressed as the main causes of this trend. In all cases, Ni(II) uptake resulted to be slightly lower than the Co(II) one, confirming all previously collected data. However, maximum metal loading obtained in static conditions (0.132 and 0.165 $mmol_{Me}\ g_{HAP}^{-1}$ for Ni(II) and Co(II), respectively, Table 42) are almost half of the Langmuir regressed nmax for the same species (Figure 16f). This behavior highlights sluggish adsorption kinetics under static conditions for these two species, thus posing a major challenge for HAP competitiveness as sorbent in an industrial-like setup.

Adsorption tests under alkaline conditions (pH 9), revealed removal efficiencies over 90% in almost cases, regardless initial metal concentration and contact time. Overcoming of the pH_{PZC} together with a contribution from chemical precipitation (see speciation diagrams in Figure 83) are the main reason for better remediation performances.

Once fully disclosed the sorption capacity of synthetic HAP towards individual Ni(II) and Co(II) solution through (*i*) the collection of the related adsorption isotherms and (*ii*) batch-experiments, aimed to evaluate the effect of common operational parameters (i.e. initial metal concentration, contact time, pH) under an industrial-like setup, competitive effects have been studied. For this purpose, an adsorption isotherm starting from an equimolar bimetallic solution of Ni(II) and Co(II) has been collected under acidic conditions (pH 4) at 30°C. All experimental details can be found at paragraph 8.3.1.1.

Experimental data and mathematical fitting of this combined isotherm are reported in Figure 34. For each experimental point, both single and total metal equilibrium concentration (C_e) and single and total adsorption uptake were measured, thus allowing to obtain three distinct isotherms. Linear regression of experimental data is graphically reported in the Supporting Material (Figure 89).

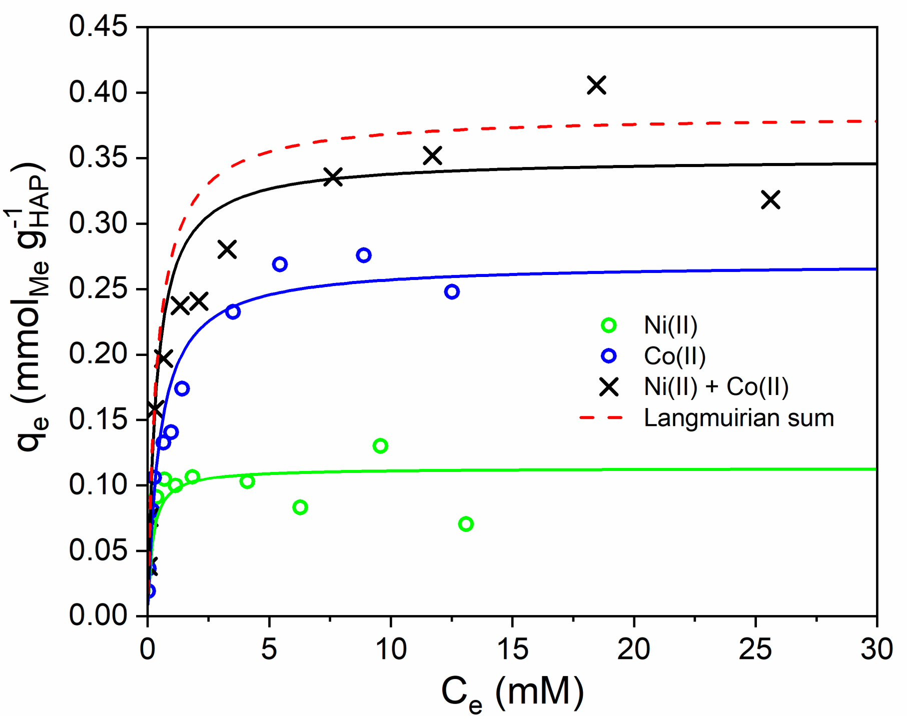

Figure 34: Experimental data (hollow circles) and Langmuir model isotherm fittings obtained from the adsorption of Ni(II) + Co(II) (equimolar solution) onto HAP surface. T = 30°C, acidic pH (4), solution volume to solid ratio equal to 100 mL g_{HAP}^{-1}.

Considering the similar nature of Ni(II) and Co(II) in terms of atomic mass and ionic radii, a competition between the two species for the same adsorption sites is expected. On this basis and from previous results, Ni(II) and Co(II) should in fact share the same trapping mechanism onto HAP surface, namely surface complexation/ion-exchange.

Ni(II) and Co(II) experimental data (green and blue hollow circle in Figure 34, respectively) have been fitted according to Langmuir model equation, based on the knowledge gained from adsorption isotherms collected on single metal containing solutions. The total amount of captured heavy metal species (experimental data represented by black crosses in Figure 34) have been calculated by simple addition of Ni(II) and Co(II) adsorbed moles. These data have been fitted according to the Langmuir model equation as well (black line); this fitting has been compared to the Langmuirian sum (red dotted line in Figure 34) of Ni(II) and Co(II), i.e. the sum of Langmuir isotherms obtained for Ni(II) (green line in Figure 34) and Co(II) (blue line in Figure 34). The application of the Langmuir isotherm model equation to the sum of experimental data (black solid line in Figure 34) better described the combined adsorption phenomenon than the sum of regressed Langmuir models of single metal species (red dotted line in Figure 34), evidencing that the adsorption phenomena of Ni(II) and Co(II) do not take place independently from each other.

All the parameters derived from mathematical regression of experimental data are collected in Table 15.

Table 15: Regressed parameters from Langmuir model application to experimental data of Ni(II) + Co(II) adsorption (equimolar solution) onto HAP surface.

Metal species	Parameter	Value	R^2
Ni(II)	n_{max} (mmol g_{HAP}^{-1})	0.113 ± 0.011	0.935
	b (L mmol^{-1})	(5.15 ± 9.68)	
Co(II)	n_{max} (mmol g_{HAP}^{-1})	0.270 ± 0.008	0.992
	b (L mmol^{-1})	(2.04 ± 0.620)	
Ni(II) + Co(II)	n_{max} (mmol g_{HAP}^{-1})	0.350 ± 0.016	0.982
	b (L mmol^{-1})	(2.79 ± 3.73)	

Fitting the separated Ni(II) and Co(II) experimental data with Langmuir isotherm model equation gives back correlation coefficients R^2 close to unity (Table 15). Indeed, the reconstructed isotherms interpret properly experimental data. As discussed in paragraph 2.3.1, the system under study does not fulfill Langmuir model assumptions, especially from the point of view of energetics of adsorption (surface homogeneity is postulated for the Langmuir model isotherm); thus, the regressed b parameter cannot be considered as physically reliable and relevant; moreover, the related standard error has of the same order of magnitude of the value itself. On the other hand, since multilayer adsorption of heavy metal cations can be ruled out because of the related repulsive interaction, n_{max} value is still representative of the adsorbate loading onto HAP surface. Computed n_{max} values were 0.113 mmol g_{HAP}^{-1} for Ni(II) (*ca*. 36% of the n_{max} value computed for single Ni(II) adsorption) and 0.270 mmol g_{HAP}^{-1} for Co(II) (*ca*. 71% of the n_{max} value computed for single Co(II) adsorption).

Since the sum of these n_{max} (0.383 $mmol_{(Ni+Co)}$ g_{HAP}^{-1}) is almost equal to the n_{max} value obtained from single Co(II) adsorption (Figure 16f), it can be guessed that Ni(II) and Co(II) are captured by the same active sites present on HAP surface. This result opens to the possibility of Ni(II) and Co(II) competition. The affinity trend of metal cations towards HAP, disclosed by previous experiments, is confirmed for Ni(II) and Co(II). As a matter of fact, Ni(II) suffers from the preferential interaction of HAP with Co(II), resulting unfavored in the competition, as reflected by the observed 2.5:1 $n_{max,\ Co(II)}$:$n_{max,\ Ni(II)}$ ratio. Although it is not the case of the present study because of the negligible carbonatation degree of the synthetic HAP employed as sorbent, according to the complexation constants reported in Table 8, Co(II) winning effect should be exerted preferentially onto carbonate-based adsorption sites ($K_{C\ -COH\ Ni(II)} << K_{C\ -COH\ Co(II)}$). This observation poses HAP carbonates content as a key parameter to tune Ni(II) and Co(II) competition/removal.

2.4 Conclusions

In the present chapter, the ability of synthetic HAP to efficiently remediate heavy metal species pollution in simulated wastewater has been assessed.

Optimizing a classical wet co-precipitation route, a strictly mesoporous stoichiometric HAP with large surface area (*ca*. 100 m^2g^{-1}) has been obtained. The material is highly crystalline, with large surface area stemming from the nanometric nature of HAP. Limited carbonatation of synthetic HAP has been disclosed by transmittance FT-IR. Structural and morphological stability of the material has been certified carrying out physical/chemical characterizations prior and after the exposure of HAP to harsh operative conditions (acidic and oxidizing aqueous environment by HNO_3).

The surface of HAP resulted to be amphoteric, slightly more basic than acidic, as expected from the stoichiometric Ca/P ratio. State-of-art gas-solid calorimetric/volumetric adsorption isotherms of acid/base probe molecules allowed the quantitative determination of surface sites' interaction strength. Thanks to calorimetric and volumetric data collected according to this technique, a large population of strong and very strong basic sites have been assessed, indicating HAP as a promising sorbent for heavy metal cations. Close-to-operando quantitative determination of surface active sites have been performed by LRCM, carrying out acid/basic titration of HAP surface in aqueous environment (i.e. at the liquid-solid interface using water as solvent). The impossibility to titrate basic sites under such experimental conditions denotes that water molecules strongly interact with surface basic sites, with the moderately acidic probe (benzoic acid, BA) not being able to displace them. Despite the inability to assess the *effective* number of basic sites in water, this result proves that the interaction strength of HAP basic surface sites is retained under such conditions.

The ability of HAP in removing some target heavy metal cations from aqueous solutions has been assessed through batch sorption tests and by means of the collection of adsorption isotherms in a broad concentration range. The modelling of experimental data, obtained from these sorption tests, allowed to quantitatively assess the HAP sorption capacity and to disclose a specific trend of affinity of HAP towards target cations, namely Pb(II) > Cu(II) > Cr(III) > Co(II) > Ni(II). The physical/chemical investigations carried out on the metal-loaded samples obtained from sorption tests allowed to have an insight on the uptake mechanisms of cations onto HAP. These results have been further corroborated by liquid-phase microcalorimetric measures, by means of which the energetics of adsorption phenomena have been directly observed. In particular, Pb(II) adsorption onto HAP resulted in the formation of a new crystalline phase, namely hydroxyl-pyromorphite ($Pb_{10}(PO_4)_6(OH)_2$), associated with heat release (exothermal phenomenon) indicating a dissolution-precipitation mechanism. Other cations, consistently with their smaller ionic radius, were deemed to be adsorbed onto HAP surface by means of an ion-exchange/surface complexation mechanism, confirmed by microcalorimetric studies to be non-thermal. On the other hand, Cr(III) exhibited a mixed behavior, with its mechanism being function of its actual concentration in simulated polluted solutions; in this specific case, the peculiar speciation of Cr(III) has been addressed as the key point in directing the adsorption mechanism.

The first of its kind microcalorimetric approach applied in the present chapter does not only corroborate the information obtained from the physical/chemical characterization of metal-loaded HAP samples. Indeed, comparing the thermal contribution of several other cations (not included in the group of target species studied through the collection of volumetric isotherms), it has been possible to demonstrate that the ionic radius of cations is not the only parameter directing the adsorption mechanism onto HAP. For example, Sr(II) exhibits a totally different energetics (and mechanism) of adsorption onto HAP in respect with Pb(II) although the almost identical ionic radius, net charge and charge density. Such results indicate that, in addition to cations' dimension and valence, other parameters partake in defining the adsorption mechanisms (and efficiency) onto HAP: metal speciation and solubility of related phosphate salts are key parameters as well, in this sense.

Leaching test, performed contacting metal-loaded HAP samples with freshwater, confirmed the almost total retention of these pollutants by the material, thus indicating HAP as an ideal sorbent even in the ambit of secondary pollution issues.

In the end, two case studies assessed the effectiveness of HAP-based sorbents in the remediation of simulated effluents from mining and electrical industries, disclosing the ability of HAP to exerts its sorption action even when several polluting inorganic species are simultaneously present in solution.

Chapter 3: Development of HAP/C composites for advanced water remediation processes and pollutants' electrochemical sensing

3.1 Introduction to pollutants co-existence and heavy metal ions sensing issues

In the following paragraphs the state of art of (*i*) sorbents for simultaneous removal of organic and inorganic hazardous species and (*ii*) heavy metal ions electrochemical detection in wastewater will be discussed. The rationale behind the design of HAP/C composites for both applications will be presented, highlighting the determining role of carbonaceous scaffold in the properties of the final composite. Scaffold choice and preliminary tests performed in order to determine the best option for each application are commented in paragraph 3.2.

3.1.1 Simultaneous organic/inorganic pollution of wastewater: state of art

Despite the promising performances exhibited by HAP in trapping heavy metal species, wastewater pollution is such a faceted problem that, as today, no single material has been able to properly tackle. As already discussed in paragraph 2, polluted water generally contains more than a single pollutant and, in most cases, the hazardous substances do not even belong to the same class of compounds [137]. Broadly, water polluting agents can be classified as inorganic and organic pollutants. The family of inorganic pollutants include monoatomic anions (e.g. F^-), polyatomic species (e.g. nitrates, phosphates, chromates) and the already thoroughly discussed heavy metal cations; these species account for *ca*. the 30% of the pollutants detected in sewage water [138]. On the other hand, organic compounds, released in the environment by industrial processes of tanning, paper production, printing and agriculture, account for the remaining 70% [138]. This family of pollutants can be further and roughly divided in dyes, herbicides and pharmaceuticals. Dyes are in particular considered heavy water pollutants, with more than 3600 species currently used in the textile sector and an average 2-20% discharge rate in the effluents [139]. Because of their complex structure, most dyes are not biodegradable and thus persist in the environment, exerting long-lasting dangerous effects. Being able to absorb part of the solar radiation, dyes reduce the intensity of sunlight received by algae and aquatic plants, limiting their photosynthetic efficiency [139]. Moreover, most of these molecules exhibit proven carcinogenic and mutagenic effects on human body when ingested [140]. Because of all these reasons, several sorbents have been synthesized and tested for dyes adsorption from aqueous solutions, with activated carbons exhibiting satisfactory results [139].

Although several sorbents showed optimal performances in the remediation of organic or inorganic pollution, the co-existence of both class of pollutants in a water stream hinders the effective treatment of the latter. As a matter of fact, the differences in physical and chemical properties of the polluting species complicate the remediation of such wastewater. Therefore, single sorbents are generally not able to guarantee fast and effective remediation of multi-polluted streams. The co-presence of organic and inorganic hazardous species has been recently assessed in 38 water streams across the United States by Bradley et al. [141]: 4 to 161 organic compounds were detected in each stream, together with hazardous inorganic species, corroborating the evidence of the complexity of the water pollution issue.

In the case of simultaneous presence of several pollutants exhibiting different chemical/physical characteristics, adsorption is more than ever the most practical and tailorable solution for wastewater remediation. Benefiting from the development of structure-controlled nanoparticles synthesis and surface functionalization, several authors have reported novel nanomaterials for the simultaneous adsorption of hazardous organic and inorganic species [141]. Some of the most significant examples are reported in Table 16.

Table 16: Overview of nanocomposites used in the simultaneous remediation of inorganic/organic pollution of wastewater [adapted from Hlongwane et al. 2019]

Nanomaterial	**Removed species**	**Maximum Ads. Capacity** *mg g^{-1}*
Thiourea-modified magnetic ion-imprinted chitosan/TiO_2 composite	Cd(II)	256.41
	2,4-dichloro phenol	98% degradation [a]
Magnetic multi-walled carbon nanotubes (MWCNTs)	Cu(II)	38.91
	Atrazine	40.16
Magnetic graphene oxide (GO) composites	Cd(II)	91.29
	Methylene blue (MB)	64.23
	Orange G	0.85
Ca-alginate encapsulated Ni/Fe nanoparticle beads	Cu(II)	Not reported
	Monochlorobenzene	
Defective titania (TiO_{2-x})	U(VI)	65
	Humic acid	142
Hierarchical vaterite spherulites	Cd(II)	984.5
	Congo red	89.0
Amino-decorated Zr-based magnetic metal-organic frameworks (MOF) composites	Pb(II)	102
	Methylene blue (MB)	128
Magnetic MOF composites	Pb(II)	219.00
	Malachite green	113.67

[a] *Under UV light exposure after 2,4-dichloro phenol capture*

Apart from rare exceptions, it can be noticed that most of the sorbents presented in Table 16 are composites. The driving force that moved scientists towards this class of materials is surely the possibility to conjugate different moieties, thus obtaining compounds with a multi-functionalized surface. Indeed, simultaneous adsorption of organic and inorganic species can be achieved only through the development of complex materials which exhibit a double nature. In addition to the base requirements for high-performing sorbents (see paragraph 2), such composites should present both an organophilic moiety (allowing for π-π interaction and retention of organic molecules by partition) and an inorganophilic one (generally allowing for ligand/ion exchange).

As reported in section 2.3, HAP has proven to efficiently remove several heavy metal cations from single-metal and multi-metal containing wastewater in a broad range of pH, temperature and initial concentration. Hence, HAP could be a promising moiety in a composite for simultaneous organic/inorganic pollution remediation. On the other hand, among the sorbents exploited in organic molecules adsorption, activated carbons represent the most used and studied ones [139]. As today, activated carbons have been proven to efficiently adsorb and retain common organic pollutants such as dyes, pesticides, pharmaceutical, personal care products and phenolic compounds [139,142,143]. With the aim to abate activated carbons' production cost, alternative feedstocks have been employed in the synthesis of this class of sorbents: since available at low cost and largely available, biomass waste and agricultural by-products are surely the most exploited carbon sources. Several authors reported the synthesis of activated carbons from different renewable resources [139,143]; such obtained materials, often functionalized in the presence of surface modifiers (e.g. H_3PO_4) and templating agents (e.g. $ZnCl_2$), have been tested as sorbents for dyes and pharmaceuticals, returning interesting adsorption capacities. The following table gathers the adsorption capacity towards a benchmark organic pollutant (a dye, methylene blue, MB) of some of the most promising activated carbons obtained from as many agricultural processes (as wastes or by-products).

Table 17: Methylene blue (MB) adsorption on various biomass-derived activated carbons. Treatments were carried out in aqueous environment. Adapted from Wong et al. (2018).

Biomass source	**Treatment**	**Adsorption capacity** $mg_{MB}\ g_{Sorbent}^{-1}$
Tobacco stalks	$ZnCl_2$, microwave	1264.51
Medical cotton	H_3PO_4 at 500°C under N_2, microwave	476.2
Cashew nutshell	$ZnCl_2$ at 400°C under N_2	476
Persea Americana nuts	H_3PO_4 at 500°C	365.6
Acorn shell	$ZnCl_2$ at 700°C	330
Spent tea leaves	H_3PO_4 at 600°C under N_2	321
Palm kernel shell	$ZnCl_2$ at 700°C under N_2	225.3
Sludge from paper industry	H_3PO_4 at 600°C	107.1
Plantain peels	H_2SO_4 at 450°C under N_2	47.3
Persian mesquite grain	H_3PO_4 at 600°C under N_2	384

Table 17 highlights how both the starting material and the carbonization procedure affect the sorption efficiency of the derived activated carbon. Although the outstanding performance in the removal of organic species (especially aromatic ones), carbon-based sorbents do not guarantee as much capacity when it comes to inorganic pollutants (i.e. metal cations) due to the low sorbent-sorbate affinity [144].

Thus, taking into account strengths and weaknesses of HAP- and carbon-based sorbent, HAP/C compositing should theoretically give birth to efficient dual sorbents if correctly designed, maximizing the sorption capacity combining the features of the two moieties while achieving stability in aqueous environment and low synthetic cost (i.e. employing biowaste derived activated carbons).

To date, a few HAP/C composites for wastewater remediation have been reported in literature. Carbonaceous scaffold varies from low-cost granular activated carbon [145,146] and biochar [147] to more expensive structures like multi-walled carbon nanotubes [148,149]. However, the vast majority of these materials have been tested in remediation of single-species polluted water. Besides, these materials often exhibit lower heavy metal ions' uptake than pristine HAP, probably because of an unsuccessful realization/design of the composite itself [145,150]. Thus, no evidences of the alleged simultaneous organic/inorganic remediation can be claimed. Moreover, limited structural-morphological characterizations and lack of investigation of the effect of fundamental features (e.g. HAP to C ratio, surface acidity and basicity of the composites) on sorption performance do not allow a proper evaluation of the potential of HAP/C composites.

With the aim to obtain novel bifunctional sorbents, HAP/C composites have been rationally designed, synthesized, characterized and tested to assess their efficiency in removing benchmark inorganic and organic polluting species: Cu(II) and methylene blue (MB), respectively.

3.1.2 Electrochemical detection of heavy metal ions in wastewater: state of art

Heavy metal ions pollution of water streams poses not only the issue of wastewater remediation: indeed, a continuous, accurate, reliable and possibly in-situ monitoring of the presence of those species in waterbodies is fundamental to avoid the release/discharge of hazardous species in the environment. As reported in Table 2, heavy metal species can be harmful at low concentrations (down to µg/L). Therefore, extremely sensitive techniques with limit of detection (LoD) in the range of tenths of nM are necessary to sense heavy metal ions traces in industrial effluents [151,152].

Several spectroscopic techniques have been implemented in environmental monitoring for the detection of heavy metal ions. Among others, atomic absorption spectroscopy (AAS), inductively coupled plasma/atomic emission spectrometry (ICP-AES), ion chromatography ultraviolet/visible spectroscopy (IC-UV/Vis) and X-ray fluorescence spectroscopy (XFS) have proven to achieve both high sensitivity and selectivity towards the main polluting species under investigation [151,152]. However, all the techniques presented share some common drawbacks: high instrument cost (both capital and operational), complex sample preparation, long time of analysis and need for trained personnel [151,152].

In this scenario, electrochemical techniques have gained an increasing interest in the last decades, representing an excellent alternative to spectroscopy-based investigation methods. As a matter of fact, electrochemical techniques are cheaper, user-friendly, reliable and suitable for in-situ measurements [153]. On the other hand, electrochemical detection of heavy metal ions reaches less satisfying LoDs, sometimes failing to achieve the sensitivity required by environmental legislation. In this context, researchers strived to improve sensitivity, selectivity and overall performance of electrochemical devices for heavy metal ions detection in aqueous solutions, mainly sharpening and optimizing the applied electrochemical techniques and seeking for highly performing electrode materials [151,152].

Electrochemical techniques for the determination of heavy metal species in waterbodies are generally classified according to the electrical signal generated by the presence of the latter: changes in registered voltage, current, electrochemical impedance or electroluminescence phenomena can be applied for the identification and quantification of heavy metal cations (with prior system calibration). Amperometric/coulometric, voltammetric, potentiometric, impedance spectroscopies and electrochemiluminescent techniques have all been reported in the literature [154,155] to serve this purpose, with voltammetry giving the best results in terms of both selectivity and sensitivity.

To date, the state of art voltammetric technique for sensing heavy metal species traces in waterbodies is anodic stripping voltammetry (ASV). In order to lower the technique's LoDs, background current is generally suppressed by application of pulses in the voltage signal. Several pulse voltammetries, characterized by different voltage/pulse time patterns, have been developed throughout the years for analytical purposes: normal pulse voltammetry (NPV), staircase voltammetry (SV), reverse pulse voltammetry (RPV), differential pulse voltammetry (DPV) and square wave voltammetry (SWV). Among those listed, DPV and SWV are certainly the most successfully applied in the field of analyte traces detection in aqueous solutions: literature indeed reports the achievement of LoDs down to the picomolar range for both differential pulse anodic stripping voltammetry (DPASV) [156] and square wave anodic stripping voltammetry (SWASV) [157].

These electrochemical analytical methods are composed of two consecutive steps (Figure 35):

1. *Reductive preconcentration*: accumulation/deposit, by electroreduction, of metal species at the working electrode by means of the application of a sufficiently cathodic potential for a determined time;
2. *Anodic stripping of reduced species*: a potential scan, in the anodic direction, starting from the potential applied in the preconcentration step. The increasingly anodic potential causes the reoxidation/dissolution of previously reduced metal species, with a related transient faradic signal. Such signal is generally a peak, whose position (potential) and height (current density) allow for the qualitative and quantitative determination of the metal species in solution, respectively.

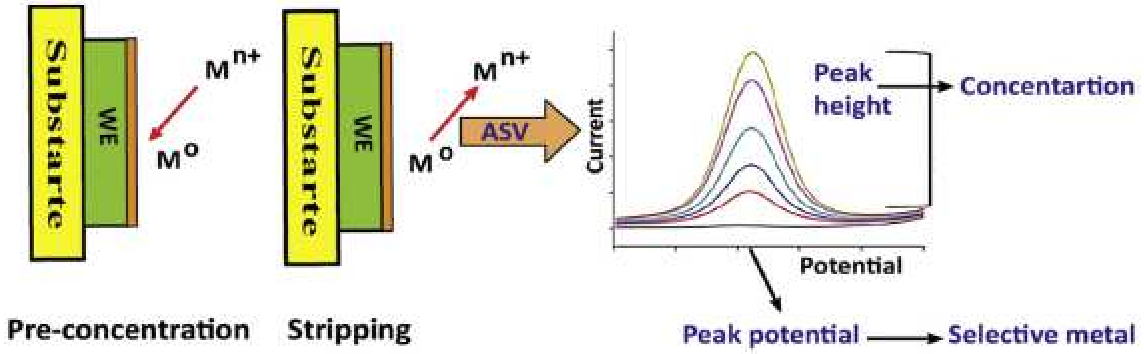

Figure 35: Graphical depiction of the steps involved in determination of heavy metal species by anodic stripping voltammetry of in aqueous solutions. From reference [Waheed et al, 2018]

Being composed by multiple steps, ASVs are complex electrochemical methods that obviously require the optimization of several electrochemical parameters such as deposition time and voltage, operative voltage window and scan rate. At the same time cell parameters, such as nature and concentration of the supporting electrolyte and the choice of the electrode material, play a fundamental role in determining the sensing ability of the system [151,152].

Apart from the improvement of the electrochemical methods, the development of a reliable, accurate and selective electrochemical sensor cannot be separated from the implementation of optimal electrodes, specifically designed for heavy metal species detection.

Historically, the dropping mercury electrode (DME) has been the electrode of choice for the early development of heavy metal ions determination techniques. DME is in fact extremely sensitive thanks to the intrinsic ability of Hg to form amalgams with several metals, thus facilitating the preconcentration step, enhancing sensitivity and lowering LoDs. In addition, wide cathodic range and reproducibility contributed to the widespread diffusion of DMEs for electrochemical analyses of metal traces in waterbodies by ASV [158]. However, due to several issues related to the handling and use of Hg, DMEs have experienced a slow but unavoidable worldwide ban in environmental monitoring applications, although remaining the benchmark electrode in terms of sensing performances.

Since the ban of Hg-based electrodes, several alternatives have been proposed: Bi, carbon, Pt and Au-based bulk electrodes have been thoroughly screened in the past decades. All bulk electrodes resulted to be affected by major limitations, such as large overpotentials for metal species reduction, high stripping potentials, narrow cathodic/anodic voltage windows and general low sensitivity [151].

With the advent and development of nanoparticles synthesis, surface modification of electrodes with the latter has paved the way to a whole new generation of promising electrochemical sensors. Improved performances in terms of sensitivity, LoDs and response stability are indeed noticed when comparing NPs modified electrodes to bulk electrodes, mainly because of the larger surface area and electron and mass transfer rates guaranteed by the former [151].

Several nanoparticles have been implemented as electrodes' modifiers; among them, metallic and metal oxide nanoparticles and nanostructured allotropes of carbon [151,152]. Each one of these families of nanoparticles evidenced some shortcomings. For example, metallic NPs are generally unstable towards oxidation and expensive (that's the case of Au and Ag NPs); metal oxides NPs, on the other hand, present higher surface area, surface functionalization and overall enhanced adsorption ability at the expenses of lower conductivity; carbon nanostructures exhibit instead optimal stability, conductivity and mechanical resistance but limited surface functionalization (i.e. sorption ability) and high production cost.

In order to overcome the drawbacks of each individual nanomaterial and obtain modifiers able to match DME's performances, the field of nanocomposite materials have been extensively explored [151,152].

HAP exhibits remarkable adsorption properties, together with medium-high surface area and porosity, as previously detailed (paragraph 0). However, its insulating nature (it only presents a modest and monoaxial ionic conductivity along the c-axis) prevented its application as bulk material in electrochemical devices. Thanks to nowadays NPs syntheses and processing technologies, HAP has experienced a renewed interest by the electrochemistry community. HAP can indeed be implemented in nanocomposite materials with the aim to exploit its sorption properties towards heavy metal ions, thus assisting the preconcentration step that is typical of ASV-based techniques. Highly conductive moieties are generally paired with HAP in these nanocomposites, to counterbalance HAP conductivity issues.

HAP-based and/or doped nanocomposite materials reported in literature to date and their performances in sensing heavy metal ions and other hazardous compounds are reported in Table 18:

Table 18: Application of HAP as electrode modifier in electrochemical sensing of hazardous species.

Electrode modification	Analyte	Linear response range	Limit of Detection (LoD)	Electrochemical technique	Ref.
HAP-modified carbon paste electrode	Paraquat[a]	0.8 to 200 μM	15 nM	SWCSV[a]	[159]
CNT-HAP nanocomposite	Cd(II)	0.02 to 3 μM	4 nM	DPASV	[160]
HAP-modified ionic liquid carbon paste electrode	Cd(II) Pb(II)	1 to 100 nM	0.5 nM 0.2 nM	SWASV	[161]
Flower-like HAP modified carbon paste electrode	Cd(II) Pb(II)	1 to 100 nM	5.31 nM 2.38 nM	SWASV	[162]
Bi-film on HAP modified GCE	Cd(II) Pb(II)	9 nM to 1.3 μM 5 nM to 0.75 μM	45 nM 25 nM	CV & SWASV	[163]
Biosynthesized HAP	Hg(II)	0.2 to 210 μM	141 nM	SWASV	[164]
HAP/Nafion nanocomposite	Hg(II) Cu(II) Pb(II) Cd(II)	0.1 to 10 μM	30 nM 21 nM 49 nM 35 nM	DPASV	[165]
Cellulose/HAP carbon electrode composite	Pb(II)	0.05 to 0.25 μM	0.55 nM	CV & SWASV	[166]
HAP-supported nanocrystalline Ag-doped ZSM-5	Hg(II) As(III) Pb(II) Cd(II)	Ca. 0.005 nM to 15 nM	< 1 nM (all)	SWASV	[167]

[a] *Organic cationic species.*

Although good results in terms of sensitivity and LoDs have been achieved for several HAP/C composite materials, many problems still hinder the transfer of this sensing technology from lab testing to on-field operations. First and foremost, LoDs are not matching law requirements in most cases and conductivity issues, due to the not ideal integration of HAP in the nanocomposites, heavily impacts on sensing performances. Secondly, several studies are carried out on glassy carbon electrodes modified by simple drop casting of HAP-based/doped nanocomposites [160,162,163,165,167]: this configuration does not meet the mechanical stability required for on-field applications and thus results can be just considered as a first screening of materials' performances. In addition, synthesis of HAP-based/doped nanocomposites is often complex and expensive (both in terms of synthetic procedures and reactants/composite moieties) [160]. On top of that, lack of structural-morphological characterization and investigation on the actual mechanisms of sensing do not allow to fully rationalize the role of HAP moieties in such nanocomposites.

With the aim to develop HAP-based/doped nanocomposites for heavy metal ions sensing in aqueous solution, HAP/C composites have been synthesized according to a simple wet co-precipitation route using different carbonaceous scaffolds. After a first screening aimed to the selection of the most suitable support, different HAP/C nanocomposites with different composition (in terms of HAP and C wt.%) have been synthesized and thoroughly characterized from the structural and morphological point of view. Self-standing modified carbon paste electrodes have been then manufactured starting from HAP/C composites powders; crafting has been optimized as to guarantee electrodes' mechanical stability. Such electrodes have been tested in the electrochemical detection of hazardous heavy metal species in simulated wastewater, with a particular focus on two benchmark species like Cu(II) and Pb(II).

3.2 Preliminary screening of different carbonaceous scaffolds

Synthesis of novel HAP/C composite materials has been carried out according to a modified co-precipitation method, in which the main difference is represented by the presence of the carbonaceous scaffold in the precipitation mixture. Optimization of HAP co-precipitation onto C-based materials entailed other major modifications, such as the precursors' concentration and the synthetic volume, time and temperature. All the experimental details about the synthesis of HAP/C composites are reported in the Experimental section, paragraph 8.1.2.

Since HAP/C composites have been developed for two distinct purposes, namely wastewater remediation from simultaneous organic and inorganic pollution and implementation in sensing devices to detect heavy metal ions traces in waterbodies, different carbonaceous scaffolds have been investigated. Indeed, although some common characteristics of carbonaceous scaffolds are beneficial to both applications (for example, high surface area), a specific tuning of the HAP/C composites' features through a careful selection of the carbon-based moiety is highly desirable. For example, the need for high surface area and high functionalization degree requested for good sorbents would push HAP/C composites towards the implementation of cheap and well-known activated carbons. On the other hand, sensing application, in which electrical conductivity is of paramount importance, would drive the choice of carbonaceous scaffolds towards highly graphitic and conductive carbon-based nanostructures, at the expenses of materials' cheapness and surface area.

On the basis of the above-presented rationale, three different carbonaceous scaffolds were selected and implemented in HAP/C composites syntheses:

- Carbon nanofibers (CNFs), type PR24-HHT (Pyrograph, Applied Science Inc.).
  Obtained through pyrolysis at > 1300°C, these nanofibers present a *ca*. 100% graphitization index, thus remarkable thermal stability and electrical conductivity, at the expenses of an almost null functionalization degree. Despite the nanometric diameter (100 ± 30 nm), such nanofibers exhibit a low surface area (*ca*. 40 m^2 g^{-1}).
- Mesoporous carbon (CMC), from renewable sources.
  Obtained through pyrolysis of wheat flour in the presence of $ZnCl_2$ as templating agent, CMC has been reported in literature by Shen et al [168]. It is characterized by its cheap and eco-friendly nature, together with high surface area and porosity (*ca*. 1400 m^2 g^{-1}, pore volume *ca*. 2.64 cm^3 g^{-1}) and functionalization degree [168,169].
- Granular activated charcoal (AC), extra pure (Sigma-Aldrich).
  Benchmark commercial material, known for its sorption capacity and high surface area.

For a preliminary screening, HAP/C composites containing *ca*. 4 wt.% of carbonaceous scaffolds have been synthesized according to the procedure reported in the Experimental Section, paragraph 8.1.2. The three composites have been labelled HAP/CNF, HAP/CMC and HAP/AC, respectively. All composites have been characterized, as to establish which C-based scaffold could guarantee the optimal features for the two alleged applications. For comparison, a batch of pristine HAP (HAP_RT) has been synthesized following the same method but in absence of any carbonaceous scaffold and characterized as well. Both HAP_RT and HAP moieties of HAP/C composites presented a stoichiometric Ca/P atomic ratio of *ca*. 1.67. It is noteworthy that HAP_RT differs from the pristine HAP presented in the previous chapter, since synthetic conditions have been modified for HAP/C composites. Thus, the differences (in terms of both structure and morphology) between HAP_RT and HAP synthesized at 80°C (presented, as above written, in the previous chapter and here labelled as "pristine HAP") are discussed as well.

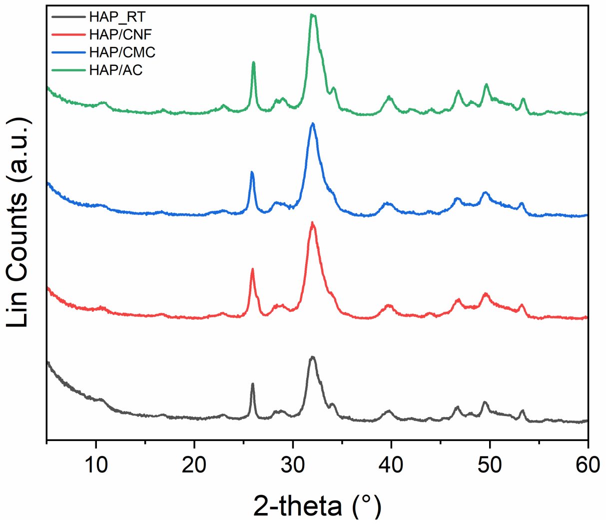

Figure 36: XRPD patterns of HAP_RT and HAP/C composites. Carbonaceous scaffold content in the composites is equal to ca. 4% wt.

XRPD patterns of HAP_RT and HAP/C composites are reported in Figure 36. Broader peaks and lower intensity of the peak at *ca*. 26° in 2θ in the HAP_RT pattern (black line in Figure 36) are indicative of lower crystallinity degree and different nanoparticles shape (i.e. no pronounced elongation along the c-axis) as compared to pristine HAP synthesized under non-template optimized conditions (see paragraph 2.2.1, Figure 10 and related comments). Application of the Scherrer equation to the XRPD data collected gives back a crystallite dimension of *ca*. 40x8 nm, confirming the differences with the *ca*. 200x8 nm nanoneedles reported in paragraph 2.2.1, Figure 10.

All HAP/C composites exhibit patterns similar to that of HAP_RT; thus, the presence of carbonaceous scaffolds in the co-precipitation slurry are proven not to influence neither the phase purity of the HAP moiety in the composite, nor its crystallinity degree and/or crystallites' dimensions. In the case of HAP/CNF (red line in Figure 36), a shoulder peak around 27° in 2θ can be detected. Such contribution can be attributed to the 002 indexed reflection plane of graphite [170], feature associated with the C-based moiety and whose low intensity can be addressed to the low wt. % of the latter in the composite. The absence of such contribution in HAP/CMC and HAP/AC patterns is consistent with their predominant amorphous nature [168,169].

TEM images of HAP_RT and of the HAP/C composites are gathered in Figure 37. HAP_RT (Figure 37a) resulted to be composed of irregularly shaped nanoplatelets with dimensions comprised between 5 to 40 nm, slightly different from those calculated through the application of the Scherrer equation. In all composite materials, HAP moieties retain the same nanoplatelet-like morphology (Figure 37b to e). TEM images of the HAP/CNF composites demonstrate the close contact between the hydroxyapatitic and carbonaceous moieties (Figure 37b). However, as observable from the magnification in Figure 37c, HAP nanoparticles tend to stack one on each other instead of being uniformly distributed onto CNFs' surface. The inhomogeneous distribution of the phases in the composite is probably ascribable to several factors, such as the low surface area and functionalization degree of CNFs and the marked disproportion in terms of wt. % of the two phases. On the other hand, TEM images of HAP/CMC (Figure 37d) depict a more homogeneous composite, in which the two moieties are not distinguishable. In this case, the high surface of CMC, together with the pronounced surface functionalization are surely the main promoters of homogeneous HAP dispersion and anchoring on the carbonaceous scaffold. Finally, HAP/AC (Figure 37e) resulted similar to HAP/CMC from a morphological point of view. However, alleged homogeneity observed by TEM cannot be observed at a macroscopic scale: indeed, the HAP/AC composite appeared visually inhomogeneous and, when stocked in lab containers, tends to settle with the formation of two different layers, thus demonstrating the poor mechanical stability of the composite and the imperfect immobilization of HAP onto AC.

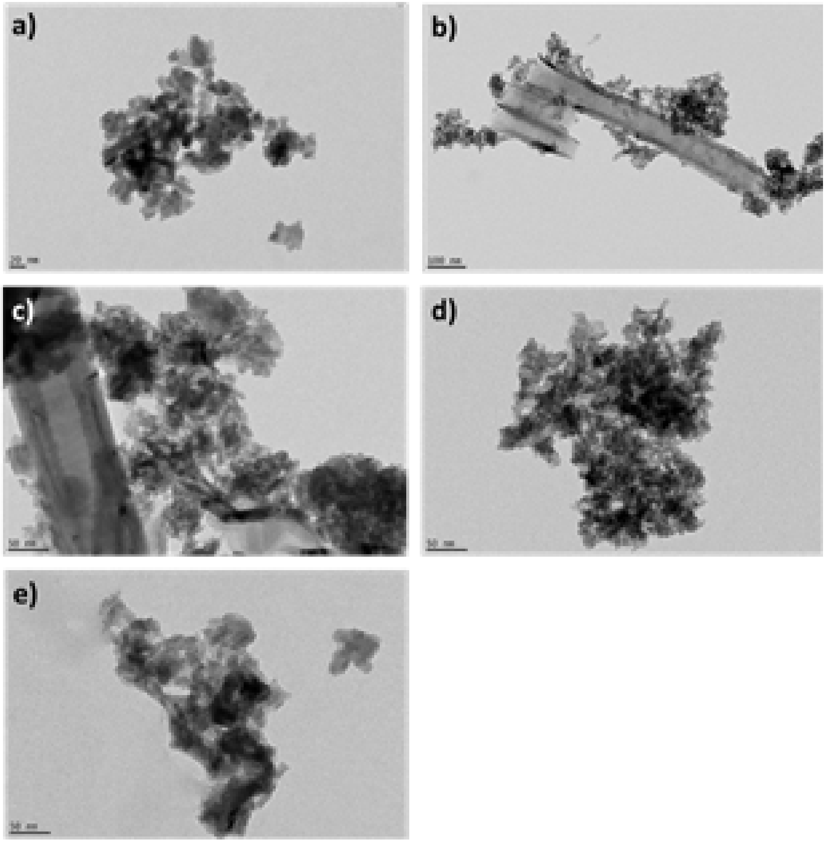

Figure 37: TEM images of a) HAP_RT, b) and c) HAP/CNF, d) HAP/CMC and e) HAP/AC. Carbonaceous scaffold content in the composites is equal to ca. 4 wt.%.

N_2 adsorption/desorption analyses have also been carried out on both HAP_RT and HAP/C composite. Adsorption isotherms, 3-parameters BET linearization and BJH pores distribution of all samples are reported in the Supporting Material (Figure 90 to Figure 93). The analytical conditions and the application of BET and BJH model were the same previously discussed and are detailed in the Experimental Section (paragraph 8.2.1).

Table 19 gathers all the numerical data obtained by N_2 adsorption/desorption analyses. HAP_RT exhibits a slightly higher specific surface area (*ca.* +15%) in comparison with the pristine HAP (Table 5) obtained from the non-template modified method, with mean pore radius and cumulative pore volume increasing accordingly. Such increases could be ascribed to the lower crystallinity (i.e. higher amorphous contribution), in concordance with XRPD patterns. The presence of a carbonaceous scaffold brings in all cases to an increase in surface area, more marked for HAP/CMC and, surprisingly, for HAP/CNF. These results suggest that, whether the surface area of the scaffold, the latter favors dispersion of HAP, diminishing aggregation of HAP nanoplatelets and thus increasing the exposed surface of the material. This experimental evidence is quite consistent with the TEM observations, although some problems of HAP dispersion has been noticed for HAP/CNF composite.

Mean pore radius and pore volume are instead only slightly affected by the presence of the scaffold, with the larger difference found in the former for HAP/CNF and HAP/CMC. However, all the HAP/C composites can be considered mesoporous materials, as expected from the typical type IV N_2 adsorption isotherms and the H2 type hysteresis loop shown, despite some minor differences, by all samples (Figure 90a to Figure 93a). It is interesting to notice that all composites exhibit a total pore volume close to the one of HAP_RT: this is particularly noteworthy in the case of HAP/CMC, in which the “bare” scaffold has been demonstrated to possess a way larger porosity (*ca.* 2.64 $cm^3\ g^{-1}$). It can be then concluded that HAP precipitation/immobilization onto the scaffold may cause the pore clogging of the latter, thus resulting in a lower than expected composite's porosity.

Table 19: Surface area, mean pore radius and cumulative pore volume of HAP_RT and HAP/C composites calculated from N_2 adsorption/desorption analyses. All composites contain a 4 wt.% of the related carbonaceous scaffold.

Sample	**Surface Area**[a]	**Mean pore radius**[b]	**Pore volume**[b]
	m^2 g^{-1}	*nm*	*cm^3 g^{-1}*
HAP_RT	100.52	5.77	0.306
HAP/CNF	142.02	2.90	0.270
HAP/CMC	136.89	2.89	0.258
HAP/AC	115.43	5.50	0.299

[a] *Evaluated according to the 3-parameter BET model equation;*

[b] *Evaluated according to B.J.H model.*

In view of a potential application of these composite materials in an electrochemical device for heavy metal ions sensing, a first approximate screening of conductivity has been performed. HAP_RT and HAP/C composites has been compacted in tablets by means of an IR press: different pressures have been applied to different materials, as to obtain compact and mechanically stable tablets. Such pressed samples underwent EIS spectroscopy measurements aimed to the determination of the resistivity/conductivity of the materials. Results are reported in Table 20.

Table 20: Tablets pressing conditions and measured resistivity/conductivity of HAP_RT and HAP/C composites.

Sample	**Tablet preparation**		**Measured resistivity**	**Conductivity**
	Pressure	**Thickness**		
	MPa	*cm*	*Ω*	*S m^{-1}*
HAP_RT	369	0.15	$4.0 \cdot 10^9$	$2.8 \cdot 10^{-9}$
HAP/CNF	369	0.10	≈ 19	≈ 1.3
HAP/CMC	886	0.080	$9.3 \cdot 10^6$	$5.0 \cdot 10^{-6}$
HAP/AC	N/A	N/A	N/A	N/A

As expected, HAP electrical insulating nature resulted in a conductivity in the order of 10^{-9} S m^{-1}. The presence of carbonaceous scaffold was confirmed to be beneficial for the conductivity, with a 1000x increase in the latter in the case of HAP/CMC and an impressive 10^9x boost for HAP/CNF. HAP/AC composite poor mechanical properties and overall inhomogeneity resulted in the impossibility to prepare a tablet for conductivity measurements.

In conclusion, this first screening of carbonaceous scaffolds for HAP/C composites indicates CNFs as a promising high conductivity platform for the creation of HAP-based composites for electrochemical sensing application, while CMC may be a cheap and eco-friendly scaffold for a new generation of HAP/C composite sorbents.

3.3 HAP/C composite materials for efficient wastewater remediation

On the basis of the preliminary screening of carbonaceous scaffolds for HAP/C composites synthesis, CMC has been deemed the most promising for the creation of novel bifunctional sorbents able to simultaneously remove organic and inorganic pollutants from wastewater.

In view of this application, several HAP/CMC composites with an increasing CMC wt.% content have been synthesized, namely 8, 12 and 16% (by design), in addition to the already presented 4%. Although the mass ratio between HAP and CMC could seem biased towards the former, taking into consideration the surface area ratio the situation is quite different (Table 21).

Table 21: CMC wt.% content by design for each HAP/CMC composite and related mass and surface area ratio.

CMC wt.% (by design)	**4**	**8**	**12**	**16**
HAP:CMC mass ratio	≈ 15.2	≈ 11.0	≈ 6.7	≈ 4.1
HAP:CMC surface area ratio[a]	1.24	0.89	0.55	0.33

[a] *Calculated as: (HAP wt.% * $S_{a\,HAP}$)/(CMC wt.% * $S_{a\,CMC}$). $S_{a\,HAP}$ and $S_{a\,CMC}$ are reported in Table 23.*

Indeed, because of the major difference in the surface area of the two pristine moieties (S_a HAP ≈ 100 m^2g^{-1} vs S_a CMC ≈ 1235 m^2g^{-1}, see Table 23), the composites actually expose preferentially the hydroxyapatitic or carbonaceous moiety in the CMC wt.% content range under investigation, with HAP/CMC8 roughly being the balance point, in which the theoretical surface area of the two moieties are equal. So, despite the low CMC wt.% content, the synthesized HAP/CMC composites should cover comprehensively a wide range of actual HAP:CMC surface area ratio and thus exhibit different physical/chemical properties and sorption performance. So, a complete structural, morphological and surface characterization of the composites has been performed in order to evaluate the HAP:CMC ratio influence on the physical/chemical features of the composites. Then, composite materials have been tested in the remediation of simulated polluted wastewater containing both single and simultaneously present organic and inorganic model pollutants (methylene blue, MB and copper, Cu(II), respectively). All experimental details, from the synthetic procedure to the operational conditions of physical/chemical characterization and sorption test are reported in the Experimental Section.

Throughout the section, HAP_RT and CMC will be referred to as reference comparison from the point of view of structural/morphological properties and sorption performance. As already stated, HAP_RT is synthesized according to the same procedure of HAP/CMC composites but in absence of the carbonaceous slurry. On the other hand, CMC has been treated under harsh basic conditions by NH_4OH under the same conditions reported for composites synthesis, as to evaluate the effect of such environment on CMC features and to obtain a proper "blank" to compare to HAP/CMC composites.

3.3.1 Structural and morphological characterization of HAP/CMC composites

First and foremost, the effective CMC wt.% content in the composites have been checked by means of thermogravimetric analyses (TGA). In fact, removing CMC by combustion at high temperature under air allows to estimate the CMC content in each composite through weight loss evaluation. All the experimental details are reported in the Experimental section, paragraph 8.2.2.

However, several phenomena could be responsible for weight losses in the scanned temperature range, like decomposition of carbonates (both from HAP and CMC moieties) and/or release/evaporation of both physically and chemically bound water molecules. For a more precise quantification of the CMC wt.%, an internal calibration has been performed, using ad-hoc prepared physical mixture of HAP and CMC with CMC content in the same range of the composites' one. Moreover, the comparison between physical mixture and composites thermogravimetric profiles can be useful to assess specific modifications induced by the synthetic route, for example a variation in the carbonates content.

Preparation of such physical mixtures is detailed in the Experimental Section (paragraph 8.2.2), while weighted masses are reported in Table 43 in the Supporting Material.

Figure 38 reports the thermogravimetric profiles of both composites (black lines) and physical mixtures (red lines) at different CMC wt.%. All samples display a major thermal phenomenon, imputable to CMC combustion, taking place in the temperature range comprised between *ca*. 400 and 650°C and reaching the maximum rate (i.e. point of inflection of the thermogravimetric profile) at *ca*. 585°C. Calculating the second derivative and applying the method of the tangents to each profile, the actual weight loss has been evaluated for both physical mixtures and composites. Weight losses versus effective CMC wt.% content in physical mixtures has been plotted to obtain a calibration line (Figure 94 in Supporting Material). Then, the same calibration line has been used to determine the actual CMC content in HAP/CMC composites from the calculated TGA weight losses, giving back the values reported in Table 22, which are slightly higher than those designed.

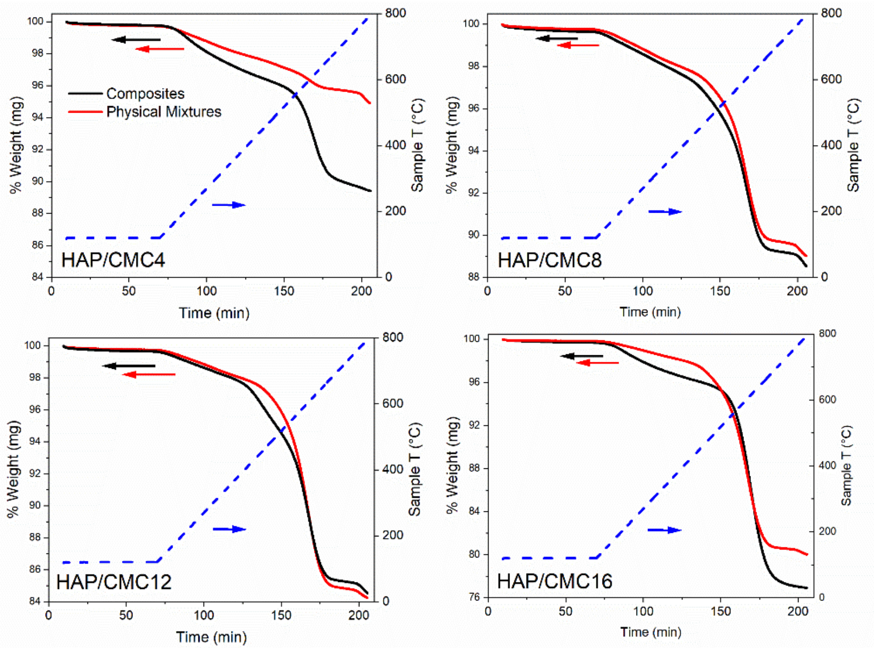

Figure 38: Thermogravimetric profiles of HAP/CMC composites and related physical mixtures.

Before the onset of CMC combustion, another thermal phenomenon takes place in the range between 120 and 400°C. The slow kinetics of the phenomenon and the temperature range in which it occurs are consistent with the thermal decomposition of surface and bulk HAP carbonate species [33]. Interestingly, the weight loss in this region is always larger for composites than physical mixtures, suggesting that the former are more subjected to carbonation than HAP_RT. Possibly, CMC slightly decomposes under harsh basic conditions typical of the synthetic slurry, thus releasing small amounts of CO_3^{2-} ions which are readily incorporated in the HAP lattice during precipitation. A reliable quantification of the carbonate species content is however not possible since chemisorbed water release takes place in the same temperature range of CO_3^{2-} decomposition.

Table 22: Effective CMC and carbonates content (wt. %) in HAP/CMC composites.

Sample	**CMC content**
	wt. %
HAP/CMC4	6.16
HAP/CMC8	8.37
HAP/CMC12	12.95
HAP/CMC16	19.60

XRPD patterns of pristine HAP and CMC and HAP/CMC composites are reported in Figure 39.

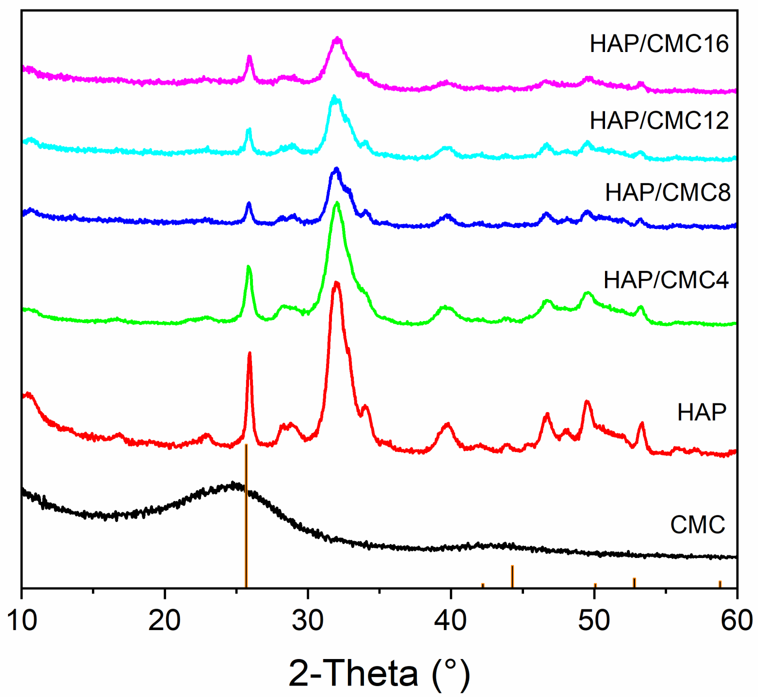

Figure 39: XRPD patterns of the pristine moieties (HAP and CMC) and of the HAP/CMC composites. HAP_RT and HAP/CMC4 composite patterns, already reported in Figure 36, are recalled for the sake of comparison. Brown vertical lines indicate attended graphite XRD reflections.

CMC pattern (black line in Figure 39) reveals the predominant amorphous nature of the carbonaceous scaffold, evidencing two weak and broad peaks centered between 20° and 30° in 2θ and 40° and 45° in 2θ, respectively assigned to 002 and 101 reflections of graphite [170]; large FWHM values derive from the highly amorphous character of CMC, which can be depicted as a carbon structure made of small and randomly stacked hexagonal aromatic sheets. This result is consistent with previously published studies in which as received CMC have been thoroughly characterized [169], thus demonstrating that the harsh basic conditions experienced by the material during the composites' synthesis do not affect its already disordered and amorphous structure.

HAP_RT and HAP/CMC4 patterns have been discussed in the previous paragraph. Diffractograms of all composite materials display HAP featured peaks, confirming the successful immobilization of the hydroxyapatitic moiety and the phase purity of the materials (i.e. no other crystalline phase is detected). The general peak broadening and loss of resolution noticed as consequence of increasing CMC content could be attributed to a possible decrease in HAP crystallinity or, more probably, to a surge in the background noise actually due to the increment in the (amorphous) CMC content. Because of this peak broadening phenomenon and taking into account the presence of two distinct phases with different crystallinity degree, Scherrer equation cannot be reliably applied to the present diffractograms.

Despite the typical black color imparted to the composites by the presence of the carbonaceous scaffold, which causes non-negligible radiation absorption, FT-IR has been registered in transmittance mode for both pure HAP and CMC and HAP/CMC composites. Although results can be considered only qualitative because of the low transmittance of the samples, a meaningful insight on the surface functional groups of CMC and composites can be obtained from a careful analysis of the FT-IR spectra reported in Figure 40a.

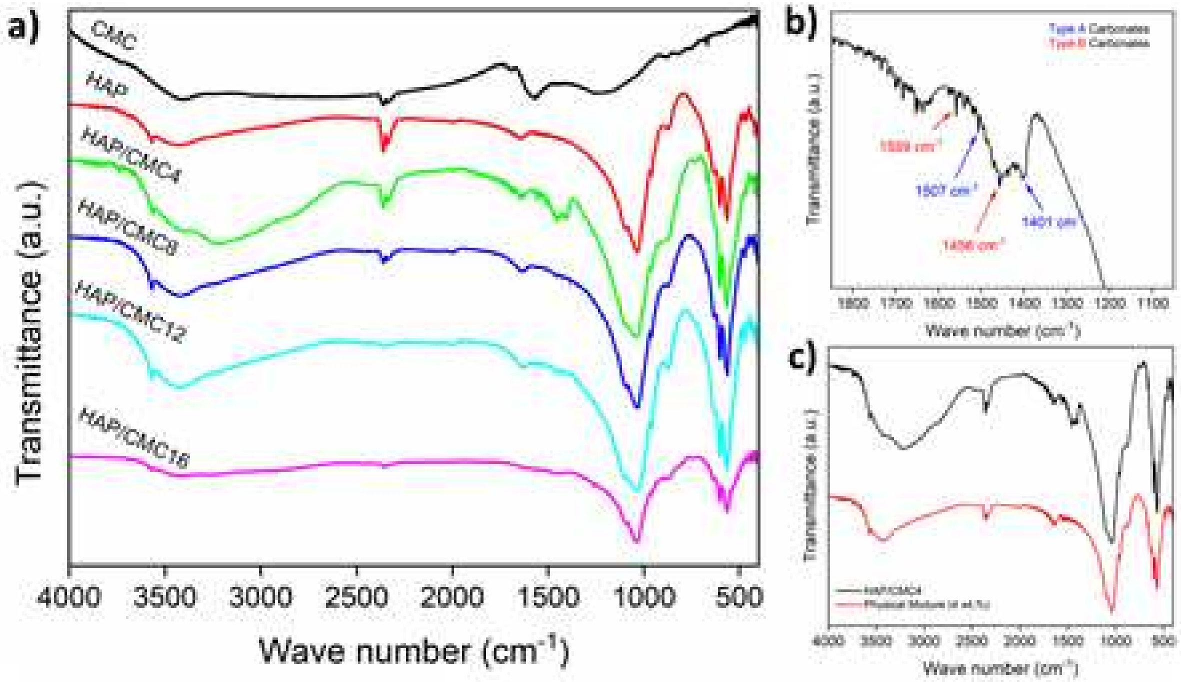

Figure 40: a) FT-IR spectra of the pristine moieties (HAP and CMC) and of the HAP/CMC composites; b) Magnification of the carbonates' region of HAP/CMC4 composite and c) comparison between the HAP/CMC4 composite and the corresponding physical mixture.

Before commenting on the recorded spectra, it is important to correctly address peaks at *ca*. 2360 cm^{-1} and *ca*. 1640 cm^{-1}. Those contributions are related to CO_2 and H_2O IR-active modes, respectively; since both molecules are present in the atmosphere, and considering possible background fluctuation, such signals will not be included in the discussion.

Notwithstanding the high extinction coefficient of CMC, the related spectrum (black line in Figure 40a), four broad peaks are detected in as many IR regions, depicting a highly functionalized carbon. These signals have been assigned to the (*i*) stretching mode of O-H (*ca*. 3404 cm^{-1}), (*ii*) stretching mode of C=O (*ca*. 1700 cm^{-1}), (*iii*) stretching mode of conjugated C=C aromatic bonds (*ca*. 1571 cm^{-1}) and finally (*iv*) stretching mode of C-O groups of esters/alcohol functionalities (*ca*. 1264 cm^{-1}) [168].

Noticeably, the typical contribution of C-H stretching (*ca*. 2930 cm^{-1}), sometimes observed for carbonaceous materials, is barely detectable in CMC, suggesting a limited presence of C-H terminal moieties at the expenses of vastly O-functionalized terminations. These observations, in agreement with the relevant oxygen content of CMC [169] and together with its high surface area, justify the improved dispersion and anchoring of HAP onto this carbonaceous scaffold in respect with CNFs and AC.

HAP_RT spectrum (red line in Figure 40a) presented all the typical feature of HAP, as already commented for pristine HAP in paragraph 2.2. An interesting difference can anyway be spotted between HAP_RT and pristine HAP synthesized at 80°C: indeed, the former does not seem to suffer from carbonation and thus exhibits an almost flat signal in the typical IR carbonates' region (*ca*. 1600 to 1300 cm^{-1}). Although higher temperature synthesis could be thought to minimize the possibility of HAP carbonation (due to the plummeting of gases solubility in liquids at high temperature), other factor could play relevant roles in determining the amount of CO_3^{2-} entering HAP lattice in the synthetic step. HAP_RT is indeed obtained through a modified co-precipitation method that involves higher concentration of precursors' solutions (i.e. increased ionic strength in the reaction slurry) and shorter dropping/synthesis time, both factors that can concur in decreasing the amount of carbonates present in solution and available to enter HAP's lattice.

Spectra of all HAP/CMC composites display the typical IR features of HAP, thus indicating that, even in the case of CMC-favorable surface area ratio (i.e. CMC wt. % > HAP/CMC8), the hydroxyapatitic moieties of composites are always present on the materials' surface. Curiously, signals in the carbonates' region are detected in HAP/CMC4 (green line in Figure 40a) and although progressively weakening, most likely because of the lowering of IR transmittance of samples as CMC content increases, carbonates related peaks are displayed by all composites up to HAP/CMC16. The magnification of the carbonates' region reported in Figure 40b confirms the presence of both A and B-type CO_3^{2-} groups. The absence of carbonates related signals in HAP_RT and in the physical mixtures (Figure 40c) suggests that carbonatation preferentially occurs when the carbonaceous scaffold is present. Possibly, these CO_3^{2-} ions could be supplied to the synthetic slurry by CMC partial decomposition under harsh basic conditions, as already proposed. However, since all the characterizations performed confirmed CMC stability, such explanation is easily arguable. Considering then that carbonates signals appear only for the composite, it could be guessed that surface carbonate groups of CMC take active part in the nucleation of HAP, serving as anchoring point and thus becoming part of HAP's lattice and originating the typical CO_3^{2-} IR signals.

The qualitative characterization of HAP/CMC composites' surface has been completed by Raman spectroscopy. Raman spectra of pristine moieties and composites are shown in Figure 41.

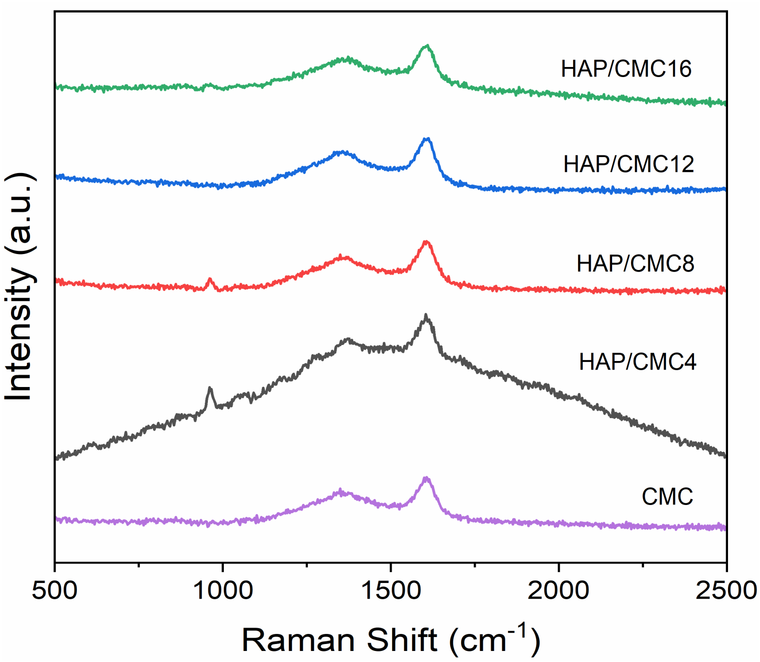

Figure 41: Raman spectra of pristine CMC and HAP/CMC composites. For pristine HAP_RT spectra, refer to Figure 95 in the Supporting Material.

Pristine CMC spectra (purple line in Figure 41) presents the two typical bands found in C-based materials: the G band (*ca*. 1530-1620 cm^{-1}), associated with the graphite in plane E_{2g} Raman active mode and the D band (*ca*. 1350 cm^{-1}), related instead to the A_{1g} D breathing mode. In simplified terms, it could be stated that G and D band are directly related to the ordered and disordered domains of carbon-based materials. An evaluation of the defectiveness of the samples can be indeed obtained from the peaks' intensity ratio (I_D/I_G).

The CMC scaffold I_D/I_G ratio stands around 0.8, indicating that the material is mostly amorphous with the presence of small graphitic domains, in the order of *ca*. 1 nm of size [171]. These observations are consistent with those drawn from the XRPD patterns (Figure 39). On the other hand, HAP_RT spectrum (Figure 95 in Supporting Material) is characterized by way higher radiation intensities and the typical semicircular pattern due to phosphorescence. Therefore, no relevant information can be obtained for pristine HAP materials from this technique.

Regarding HAP/CMC composites, all spectra exhibit both G and D bands and an I_D/I_G ratio similar to that of CMC. It can be noticed that, as CMC content in the composites gradually grows, spectra tend to resemble pristine CMC one. The presence of HAP in the composites can be spotted only up to *ca*. 8 wt.% CMC content (HAP/CMC8) by the appearance of a peak at *ca*. 961 cm^{-1}; this signal is commonly attributed to the ν_3 symmetric stretching mode of PO_4^{3-} groups [172]. The disappearance of such contribution at higher CMC wt.% can be interpreted as a lower surface exposure of phosphate groups (and thus HAP in general) in HAP/CMC12 and HAP/CMC16, in accordance to the surface area balance of the two moieties of the composites (Table 21).

The results of N_2 adsorption/desorption analyses on all samples are gathered in Table 23, while isotherms, BET linearizations and PSD graphs are reported in Figure 96 to Figure 98 in the Supporting Material. HAP_RT and HAP/CMC4 data are reported once more in Table 23 for the sake of clarity, as well as CMC ones.

Table 23: Surface area, mean pore radius and cumulative pore volume of HAP/CMC composites calculated from N_2 adsorption/desorption analyses. HAP_RT and CMC values are reported for the sake of clarity.

Sample	Surface area	Mean pore radius	Pore volume
	$m^2\ g^{-1}$	nm	$cm^3\ g^{-1}$
HAP_RT	100.52	5.77	0.306
HAP/CMC4	136.89	2.89	0.258
HAP/CMC8	129.90	3.52	0.221
HAP/CMC12	149.06	3.28	0.224
HAP/CMC16	128.81	3.12	0.113
Pristine CMC	1235.93	3.11	1.18

Despite no clear trend in S_a vs. CMC wt.% is disclosed, all composites exhibit a higher surface area than HAP_RT. Qualitatively, differences can be spotted among isotherms (Figure 96, Supporting Material): indeed, the adsorption branch and the desorption hysteresis show a transition from the typical type IV and H2 ones, respectively, to a mixed type I/IV and H2/H4 going from HAP/CMC4 to HAP/CMC16. These evidences confirm the influence of CMC content on the morphological features of composites and are consistent with the partially microporous nature of the carbonaceous scaffold. However, as reported in Table 23, both surface area and mean pore volume of composites are way lower than CMC values; at the same time, these values are not determined solely by the mathematical weighted average between HAP_RT and CMC, thus suggesting that the moieties are not distinct but effectively form composites. The plummeting of surface area and especially mean pore radius values from CMC to composites suggest that a disordered HAP precipitation takes place on both the surface of the carbonaceous scaffold and inside the pores of the latter: pore clogging and embedding of CMC particles in HAP could then explain the V_{pore} and S_a values.

TEM images of the composites are reported in Figure 42. No difference between HAP_RT and composites' morphology of composites can be noticed for CMC content as high as *ca*. 12% (HAP/CMC12). Only HAP/CMC16 presents a different, sponge-like morphology (Figure 42c), which resembles that of the CMC scaffold (Figure 42d). This observation agrees with the morphology transition alleged from N_2 adsorption/desorption isotherms for the high-content CMC composites. However, in all composites HAP retains a platelets-like morphology and all composites exhibit a homogenous distribution of HAP and CMC moieties.

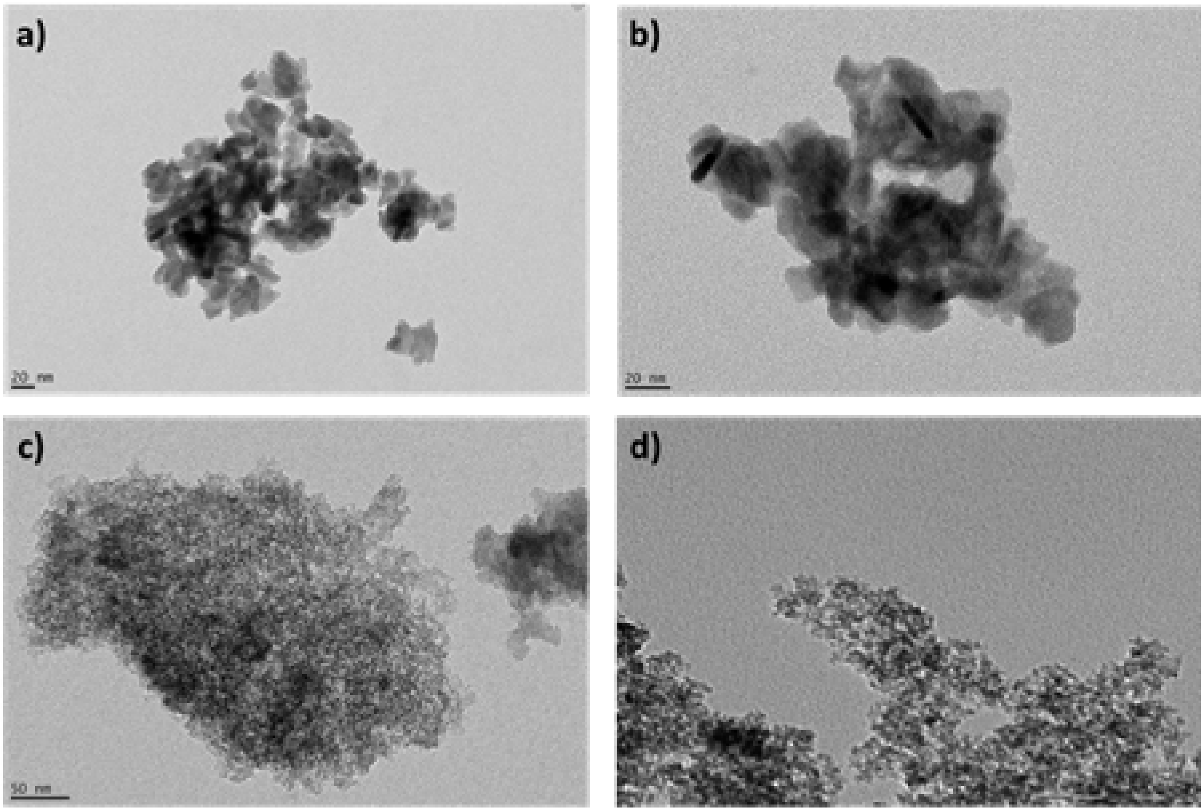

Figure 42: TEM images of a) HAP_RT; b) HAP/CMC8; c) HAP/CMC16 and d) pristine CMC.

Surface acidity and basicity of the composites have been investigated by liquid-solid titration. The applied technique slightly differs from that presented in paragraph 2.2.2 (LRCM) and applied for the determination of surface features of pristine HAP: indeed, in this case, samples have been titrated under flowing conditions, performing pulsed injections of probe molecules while continuously flushing fresh solvent (differently from the closed-line LRCM set-up presented in paragraph 2.2.2). The experimental details of liquid-solid acid/base titrations are reported in the Experimental Part, paragraph 8.2.4.2; further discussion on the underpinnings of this technique can be found in the Supporting Material, paragraph 10.2.2.1. Briefly, the pulsed injection method is best suited for the study of these (carbonaceous) samples since the continuous flow of solvent minimizes physisorption phenomena. Indeed, π-π interaction between CMC containing samples and the probe molecules (PEA and BA, both bearing an aromatic ring) would lead to misleading results under LRCM closed-line conditions. On the other hand, the pulsed injections technique does not allow a proper discrimination between strong and weak acid/basic sites and obtained acidity/basicity results may be less accurate because of the "transient" nature of the technique versus the "equilibrium" one typical of LRCM.

The intrinsic (i.e. measured in cyclohexane) number of acid and basic surface sites has been determined for all composites. Results are reported in an "isotherm-like" plot in Figure 43a, where the actual amount of adsorbed probe is plotted against the injected amount. The quantity of composites' surface acid/basic sites, obtained from the adsorption plateaus shown in Figure 43a, is graphically reported as meq g^{-1} and meq m^{-2} versus CMC wt.% in Figure 43b and Figure 43b inset, respectively. The endpoints, 0 and 100% CMC, represents HAP_RT and pristine CMC, respectively. The numerical results, obtained from the titrations, are gathered and presented in the Supporting Material, Table 44.

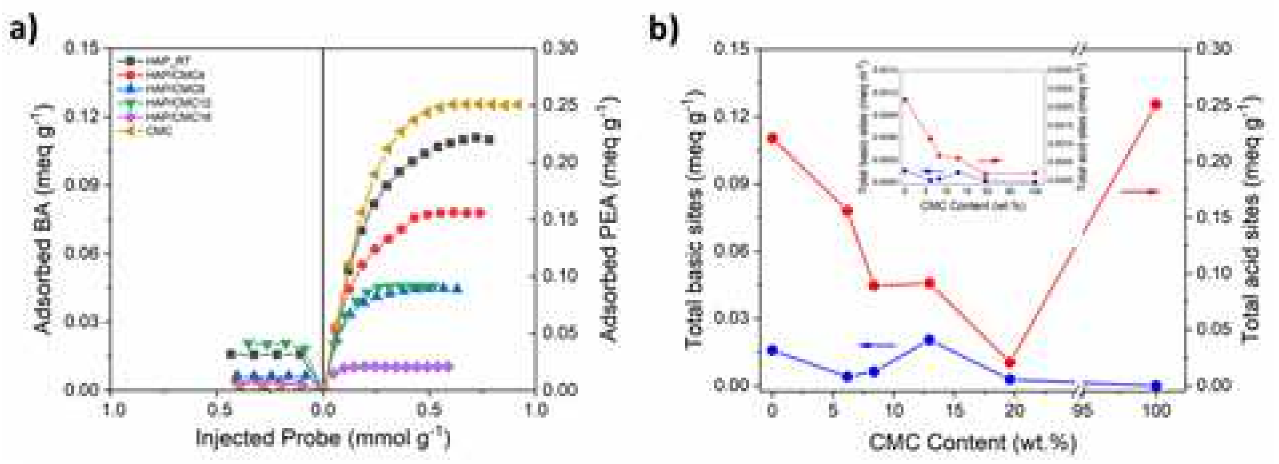

Figure 43: a) Isotherm-like plots obtained from pulsed injection acid and base titrations of HAP/CMC composites and pristine moieties; b) Trends of the intrinsic surface basicity (blue, left Y axis) and acidity (red, right Y axis) of HAP/CMC composites, plotted in meq g^{-1} versus CMC wt. % and in meq m^{-2} in the inset. End points, at 0 and 100%, are represented by HAP_RT and CMC, respectively. Titrations have been performed at 30°C, in cyclohexane.

Starting from the meq g^{-1} intrinsic surface acidity (red points and curve in Figure 43b), it can be noticed that both pristine moieties exhibit a remarkable amount of sites (*ca*. 0.220 meq g^{-1} for HAP_RT and *ca*. 0.250 meq g^{-1} for CMC), consistently with previous results (for HAP, Figure 14 and Table 7) and literature (for CMC, [168,169]). Despite the elevated number of sites onto HAP_RT and CMC surfaces, a constant decrease in the number of acid sites occurs as the content of CMC in composites increases. This result agrees with the pore clogging action of HAP precipitation onto the carbonaceous scaffold (suggested by N_2 ads/des analyses) and the -COOH groups acting as anchoring points (indicated by FT-IR spectra) during the formation of the composites themselves, thus resulting in an overall diminished exposure of surface acid sites. The same decreasing trend in composites' acidity can be spotted when plotting the number of sites as meq m^{-2} (i.e. normalizing by each material's surface area, Figure 43b inset), although in this case CMC acidity is majorly downgraded because of its large surface area (Table 23).

Regarding intrinsic basicity (blue points and line in Figure 43b), it resulted almost null for both composites and pristine moieties, giving back results near to the lower limit of detection of the technique. Regarding pristine CMC, the limited amount of basic surface functionalities is consistent with the nature of active carbons obtained from pyrolysis, which are well known in literature to be markedly acidic materials [173]. On the other hand, HAP_RT basicity is almost zeroed as well, in contrast with the marked basicity measured under similar conditions but applying the LRCM closed-line set-up (paragraph 2.2.2, Figure 14 and Table 7). The difficulties in determining the intrinsic basicity of samples through this pulsed injection methodology is probably related to the slow kinetics of adsorption and constant desorption of the probe molecule (BA) from the samples' surface, which are, under these conditions, further exacerbated by the continuous flow of fresh solvent. A qualitative confirmation of the slow adsorption/desorption kinetics of BA in comparison to PEA can be deduced from the chromatograms registered during the titration of HAP/CMC composites (Figure 99, Supporting Material).

Effective surface acidity and basicity (i.e. measured in H_2O) could not be detected by this titration method: the strong interactions of H_2O with the samples' acid/basic surface sites, the limited contact time between solids' surface and probe molecules and the continuous flushing of the samples with fresh solvent are allegedly all concurring in minimizing probe-site interactions.

The next paragraph will present and discuss the sorption ability of the composite materials herein fully characterized.

3.3.2 Simultaneous removal of organic and inorganic pollutant in simulated wastewater by HAP/CMC composites

The ability of HAP/CMC composites to remove both organic and inorganic pollutants from simulated wastewater has been tested. Stirred batch adsorption tests were performed on Cu(II), Ni(II) and methylene blue (MB) containing solutions, both present individually and at the same time. Operative conditions are detailed in the Experimental Section, paragraph 8.3.2. As comparison, pristine moieties of the composites (i.e. HAP_RT and CMC) have been tested under the same conditions.

First and foremost, sorbents have been tested in the removal of solutions containing individual heavy metal cations, like Cu(II) (generally accepted benchmark for metal wastewater pollution) and Ni(II) (emerging pollutant). Figure 44 shows the percentage removal of Cu(II) (Figure 44a) and Ni(II) (Figure 44b) by composites and "bare" moieties starting from different initial pollutants' concentration; numerical results, both in percentage and in $mg_{Cu(II)}\ g^{-1}_{Sorbent}$, are reported in the Supporting Material, Table 45 and Table 46.

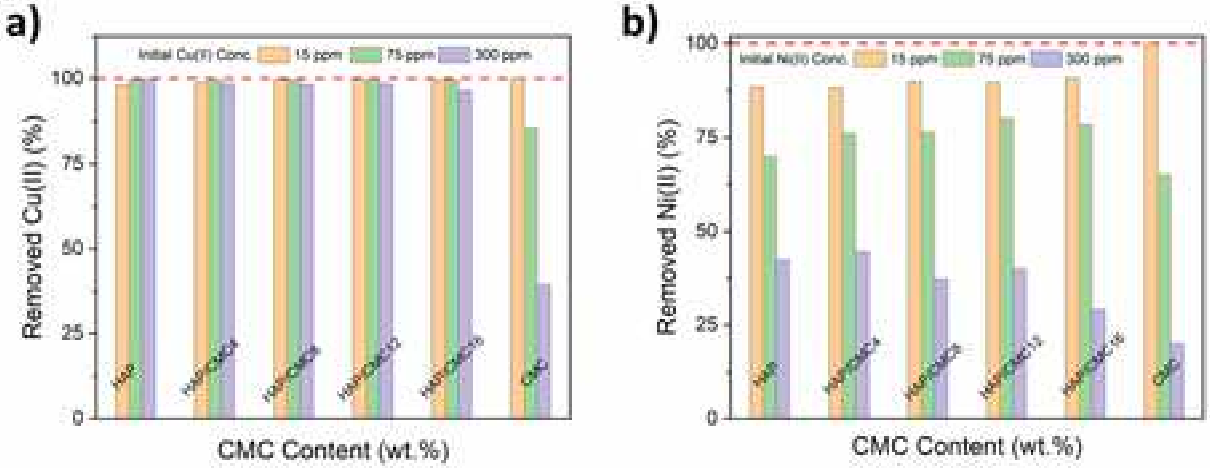

Figure 44: Percentage of removal of Cu(II) (a) and Ni(II) in single component solutions by pristine moieties and different CMC containing HAP/CMC composites, at different Me^{n+} initial concentrations. Sorption tests performed according to a stirred batch method, T = 30°C, contact time = 2 h, natural pH (ca. 6).

Starting from Cu(II) (Figure 44a), HAP_RT showed an overall 100% removal ability towards Cu(II), despite the initial concentration. These results are consistent with those obtained for pristine HAP, paragraph 2.3.1. Actual $q_{Cu(II)}$ (Table 45) does not exceed the $q_{max\ Cu(II)}$ calculated from the isotherm presented in Figure 16. On the other hand, pristine CMC exhibits a limited ability of Cu(II) sorption: the almost 100% removal of the cation at low initial concentration (15 ppm), drops down to *ca.* 40% when concentration raises to 300 ppm. Low affinity with inorganic cations and the modest amount of (basic) surface functionalities of C-based materials [173] is the alleged reason of such behavior at high Cu(II) concentration. All HAP/CMC composites, probably because of the low CMC content (≤ 20wt.%), are as efficient as HAP_RT in Cu(II) removal, reaching *ca.* 100% Cu(II) uptake regardless of the initial concentration.

Similarly, Ni(II) adsorption onto HAP/CMC composites is quantitatively close to that onto HAP_RT. Moreover, HAP/CMC composites sorption performances are slightly affected by the CMC wt.%, i.e. HAP/CMC4 operate as efficiently as HAP/CMC16 and moderately more than pristine CMC when Ni(II) initial concentration is < 75 ppm. Overall, Ni(II) is confirmed to be hardly adsorbed onto both HAP (paragraph 2.3.1 and [16,79,85]) and/or C-based materials [174,174].

Cu(II) and Ni(II) adsorption tests onto HAP/CMC composites demonstrate that typical HAP affinity towards heavy metal cations is retained in the composition range studied (*ca.* 4 to *ca.* 20 wt.%).

The ability of HAP/CMC composites and pristine moieties in removing a benchmark organic pollutant like MB has been tested according to the same methodology (details can be found in paragraph 8.3.2, Experimental Section). The percentage removal of MB by the sorbents at different initial concentrations is reported in Figure 45a; numerical data (percentages and $mg_{MB}\ g^{-1}_{Sorbent}$) are instead gathered in Table 47, Supporting Material.

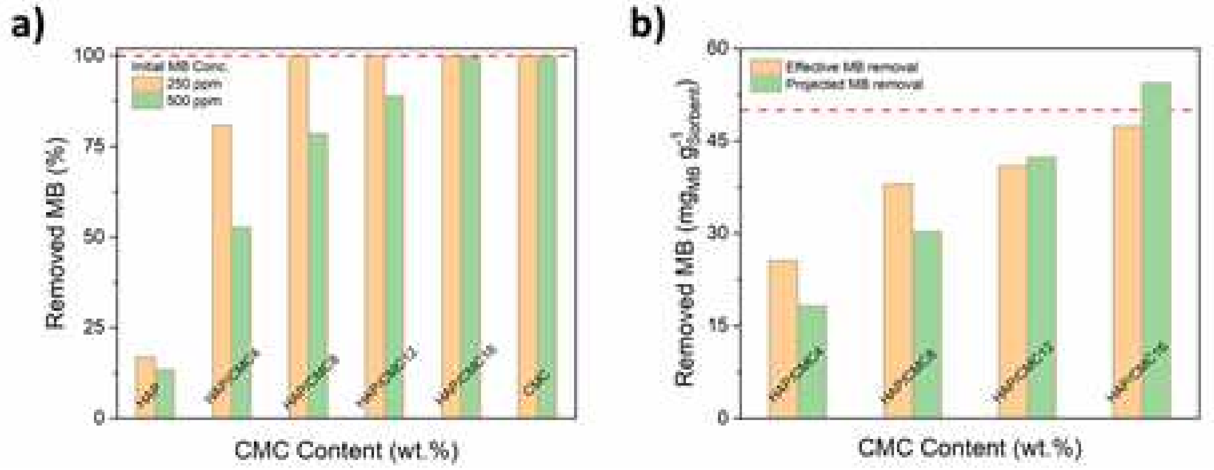

Figure 45: a) Percentage of removal of MB in single component solutions by pristine moieties and different CMC containing HAP/CMC composites, at different MB initial concentrations; b) Effective vs. projected removal of MB in single component solutions by HAP/CMC composites. Projected values calculated from the maximum MB uptake on CMC and CMC wt.% in the composites under study. Sorption tests performed according to a stirred batch method, T = 30°C, contact time = 2 h, natural pH (ca. 6).

MB uptake onto HAP_RT surface is limited, as expected [149], underlining the scarce affinity of hydroxyapatitic materials towards organic pollutants, although the cationic nature of MB at nearly neutral pH [149]. Conversely, CMC exhibits outstanding sorption performances, conferred to the material by its high surface area, porosity and C-based nature, which allows the trapping of aromatic ring-bearing molecules through π-π interactions [142,149]. The maximum MB uptake onto CMC has been evaluated through subsequent adsorption tests and stood around 300 $mg_{MB}\ g^{-1}_{CMC}$ (Table 48, Supporting Material). Interestingly, the low CMC content in HAP/CMC composites results to be enough to impart to the materials excellent MB sorption properties. Indeed, MB is totally removed from 250 and 500 ppm MB solutions by HAP/CMC composites containing *ca*. 12 wt.% and 20 wt.% CMC, respectively.

To disclose possible synergistic effects between the two moieties of the composites, the actual MB uptake values (measured at MB initial concentration equal to 500 ppm) have been compared to theoretical uptake projections (Figure 45b) calculated assuming that (*i*) the two components (HAP and CMC) exert their adsorbent action independently of each other and (*ii*) there is a direct relationship between the adsorption capacity and relative amount (wt.%) of the components themselves. The red dotted line in Figure 45b represents the upper MB loading limit imposed by the operative conditions. Even if for low CMC content (HAP/CMC4 and HAP/CMC8) a synergistic effect between HAP and CMC components could be allegedly spotted, the measured and calculated uptakes are closed enough to be considered practically the same.

Once the composites' capacity to individually adsorb inorganic (Cu(II) and Ni(II)) and organic (MB) pollutants in water solution, sorption ability of HAP/CMC materials has been tested in ternary solutions, containing Cu(II), Ni(II) and MB at fixed concentrations (*ca*. 300 ppm for inorganic cations, *ca*. 250 ppm for MB). Even in this case, the whole experimental procedure is reported in the Experimental Section (paragraph 8.3.2).

The results of ternary solutions adsorption tests are graphically reported in Figure 46, in terms of percentage removal of pollutant by each composite, with HAP_RT and pristine CMC representing the end points of the graph. As usual, numerical results (removal percentages and mg$_{Pollutant}$ g^{-1}$_{Sorbent}$) are gathered in Table 49, in the Supporting Material.

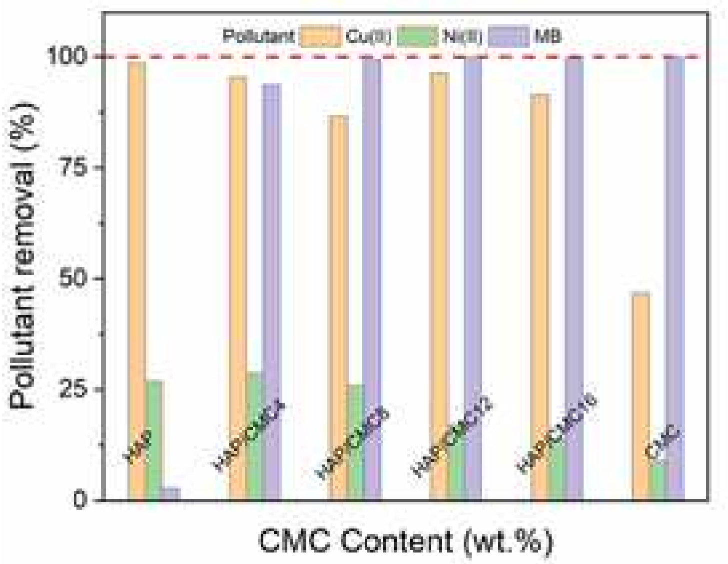

Figure 46: Percentage of removal of Cu(II), Ni(II) and MB in ternary solutions by pristine moieties and different CMC containing HAP/CMC composites. Sorption tests performed according to a stirred batch method, T = 30°C, contact time = 2 h, natural pH (ca. 6), Cu(II) & Ni(II) initial concentration ca. 300 ppm and MB initial concentration ca. 250 ppm.

Optimal inorganic cations adsorption is registered onto HAP_RT surface, with an almost 100% removal efficiency towards Cu(II) and a *ca*. 25% towards Ni(II). The removal percentage and the actual metal loading of Ni(II) onto HAP_RT (Table 49, Supporting Material) are consistent with previous results of Ni(II) adsorption onto hydroxyapatitic materials and confirm the modest affinity between such cation and HAP. Regarding the organic benchmark pollutant, the amount of MB trapped by HAP_RT is practically null.

Pristine CMC on the other hand exhibited a remarkable sorption capacity towards MB even in ternary solutions, completely removing the organic pollutant under the operative conditions. By contrast, heavy metal cations removal is way less efficient on CMC than HAP, reaching maximum removal values of *ca*. 50 and *ca*. 10% for Cu(II) and Ni(II) respectively, confirming the scarce affinities previously assessed in single-metal solutions' adsorption tests (Figure 44).

Overall, HAP_RT and CMC possess different and complementary sorption features which could be exploited together in the composites materials to obtain novel sorbents with a dual nature.

Indeed, HAP/CMC composites showed promising adsorption capacities towards both organic and inorganic pollutants. Cu(II) is captured with a removal efficiency comprised between 85 and 95% at every CMC wt.%, indicating that diminishing HAP content in the composite do not affect the uptake of such cation. Unfortunately, the same conclusion cannot be stated for Ni(II), whose removal efficiency decreases from *ca*. 25 to *ca*. 17% going from HAP/CMC4 to HAP/CMC16, highlighting once more the challenging issue of Ni(II) adsorption. Regarding the organic fraction, the complete removal of MB is achieved for all composites besides HAP/CMC4; this result suggests that a slight amount of the carbonaceous scaffold (CMC wt.% > *ca*. 6-7%) is sufficient to impart to HAP/CMC composites the desired adsorption properties towards organic pollutants.

Since Ni(II) adsorption is a constant issue for both HAP and carbon-based sorbents and, allegedly, for HAP/C composites too, long contact time adsorption tests have been carried out, in order to disclose the effect of the latter on Ni(II) removal efficiency. Main results are reported in Figure 47.

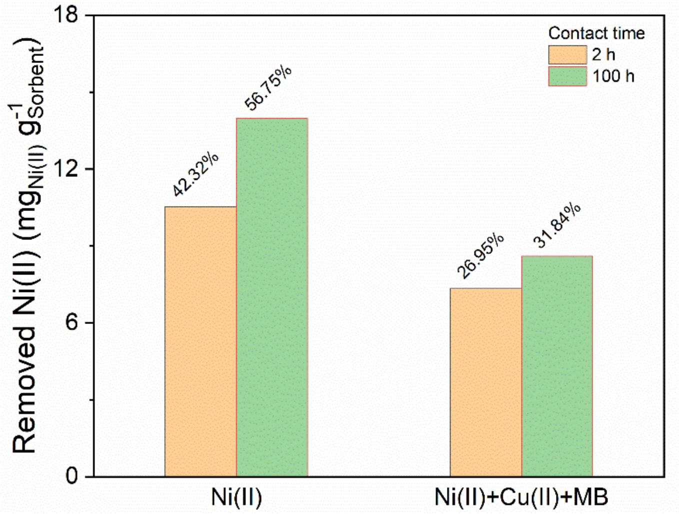

Figure 47: Effect of contact time on nickel uptake on HAP_RT from single component (C_0 ≈ 300 ppm Ni(II)) and ternary (C_0 ≈ 300 ppm of each Cu(II), Ni(II) and MB) solutions. Sorption tests performed according to a stirred batch method, T = 30°C, contact time = 2 h, natural pH (ca. 6).

As it can be noticed, Ni(II) adsorption onto "bare" HAP_RT is only modestly affected by the contact time: indeed, passing from 2 to 100 h contact time, Ni(II) removal only increases of *ca*. 14% in single component solution (Figure 47, bars on the left), while the increment is even slighter in the case of ternary solutions, where it stood around 5% (Figure 47, bars on the right). Therefore, considering the almost negligible advantages and the operative drawback represented by the long contact time, the latter cannot be deemed a key parameter in determining Ni(II) uptake onto HAP-based sorbents.

Finally, leaching tests have been carried out on selected used sorbents, as to assess the risk of secondary pollution and the permanent or not nature of pollutants' confinement on the materials. The operative conditions applied for leaching tests are fully detailed in the Experimental Section, paragraph 8.3.2.

Since HAP/CMC8 resulted to be the optimal composition for simultaneous removal of organic and inorganic pollutants, leaching tests have been carried out on those "spent" sorbents and on pristine components, HAP_RT and CMC. The outcomes of leaching tests are reported in Figure 48.

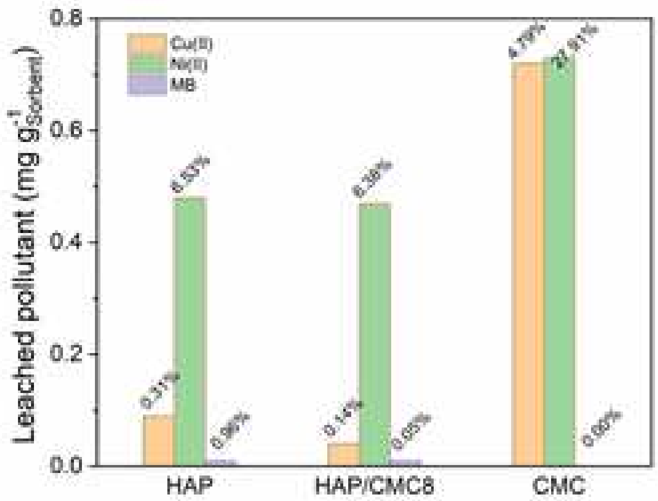

Figure 48: Mass (left y axis) and percentage (labels on top of bars) of leached pollutants from selected used sorbents.

When contacted with fresh water, HAP_RT retains almost totally Cu(II) and MB, although the latter has been adsorbed in practically negligible amounts. Conversely, *ca*. 6.5% of the previously trapped Ni(II) is release in solution. The results agree with those presented in the previous chapter for pristine HAP (paragraphs 2.3.1 and 2.3.4).

Pristine CMC confirmed to be an ideal sorbent for organic pollutants, exhibiting a perfectly permanent confinement of MB onto its surface. Regarding metal cations instead, despite the small amount trapped during the adsorption tests, both Cu(II) and Ni(II) are significantly released in solution.

In HAP/CMC8 the complementary nature of the two moieties of the composite shows once more: indeed, Cu(II) and MB, trapped in relevant quantities during adsorption tests, results to be permanently confined onto the sorbent. Ni(II) leaching persist being an issue, with a percentage release close to that registered for “bare” HAP_RT.

In conclusion, the novel HAP/CMC composites resulted to be efficient dual sorbents, able to simultaneously remove organic (i.e. dyes) and inorganic (i.e. heavy metal cations) water pollutants. The optimal CMC content in composites was deemed to be > *ca*. 7-8 wt.%. Confinement of Cu(II) and MB has been proved to be permanent. Overall, the composites satisfactorily merge HAP and CMC adsorption and retention of organic/inorganic pollutants.

3.4 Development of HAP/C based electrodes for electrochemical sensing of heavy metal cations' traces in waterbodies

In the view of a possible application in an electrochemical sensing device, the conductivity of HAP/C composites presented in paragraph 3.2 have been further evaluated: in addition to the data already reported in Table 20, self-standing electrodes have been prepared starting from each composite (procedure can be found in the Experimental Section, paragraph 8.4.1) and their conductivity measured. Results are listed in the second column of Table 24.

Table 24: Conductivity of pressed powders (tablets) and processed (to craft self-standing electrodes) HAP/C composites (4 wt.% in C)

Sample	**Conductivity** *S m⁻¹*	
	Tablets	*Self-standing electrodes*
HAP_RT	$2.8 \cdot 10^{-9}$	n.d.
HAP/CNF	≈ 1.3	$9.4 \cdot 10^{-3}$
HAP/CMC	$5.0 \cdot 10^{-6}$	$9.1 \cdot 10^{-8}$
HAP/AC	n.d.	n.d.

As already commented, HAP exhibited scarce conductivity when tested as pressed powder [57] but compositing HAP with a carbonaceous scaffold conferred enhanced electrical properties to the materials, as testified by the improved conductivity of HAP/C composites.

Conductivity of the final electrodes have been checked as well and numerical values are reported in the second column of Table 24. Although composites' ranking is confirmed, lower conductivity values have been registered for electrodes in comparison with pressed powders. This discrepancy (decrease of *ca.* 3 orders of magnitude) can be related to the addition of a chemical binder (PTFE, insulator) in the electrode crafting process, required to impart processability to the composites' paste and mechanical stability to the final electrodic structure.

The performance of HAP/C-based electrodes as heavy metal ion sensors has been tested in the presence of low concentrations of a benchmark pollutant like Pb(II). All experimental details are reported in the Experimental Section, paragraph 8.4.2. Briefly, in a typical three-electrode electrochemical cell, HAP/C-based electrodes operated as working electrodes, with a Pt wire and a saturated calomel electrode (SCE) as counter and reference electrodes, respectively. The electrolyte was a 0.1 M KNO_3 aqueous solution with a concentration in the analyte (Pb(II)) equal to 10^{-5} M. Because of the previously discussed reasons (paragraph 3.1.2), the selected electroanalytic technique has been SWASV, with the addition of a further step prior to the reductive preconcentration one. Indeed, since the adsorption process of cations onto HAP surface does not take place instantaneously, an initial diffusion-controlled preconcentration is performed by simply dipping the electrode in the analyte-containing solution at the open circuit potential (OCP). This step will be hereinafter indicated as "OCP preconcentration".

Main results of the preliminary screening of different HAP/C-based electrodes are graphically reported in Figure 49.

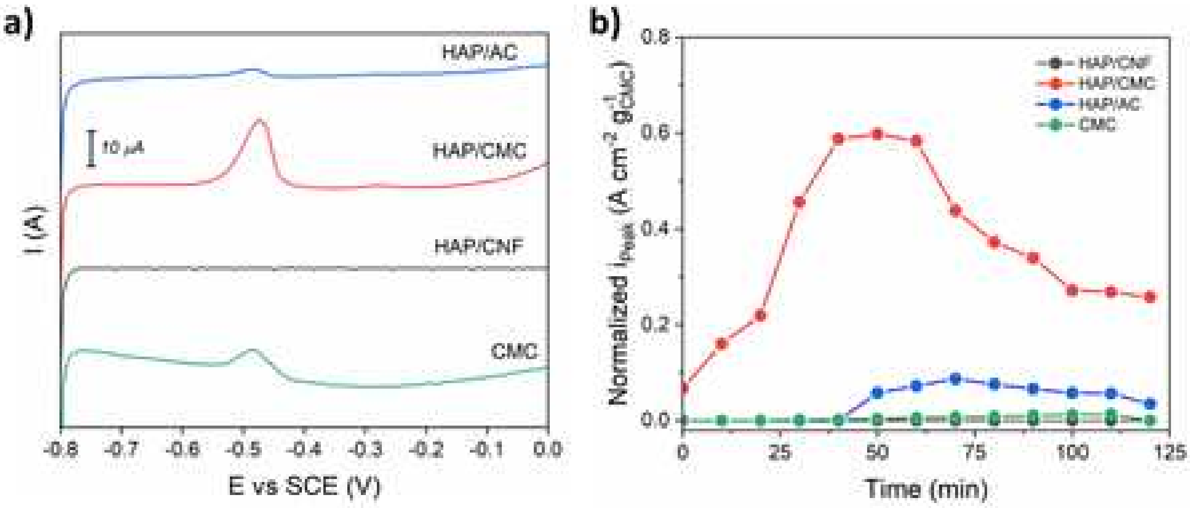

Figure 49: a) Stripping voltammograms of Pb(II) on different HAP/C-based electrodes (4 wt.% C-based scaffold), obtained after 50 minutes of OCP preconcentration, 1 minute of reductive preconcentration (-1 V vs SCE). Potential scan rate = 50 mV s^{-1}; b) Dependence of Pb(II) peak current (i_{Peak}) on OCP preconcentration time for different HAP/C-based sensors.

From the stripping voltammograms of Pb(II) reported in Figure 49a, it can be noticed that, notwithstanding its higher conductivity, no Pb(II) stripping peaks can be detected on HAP/CNF-based electrodes. On the other hand, voltammograms of both HAP/CMC and HAP/AC-based electrodes display a faradic peak at *ca*. -0.5 V vs SCE, attributed to Pb(II) stripping (literature reports Pb(II) stripping potentials in the range from -0.380 to -0.5 V vs Ag/AgCl [165,167,175]), with the former delivering a more definite and intense peak (i_{Peak} ≈ 20 µA). Control experiments, performed on a pristine CMC-based electrode crafted following the same procedure, showed that the electrode modification with the "bare" carbonaceous scaffold impart as well moderate sensing ability to the device (green curve in Figure 49a), despite a less stable and linear baseline. Based on this preliminary screening, it can be concluded that the most promising HAP/C composite for the development of heavy metal ions electrochemical sensing devices is HAP/CMC. Moreover, the comparison between HAP/CMC and CMC-based electrodes' voltammograms evidence the added value of the composite (i.e. of HAP presence), conferring to the system an overall higher sensitivity in terms of delivered current at fixed analyte concentration.

Consistently with the rationale behind HAP-based electrode modifiers, HAP sorption properties demonstrated to improve sensors' performances when implemented in the working electrode. However, the systematic study of the influence of OCP preconcentration time and i_{Peak} revealed a non-linear relationship. In Figure 49b, the trend of Pb(II) stripping peak current versus OCP preconcentration time demonstrate, for HAP/CMC-based electrodes, the presence of a plateau of delivered current between *ca*. 35 and 60 minutes of OCP preconcentration. Ascending i_{Peak} values up to *ca*. 35 minutes could be ascribed to diffusional limitations, impeding the complete exertion of HAP sorption action in a brief time. Conversely, the plummeting of i_{Peak} for OCP preconcentration times > 60 minutes could be indicative of permanent electrode modification, thus posing a threat to the reusability of the sensor itself.

3.4.1 HAP/CMC-based electrodes for heavy metal cations sensing in waterbodies

Despite the above-discussed limitations (common to all the electrode modifiers tested), CMC returned the best sensing performance among the three carbonaceous scaffolds. Therefore, the whole series of HAP/CMC samples, already presented in the previous paragraph (CMC wt. % ranging from *ca*. 4 to *ca*. 20%), has been implemented in electrodes fabrication and testing, with the aim to evaluate the effect of CMC content on the sensing performance.

First and foremost, the conductivity of powders has been measured. The results, listed in the Supporting Material (Figure 100), disclosed an expected direct relationship between CMC wt.% in the composite and conductivity. Interestingly, composites conductivity practically matches that of pristine CMC for CMC content > *ca*. 8%, with *ca*. one order of magnitude increase when compared with HAP/CMC4 (Table 24).

Electrodes crafted from the HAP/CMC samples series have then been tested for their electrochemical sensing ability towards traces of Pb(II) and Cu(II) in aqueous solutions. In the following figure, voltammograms and i_{Peak} versus time dependence are graphically reported.

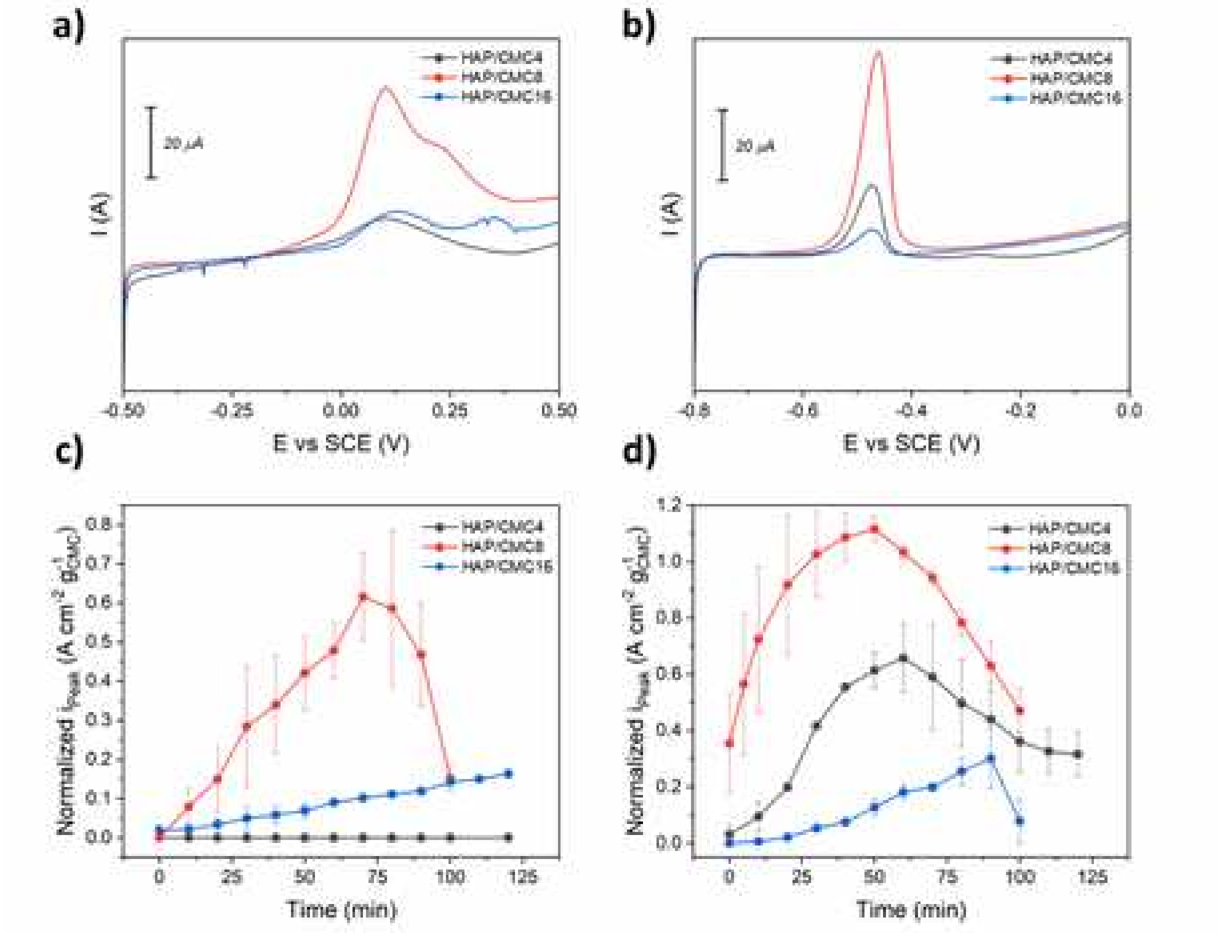

Figure 50: a, b) Anodic stripping voltammograms registered on HAP/CMC-based electrodes for Cu(II) (a) and Pb(II) (b), after 70 and 50 minutes of OCP preconcentration respectively, 1 minute at -1 V vs SCE as reductive preconcentration and an anodic potential sweep rate of 50 mV s^{-1}. c, d) Mean i_{Peak} versus OCP preconcentration time for Cu(II) (c) and Pb(II) (d) solutions. [Cu(II)] = 10^{-4} M and [Pb(II)] = 10^{-5} M

From Figure 50a and b, differences in the profile of the anodic voltammograms in the presence of Cu(II) and Pb(II) can be spotted. Indeed, the stripping peaks of these two common water pollutants are positioned at different potentials, thus indicating that a simultaneous qualitative and quantitative determination of Cu(II) and Pb(II) should be possible on these electrodes. Considering the shape of voltammograms, Cu(II) signal results to be more complex than Pb(II) one, presenting a peak shoulder at a slightly more anodic potential ($\Delta E \approx 0.1$ V) than the major contribution ($E \approx 0.15$ V vs SCE). Moreover, it has to be stressed that to have comparable signals in terms of peak current, Cu(II) concentration had to be set at 10^{-4} M, 10 times higher than Pb(II) one (10^{-5} M), therefore highlighting a different sensitivity of the electrode towards the two benchmark pollutants.

Apart from these general considerations, results demonstrate that CMC wt.% in the composites and HAP/C ratio clearly play a role in determining the sensing ability. As in the case of different scaffolds, higher materials conductivity does not correspond to superior performances. Indeed, HAP/CMC8-based electrodes grant almost double peak current intensities at the same Pb(II) concentration and up to 6x increase in the case of Cu(II). The reason for the improved activity of HAP/CMC8 could be correlated to its HAP/C ratio (as commented previously, more or less 1:1 in terms of surface area of the two moieties). The decreased activity at higher CMC wt.% could instead be due to the lower surface exposure of phosphate groups (as evidenced by Raman spectroscopy, Figure 41), surely the main actors in the exertion of cations sorption by the hydroxyapatitic moiety of the composites.

The effect of the OCP preconcentration time on the peak intensity has been investigated as well (Figure 50c and d). As observed for HAP/CMC4 in Figure 49b, a typical volcano trend of i_{Peak} with OCP preconcentration time is registered for the other CMC-containing composites. In agreement with the voltammograms in Figure 50a and b, HAP/CMC8 exhibits the higher i_{Peaks} throughout the whole time range examined and especially reaches the maximum i_{Peak} values at shorter OCP preconcentration time. For example, in the case of Cu(II) sensing (Figure 50c), HAP/CMC4 and HAP/CMC16 composite seems to not even approach the maximum after OCP preconcentration periods as long as 125 minutes, presumably because of the moderate or almost absent content of surface phosphate groups (same reason above exposed to justify the overall improved performances of HAP/CMC8).

Experimental points reported in Figure 49b and Figure 50c and d have been collected on single electrodes, dipped in the electrolyte/analyte solution and sequentially subjected to SWASV analyses. Therefore, further tests have been carried out on HAP/CMC-based electrodes as to rule out the possibility that the peculiar trends of i_{Peak} with OCP preconcentration time are caused by a gradual increment of reduced analyte on the electrode surface after incomplete stripping steps. To do so, timely analyses have been conducted as opposed to those sequential analyses.

The differences between sequential and timely analyses in terms of trends of i_{Peak} versus OCP preconcentration time in the presence of Pb(II) as analyte are gathered in Figure 51.

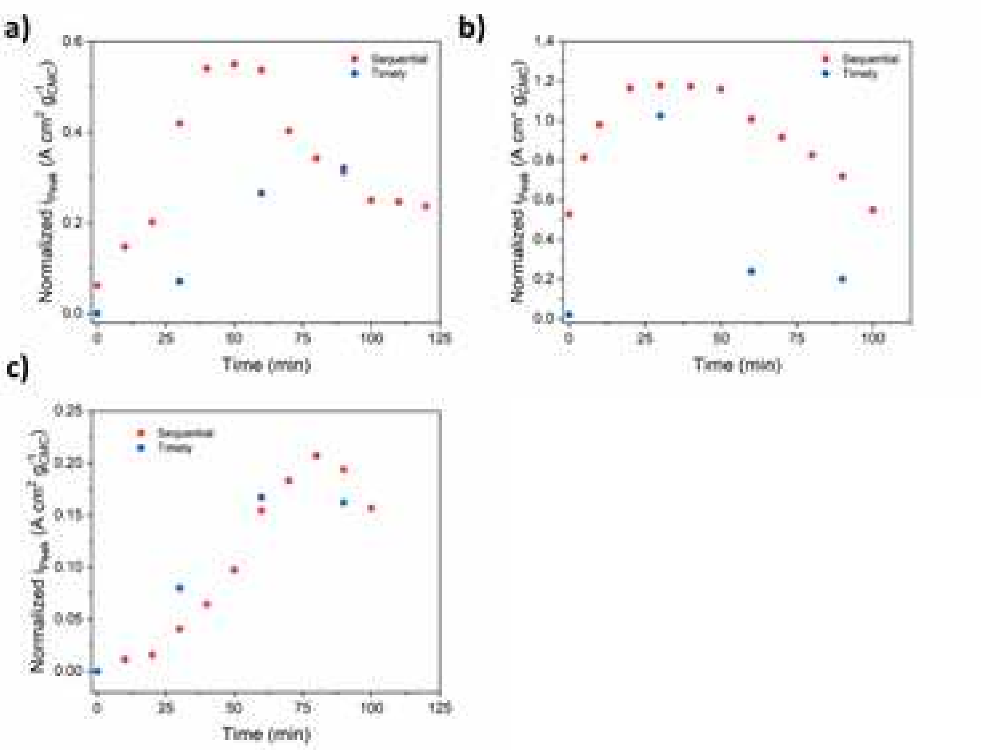

Figure 51: Sequential (red dots) versus timely (blue dots) analyses i_{Peak} trends with OCP preconcentration time. Analyte: Pb(II) 10^5 M, SWASV parameters as reported in the Experimental Section, paragraph 8.4.2. a) HAP/CMC4; b) HAP/CMC8 and c) HAP/CMC16-based electrodes.

In a timely analysis, a fresh electrode is subjected to a definite OCP preconcentration time, then to a single SWASV analysis. Therefore, there are no previous and allegedly incomplete anodic stripping steps that could affect i_{Peak} values; since analyte concentration is kept constant, OCP preconcentration is the only parameter determining the stripping peak current density.

With the exception of HAP/CMC4 (Figure 51a), timely analyses reproduce the trends observed for sequential ones (Figure 51b and c). Hence, the dependence of the electrodes response on solution contact time is confirmed (curve envelopes of stripping voltammograms are available in the Supporting Material, Figure 101).

Once established the ideal OCP preconcentration step length (70 minutes for Cu(II) and 50 minutes for Pb(II) containing solutions, respectively), SWASV operativity has been optimized accordingly. Since HAP/CMC8 has proven to be the most responsive modifier, i_{Peak} versus [Me] calibrations have been carried out on such electrodes. Both protocols, sequential and timely analysis, have been considered. Result are graphically presented in the following Figure 52, while numerical data (slope and intercept of regression lines) are gathered in Table 50 in the Supporting Material.

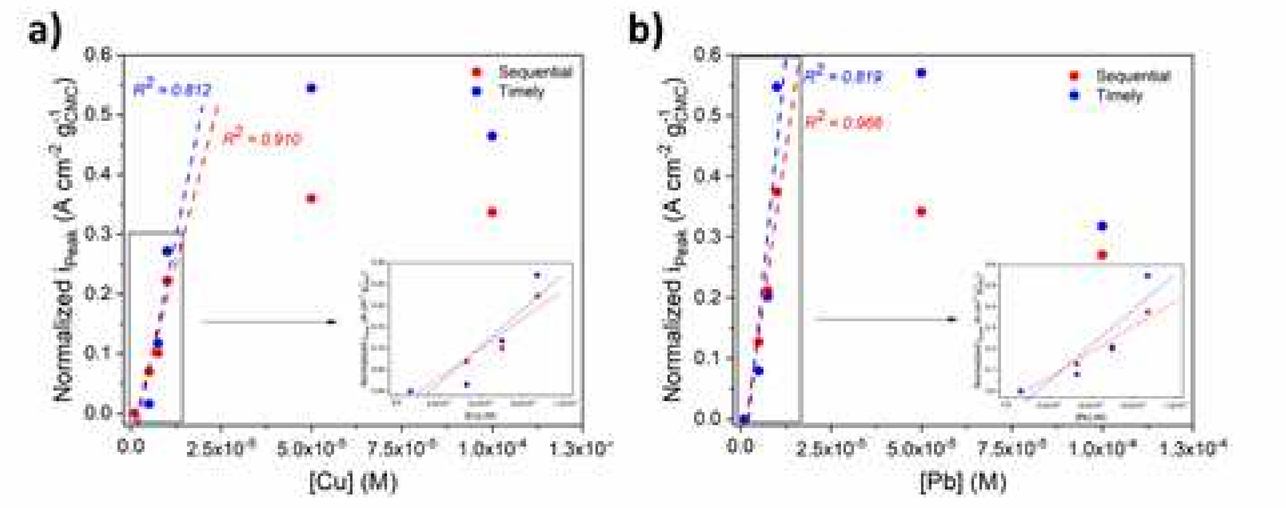

Figure 52: i_{Peak} vs [Me] calibration lines registered on HAP/CMC8-based electrodes in the presence of a) Cu(II) and b) Pb(II) as analyte. SWASV parameters can be found in the Experimental Section, paragraph 8.4.2. OCP preconcentration step equal to 70 and 50 minutes for Cu(II) and Pb(II), respectively.

Independently of the analyte and/or the applied protocol, the stripping peak current grows linearly with the metal species concentration only up to indicatively $1 \cdot 10^{-5}$ M. In these linear ranges, calibration lines have been regressed. Correlation coefficients indicate that the sequential protocol returns more reliable and accurate data. In numerical terms, linear range and LoD of HAP/CMC8-based electrodes for Cu(II) and Pb(II) are gathered in Table 25.

Table 25: Linear response range and LoD for HAP/CMC8-based electrodes.

	Linear response range		**LoD^a**	
Cu(II)	≈ 5 µM to ≈ 10 µM	*(≈ 315 ppb to 635 ppb)*	≈ 2.1 µM	*(≈ 133 ppb)*
Pb(II)	≈ 5 µM to ≈ 10 µM	*(≈ 1.04 ppm to 2.07 ppm)*	≈ 1.8 µM	*(≈ 373 ppb)*

^{a} *Calculated by interpolation on the regressed calibration line, considering i_{Peak} = 1 µA as the lowest detectable signal in terms of signal to noise ratio.*

Despite the applied protocol and the nature of the analyte, at metal concentrations higher than *ca.* $3.5 \cdot 10^{-5}$ M the signal to concentration linearity is lost and the registered peak currents even decrease. This behavior, similar to that observed at long contact time between electrode and analyte solution (i.e. long OCP preconcentration step), suggests that relatively high heavy metal concentrations may modify the electrode itself (presumably because of the irreversible adsorption of such species onto the HAP moiety of the composite), thus altering the electrochemical response of the sensor.

3.4.2 Ex-situ sensing applications: metal species detection beyond in-situ SWASV

Studying the sensing ability of HAP/CMC8-based electrodes by in-situ SWASV (i.e. running the electrochemical tests in the analyte containing solution) evidenced two main practical limitations: (*i*) the strict dependence of the analytic signal on the OCP preconcentration time and (*ii*) the possible modification of the electrode surface at long contact times and/or in the presence of high concentrations of pollutants. In order to minimize these shortcomings, alternative heavy metal detection methods have been experimented.

Since OCP preconcentration time plays a major role in defining the intensity of the analytical signal (i_{Peak}) and thus the overall technique sensitivity, it can be guessed that a consistent share of the heavy metal cations present in the solution are captured by the hydroxyapatitic moiety on the electrode surface. Therefore, the adsorption of the pollutants onto the electrode surface should allow the use of the device as a “sampler”, permitting to run ex-situ analyses. In brief, the SWASV steps subsequent to the OCP preconcentration period (reductive preconcentration and anodic stripping) are carried out in fresh electrolyte solution (0.1 M KNO_3 in MilliQ water) on a working electrode previously immerged for a definite time into the analyte containing solution. Figure 53a describes the trend of i_{Peak} versus time for in-situ and ex-situ analyses (analyte: Cu(II) $5\cdot10^{-5}$ M, HAP/CMC8-modified electrode).

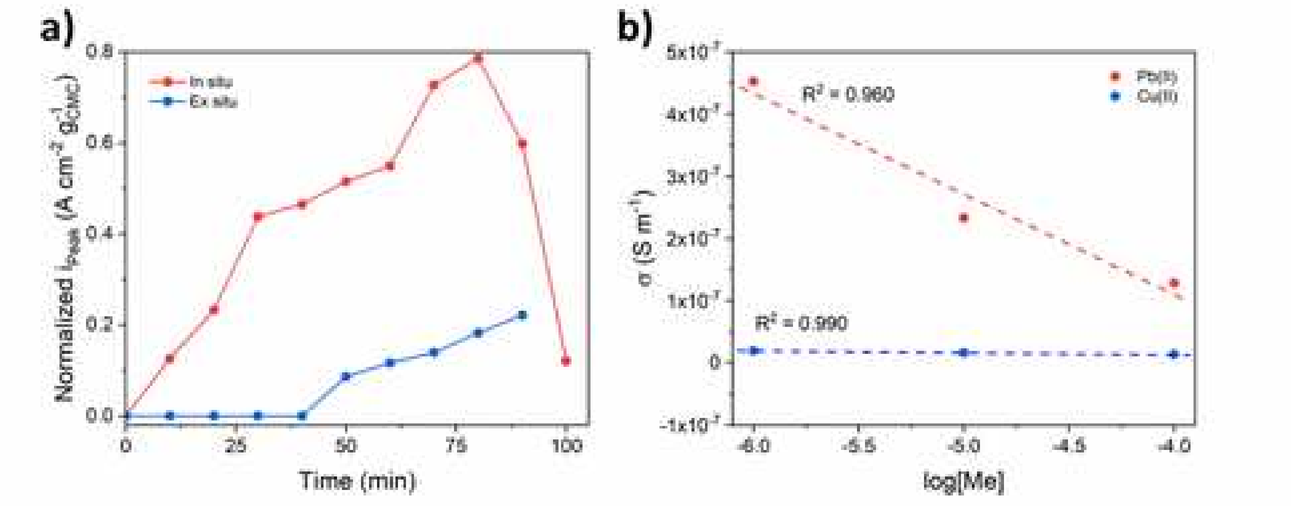

Figure 53: a) In situ versus ex situ trends of i_{Peak} at different OCP preconcentration times (analyte: Cu(II) $5\cdot10^{-5}$ M, HAP/CMC8-based electrode); b) Ex situ conductivity of electrodes versus analyte (logarithmic) concentration. Electrodes were immerged in the Cu(II) and Pb(II) containing solutions for 70 and 50 minutes, respectively.

Two conclusions can be drawn from the graph: (*i*) adsorption of heavy metal species onto the electrode surface effectively takes place for OCP preconcentration periods longer than *ca*. 35 minutes but (*ii*) the lower i_{Peak} registered indicate that the ions present in the solution when the in situ technique is applied largely contribute to the global signal. Such critical contribution of the ions not captured during the OCP period leads to invariably diminished analytical signals, thereby negatively impacting on the linear response range and the LoD of the system.

Determination of the variation of electrodes conductivity with pollutants concentration has been another possibility explored in the field of ex situ analyses. Briefly, HAP/CMC8-based electrodes have been immerged into analyte containing solutions (metal concentration ranging from 1 to 100 µM) for a definite amount of time (see Figure 50c and d and related discussion), then rinsed with MilliQ water, dried and their conductivity measured.

Figure 53b reports the experimental data and the regression line of conductivity versus the logarithm of Pb(II) and Cu(II) concentration. Numerical data can be found in the Supporting Material (Table 51). Although presenting a correlation coefficient R^2 close to the unity, Cu(II) conductivity versus [Cu(II)] calibration line is drawn in a very limited range of measured σ. Indeed, the electrodes conductivity plummets down to *ca*. 30% of the pristine electrode at relatively low Cu(II) concentrations (1 μM), therefore "blinding" the sensing method. On the other hand, this ex situ method guarantees better results for Pb(II) quantification: an almost linear response seems to be provided in the concentration range examined. However, considering the slope of the regression line, the electrode conductivity variation at [Pb(II)] equal to 1 μM and that correlated to the mere immersion of the electrode in MilliQ water (i.e. the blank/background measure), the LoD associated with this method results similar to the one calculated for in situ SWASV.

3.5 Conclusions

HAP/C composites represent a promising solution for the simultaneous remediation of organic and inorganic pollution of industrial wastewaters; at the same time, the presence of a carbonaceous scaffold paves the way to possible applications of HAP-based/doped materials in electrochemical devices, for example electrochemical sensor for the monitoring of heavy metal ions content in waters streams.

After a preliminary investigation, Chinese Mesoporous Carbon (CMC) has been selected as the ideal carbonaceous scaffold for both composites' applications. CMC is a mesoporous carbon generated from renewable sources and offers several peculiar features such as large surface area and high surface functionalization degree [169]. Composites syntheses have been carried out by an optimized wet co-precipitation route, that provided homogeneous materials at easily tunable HAP/C wt. %. In particular, four HAP/CMC composites have been synthesized in the range from *ca*. 4 to *ca*. 20 wt.% in CMC with HAP/CMC8 acting as a watershed: indeed, a CMC content of *ca*. 8 wt.% roughly correspond to a balance in the surface area of the two (pristine) moieties.

A thorough physical/chemical characterization of HAP/CMC composites and pristine HAP and CMC have been performed, as to shed light on the effect of HAP:CMC ratio on the structure and morphology of the formers. The presence of the two unaltered moieties in the composites was proven through several techniques (TGA, XRPD, FT-IR). Despite the absence of a specific trend of surface area with CMC content, all composites have been identified as predominantly mesoporous materials, with a slight shift towards microporosity at high CMC content (HAP/CMC16, presenting and an effective CMC content of *ca*. 20 wt %). A transition from HAP-like to CMC-like materials can be indeed spotted in the composites when CMC wt. % overcomes 8-10%, both from the morphological (N_2 ads/des, TEM images) and structural (FT-IR, Raman spectroscopy) point of view. Specifically, Raman spectra of HAP/CMC composites evidence the disappearance of PO_4^{3-} related signals for CMC content > *ca*. 8% (> HAP/CMC8), confirming the ridge represented by such mass (and surface area) ratio.

Adsorption tests have been then carried out, with the aim to examine the sorption ability of HAP/CMC composites towards some benchmark inorganic and organic pollutants, namely Cu(II) and methylene blue (MB). HAP/CMC composites proved to be promising sorbents for the remediation of polluted wastewater where organic and inorganic hazardous species are co-present. Indeed, adsorption tests on simulated wastewaters containing a single pollutant demonstrated that for all composites the adsorption ability of both moieties are retained (i.e. HAP capture heavy metal cations whilst CMC traps organic species), albeit no clear synergistic effects between the two constituents can be identified.

However, sorption test on multi-pollutant solutions evidenced that HAP/CMC composites gather in a single material the complementary sorption features of HAP and activated carbons. Results indicate that a weight percentage > *ca*. 8-10% in the carbonaceous scaffold guarantees optimal performances. Leaching tests on used HAP/CMC8 sorbent confirmed that the composites combine the permanent confinement ability of inorganic and organic pollutants exerted by HAP and CMC respectively, suggesting such dual materials as a possible solution for secondary pollution issues as well.

Notwithstanding the lower conductivity when compared to other carbonaceous scaffolds like carbon nanofibers (CNFs), CMC resulted the ideal C-based moiety even for sensing applications. HAP/CMC composites have been implemented as modifiers in self-standing and mechanically stable electrodes for the detection of trace amounts of heavy metal cations in aqueous solution by square wave anodic stripping voltammetry (SWASV). Best sensing performance was delivered by HAP/CMC8, possibly for the previously discussed ideal ratio between the two moieties. Limits of detection of *ca*. 2.1 and 1.8 µM have been achieved for Cu(II) and Pb(II) respectively, with linear response ranges standing around 5 to 10 µM.

Anyway, as to allow the hydroxyapatitic moiety of the composite to exert its preconcentration assist, the typical SWASV analytical procedure had to be modified, with the addition of an OCP preconcentration step prior to the reductive one. In contrast with the beneficial effect of cations adsorption, the incorporation of HAP into electrodes causes (*i*) a strict dependence of the analytical signal on the electrode exposure time to the pollutants (OCP preconcentration period) and (*ii*) a possibly permanent modification of the electrode itself for long exposure time and/or high concentration of pollutants. These shortcomings must be taken into account, possibly applying HAP/CMC-modified electrodes to moderately polluted systems where long "acquisition" time can be afforded, and a continuous in-line monitoring is not mandatory.

Chapter 4: HAP-doped electrocatalysts for electrochemical CO_2 reduction reaction (CO_2RR)

4.1 Introduction to CO_2RR

This chapter reports on the development of novel electrocatalysts, designed for selective production of high added-values hydrocarbons and alcohols by electrochemical CO_2RR. The objective has been pursued designing carbon-supported and HAP-doped Cu-based electrocatalysts (Cu+HAP/C).

Following, a brief overview on the effects of increasing atmospheric CO_2 concentration is presented together with possible solutions to the issue. Then, electrocatalytic CO_2 reduction reaction will be introduced, discussing advantages and drawbacks of the process. A digest of the most common metallic and non-metallic CO_2RR electrocatalyst will be provided. The state of art of Cu-based and heteroatom-doped carbon nanostructures CO_2RR electrocatalysts will be detailed, insofar strictly inherent to the matter of study of this chapter. The use of HAP as effective dopant in CO_2RR catalysts is also discussed.

Finally, the rationale behind the design of novel Cu+HAP/C materials as electrocatalysts for selective CO_2RR towards high added-value products is presented.

4.1.1 The increase of atmospheric CO_2: an overview

First measurements of the atmospheric CO_2 concentration are dated early 1800s and stood around 270 ppm. Industrialization, world population growth and general improvement of life quality caused a continuously increasing energy demand, to which mankind responded by means of fossil fuel combustion/consumption. Nowadays, *ca*. 35 Gtons/year of anthropogenic CO_2 are generated, and the average CO_2 concentration had risen to 403.38 ppm (September 2017, data released by the National Oceanic and Atmospheric Administration of the US Department of Commerce [176]) against a safety limit estimated around 350 ppm. In absence of a radical change in energy sourcing, atmospheric CO_2 is predicted to reach 600-700 ppm concentration by the end of the century [177]. This increasing trend poses a major threat in terms of global warming and climate patterns, which in turn will impact on sea levels and biodiversity. A logic solution to the problem could be represented by the development of technologies for CO_2 capture, conversion and utilization, with conversion representing the most challenging and at the same intriguing option.

It is rather obvious indeed that CO_2, as the product of complete combustion of carbon-based fuels, possesses a stable molecular configuration. From the structural point of view, CO_2 is a linear molecule with two equivalent C=O bonds and high molecular symmetry. The latter is the key contributor to the activation barrier, with a price in energy that makes difficult thinking about CO_2 as a chemical feedstock. Alleged conversion of CO_2 in valuable C-based molecules means the transformation of C=O bonds (*ca*. 750 kJ mol^{-1}) in C-C (*ca*. 350 kJ mol^{-1}), C-O (*ca*. 330 kJ mol^{-1}) and/or C-H (*ca*. 410 kJ mol^{-1}) bonds, implying massive energy consumption [178]. However, the chemical transformation of CO_2 into value-added products has been pursued since the early days of catalysis, with Sabatier reaction ($CO_2 + H_2 \rightarrow CH_4$) being the most representative example.

At present, only few industrially relevant processes use CO_2 as feedstock. With a market volume over 100 Mtons/year, the synthesis of urea ($CO_2 + NH_3 \rightarrow CO(NH_2)_2$) is for sure the main one and can be undisputedly claimed as vital for humanity in the fact that it guarantees fertilizers to sustain the population growth [179]. Nonetheless, CO_2-based fertilizers/chemicals market is not even comparable in scale to the energy one, so the former cannot be thought as an adequate "reservoir" where to funnel worldwide CO_2 emissions [179].

In recent years, renewed socio-economical driving forces towards a more sustainable future are causing a net growth in processes like photo- and/or electrocatalytic CO_2 conversion. Among all CO_2 conversion technologies, electrocatalytic CO_2 reduction (CO_2RR) attracted major attention from both academic and industrial researchers because of some peculiar features. CO_2RR can in fact be performed under mild temperature and pressure and the process could be easily controlled by the imposed electrode potentials. From an engineering point of view, reaction systems (electrolyzers) could be designed as compact, modular and on-demand. Moreover, supporting electrolytes (preferentially aqueous) can be fully recycled reducing waste production. Finally, the energy input of the process, electricity, could be generated from renewable sources allowing to (*i*) efficiently stock the energy (in chemical form) produced by intrinsically intermitting sources while (*ii*) ideally “close” the carbon cycle, converting CO_2 in high value-added C-based molecules without any extra generation of CO_2 itself. Products of CO_2RR may then be directly fed to energy producing devices and/or reconverted in liquid fuels [176,177,179,180].

4.1.2 Electrocatalysts for CO_2RR

Since the pioneering work of Hori and Ikeda [181,182], who demonstrated the feasibility of CO_2 electrocatalytic reduction on bulk metal electrodes, a plethora of catalysts have been tested in CO_2RR, from metal-based to metal-free materials, passing through metal complexes [183,184].

In accordance to the materials studied in the present dissertation and for the sake of conciseness, only the two families of metallic and non-metallic catalysts will be presented. After this overview, the most promising catalysts in terms of generation of high added-value products will be further discussed in paragraph 4.1.4.

4.1.2.1 Metal-based electrocatalysts

Polycrystalline bulk metal electrodes have been the first catalysts exploited in CO_2RR [181,182]. In recent years, the development of nanoparticle synthesis brought on the scene nanostructured metal-based catalyst, offering high surface area and the possibility to tune product selectivity by means of particle size control, alloying, core-shell structuring and/or selective exposure of determined crystal facets (i.e. shape-controlled syntheses) [178,184]. Moreover, nanoparticles dispersion onto conductive supports (mainly C-based) paved the way to a new generation of catalysts, characterized by lower cost and higher efficiency.

Extensive studies were performed on both bulk and nanostructured metal electrodes. Based on the primary product of CO_2RR, metals were divided in three subgroups [176,177]:

- Hydrogen (H_2) evolving metals, i.e. CO_2RR inactive metals (e.g. Pt, Fe, Ni);
- Carbon monoxide (CO) selective metals (e.g. Au, Ag, Zn);
- Formate ($HCOO^-$) selective metals (e.g. Sn, Pb, In).
- Higher order products (C_1 and C_{2+} hydrocarbons and oxygenates) generating metals (Cu).

To date, the mechanisms of CO_2RR on metallic surfaces are still not fully understood. However, literature generally agrees on a first common step: an electron transfer (ET) to form the radical anion species $CO_2^{\bullet-}$, common to all reaction pathway regardless the final product [176,177,184,185]. $CO_2^{\bullet-}$ species are supposed to be stabilized on the surface of CO generating metals ($^*CO_2^{\bullet-}$) and converted in fact to CO by means of two further steps: a first proton transfer (PT) to form a *COOH intermediate and a final coupled proton-electron transfer (CPET) to obtain *CO, readily desorbed as CO (Figure 54a).

On the other hand, the mechanism of $HCOO^-$ generation is still under debate. Three possible pathways have been envisaged, comprising both $CO_2^{\bullet-}$ coordinative and non-coordinative routes, sharing an overall one proton-two electrons transfer (Figure 54b).

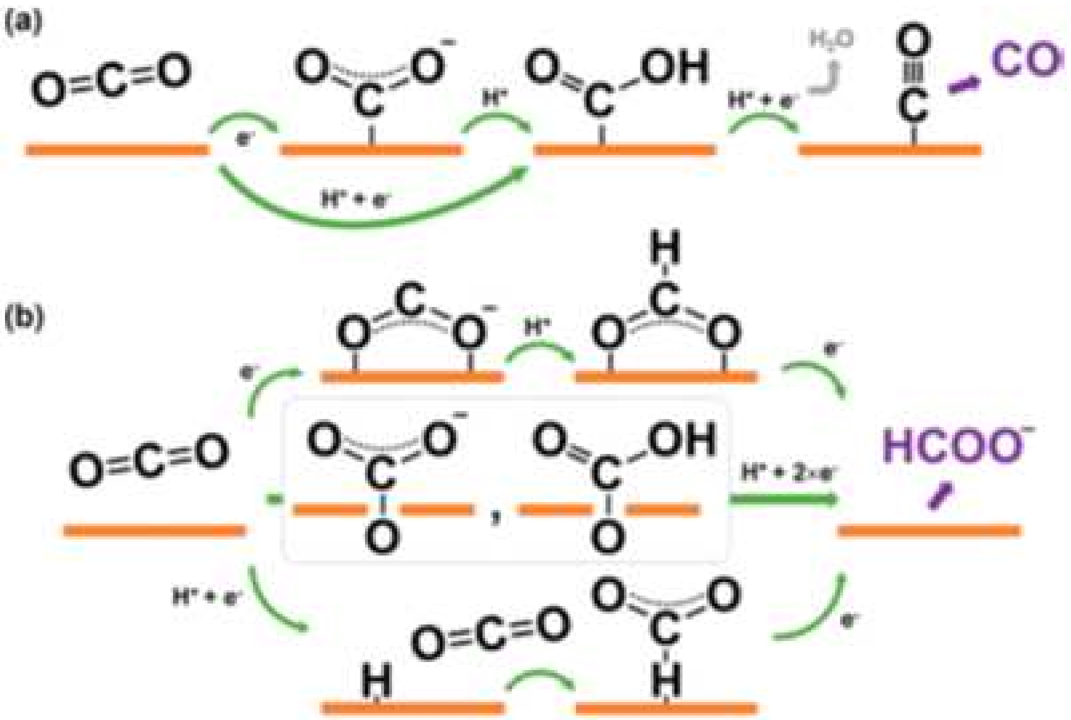

Figure 54: Proposed pathways of reaction to a) CO and b) HCOO$^-$ on metallic surfaces. From reference (Yang et al, 2020).

Noticeably, Cu stood alone as the only metal able to promote further reduction (> 2 e$^-$ transfers), generating a wide range of so-called higher order products, with CH_4, CH_3CH_2OH and C_2H_4 representing the most relevant besides the common H_2, CO and HCOO$^-$ [178,184]. The reason of this peculiar feature derives from the optimal CO binding energy exhibited by Cu surface, unraveled by the application of scaling relations (i.e. linear correlations between sets of adsorption energies) on the basis of DFT calculation results [185]. Indeed, plotting the calculated limiting potential U_L for CO_2RR versus the CO binding energy on different metal surfaces, a volcano-type plot is obtained (Figure 55).

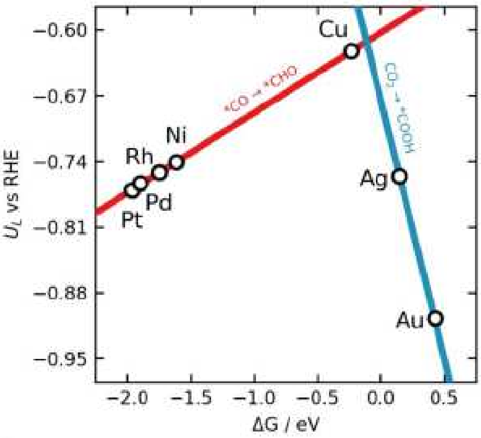

Figure 55: Scaling relations volcano plot for CO_2RR on different metal surfaces. Limiting potentials (U_L) correspond to the two first CPETs. From reference [Rendon-Calle et al, 2018]

Cu sits near to the volcano apex and, according to the Sabatier principle, allows optimal stabilization and thus further electron transfer to the *CO intermediate postulated in Figure 54a. Conversely, strong CO binders (e.g. Pt) suffers from surface poisoning of CO_2RR active sites, therefore favoring HER, while weak CO binders (e.g. Ag) are not able to stabilize the *CO intermediate and catalyze further electron transfers. The unique ability of Cu-based catalysts to yield high added-value products (C_1 and C_{2+} hydrocarbons and oxygenates) put this metal at the center of CO_2RR scene in the last decades [178]. Further details on Cu-based electrocatalysts will be discussed in paragraph 4.1.4.1.

Besides the zero valent metallic elements discussed above, other metallic systems exhibited noteworthy activity in CO_2RR. In the realm of 2e$^-$ transfer reaction products, several transition metal chalcogenides and cobalt oxides were proven to generate CO and HCOO$^-$, respectively. After the discovery of MoS_2 activity in CO_2RR, a thorough screening of transition metal dichalcogenides identified 2D WSe_2 nanoflakes as a potential candidate to replace noble metals in CO generation, exhibiting high FE (> 80%) at low overpotential (*ca*. 54 mV) in ionic liquids [186]. On the other hand, cobalt, slightly active in CO_2RR as zero valence species, resulted to efficiently generate $HCOO^-$ (FE > 90%) when oxidized to Co_3O_4 [187]. No metal chalcogenides and/or oxides are reported to yield higher order products under CO_2RR operative conditions.

Particularly interesting is the case of Cu oxides, which activity in CO_2RR is currently under debate. Despite metallic Cu is the most thermodynamically stable phase under CO_2RR conditions [188], various oxide derived catalysts exhibited peculiar selectivity towards C_{2+} products [184]. Several authors attributed this behavior to the residual presence of subsurface oxygen atoms in CuO and CuO_2-derived catalyst [189]: energy electron-loss spectroscopy (EELS) and positron annihilation spectroscopy detected an amorphous Cu outlayer with O atoms at its subsurface [184]. Conversely, Nilsson et al. [190] monitored by in situ X-ray adsorption spectroscopy (XAS) the evolution of Cu_2O and $CuCO_3/Cu(OH)_2$ under CO_2RR conditions, reporting the complete reduction to Cu^0 and negligible influence of the initial oxidation state/O content.

4.1.2.2 *Non-metallic and metal-free electrocatalysts*

Dating back to the development of fuel cells technology, noble and transition metals have been the cornerstones of electrocatalysts for energy conversion and storage [184,191] and the same applies nowadays to CO_2RR. High cost and scarcity of noble metals, together with poor durability/stability, pushed the fuel cell market towards the development of alternative catalysts, presenting wide elemental availability and comparable performances. Reminiscent of ORR transition towards non-precious metal catalysts (or at least with reduced Pt content) [184,191], researchers have been recently testing several nanostructured carbon-based catalysts, including heteroatom doped ones (mainly N-doped) in CO_2RR [192].

Common nanostructures of these materials include, but are not limited to, 0D carbon quantum dots, 1D nanotubes and fibers, 2D graphene sheets and 3D nanodiamonds [192]. Tunable molecular symmetries and dimensions, together with the possibility to introduce electron modulations through heteroatomic doping, are the reasons underpinning the successful implementation of metal-free carbon-based materials as efficient electrocatalysts. In addition to that, cheapness, large availability of the constitutive elements, high conductivity, high surface area and corrosion resistance are all promising features for a vast application of such materials in energy related electrocatalytic processes [192].

Although the implementation of carbon-based metal-free catalysts in CO_2RR is quite recent, previous studies conducted in the field of ORR demonstrate that the catalytic activity of these materials arises from the doping-induced charge-transfer [193]. Therefore, the nature of the heteroatom, its position in the lattice and its percentage content all contribute in determining catalytic performances. Accessibility of the active sites and facilitated diffusion of reactants are equally important issues. Consequently, considerable effort has been made to develop synthetic routes that enable fine control on dopant location and quantity while obtaining 3D carbon structures with tunable macro, meso and microporosity [192].

A detailed state of art of carbon-based metal-free catalysts in CO_2RR will be presented in paragraph 4.1.4.2.

4.1.3 Common CO_2RR issues

Whether the catalyst nature, CO_2RR is a rather immature technology and it is still suffering from several drawbacks that hinder its industrial application. In the following section the main ones will be introduced, and the possible solutions discussed.

1) *<u>CO_2 thermodynamic stability:</u>* the marked CO_2 stability results in sluggish CO_2 reduction kinetics (i.e. high activation barrier) and associated high overpotentials. Despite standard reduction potentials of several CO_2 half-reactions to interesting products are modest (Table 26), the real applied potential needed to sustain relevant currents (i.e. reaction rates) is normally far more negative, in the order of magnitude of hundreds of millivolts or even units of volts. Moreover, the application of largely cathodic potentials leads to a decreased faradic efficiency of the process, due

to the onset of parasitic reactions like decomposition of the electrolyte (hydrogen evolution reaction, HER, in the case of aqueous electrolyte). For all the reduction products, besides the number of electrons transferred to the CO_2 molecule, the first intermediate suggested is the radical anion $*CO_2^{\bullet -}$, where * denote an active site (i.e. the radical anion exists as surface adsorbed species). Literature almost unanimously agrees on this first single-electron electron transfer (ET) to be the rate determining step (RDS) of the process, with a standard reduction potential estimated around -1.9 vs NHE (Normal Hydrogen Electrode) [180]. In confirmation, foils of polycrystalline CO_2RR metals (e.g. gold, silver, copper) exhibit Tafel slopes of *ca*. 120 mV dec^{-1} [180], indicative of a single electron transfer as the rate-limiting step when operating under nearly neutral conditions. Therefore, a surface able to activate CO_2 (i.e. break CO_2 linearity by adsorption) while stabilizing the intermediate radical anion $*CO_2^{\bullet -}$ would facilitate the reduction process, lowering the associated overpotential.

Table 26: Half-cell CO2RR electrochemical reaction. Adapted from reference (Yang et al, 2020).

Half electrochemical reaction (CO_2 reduction)	E vs RHE
$CO_{2(g)} + 2H^+ + 2e^- \rightarrow HCOOH_{(l)}$	-0.02 V
$CO_{2(g)} + 2H^+ + 2e^- \rightarrow CO_{(g)} + H_2O_{(l)}$	-0.11 V
$CO_{2(g)} + 6H^+ + 6e^- \rightarrow CH_3OH_{(l)} + H_2O_{(l)}$	0.03 V
$CO_{2(g)} + 8H^+ + 8e^- \rightarrow CH_{4(g)} + 2H_2O_{(l)}$	0.17 V
$2CO_{2(g)} + 12H^+ + 12e^- \rightarrow CH_2CH_{2(g)} + 4H_2O_{(l)}$	0.07 V
$2CO_{2(g)} + 12H^+ + 12e^- \rightarrow CH_3CH_2OH_{(l)} + 3H_2O_{(l)}$	0.08 V
$3CO_{2(g)} + 18H^+ + 18e^- \rightarrow CH_3CH_2CH_2OH_{(l)} + 5H_2O_{(l)}$	0.10 V

2) <u>*CO_2 solubility/equilibria in water:*</u> as many gases, CO_2 is scarcely soluble in water (*ca*. 1.45 g L^{-1} ≈ 33 mM at ambient temperature and pressure), posing the major issue of diffusive limitation to CO_2RR processes in aqueous electrolyte [176,177,194]. Moreover, after dissolution in water, CO_2 can further react according to the following equilibria:

$$CO_{2(g)} \rightarrow CO_{2(aq)}$$

$$CO_{2(aq)} + H_2O \rightarrow H_2CO_3$$

$$H_2CO_3 + H_2O \leftrightarrow HCO_3^- + H_3O^+ \qquad pK_a \approx 6.35$$

$$HCO_3^- + H_2O \leftrightarrow CO_3^{2-} + H_3O^+ \qquad pK_a \approx 10.33$$

Several studies demonstrated that only molecular dissolved $CO_{2(aq)}$ has an active role in CO_2RR [194], thus limiting the operative pH range.

Use of non-aqueous electrolytes (e.g. alcohols or ionic liquids) or CO_2 pressurization has been explored as possible alternatives [176,177]. However, all CO_2 diffusion limitations can be minimized thanks to a proper cell design. The use of gas diffusion electrodes (GDE) is indeed ramping in CO_2RR, starting from lab-scale testing [195,196], guaranteeing continuous deployment of CO_2 at the catalyst's surface and almost eliminating CO_2 diffusional issues.

3) <u>*Cost-effectiveness:*</u> limited durability and stability of catalysts, especially when coupled with massive use of expensive elements, threaten the implementation of CO_2RR as an efficient and cost-effective process.

According to the know-how gained from other catalytic process, CO_2RR electrocatalysts are moving towards nanostructuring of active metal phases, thus maximizing the atomic efficiency of the process while lowering the overall metal consumption. Metal nanoparticles are commonly supported on high conductivity and surface area carbon-based materials. Following the way paved by ORR and OER, even nanostructured metal-free carbon-doped materials are being tested in CO_2RR.

4) *Product selectivity:* under the application of a cathodic potential, the majority of CO_2RR catalysts are prone to catalyze HER as well, thus lowering faradic efficiencies (FE) in C-based products. As previously discussed in point 1, this problem could be overcome by a proper catalyst design aimed to lower the overpotential for CO_2RR onset. However, in the case of Cu-based catalysts, the high number of electron transferred and the increase in intermediates bonding energy, deducible from scaling relations, impede the generation of C_1 and C_{2+} hydrocarbons/oxygenates at mild potentials (less cathodic than $E_{Onset\ HER}$). Moreover, DFT simulations of CO_2RR on Cu depict complex mechanisms, where different products of reaction share common intermediates, necessarily leading to mixtures of products.

   Selective generation of higher order products on Cu-based materials can be achieved by a deep understanding of reaction mechanisms and structure/activity relationships. This topic is further discussed in paragraph 4.1.4.1.

To conclude, although several operational parameters (electrolyte nature, concentration and pH, pCO_2, temperature etc.) and the cell design have proven to affect both the efficiency and selectivity of the process [176,177,184], CO_2RR technology cannot refrain from a deeper comprehension of the phenomena itself and from the development of rationally designed catalysts on the basis of the present knowledge of the process.

4.1.4 Generation of high-added value products by electrocatalytic CO_2RR

The selective electrochemical conversion of CO_2 to CO and $HCOO^-$ can be further valorized generating higher order products through Fischer-Tropsch process [197] and/or cascade reactions [198] respectively. However, the pioneering work of Hori [199] on bulk copper electrodes triggered the chase toward the development of direct electrochemical conversion of CO_2 to hydrocarbons. In the following section, the state of art of CO_2RR on Cu-based electrocatalyst is reviewed.

Recently, metal-free catalysts joined Cu in the pursuit of high FE and selectivity towards high added-value products [192]. The promising family of carbon-based metal-free CO_2RR electrocatalysts is reviewed as well, highlighting advantages and drawbacks in respect with Cu ones.

Finally, the novel application of HAP in CO_2 conversion technologies is discussed. Although still not applied in the field of electrocatalytic CO_2RR, HAP has found use in photocatalytic CO_2RR [63,200] where it has been exploited as dopant in the role of CO_2 activator/reservoir.

The unique features of each of the above-mentioned materials set the stage for the rationale design of novel Cu+HAP/C composite electrocatalysts for the efficient generation of high added-value products by electrochemical CO_2RR.

4.1.4.1 Cu-based electrocatalysts

Copper is hitherto the only metallic element able to catalyze more than $2e^-$ transfers towards CO_2, thus allowing the generation of higher order products. More than 16 reaction products have been reported for CO_2RR on Cu-based electrocatalysts [176,177], with a consistent share of them being present in traces or however negligible amounts. Among high added-value products, methane, ethylene and ethanol are those generally detected in relevant quantities (FE > 10%). Despite the remarkable activity, selectivity of Cu-based catalysts is far from ideal. Extensive studies on these class of catalysts pointed out that both activity and selectivity towards higher order products are strictly related to Cu structural features. Therefore, mechanistic insight provided by computational studies, together with experimental evidences and synthesis control, are leading the way towards more active and selective catalysts.

The most common product of CO_2RR requiring more than $2e^-$ transfers is undisputedly methane. CH_4 formation has been first observed on bulk Cu electrodes with encouraging selectivity (*ca*. 40%) at applied potentials as negative as -1 V vs. RHE [201]. Cu-based nanostructures also proven to generate CH_4, with different FE depending on Cu NP shape, size and support [178,202–205].

Although a proper determination of active sites for hydrocarbons formation onto Cu surfaces have not been reported yet, DFT calculations suggest two possible pathways for CH_4 generation (Figure 56).

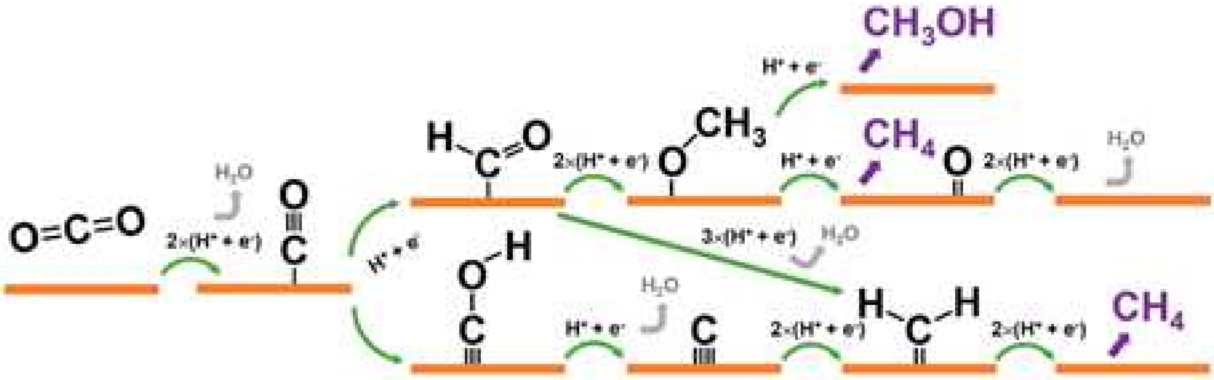

Figure 56: Proposed mechanism of methane and methanol formation onto Cu surfaces. From reference (Yang et al, 2020).

The pathway of CH_4 formation is surely the less understood amid C_1 products because of the complexity associated to the required $8e^-$ transfers and the numerous intermediate species involved. Literature widely agrees on the initial formation of a *CO intermediate, shared with the CO generation route [184]. Discussions is instead open on the following steps, especially on the timing of C-O bond cleavage. A first reaction route (upper scheme in Figure 56) proposes the protonation on the carbon atom of *CO, leading to the formation of formyl *CHO adsorbed species. After a double CPET, the resultant methoxy intermediate *OCH_3 would finally yield CH_4 through a last CPET and C-O cleavage. However, both DFT calculation and experimental evidences (H_2CO reduction on copper [206]) consistently point to CH_3OH as the favorite product of CPET on *OCH_3 intermediate. Considering the negligible amount of CH_3OH generally detected from CO_2RR on Cu surfaces, another mechanism must be involved in CH_4 generation. A pathway passing through a carboxyl *COH intermediate and then a carbene one is to date the most credited [184,207].

C_{2+} products generate upon C-C coupling onto Cu surfaces. Ethylene is so far the most studied C_2 product of CO_2RR and, thanks to advanced catalyst design, FE_{C2H4} up to 60% have been recently achieved [184]. Studies on single crystal Cu catalysts evidenced the preferential formation of C-C bonds on specific Cu facets, thus favoring the generation of ethylene over methane and vice versa [208,209]. In particular, CH_4 resulted to be produced preferentially on Cu(111) facets [209], with a FE ≈ 50% at -1.52 V vs SHE [208]. C-C coupling was instead deemed to take place through *CO dimerization on Cu(100) and other high indexed surfaces like (911), (711) and (511), yielding ethylene (FE up to *ca*. 60%) and ethanol (FE up to *ca*. 18%) at -1.3 V vs SHE [209]. Since the *CO intermediate is common to C_1 generation mechanisms too, a competition among C_1 and C_{2+} products can be guessed. Commonly, this balance is rationalized using the ethylene to methane molar production ratio.

Although still unclear, the proposed mechanism of ethylene generation (Figure 57) is to date the most reliable among C_{2+} products.

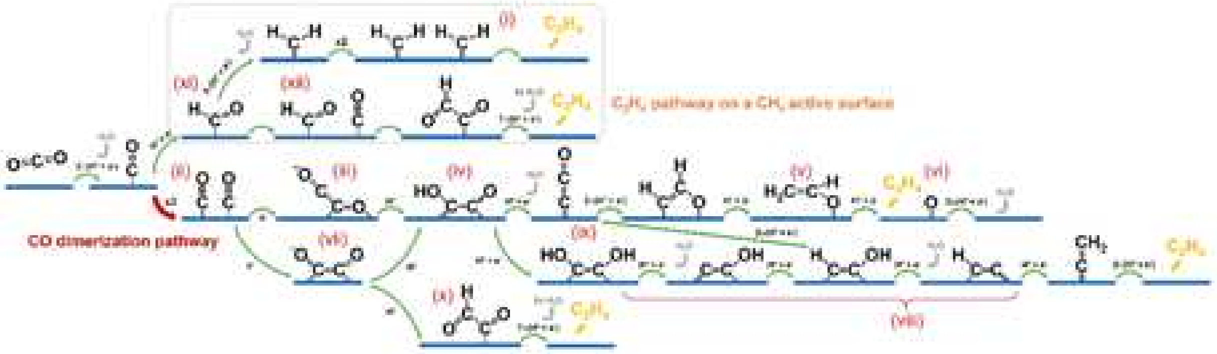

Figure 57: Proposed mechanism of formation of ethylene on Cu surfaces. From reference (Yang et al, 2020).

Early studies proposed that generation of ethylene onto Cu surface took place through *CHO and subsequent carbene (*CH_2) intermediates (upper box in Figure 57). Thanks to the awareness brought by single crystal studies, protonation to *CHO intermediate has been confirmed to occur preferentially on Cu (111) facet, with further CPET steered towards CH_4 generation [208]. To date, the most accredited pathway passes though *CO dimerization on Cu(100) facet. Electrokinetic data support *CO dimerization, identifying as RDS a pH-independent single ET for CO reduction onto Cu(100) crystal plane [184]. This claim is experimentally supported by the facilitated formation of C_{2+} products in alkaline conditions, under which both HER and CH_4 generation are suppressed because of the lack of protons. The steps following *CO dimerization are uncertain but recently the *COCOH intermediate (labelled *(x)* in Figure 57) have been identified by in-situ DRIFT spectroscopy and further supported by DFT calculation [210].

The fundamental role played by Cu crystal facets in determining the mechanisms and thus the products of CO_2RR onto Cu surfaces generated interest towards differently shaped Cu NPs. In particular, Cu nanocubes [205] demonstrated a pronounced selectivity towards CO_2RR (FE_{CO2RR} *ca*. 80% at -1.1 vs SHE) and specifically towards the generation of ethylene (FE = 41%, with an C_2H_4/CH_4 ratio of 2.03 at -1.1 vs SHE). According to the above-discussed mechanisms and the experimental evidences, the enhanced selectivity of nanocubes was deemed to originate from the preferential exposure of (100) facets. Simultaneously, the abundance of low-coordinated edge sites guaranteed efficient stabilization of reaction intermediates. Best results were obtained for nanocubes with an edge length of 44 nm, that the authors claimed to exhibit an optimal balance between plane and edge-sites (N_{edge}/N_{100} plane = 0.025, Figure 58a).

Cu NP size effects have been investigated as well. Testing CO_2RR performances of spherical Cu NP in the range from 2 to 15 nm and comparing the results with those obtained from a Cu foil, Strasser et al. demonstrated a strict size dependency of both catalytic activity and selectivity [204]. As a matter of fact, catalytic activity and selectivity towards H_2 and CO increased with decreasing particle size. For dimensions < 5 nm, the exponential increment of H_2 and CO production implied an almost complete suppression of hydrocarbons generation. CH_4 and C_2H_4 FE reached *ca*. 15 and *ca*. 7% respectively at -1.1 V vs RHE on 15 nm Cu NP, while standing around 60 and 20% on copper foil (Figure 58b). Thanks to DFT modelling, the authors correlated the change in the population of low-coordinated surface sites with the catalytic activity/selectivity of Cu NP. Indeed, the smaller the nanoparticle, the higher the fraction of low-coordinates surface sites, thus the stronger the *H and *CO chemisorption. Strong interactions limit the mobility of surface species and therefore *H and *CO recombination (towards CH_4) and/or *CO dimerization (towards C_2H_4).

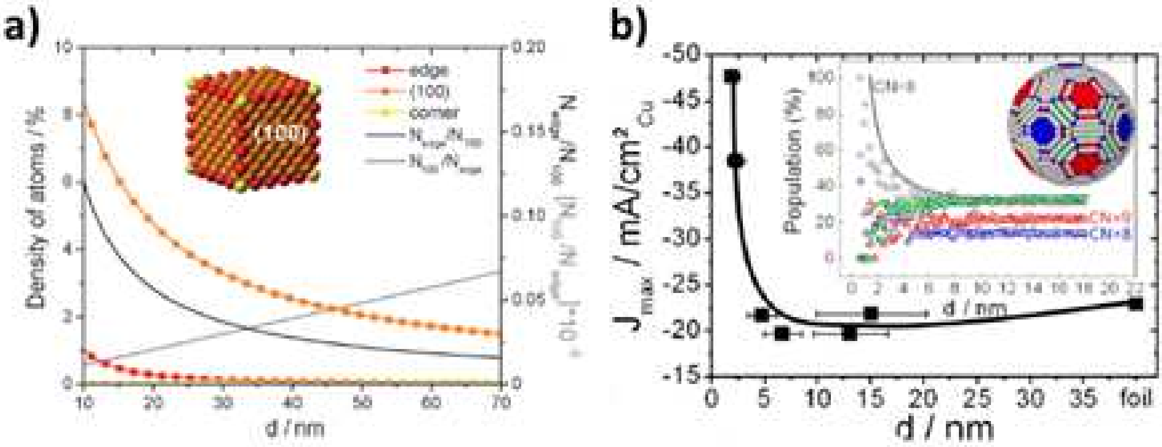

Figure 58: a) Density of adsorption sites in Cu NC cubes (left) and trend of N_{edge}/N_{100} versus nanocube edge length. From reference (Buonsanti et al. 2016); b) Particle size effect during catalytic CO_2 electroreduction. In the inset, ball model of a 6.9 nm Cu NP and the population of surface atoms with specific coordination number as function of particles' dimension. From reference (Strasser et al. 2014)

Although ethylene is the main multi-carbon product on Cu surfaces under CO_2RR conditions, several efforts has been made to boost other C_{2+} products like ethane, ethanol or n-propanol, to cite the most studied. Given that Cu(100) facet exhibits the lowest potential for *CO dimerization and thus for C-C bonding, further single crystal studies have been performed on the subject. Even if the molecular pathways for such products is still unclear, stepped (100) and (110) terraces resulted the most selective surface towards C_{2+} oxygenates [178,184].

Noticeably, altering the retention time of reactants and intermediates within the catalyst structure has also been reported to increase selectivity towards multi-carbon products. For example, the hierarchical Cu nanofoams synthesized and tested by Palmore et al. [211], produced detectable amounts of ethane and propylene (FE ranging from 0.2 to 1.5% for potentials down to -1.8 V vs Ag/AgCl) together with H_2, CO, $HCOO^-$, CH_4 and C_2H_4. Generation of unexpected C_3 products was attributed to the gradient of pores' diameter in the foam which increases retention time of intermediates, thus allowing further electron transfers and C-C bonding [211].

Other examples of highly porous 3D Cu structures were reported by Mul et al. and Jiao et al. [212,213]. The latter registered a FE ≈ 62% towards C_{2+} products in an electrolyzer operating at -0.67 V vs RHE, delivering an impressive current of *ca*. 653 mA cm^{-2}. Specifically, the detected multi-carbon products were ethylene, ethanol, and n-propanol, with FE of 38.6%, 16.6% and 4.5%, respectively. The authors demonstrated that C_{2+} products generation was boosted by the application of high overpotentials (less negative potentials favored HER and CO generation) and correlated the rate of C-C coupling to the basic pH at the catalyst's surface. Indeed, when operating at such high current densities, OH^- generation due to the high initial rate of HER and PTs causes a significant increase of the pH at the catalyst's surface, suppressing further HER and CPET to CH_4 while favoring pH-independent *CO dimerization to C_{2+} products.

Apart from 3D Cu-based structures, which are intrinsically "self-standing", active phase/support interaction can be exploited to boost Cu NPs activity and selectivity towards specific products, as well as to alter intermediates' retention time on the catalyst surface [178,184,202,203]. In modern catalysis, supports with high surface area and a proper degree of functionalization are used to disperse and stabilize NPs against aggregation under reaction conditions [178]. In electrocatalysis, another compulsory feature of the support is conductivity. Possessing all these requisites, carbon-based materials find large application in the field, in the form of carbon black, nanotubes, nanofibers and graphene to cite the most common. However, support must not be considered as an inactive beholder in the catalytic process: indeed, understanding active phase/support cooperation in reactants' adsorption, electron transfer and intermediates' stabilization is fundamental to design performing catalysts.

For example, it has been reported that, thanks to an optimal dispersion and consequently larger electrochemically active surface area, 25 nm Cu NPs on single-wall carbon nanotubes resulted way more selective towards C_2H_4 at -2.2 V vs Ag/AgCl than electrodeposited Cu films (FE ≈ 41% vs. ≈ 19%) [202].

The importance of support effects was evidenced even by Sun et al. when studying the catalytic activity and selectivity of 7 nm Cu NPs deposited on conventional carbon black and on N-doped graphene [214]. When supported on conventional carbon black, Cu NPs yielded a modest C_2H_4 FE of *ca*. 6.3% at -1.1 V vs RHE while when supported on N-doped graphene FE towards hydrocarbons spiked to 79% for the same applied potential. The authors attributed this improvement to the active phase/support cooperation. Indeed, N moieties of doped graphene tightly anchor Cu NPs and contemporary, as Lewis basic sites, act as reservoir of CO_2 and *H species that can then spillover to CO_2RR active sites, facilitating the overall process.

An outstanding performance was delivered by Cu NPs supported on N-doped carbon nanospikes, which converted CO_2 into ethanol with a remarkable FE of *ca*. 63% at -1.2 V vs RHE [215]. Although mechanisms of ethanol formation on such a complex surface cannot easily be guessed, DFT calculation confirmed the synergistic interaction between support and Cu NPs. In particular, the authors reported that the C atoms adjacent to N moieties exhibited a partial positive charge, providing an adsorption site for intermediates and thus preventing further reduction to CH_4 and/or C_2H_4..

To conclude, Cu-based electrocatalysts are the only metal-based materials able to catalyze CO_2 reduction to higher order hydrocarbons/oxygenates such as methane, ethylene and ethanol among others. The generation of these high added-value products is strongly influenced by structure, size and shape of Cu NPs as well as by support effects. Even though the mechanisms of generation of hydrocarbons and oxygenates are not clear to date, the consistent number of systematic studies and DFT simulations reported in literature outline various pathways for the design of efficient and selective Cu-based catalysts.

4.1.4.2 *Carbon-based metal-free electrocatalysts*

As previously discussed in paragraph 4.1.2.2, carbon-based metal-free electrocatalysts present potential advantages over the classic metal-based catalysts, resumable in relative cheapness, large availability of compositional elements and operative stability. The success of heteroatom-doped carbon structures in another electrocatalytic reduction of interest like ORR paved the way to the application of the same materials to CO_2RR, with N-doped carbon structures being the most studied to date.

Whether the determination of CO_2RR active sites on N-doped carbon structures is still a matter of debate, previous ORR-related studies suggest that the catalytic activity of these materials arise from the charge-transfer effects induced by the heteroatom [193,216]. So, N atoms percentage content and lattice position in the catalyst determine activity and selectivity. Figure 59 illustrates the four different N-sites that are generally identified in N-doped carbon structures [217]. Total N content and relative sites percentages can be tuned by controlling the doping during the synthetic step [192].

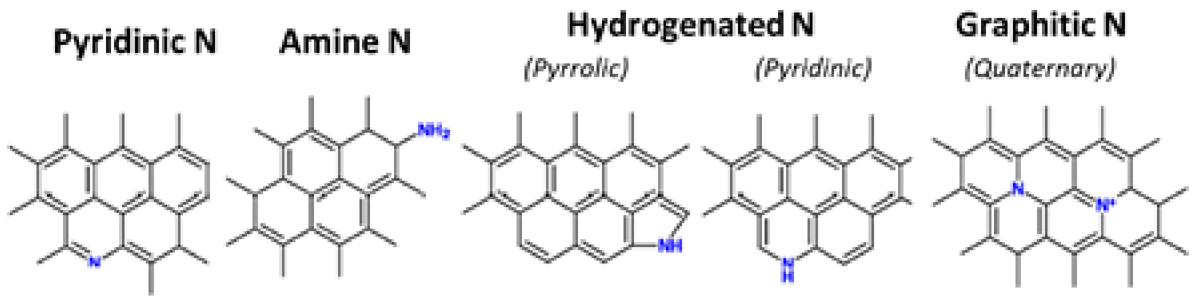

Figure 59: Schematic representation of the variety of N-sites commonly detected in N-doped carbon-based structures. From reference (Atanassov et al. 2018).

Several studies demonstrated that the incorporation of N-moieties in porous carbon structure remarkably enhanced the adsorption/absorption of acidic gases [218,219]. A detailed study conducted by Lu et al. [220] reported for a N-doped carbon monolith a maximum CO_2 capture of *ca*. 3.13 $mmol_{CO2}$ g^{-1} at ambient temperature and pressure. Adsorption and desorption tests were performed, demonstrating the almost complete reversibility of the process. Authors also confirmed the dependence of CO_2 capture performance from samples' N wt.% content and surface area, although without specifying the influence of N-sites distribution.

Enhanced CO_2 adsorption properties are for sure beneficial in the view of the application of this class of materials in CO_2RR, ensuring an increased CO_2 concentration at the catalyst's surface.

To discriminate between adsorption/absorption phenomena and shed light on the geometry of CO_2 adsorption onto N-moieties, Harada et al. [221] extensively studied CO_2 coordination on the surface of N-doped highly oriented pyrolytic graphite (N-HOPG). Collecting O 1s XPS spectra under CO_2-rich atmosphere, the authors observed a CO_2 binding energy on N-HOPG (533 keV) in the range of chemisorption. According to the Walsh diagram of CO_2 (Figure 60), the authors proposed that adsorbed CO_2 was stabilized onto N-HOPG surface in bended configuration. Indeed, $2\pi_u$ LUMO splits into $6a_1$ (parallel to CO_2 plane) and $2b_1$ (orthogonal to CO_2 plane) orbitals upon CO_2 bending. Thus, charge-transfer from the substrate to the low-energy $6a_1$ orbital should result in bended CO_2 stabilization on the surface. However, further XAS and IR adsorption analyses confuted the conclusions drawn from XPS, suggesting CO_2 to be lying flat on N-HOPG surface.

CO_2 is then confirmed to be chemisorbed on N-moieties of N-doped carbon structures. Anyway, the adsorption phenomenon does not imply the bending of the molecule, thus no lowering of the $CO_2 \rightarrow *CO_2^{\bullet-}$ overpotential is foreseen.

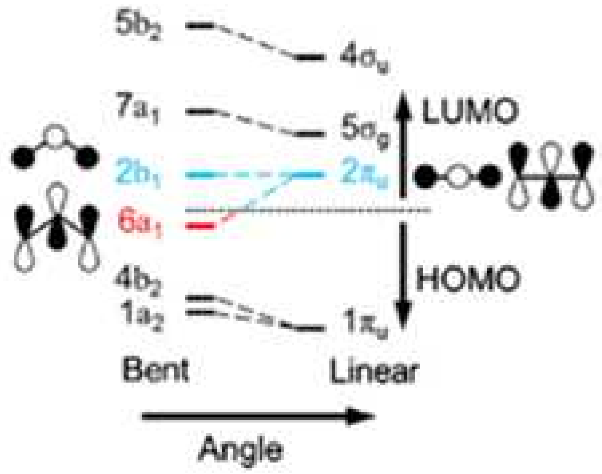

Figure 60: Walsh diagram for CO_2. From reference (Harada et al. 2016)

Although N-moieties have been attested as CO_2 adsorption sites, the identification of the active sites for CO_2RR on N-doped carbon is not trivial.

Regarding C_1 products, Ozin et al. [222] obtained an outstanding 81% FE towards $HCOO^-$ using a N-doped nanoporous carbon/carbon nanotubes. The improvement of catalytic activity and selectivity in respect with unsupported N-doped nanoporous carbon was attributed by the authors to the 4x higher content in pyridinic N-moieties in the former. Nonetheless, DFT calculations did not indicate pyridinic N-moieties as the CO_2RR active sites but rather the adjacent carbon atoms. The proposed mechanism is reported in Figure 61a and vaguely resembles those schemed in Figure 54b. Indeed, it suggests CO_2 chemisorption to occur by interaction of one of its O atoms (δ^-) with a basic carbon (δ^+).

On the other hand, Zhou et al. [223] correlated the different catalytic activity and selectivity towards CO of several N-doped carbon nanotubes arrays to the content of both pyridinic and graphitic N-sites. No identification of the actual CO_2RR active sites was claimed.

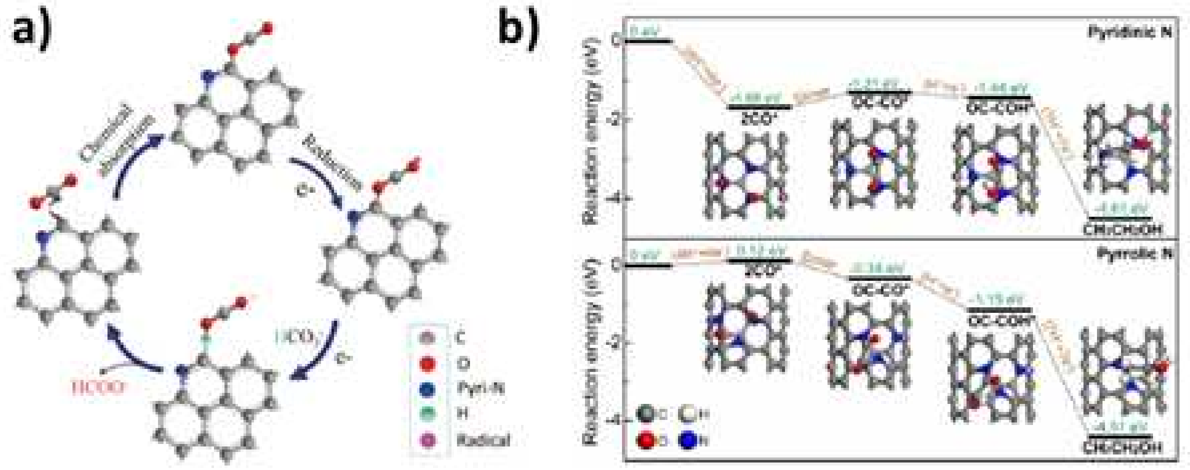

Figure 61: a) Proposed mechanism of CO_2 electrocatalytic reduction to $HCOO^-$ on N-doped nanoporous carbon/carbon nanotubes. From reference (Ozin et al. 2017); b) Calculated energy diagrams for the electrocatalytic reduction of CO_2 to ethanol on pyridinic and pyrrolic N moieties. From reference (Sun et al. 2017).

Determination of reaction mechanisms and identification of CO_2RR active sites is further hindered in the case of multiple electron transfer towards C_{2+} products. Recently, Ajayan et al. [224] reported optimized N-doped quantum dots able to reach a total 90% conversion of CO_2 at -0.75 V vs RHE. Apart from CO (FE ≈ 20%), the major products detected under this potential were C_2H_4 (FE ≈ 31%) and ethanol (FE ≈ 16%). Even in this case, the authors indicated pyridinic N-moieties as active sites for CO_2RR. The boosted C_{2+} selectivity was imputed to the higher number of pyridinic N edge-sites that can be obtained by doping 0-dimensional allotropes like quantum dots.

Among high added-value C_2 products, selective CO_2 conversion to ethanol on mesoporous N-doped carbon with highly order cylindrical structure have been reported by Sun et al. [225]. The catalyst completely suppressed CO generation, yielding only ethanol (FE ≈ 77% at -0.56 V vs RHE) and H_2 as by-product. DFT calculations were performed by the authors, disclosing that C atoms and quaternary (graphitic) N-sites present unfavorable reaction energies towards the first ET ($CO_2 \rightarrow {}^*CO_2^{\bullet-}$). CO_2 reduction should instead take place on pyridinic and/or pyrrolic N sites, with the former presenting a way lower reaction energy (-1.68 eV vs. -0.12 eV). Then, *CO dimerization and further CPET to ethanol were all calculated to be downhill reactions. Pathways of CO_2 reduction to ethanol on both sites are reported in Figure 61b; the higher activity of pyridinic N moieties (due to the higher electron-richness of the site) can be easily guessed from the diagram obtained by the Bader analysis. *CO stabilization by a regular mesoporous surface with high electron density was claimed by the authors to favor C-C coupling, thus completely suppressing C_1 products generation.

To an even greater extent than for Cu-based electrocatalysts, the comprehension of CO_2RR mechanisms on N-doped carbon structures is far from being achieved. However, the origin of N-doped carbon materials activity can be surely addressed to N-moieties and specifically to pyridinic N-sites. Although we are still at the beginning of the exploitation of carbon-based metal-free catalysts in CO_2RR, the results already achieved include this class of materials among the most promising for the selective CO_2 reduction to valuable C_{2+} compounds.

4.1.4.3 HAP as dopant in electrocatalytic CO_2RR

Doping of catalytic materials is a well-established and widespread procedure to improve catalytic performances by boosting of the adsorption/activation of reagents, stabilization of reaction intermediates or simply by modification of the electronic properties of the active phase. In the relatively immature field of CO_2RR processes, the use of dopants has not been properly investigated yet. Indeed, even the application of active supports, specifically designed to assist the reaction pathway, is of quite recent exploration for this technology.

As presented in paragraph 1.2.2.3, the highly functionalized and amphoteric HAP surface shows a particular affinity towards CO_2. Among all the possible interactions of CO_2 with surface basic and acid sites of HAP, adsorption on O^{2-} Lewis basic surface groups is surely the most intriguing in the view of HAP application as dopant for CO_2RR electrocatalysts. Indeed, chemisorption of CO_2 on surface phosphate groups entail the bending of the molecule to form reversible $(PO_x)_s$-carbonates. As previously stated, literature agrees on the first ET ($CO_2 \rightarrow {}^*CO_2^{\bullet-}$, associated overpotential of *ca*. -1.9 vs NHE) to be the RDS of CO_2 electrocatalytic reaction on almost all surfaces [176,177,180]. Considering that the high overpotential allegedly derives from the breakage of CO_2 linearity and stabilization of the radical anion intermediate, doping with HAP could diminish the activation energy of CO_2 itself thus pushing CO_2RR onset to less cathodic potentials.

To date, only two articles regarding the implementation of HAP in CO_2RR have been published, both dealing with photocatalytic processes. To the best of our knowledge, no application of HAP in electrocatalytic CO_2RR has been reported to date.

In a recent work, Zhang et al. [62] studied Ti-F-doped HAP as photocatalyst for CO_2RR. After determining the optimal content of dopants (Ti/Ca atomic ratio ≈ 0.1, F ≈ 5.6 wt.%), the authors tested Ti-F-HAP under UV irradiation in the presence of CO_2, obtaining CO and CH_4 as main products. Besides the typical low throughputs of photocatalytic processes, it is noteworthy that control test on pristine TiO_2 and F-doped TiO_2 showed lower catalytic activity and no CH_4 generation. The authors attributed this behavior to the peculiar CO_2 adsorption/activation properties of HAP, but no evidence of such phenomena was reported.

HAP has been instead implemented as a dopant by Li et al. [63] on Pt/TiO_2 catalysts. The authors synthesized four catalyst with increasing amount of HAP and tested them in the photocatalytic CO_2RR (λ = 254 nm). All HAP-doped catalysts exhibited an increased CO_2RR activity (up to 40x for sample n°2, Figure 62a); moreover, the selectivity of the process shifted towards CH_4, reaching a maximum of *ca*. 95% (sample n°2 as well, Figure 62b). The volcano-type trends of activity and selectivity suggest that a precise content of HAP allows to achieve the best performances; however, the authors did not report a precise quantification of HAP onto catalysts' surface.

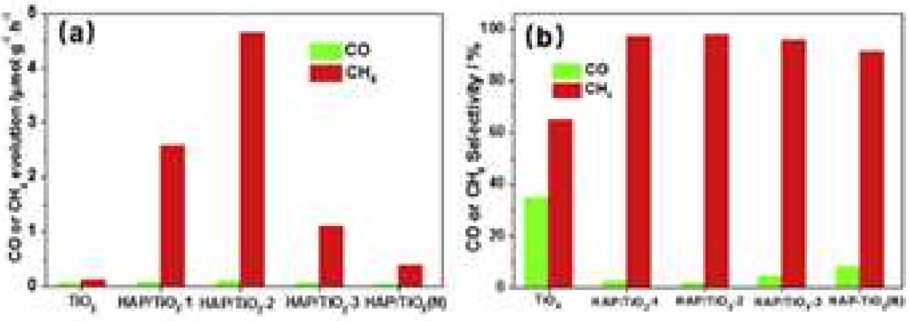

Figure 62: a) Average production rates and b) CO and CH_4 selectivity for Pt/TiO_2 and $Pt/HAP/TiO_2$ with variable HAP content. From reference (Li et al. 2018)

One of the reasons of the boosted catalytic activity of HAP-doped materials is surely the more efficient separation of photogenerated charges due to the insulating nature of HAP. However, HAP was even proved to take an active part in directing CO_2 reduction. By means of in-situ FT-IR spectroscopy it is indeed possible to detect the presence of hydrogenocarbonates (1255 cm^{-1}) and especially surface $(PO_x)_s$-carbonates (1385 cm^{-1}) [95], on the surface of Pt/HAP/TiO_2 catalyst (green line in Figure 63b). Both species generated upon adsorption of CO_2 onto the HAP moieties of the composite. Other peaks, at 3242 and 1640 cm^{-1}, are instead ascribable to HAP structural -OH groups and physisorbed water, respectively (Figure 63a and b) [95]. Practically no peaks were detected when monitoring the surface of undoped Pt/TiO_2 catalysts under the same conditions, highlighting the role of HAP doping in increasing both CO_2 and H_2O concentration on the catalyst's surface. Under light irradiation, the intensity of CO_2 and H_2O related peaks decreased steadily, indicating the participation of these surface-adsorbed species to the reduction process. At the same time, new peaks arose in the 3000-2800 cm^{-1} region. Such peaks could be attributed to symmetric and/or asymmetric stretching of alkyl C-H bonds or to a combination of C-O stretching and C-H bending modes. Both attributions support an adsorption/stabilization of alkyl-type intermediates probably on the HAP moieties of Pt/HAP/TiO_2. Stabilization of intermediates can then explain the selectivity towards CH_4 instead of CO.

On the basis of these evidences, the authors proposed the mechanism reported in Figure 63c for CH_4 formation. In the first step, CO_2 is adsorbed on HAP Lewis basic sites (phosphate groups' O^{2-}) to form $(PO_x)_s$-carbonates while H_2O coordinates to HAP Lewis acid sites (Ca^{2+} or OH^- vacancies). Then, under light irradiation, CO_2 is converted to the intermediate radical anion $*CO_2^{\bullet-}$ by ET while H_2O dissociates, generating Ca-OH and PO-H surface groups. Finally, the $*CO_2^{\bullet-}$ and a neighbor PO-H complete a CPET transfer to form a *COOH intermediate that is converted to CH_4 via consecutive CPETs.

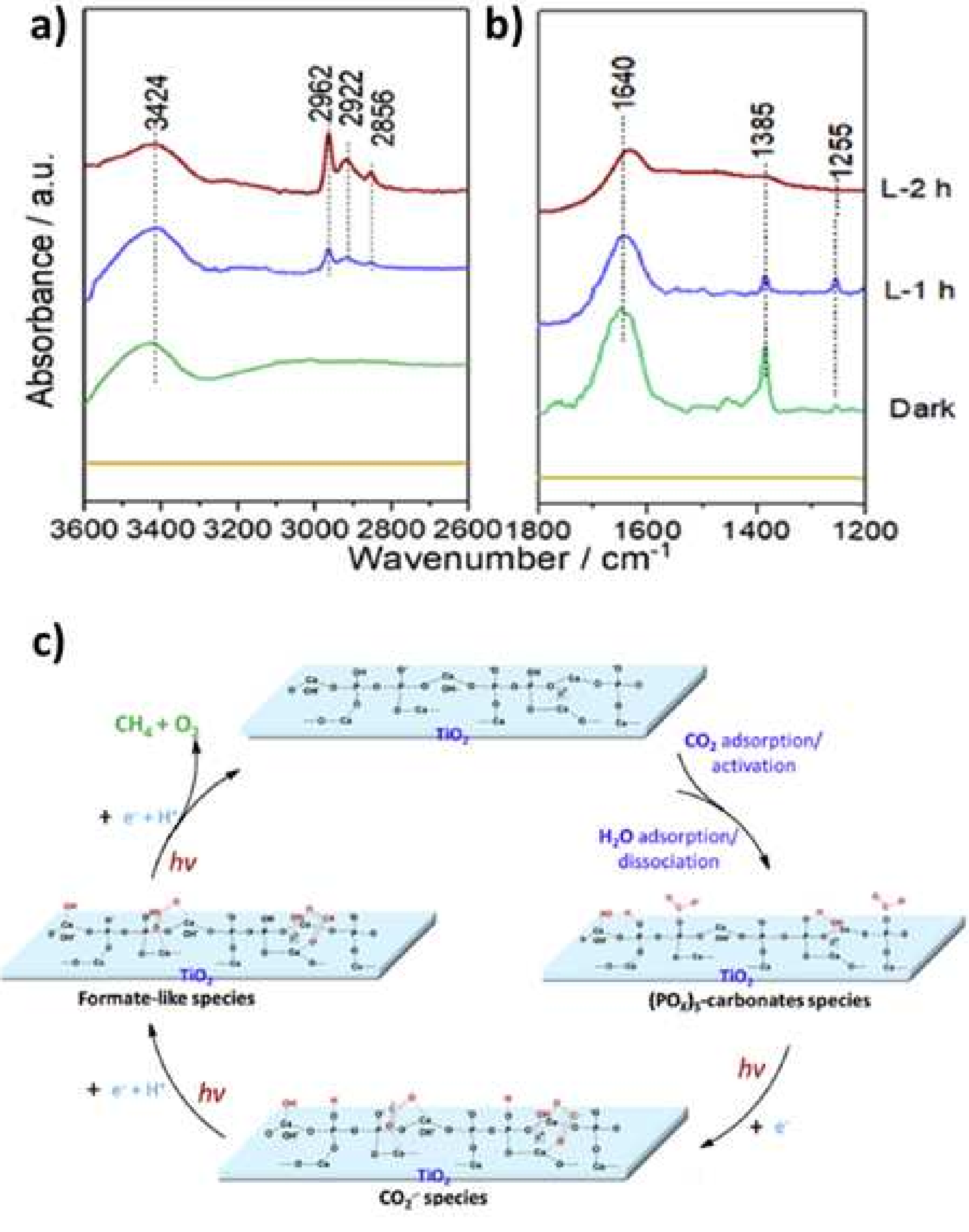

Figure 63: a, b) Monitoring of CO_2 and H_2O adsorption onto the surface of Pt/HAP/TiO_2 catalysts under dark (green line) and light irradiation (red and blue lines). c) Proposed mechanism of CH_4 generation from CO_2 reduction onto Pt/HAP/TiO_2 surface. From reference (Li et al. 2018)

In summary, HAP proved its ability to coordinate CO_2 molecules at its surface, thus boosting CO_2RR processes. Despite the different energetic input to CO_2 reduction, these premises lay the foundation for the application of HAP (as dopant) in electrocatalytic CO_2RR. However, differently from photocatalytic processes, HAP insulating nature could pose serious fulfillment problems to its implementation in electrochemical

CO_2RR. A thoughtful design of HAP-doped catalysts is then mandatory to maximize HAP-doping advantages over conductivity drawbacks.

4.1.5 Rational design of novel Cu+HAP/C electrocatalysts for CO_2RR

The state of art of electrocatalytic CO_2RR towards high order products evidences that hydrocarbons and C_{2+} oxygenates selectivity is driven by multiple factors on different materials. In absence of a clear mechanism of generation of these products, the nature of the catalytic motifs able to promote multiple ETs and C-C bonding remains unknown.

Based on experimental evidences and DFT calculations, Cu NPs with size > 15 nm seem to be the most promising metal-based catalyst for enhanced selectivity towards high added-value compounds. Regarding metal-free catalysts, best performances should be guaranteed by N-doped carbon structures with high surface area, controlled porosity, high conductivity and high N content (specifically in pyridinic N-sites). In addition, doping with materials exhibiting marked Lewis basicity could further enhance catalytic activities through CO_2 activation.

In the view of combining the unique features of Cu-based and N-doped carbons catalysts, commercial Cu NPs (Ø = 25 nm) were supported on three-dimensional N-doped graphene nanosheets (3D-GNS), synthesized by sacrificial support method [226]. The resulting Cu/3D-GNS should benefit from (*i*) optimal dispersion and stabilization of Cu NPs onto the carbonaceous support (*ii*) enhanced CO_2 adsorption capacity and (*iii*) partaking of both moieties of the composite (Cu and pyridinic N-sites) to the process. Moreover, thanks to the three-dimensional structure and controlled porosity of 3D-GNS, time of retention of reagents and intermediates is supposed to be increased, thus favoring multiple ETs and C-C bonding towards C_{2+} products.

Further doping with HAP will result in the final Cu+HAP/3D-GNS composite. A proper dispersion of HAP onto the surface of the catalyst will introduce numerous Lewis basic sites, complementary to those exhibited by 3D-GNS. Indeed, while N-moieties of the carbonaceous support adsorbs and convert CO_2, O^{2-} basic groups of HAP are supposed to exert the function of CO_2 reservoirs/activators by adsorption of CO_2 in bended configuration. In addition, HAP remarkable adsorption properties are expected to further increase intermediates' retention time on the catalyst surface, thus suppressing CO and $HCOO^-$ generation.

Synthesis, physical-chemical characterization and electrocatalytic performances of novel Cu+HAP/C are reported in the following sections.

4.2 Synthesis and characterization of HAP-doped electrocatalysts for CO_2RR

Cu+HAP/3D-GNS samples have been synthesized according to the procedure reported in the Experimental Section, paragraph 8.1.3. Briefly, 3D-GNS has been synthesized following the patented method known as Sacrificial Support Method (SSM) [226]. The obtained N-doped carbonaceous material has been employed as support for the metallic active phase (commercial Cu NPs, ø = 25 nm) and the dopant (HAP_RT, synthesized as reported in the Experimental Section, paragraph 8.1.2). Cu NPs and HAP immobilization onto 3D-GNS have been performed by a two-step procedure, exploiting the different pH_{PZC} of the individual components. Cu/3D-GNS has been obtained by mixing/stirring 3D-GNS and Cu NPs dispersions in IPA, adjusting the pH at *ca*. 10. Cu+HAP/3D-GNS has been instead synthesized by mixing/stirring Cu/3D-GNS and HAP_RT aqueous dispersions at neutral pH. This stepwise procedure has been developed in order to guarantee the maximum dispersion of both Cu NPs and HAP onto 3D-GNS. Moreover, such procedure prevents Cu NPs to be deposited onto HAP decorations, therefore avoiding the presence of electrochemically inactive Cu sites (i.e. electrically insulated) in the final Cu+HAP/3D-GNS electrocatalyst. Cu and HAP wt. % loadings (by design) were 20 and 10% respectively.

All synthetic details are reported at paragraph 8.1.3.

N_2 adsorption/desorption analyses (experimental details reported in the Experimental Section, paragraph 8.2.3) have been carried out on pristine 3D-GNS, Cu/3D-GNS and Cu+HAP/3D-GNS electrocatalysts. All adsorption/desorption isotherms, 2-parameter BET linearization and pore size distribution (according to N_2 – DFT model) are reported in the Supplementary Material (Figure 102, Figure 103 and Figure 104, respectively), while numerical data of surface area and pore volume are gathered in the following Table 27.

Table 27: Surface area and pore volume from N_2 adsorption/desorption analyses on pristine 3D-GNS and supported electrocatalysts

Sample	**Surface area**[a] *$m^2\ g^{-1}$*	**Pore volume**[b] *$cm^3\ g^{-1}$*
3D-GNS	209.17	0.214
Cu/3D-GNS	168.88	0.188
Cu+HAP/3D-GNS	190.74	0.187

[a] *Calculated by linear (2-parameters) BET equation;*

[b] *PSD calculated according to N_2 – DFT Model*

All isotherms presented in Figure 102 can be identified as type IV according to IUPAC classification, with a H2 hysteresis loop. It is worth noting that, differently from “pure” type IV isotherms, those registered on the present samples do not exhibit marked inflection over the low p/p^0 range. The typical “knee” that the adsorption branch of the isotherm displays at low p/p^0 values is generally associated with microporosity [113]. Therefore, all samples can be considered as strictly mesoporous materials, with null or at least negligible microporosity. The similarities between 3D-GNS, Cu/3D-GNS and Cu+HAP/3D-GNS isotherms indicate that neither the functionalization with Cu NPs nor the doping with HAP alter the mesoporous nature of pristine 3D-GNS.

Surface area, calculated applying linear (2-parameters) BET model equation (Figure 103), are in the range of 200 $m^2\ g^{-1}$. Numerical data gathered in Table 27 indicate that the functionalization of 3D-GNS with Cu NPs leads to a substantial decrease of surface area (*ca*. 20%) while further doping with HAP results in slight increment of the latter, although always being lower than the pristine 3D-GNS one. Conversely, pore volume is equal for Cu/3D-GNS and Cu+HAP/3D-GNS, exhibiting a *ca*. 12% decrease when compared to pristine 3D-GNS. As for adsorption/desorption isotherms, pore size distribution (calculated according to N_2 – DFT model, Figure 104) are similar for all three samples, assessing that neither the porosity of pristine 3D-

GNS is altered by functionalization/doping. Mesopores distribution of all sample exhibits peaks at *ca*. 10 and 25 nm in pore width, consistently with the mean diameter of the silicon-based templates used in the synthetic route [226].

Overall, the decrease in pore volume after Cu functionalization (maintained even after the doping with HAP) could be caused by the Cu NPs themselves, their diameter being sufficient to clog some of the pores of the support. This phenomenon could even rationalize the marked decrease of surface area noticed after Cu functionalization. On the other hand, decoration with HAP may be the responsible for the increased surface are of Cu+HAP/3D-GNS samples, despite part of the former 3D-GNS porosity remains hindered.

Further investigation of structure and morphology of the samples has been carried out by means of STEM imaging, coupled with an EDX probe for elemental mapping. Experimental details are reported in the dedicated section, paragraph 8.2.3.

STEM images of pristine 3D-GNS are gathered in Figure 64. 3D-GNS exhibit the expected flake-shaped three-dimensional morphology [226]. The material is characterized by the presence of an extended network of porous channels (mainly with mesoporous nature), introduced upon HF etching of the silicon-based templating agent [227]. The numerous defects and the enhanced porosity impart to 3D-GNS high surface area (as previously disclosed by N_2 adsorption/desorption analyses) while favoring mass diffusion and transfer phenomena [228].

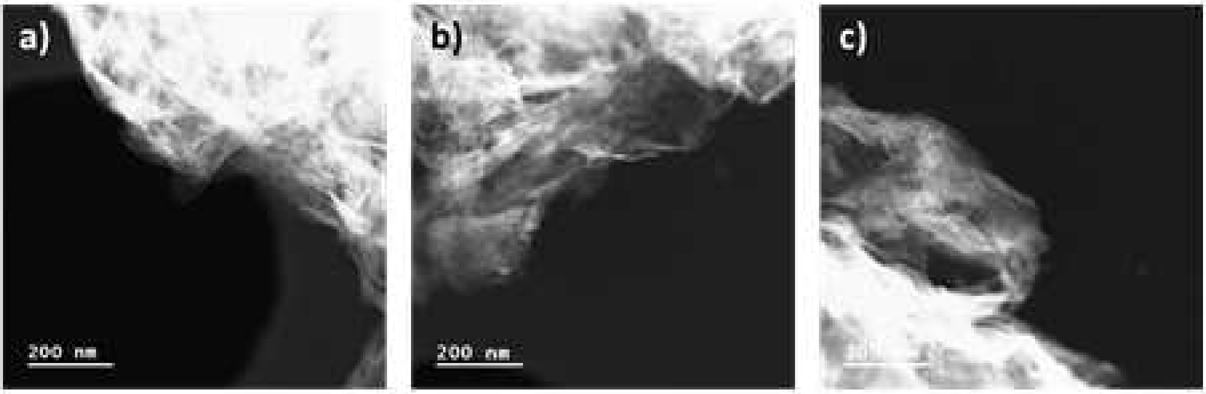

Figure 64: STEM images of pristine 3D-GNS.

Cu/3D-GNS and Cu+HAP/3D-GNS samples have been characterized as well. STEM images, together with EDX elemental maps, are reported in Figure 65 and Figure 66.

In Cu/3D-GNS the support structure is still visible. The brighter contrast of the material in respect with pristine 3D-GNS suggests a homogenous dispersion of the metallic nanoparticles throughout the whole support area (Figure 65a and b), despite both Cu aggregates (Figure 65c) and Cu-free zones can be spotted on the sampel. EDX elemental mapping (Figure 65d) confirms an overall acceptable dispersion of Cu NPs onto 3D-GNS has been achieved. Although oxygen is a known constituent of 3D-GNS (with an atomic wt.% of *ca.* 2.7, [217]), its EDX map resembles the copper one more than that of carbon. Converting 2D elemental maps in counts versus spatial coordinate surface plots, the pairing of Cu with O can be roughly assessed (Figure 105b in the Supporting Material). From a qualitative point of view, subtractions between elemental EDX maps indicate that Cu and O are present in higher amount in the same zones of Cu/3D-GNS (Figure 106, Supporting Material). Such results suggest that immobilized Cu NPs could be coated with cuprous and/or cupric oxide (Cu_2O and/or CuO, respectively). The tendency of Cu^0 nanoparticles to rapidly grow surface oxides has been indeed extensively observed in literature and assessed to be thermodynamically favored [188]. Apart from this first rough and qualitative evaluation, a proper insight on copper chemical neighbor and oxidation state will be provided by XPS measures, discussed hereafter in the present paragraph.

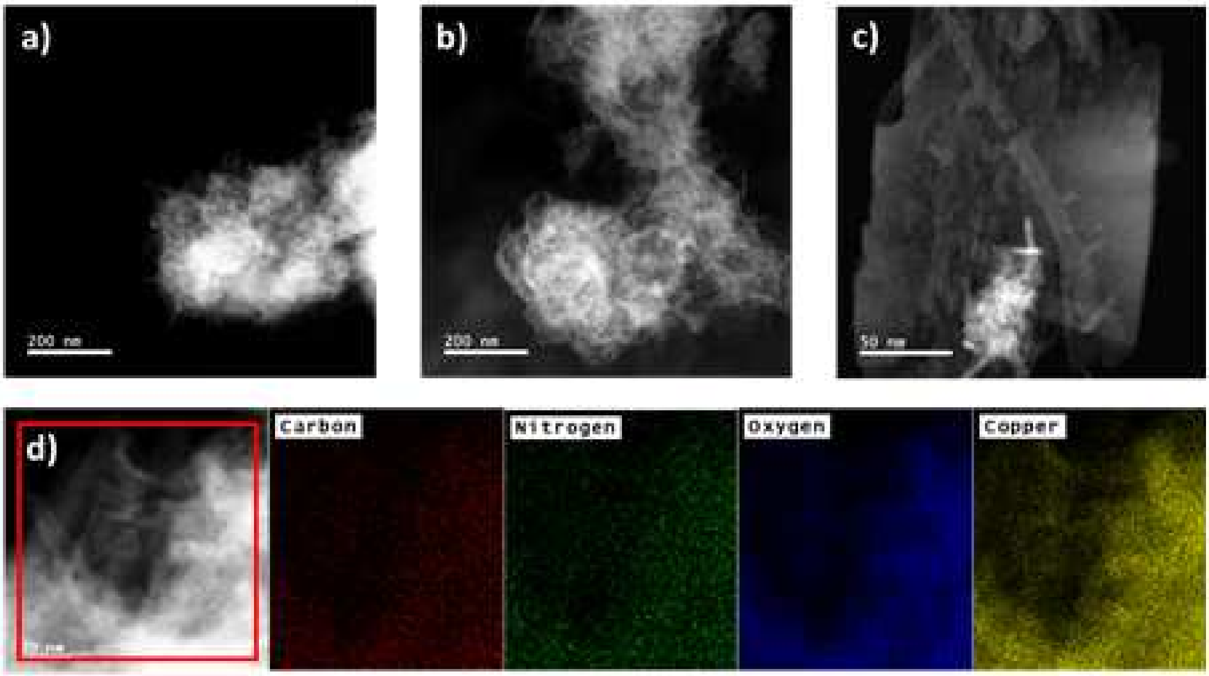

Figure 65: a → c) STEM images of Cu/3D-GNS samples and d) related elemental EDX mapping

Same considerations made for Cu/3D-GNS structure apply to Cu+HAP/3D-GNS, in which slightly aggregation phenomena of Cu NPs can likewise be spotted when surveying the material (see brighter zones in Figure 66a and b). However, EDX mapping (Figure 66d) indicate an overall satisfying dispersion of both active phase and dopant on 3D-GNS surface. In this case, oxygen map pairs principally with phosphorous, as expected from the elemental composition of HAP (containing P in the form of PO_4^{3-} groups); visual confirmation can be obtained (always from a qualitative point of view) comparing elemental surface plots of Ca, P and O (Figure 107b in Supporting Material). On the other hand, copper map does not match with any one of HAP constitutive elements (Ca, P and O). From the rough estimation performed as for Cu/3D-GNS by EDX maps subtraction (Figure 108), Cu pairing results quite unlikely (especially considering phosphorus chemistry) while pairing with O (i.e. presence of Cu(I) or Cu(II) oxides on the surface of/together with Cu^0 NPs) cannot be ruled out.

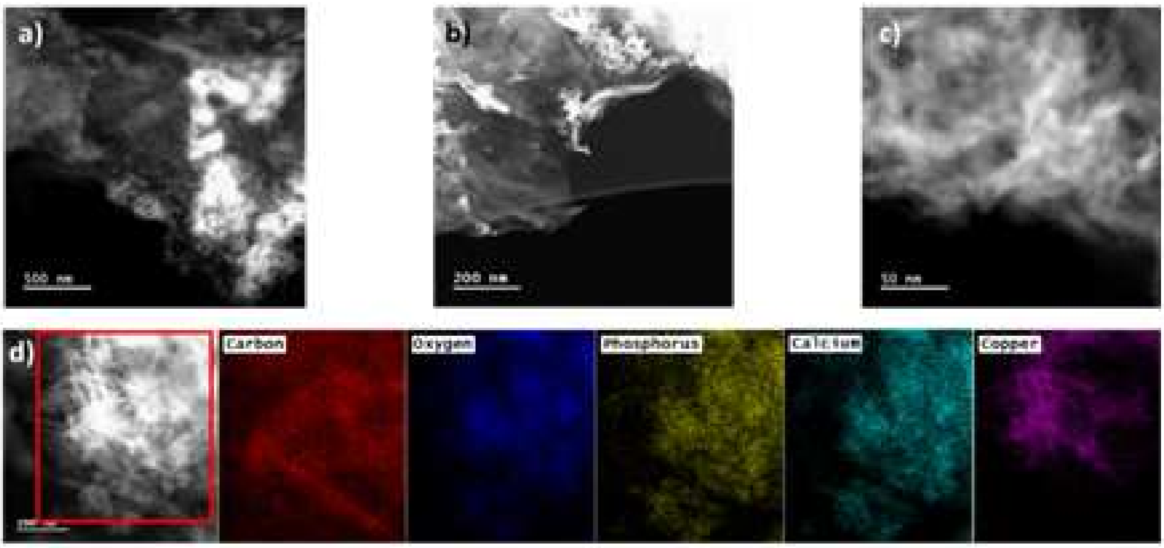

Figure 66: a → c) STEM images of Cu+HAP/3D-GNS samples and d) related elemental EDX mapping

XPS spectra have been collected on the pristine 3D-GNS support and on both doped and undoped electrocatalysts. XPS surveys are reported in Figure 67; the quantitative elemental analysis results are reported in the associated Table 28.

3D-GNS survey (Figure 67a) displays the typical contributions of the constitutive elements of the support, namely carbon (C 1s, *ca*. 285 eV), oxygen (O 1s, *ca*. 533 eV) and nitrogen (N 1s, *ca*. 400 eV). In Cu/3D-GNS spectrum (Figure 67b), a further contribution appears in the region between *ca*. 930 and *ca*. 960 eV (Cu $2p_{3/2}$ and Cu $2p_{1/2}$), addressable to the presence of Cu NPs; consistently, other Cu-related peaks can be assigned (Cu 3s at *ca*. 125 eV and Cu 3p at *ca*. 80 eV). Finally, Cu+HAP/3D-GNS spectrum (Figure 67c) displays the expected Ca (Ca 2p at *ca*. 350 eV and Ca 2s at *ca*. 440 eV) and P (P 2p at *ca*. 140 eV and P 2s at *ca*. 195 eV) contributions in addition to the previously discussed signals.

The quantification of constitutive elements of 3D-GNS, performed by integration of the XPS signals, gives back results which are consistent with literature [217]. Indeed, a slight amount of oxygen can be found at the 3D-GNS surface (possibly a residue of imperfect GO reduction, see 3D-GNS synthesis in the Experimental Section, paragraph 8.1.3) while N-doping results in the presence of *ca*. 1.25 at.% of nitrogen.

Upon immobilization of the active phase, the at.% of XPS probed N-moieties is maintained, indicating that Cu NPs do not agglomerate massively onto such functional groups, thus blocking them. In addition, the increased O 1s at.% in comparison with pristine 3D-GNS suggest that Cu is present in Cu/3D-GNS as oxide and/or hydroxide, consistently with previous STEM/EDX observations. However, Cu at.% assessed by XPS is *ca*. one order of magnitude lower than the expected value (Cu loading in Cu/3D-GNS = 20 wt.%, which is ≈ 4 at.%). Since only a slight Cu NPs aggregation could be assessed by STEM (Figure 65) and considering that TEM/EDX mapping disclosed relatively wide zones where Cu is homogeneously dispersed in Cu/3D-GNS samples, these results could be addressed to (*i*) the combination of 3D-GNS large surface area and moderate Cu loading, which could result in a homogenous Cu dispersion without actually covering the whole support surface and (*ii*) the fact that XPS, as a surface technique, yields an at.% quantification which may not be relatable to the volume ratio of the samples' constitutive elements, especially for composite materials.

For doped Cu+HAP/3D-GNS catalysts, the at.% of Ca and P are instead adherent to the effective HAP wt.% loading and the same applies to the increase in O 1s at.%. This result indicates an optimal dispersion of the dopant, corroborating prior EDX mapping (Figure 66). Moreover, the atomic Ca/P ratio obtained is *ca*. 1.62, confirming that the stoichiometry of HAP has been retained. Interestingly, the nitrogen content is halved in respect with bare support and undoped Cu/3D-GNS, suggesting that HAP doping physically covers 3D-GNS N-moieties, possibly compromising their reactivity.

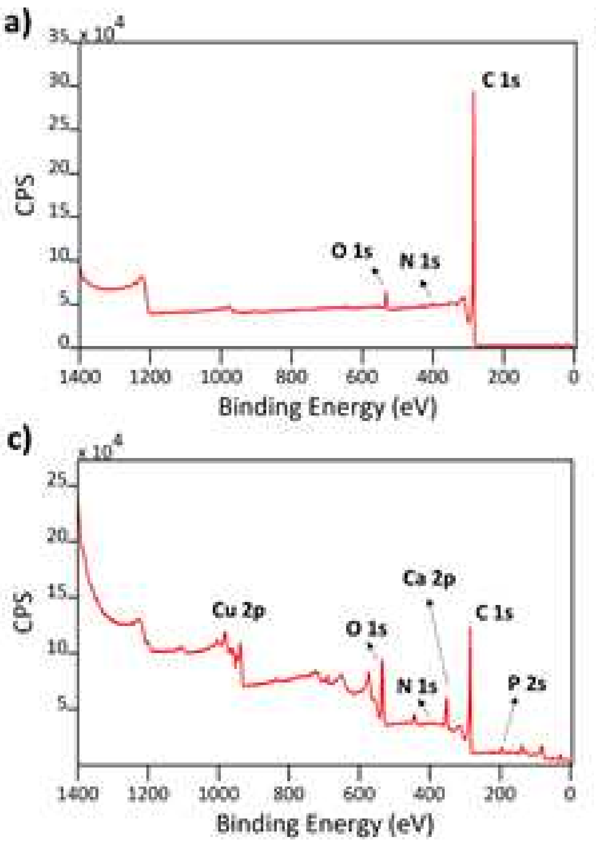

Figure 67: XPS survey spectra of a) 3D-GNS, b) Cu/3D-GNS and c) Cu+HAP/3D-GNS. For the sake of clarity, only XPS contributions used for the elemental quantification (Table 28) are indexed in the figure; other contributions of the samples' constitutive elements are addressed in the main text.

Table 28: XPS elemental quantification of samples' components.

Sample	**Elemental composition (*at.%)***					
	C 1s	O 1s	N 1s	Cu 2p	Ca 2p	P 2s[a]
3D-GNS	95.97	2.98	1.25	-	-	-
Cu/3D-GNS	92.71	5.81	1.21	0.27	-	-
Cu+HAP/3D-GNS	75.20	13.52	0.57	0.27	6.46	3.99

[a] P quantification was performed on P 2s peak and not on P 2p one as to avoid integration errors caused by the overlapping of P2p and Cu 3s contributions.

High resolution XPS spectra of C 1s, O 1s, N 1s, Cu 2p, Ca 2p and P 2s regions have been collected on the samples depending on their composition. N 1s and C 1s HR spectra of pristine 3D-GNS, which are representative for all materials, are reported in Figure 68, while other ones can be found in the Supporting Material (Figure 109 and Figure 110).

The nature of N-moieties has been further investigated by means of peak deconvolution (Figure 68a) following a method previously reported in literature and specifically optimized for these materials [217]. The related numerical data are reported in Table 29.

From literature, it is known that nitrogen may be present within graphitic carbon structures in the form of different chemical group (Figure 59), which relative abundance can be assessed by XPS. Performing a deconvolution of the nitrogen signal according to the 70% Gaussian/30% Lorentzian peak fitting technique, the presence of six main types of nitrogen moieties in 3D-GNS have been assessed, which relative abundance has been calculated and reported in Table 29. Both pristine 3D-GNS and functionalized/doped electrocatalysts showed a major presence of pyridinic N moieties (N-pyr), addressed by literature as CO_2RR active [222–224], together with amine, pyrrolic, graphitic, NH-bulk and NO moieties.

Peak deconvolution and assignment of specific contributions have been performed in the C 1s region as well (Figure 68b and Table 29), always following an established procedure [217,229].

The results of the deconvolution, even in this case performed according to the 70% Gaussian/30% Lorentzian peak fitting technique, revealed the primary presence of sp2 carbon species (graphitic C) in concomitance with sp^3 species (sp^3 C). C-N and C_x-O_y account for the remaining *ca.* 30 at.% of carbon species.

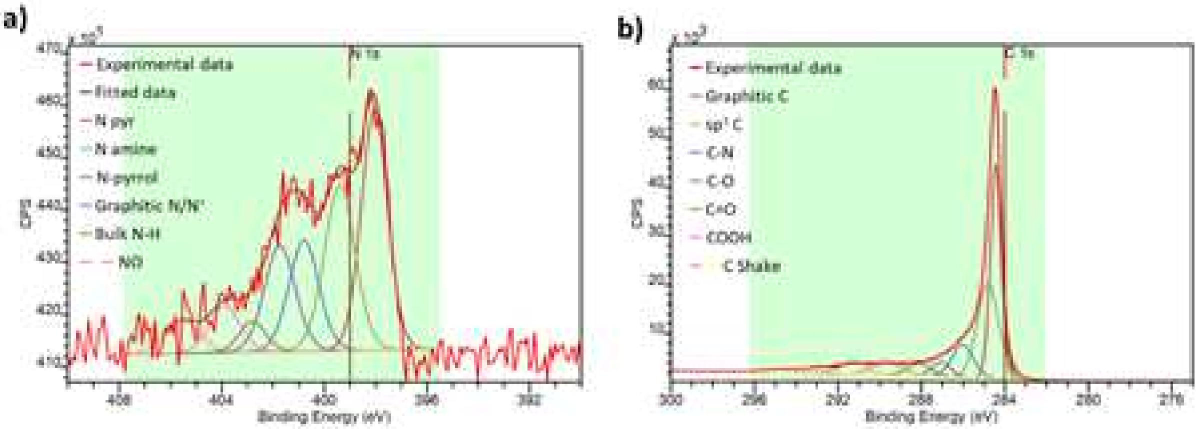

Figure 68: HR XPS spectra of a) N 1s and b) C 1s regions, collected on the pristine 3D-GNS support.

Table 29: Contribution of different N-moieties and different C bonding obtained from deconvolution of the HR N 1s and C 1s spectra reported in Figure 68.

	Contributions from HR spectra deconvolution (*at.%*)						
	N pyr	*N amine*	*N-pyrrol*	*Graphitic N/N⁺*	*Bulk NH*	*NO*	
N 1s	31.21	23.15	16.33	13.47	5.85	10.02	
	(398.0 eV)	*(399.4 eV)*	*(400.8 eV)*	*(401.7 eV)*	*(402.8 eV)*	*(403.9 - 405.5 eV)*	
	Graphitic C	*sp^3 C*	*C-N*	*C-O*	*C=O*	*COOH*	*C Shake*
C 1s	35.72	31.98	10.45	5.43	4.28	5.47	6.69
	(284.4 eV)	*(284.8 eV)*	*(286.0 eV)*	*(287.0 eV)*	*(288.1 eV)*	*(289.6 eV)*	*(291.3 – 293.0 eV)*

The HR spectrum of Cu 2p (Supporting Material, Figure 110) has not been deconvolved for two main reasons: first, the scarce intensity of the signal (resulting from the low Cu at.%), which do not allow for reliable interpretation, and secondly because any result would not be representative of the actual electrocatalysts' surface under reaction conditions. Indeed, under the application of the operative cathodic potential required for CO_2RR, any copper species detectable by ex-situ XPS would likely reduce to Cu^0, which is universally acknowledged to be the electrocatalytically active phase for CO_2 reduction.

Although no deconvolution was performed, the peaks pattern disclosed by the Cu 2p HR spectrum is consistent with the reference CuO one [230], exhibiting the typical Cu $2p_{3/2}$ and Cu $2p_{1/2}$ peaks with a *ca.* 20 eV spacing (934.5 eV and 954.5 eV, respectively) and the correlated Cu^{2+} satellite peaks at *ca.* 944.1 and 963.8 eV. Interestingly, the spectrum obtained from doped Cu+HAP/3D-GNS (Figure 110b) slightly differs from that collected on the undoped electrocatalysts (Figure 110a). At this point of the study, it cannot be stated if the differences are caused by a shift in the binding energy of CuO contributions due to support insulation (caused by HAP presence) or if such peaks are instead associated with a new phase/compound formed upon HAP doping that has not been identified, with 934.5 eV peak of CuO being still present as shoulder of the novel 938.7 eV one.

In summary, the structural/morphological characterizations depict both doped and undoped electrocatalysts as high surface area, mesoporous materials, with a pronounced pore volume which is foreseen to ensure optimal mass transport of the reactants under reaction conditions, therefore minimizing diffusional issues. The results of n-doped 3D-GNS characterizations are in general agreement with what reported in literature and patents on this material. The overall successful dispersion of both active phase (Cu NPs) and dopant (HAP) in doped and undoped samples guarantees the close contact of the two phases, as desired from design. Under ex-situ conditions, Cu NPs were assessed to effectively be CuO, while upon HAP doping the creation of a novel Cu-based phase cannot be ruled out.

4.3 Electrochemical CO_2RR: performances of HAP-doped and undoped electrocatalysts

Undoped Cu/3D-GNS and doped Cu+HAP/3D-GNS electrocatalysts performance in electrochemical CO_2RR have been tested in a lab-scale electrolyzer (namely, an electrochemical flow-cell). All the experimental details are reported in the Experimental Section, paragraph 8.5.

Briefly, inks of the catalysts have been prepared dispersing the related powders in IPA and Nafion by ultrasonication. The resulting suspensions have been sprayed onto a gas diffusion layer (Sigracet BC29), thus obtaining a gas diffusion electrode (GDE, details reported in paragraph 8.5.1.1, Experimental Section). Electrocatalysts' GDE served as cathode in the electrochemical flow-cell, with a Pt GDE serving as anode and an Ag/AgCl electrode acting as reference; a scheme of the electrochemical cell used and of the overall electrochemical setup can be found in Figure 77a and b, Supporting Material. The electrolyte was an aqueous 0.5 M $KHCO_3$ solution ($pH \approx 8.1$).

Electrochemical tests, aimed to assessing the electrocatalytic activity of each catalyst, are listed in Table 31, Supporting Material. Briefly, cathodes have been conditioned by means of consecutive voltammetric cycles (CV) under inert atmosphere (flowing N_2). The overall system resistance has been evaluated by means of potentiostatic electrochemical impedance spectroscopy (PEIS) and further used to correct all applied potentials, as described in paragraph 8.5.1.2, Experimental Section. Linear sweep voltammetry (LSV) under both inert (flowing N_2) and reactive (flowing CO_2) atmosphere have been run to extrapolate CO_2RR onset potentials (E_{Onset}) and to evaluate the effect of CO_2 presence/absence on delivered current. Finally, 30-minutes long chronoamperometric tests were run applying increasingly cathodic potentials. The quantitative evaluation of both gaseous and liquid CO_2RR products, respectively performed by GC/TCD and ^1H NMR (for details, paragraph 8.5.2, Experimental Section), allowed the calculation of electrocatalysts' selectivity and the assessment of products distribution in terms of faradic efficiency (FE) versus applied potential.

Before embarking in the discussion of the CO_2RR performances of the doped and undoped electrocatalysts, it is worth to highlight the results obtained from PEIS, which are reported in the form of Nyquist plot in Figure 111 (Supporting Material). For both doped and undoped electrocatalysts, the ohmic resistance of the circuit is *ca*. 20 Ω. This result confirms that the synthetic route applied for the HAP-doped electrocatalyst allowed the optimal dispersion of HAP onto the carbonaceous scaffold (an insulating ceramic material) without compromising the overall electrode conductivity.

The electrochemical performance of the undoped Cu/3D-GNS electrocatalysts can be assessed from the data collected in Figure 69.

Figure 69a reports the LSV curves under both inert and reactive atmosphere, i.e. feeding respectively N_2 and CO_2 to the cathode through the gas chamber of the electrochemical flow-cell. *i* vs E vs RHE – IR corrected curves exhibit a similar shape; only slight differences (*ca*. 100 mV) can be spotted in the onset potential which under N_2 and CO_2 flow should relate to HER and CO_2RR, respectively. The similar E_{Onset} and the almost identical delivered currents in the presence and absence of CO_2 suggest that HER and CO_2RR share the majority of the catalytically active sites (presumably, Cu facets). The $i \neq 0$, delivered by the catalyst before the actual onset of HER and/or CO_2RR, can be addressed to oxygen reduction reaction (ORR). This phenomenon is caused by the dissolution of atmospheric oxygen into the electrolyte, which is unavoidable in the configuration reported in Figure 77b (Supporting Material), where the electrolyte reservoir is open.

Figure 69b reports chronoamperometric *i* vs time curves. As expected, the delivered current increases in absolute value as the applied potential becomes more cathodic. It can be moreover noticed that when the CO_2RR (and parasitic HER) reaction rate increases as function of the applied potential, the consequent evolution of larger quantities of gaseous products of CO_2 (or proton) reduction causes violent bubble generation and therefore noisy electrochemical patterns.

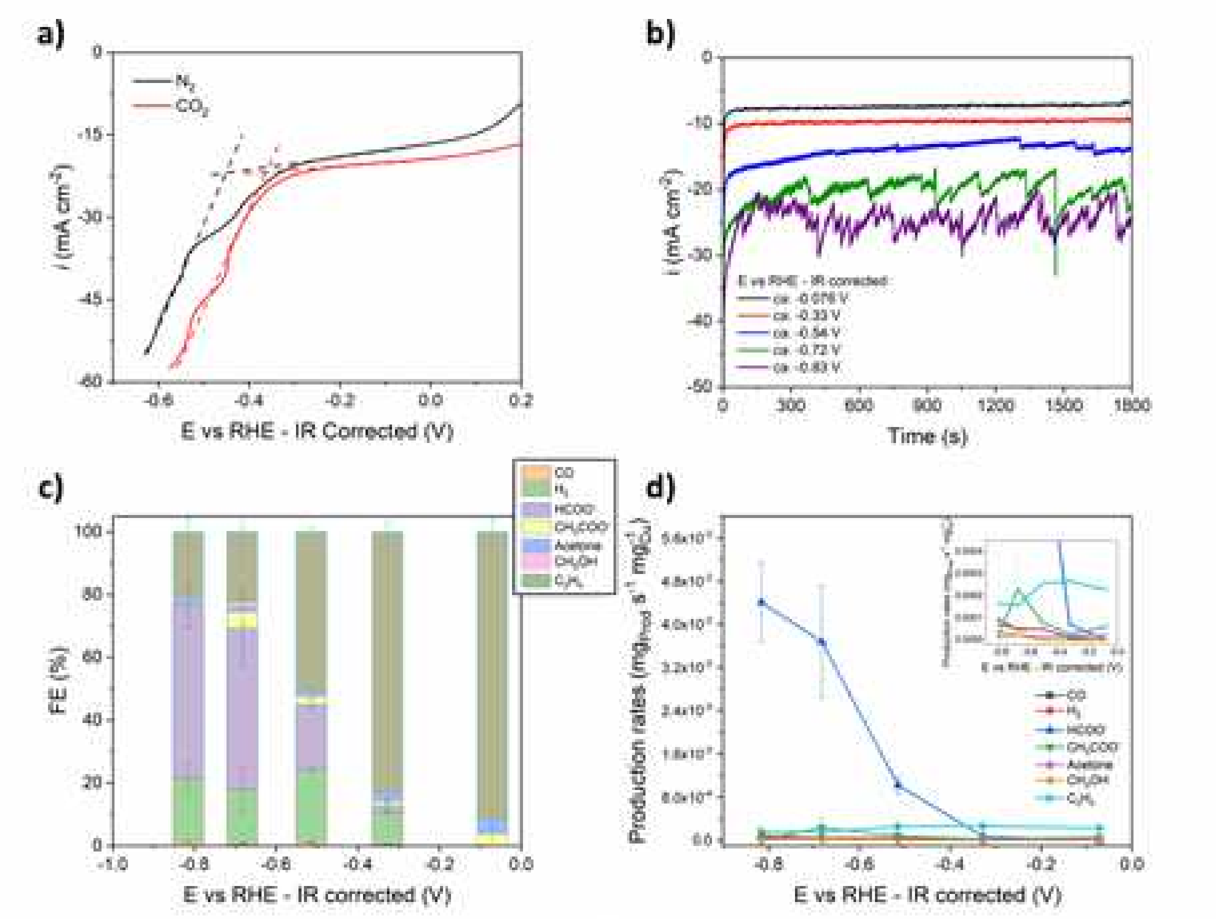

Figure 69: Electrochemical performance of undoped Cu/3D-GNS electrocatalysts in CO_2RR. a) LSV curves collected under inert (N_2) and reactive (CO_2) atmosphere; b) Chronoamperometric i vs. time curves. Combination of electrochemical data and quantitative evaluation of reaction products allowed to establish the products distribution in terms of c) products' faradic efficiency vs. applied potential and/or d) products' generation rate vs. applied potential.

Combining the quantitative results from GC/TCD and ^1H NMR analyses on gaseous and liquid products with the information collected from electrochemical tests (i.e. total quantity of charge Q_{Tot} delivered by the system in a definite amount of time), it has been possible to disclose the products distribution yielded by Cu/3D-GNS, reported in Figure 69c as faradic efficiency (FE, %) vs. applied potential.

Before focusing the attention on CO_2RR products distribution, it should be noticed that the faradic efficiency of H_2 (green bars in Figure 69c) does not exceed 20% even under the application of largely cathodic potentials. Cu/3D-GNS therefore exhibits an overall $FE_{CO2RR} \geq 80\%$ in the potential range under study (roughly, from 0 to -1 V vs RHE), a result comparable with state-of-art Cu-supported and carbonaceous N-doped electrocatalysts [215,223].

Under moderate cathodic potentials (E > -0.2 V vs RHE), Cu/3D-GNS catalyzes the almost selective production of ethylene (grey bars in Figure 69c), with traces of other valuable C_{2+} products like acetate and acetone. Detection of such complex products at such low applied overpotential (see Table 26) is unusual and may be related to the peculiar structure of the electrocatalyst. Factors like large pore volume and mesoporous structure of the carbonaceous supports are indeed known to cause an increase in the retention time of both pristine CO_2 and reaction intermediates, therefore favoring C-C coupling and multiple electron and/or proton transfers [225,231]. Despite the high-added value of these products, the small driving force of the process under such moderate applied potentials results in low delivered current densities and thus industrially irrelevant production rates (Figure 69d).

Under the application of more cathodic potentials (E < - 0.3 V vs RHE), parasitic HER causes the production of H_2, while CO_2RR products selectivity changes: indeed, ethylene faradic efficiency diminishes steadily with decreasing potential, mainly in favor of formate (purple bars in Figure 69c). An almost stable $FE_{HCOO-} \approx 55\%$ is achieved at E < -0.6 V vs RHE, in this case with interesting production rates (*ca.* $4.4 \cdot 10^3$ $mg_{HCOO-}\ s^{-1}\ mg_{Cu}^{-1}$, equal to *ca.* 16 $g_{HCOO-}\ h^{-1}\ g_{Cu}^{-1}$, Figure 69d).

Altogether, Cu/3D-GNS is a CO_2RR selective catalysts, with an overall FE towards $CO_2 \geq 80\%$. C_{2+} products (principally ethylene) are generated under the application of slightly cathodic potentials but biased by their low production rate. More cathodic potentials change Cu/3D-GNS products distribution, with a slight contribution of H_2 (from HER) and formate being generated at the expense of ethylene.

Although electrochemical CO_2RR is a relatively recent technology and pathways of reaction are not fully understood, comparison with results reported in literature for conceptually similar electrocatalysts may help to rationalize the performances of Cu/3D-GNS. Sun et al. reported an almost selective ethylene production over Cu dispersed onto pyridinic N-doped graphitic supports [214], postulating the co-operation of the two active sites. In the specific, pyridinic N-moieties (known in literature as CO_2RR active mainly towards 2e^- transfer products like CO and $HCOO^-$ [214,222,223]) were deemed by the authors to act as *CO species producer. *CO intermediates were then supposed to spillover, in virtue of the close contact and optimal dispersion of Cu onto the N-doped support, to Cu active sites, where *CO dimerization to C_2 products (i.e. ethylene) may occur. Differently from what reported by Sun et al., ethylene selective production on the here presented Cu/3D-GNS catalysts is obtained at applied potentials < -0.2 V vs RHE, indicating a relevant lowering of ethylene formation overpotential in respect with the systems investigated by Sun et al. (the selective ethylene production was achieved under the application of -0.9 V vs RHE, [214]). Possibly, this difference arises from the bigger dimensions of the Cu NPs in Cu/3D-GNS (ø ≈ 25 nm vs. ø ≈ 7 nm reported by Sun et al. [214]), known to favor C-C coupling over H_2 and/or CO production [204], as discussed in paragraph 4.1.4.1.

Interestingly, the application of increasingly cathodic potentials shifts the products distribution of Cu/3D-GNS towards formate, with a net diminishing of ethylene generation in terms of faradic efficiency. This trend is unexpected, since generally the formation of multiple electrons transfer products is boosted by increasingly cathodic potentials. The enhanced formate production at the expenses of ethylene may be explained considering that, under largely cathodic potentials, HER triggers; proton reduction partially occupies CO_2RR active sites of Cu NP (see Figure 69a and related considerations), thus hindering *CO dimerization. Moreover, the combination of HER and the overall enhancement of reaction rates causes a major depletion of protons at the electrode interface; the consequent alkalization favors the generation of oxygenates CO_2RR products (i.e. formate) instead more reduced and proton-demanding compounds (i.e. ethylene).

The effect of HAP doping onto CO_2RR onset potential and products distribution was assessed performing the same set of electrochemical tests onto the doped Cu+HAP/3D-GNS electrocatalyst. The results are reported in Figure 70.

Figure 70a and Figure 70b, reporting Cu+HAP/3D-GNS LSV curves and chronoamperometric electrochemical data, do not present major differences from those collected on undoped Cu/3D-GNS in Figure 69a and b. Indeed, a similar E_{Onset} is disclosed by LSV curves, with the same considerations made about CO_2RR and HER active sites holding for the doped electrocatalyst as well. Figure 70b indicates that the delivered currents upon increasingly cathodic potentials are similar for doped and undoped electrocatalysts; however, less noisy chronoamperometric patters are obtained for the doped Cu+HAP/3D-GNS catalysts. The deliverance of similar current densities under the application of the same potential indicates that doped and undoped electrocatalysts are characterized by comparable reaction rates. The limited electrochemical noise registered for Cu+HAP/3D-GNS chronoamperometric tests suggests that the doped catalysts produce lower amounts of gaseous products under the application of large cathodic potentials. This supposition will be confirmed by the analysis of products distribution in Figure 70c.

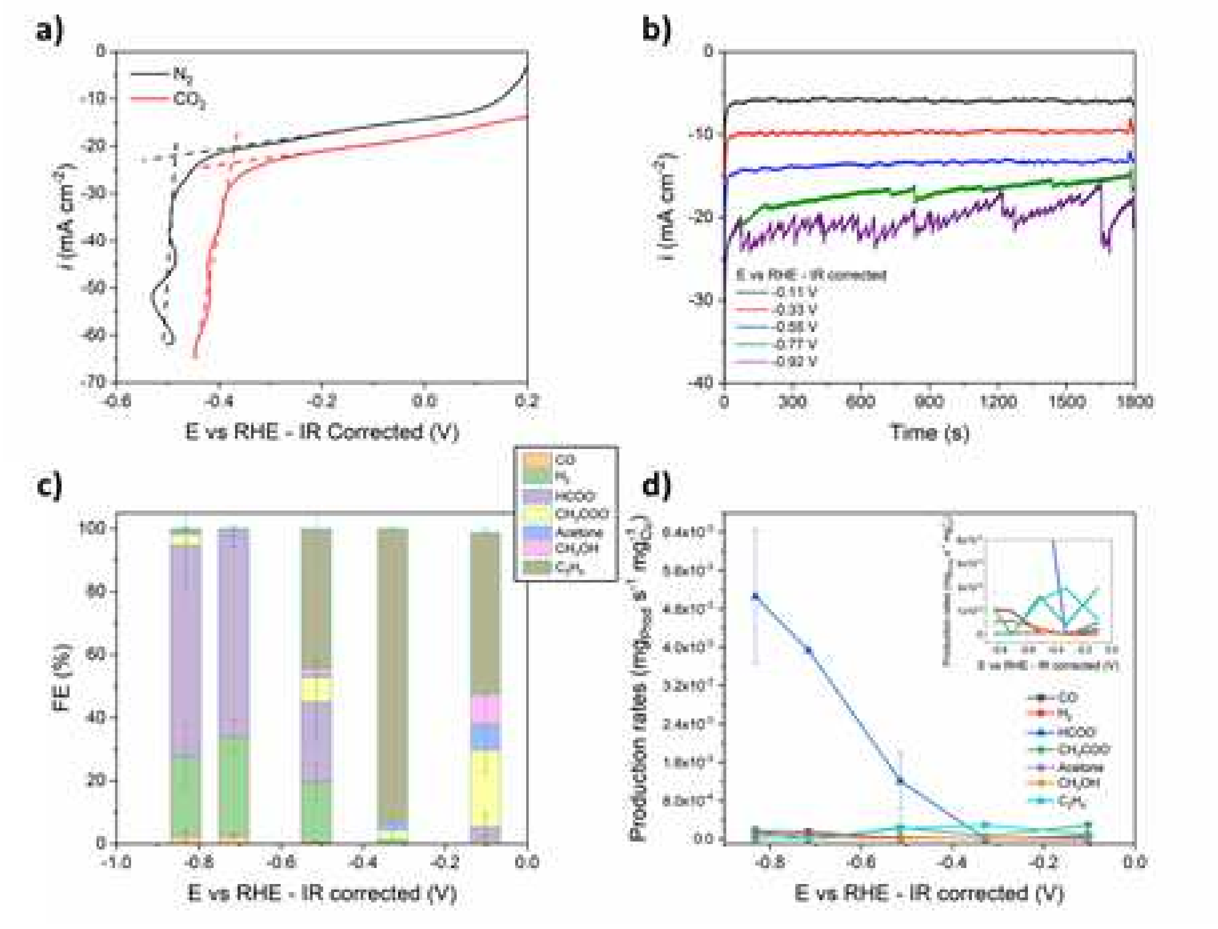

Figure 70: Electrochemical performance of doped Cu+HAP/3D-GNS electrocatalysts in CO$_2$RR. a) LSV curves collected under inert (N$_2$) and reactive (CO$_2$) atmosphere; b) Chronoamperometric i vs. time curves. Combination of electrochemical data and quantitative evaluation of reaction products allowed to establish the products distribution in terms of c) products' faradic efficiency vs. applied potential and/or d) products' generation rate vs. applied potential.

First and foremost, the doping with HAP does not alter the optimal selectivity of the catalyst towards CO$_2$RR; FE$_{H2}$ (green bars in Figure 70c) is indeed always ≤ 20% in the potential range under investigation, leading to an overall FE$_{CO2RR}$ ≥ 80%, as previously assessed for undoped Cu/3D-GNS. On the other hand, products distribution is altered by HAP doping, both under moderate and large cathodic potentials.

Under the application of moderate cathodic potentials (E > -0.4 V vs RHE), doped Cu+HAP/3D-GNS catalyzes the production of high added-value C$_{2+}$ products. In comparison with undoped Cu/3D-GNS, a shift towards more cathodic potentials in the maximum selectivity towards ethylene can be spotted. At the same time, HAP doping seems to favor the formation of uncommon C$_2$ and C$_3$ CO$_2$RR products, namely acetate and acetone (yellow and blue bars in Figure 70c), at the expenses of ethylene itself. Although it is difficult to rationalize the effect of the HAP doping on reaction mechanisms that are not fully disclosed to date, it can be envisaged that HAP peculiar adsorption features (paragraph 1.2) may lead to a strong retention of oxygenated CO$_2$RR intermediates, thus preventing further reduction to ethylene. In addition, the increased retention time of intermediates may itself account for the production of C$_3$ species like acetone.

As in the case of undoped Cu/3D-GNS, the application of more cathodic potentials results in the increase of formate faradic efficiency and production rates (Figure 70c and d). However, upon HAP doping, ethylene production drops to zero in favor of $HCOO^-$, which is then produced with FE ≈ 70%. The only C_2 product detectable in slight amount under E < -0.8 V vs RHE is acetate (FE ≈ 2%). Both formate and acetate production are consistent with the preferential formation of oxygenated CO_2RR products consequent to interface alkalization (as previously discussed for Cu/3D-GNS products distribution under largely cathodic potentials).

The boosting of $HCOO^-$ production at the expense of C_2 products under these conditions may be addressed to HAP doping. Figure 54b indicates that formate exhibits peculiar reaction intermediates, formed upon stabilization of the $CO_2^{\bullet -}$ radical anion through oxygen coordination to the reactive surface. Conversely, all the other CO_2RR products (i.e. CO, C_1 and C_{2+} species) share the same radical anion as common intermediate but with a different stabilized configuration onto the catalysts' surface: in the specific, a carbon-coordinated intermediate (Figure 54a, Figure 56 and Figure 57). Therefore, the boosting of formate production upon HAP doping suggests that HAP plays an active role in stabilizing O-bound radical anion species over C-bound ones. A possible stabilization effect of HAP can be envisaged considering the presence of acid sites onto its surface (Figure 71): indeed, HAP's Ca^{2+} and/or hydroxyl groups vacancies (δ_{OH-}) can establish electrostatic interactions with the partially negative oxygen atoms of the $CO_2^{\bullet -}$ radical anion, thus leading to O-bound species stabilization onto HAP surface. A graphical depiction of the phenomenon is presented in the following figure:

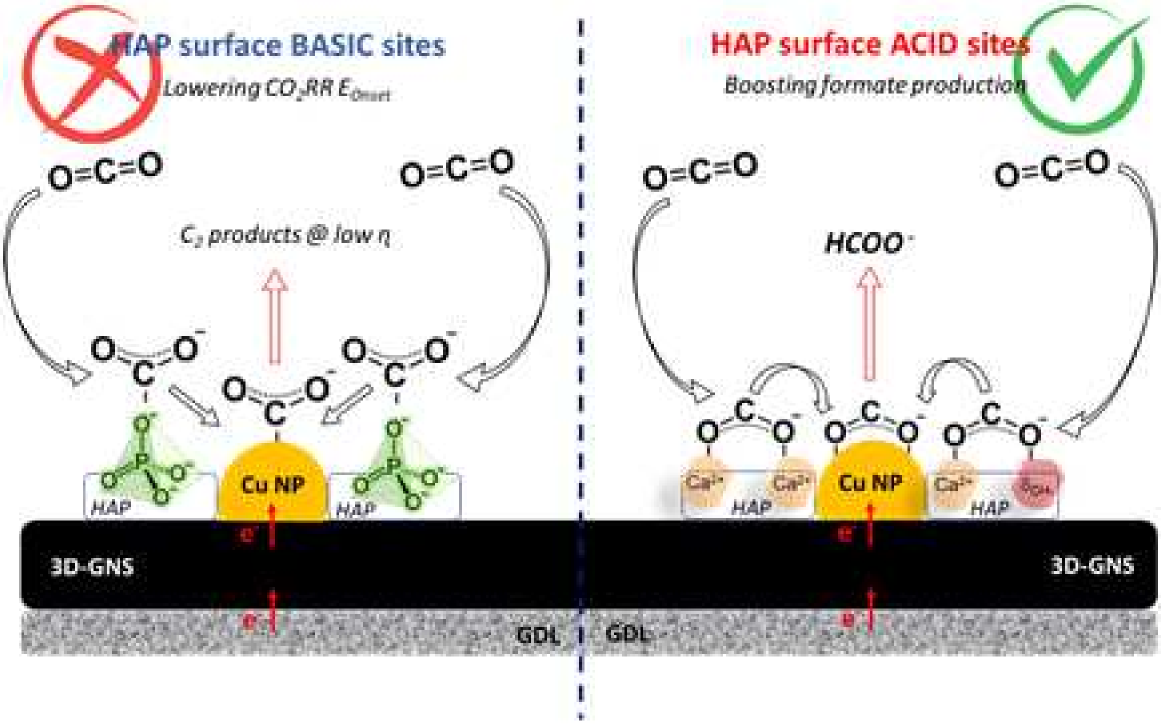

Figure 71: Graphical depiction of the hypothesized effect of HAP doping on CO_2RR in Cu+HAP/3D-GNS electrocatalysts. On the left, the expected (and not verified) action of HAP surface basic groups in CO_2 destabilization. On the right, the alleged stabilizing effect exerted by HAP acid surface groups onto the $CO_2^{\bullet -}$ radical anion.

The rationale design of the HAP-doped electrocatalyst envisaged a beneficial effect of HAP surface basic sites onto CO_2RR E_{Onset} and/or products distribution that was not verified. However, the alleged action of acidic sites on $CO_2^{\bullet -}$ stabilization may explain the boosting of formate production on Cu+HAP/3D-GNS electrocatalysts. Although the result obtained is not the one foreseen during catalyst's design, acid/base doping of electrocatalysts proved to be a valuable tool to tune the selectivity of electrochemical CO_2RR processes.

4.4 Conclusions

In the present chapter, novel Cu-based HAP-doped electrocatalysts for CO_2RR have been rationally designed, synthesized, characterized and tested.

With the aim to maximize the production of C_{2+} compounds at low applied overpotentials, composite electrocatalysts composed by a carbonaceous support (N-doped 3D-GNS), an active phase (Cu NPs) and a dopant (HAP) have been synthesized.

The obtained electrocatalysts exhibited large surface area and a mesoporous nature together with a large pore volume; these features ensured optimal mass diffusion and reagents/products transfer under reaction conditions. TEM/EDX mapping and XPS analyses disclosed that a satisfactory dispersion of both Cu NPs and HAP onto 3D-GNS have been achieved, realizing the close-contact between active phase and dopant that was envisaged by design.

Catalytic inks of both the undoped (Cu/3D-GNS) and doped (Cu+HAP/3D-GNS) electrocatalysts have been sprayed onto a GDL, thus realizing GDEs that were employed as cathodes in a lab-scale electrolyzer (i.e. an electrochemical flow-cell).

PEIS measures reveal a low and comparable ohmic resistance for both GDEs (*ca*. 20 Ω), evidencing that, despite its insulating nature, HAP decoration did not affect the overall conductivity of the material thanks to the thoughtful design and optimized synthetic route of doped Cu+HAP/3D-GNS electrocatalysts.

Regarding electrochemical performances, both Cu/3D-GNS and Cu+HAP/3D-GNS catalysts minimized parasitic HER, displaying a $FE_{CO2RR} \geq 80\%$ throughout the whole potential range under investigation (from *ca*. 0 to *ca*. -1 V vs RHE – IR corrected).

Both electrocatalysts produced high added-value C_2 and/or C_{2+} compounds under the application of relatively small overpotentials. Cu/3D-GNS selectivity towards ethylene under such conditions have been addressed to the co-operation between 3D-GNS pyridinic N-moieties (converting CO_2 to *CO intermediates) and Cu NPs (favoring *CO dimerization and further electron and proton transfers). HAP doping in Cu+HAP/3D-GNS affected the CO_2RR products distribution under such conditions, catalyzing the generation of uncommon C_{2+} compounds (namely acetate and acetone) in spite of ethylene, whose maximum selectivity is reached towards more cathodic values. Such results indicate that HAP unique sorption ability alters both retention time and energy of CO_2RR intermediates towards C_{2+} products, although the still unclear reaction pathways do not allow to properly point out the actual species.

Under the application of large cathodic potentials, both undoped and doped catalysts exhibited an increase in formate production at the expenses of C_2 compounds (i.e. ethylene). This transition from reduced C_2 products towards a C_1 oxygenate like formate has been rationalized considering the triggering of HER competition with CO_2RR onto Cu NPs and the alkalization of the electrode interface due to proton depletion. Formate faradic efficiency at $E < -0.6$ V vs RHE passes from *ca*. 55% to *ca*. 70% upon HAP doping, with ethylene generation being completely suppressed by Cu+HAP/3D-GNS catalysts. The boosting in formate production has been attributed to HAP sorption properties as well: in particular, the presence of acid sites onto HAP surface has been deemed to stabilize the $CO_2^{\bullet-}$ radical anion under O-bound configuration, favoring the reaction pathway toward formate production at the expenses of ethylene and generally all C_{2+} products.

Although the catalysts have been designed to principally exploit HAP surface basic sites (i.e. O^{2-} functionalities of phosphate groups), the present results likewise evidence that acid/base doping may be a useful tool in directing the selectivity of electrochemical CO_2RR processes.

5 Final remarks

In this dissertation the possible use of HAP-based and doped materials for environmental protection processes have been studied. The peculiar structural flexibility and surface properties of the material are at the basis of HAP ability to efficiently remediate heavy metal cations pollution of industrial wastewater. Compositing with a carbonaceous moiety generated novel HAP/C composites which were assessed to simultaneously remediate organic and inorganic pollution of wastewater thanks to their dual nature. The implementation of HAP in Cu-based CO_2RR electrocatalysts indicated that acid/basic dopants may be a tool in directing CO_2 reduction pathways, thus allowing to tune the selectivity of such processes.

The research projects and results herein reported are encased in a bigger framework, which is the ideal "valorization cycle" of HAP, ideated by our research group. Adhering to the principles of circular economy, the cycle aims to exploit HAP as a 360 degrees material for environmental processes, from water to air quality control.

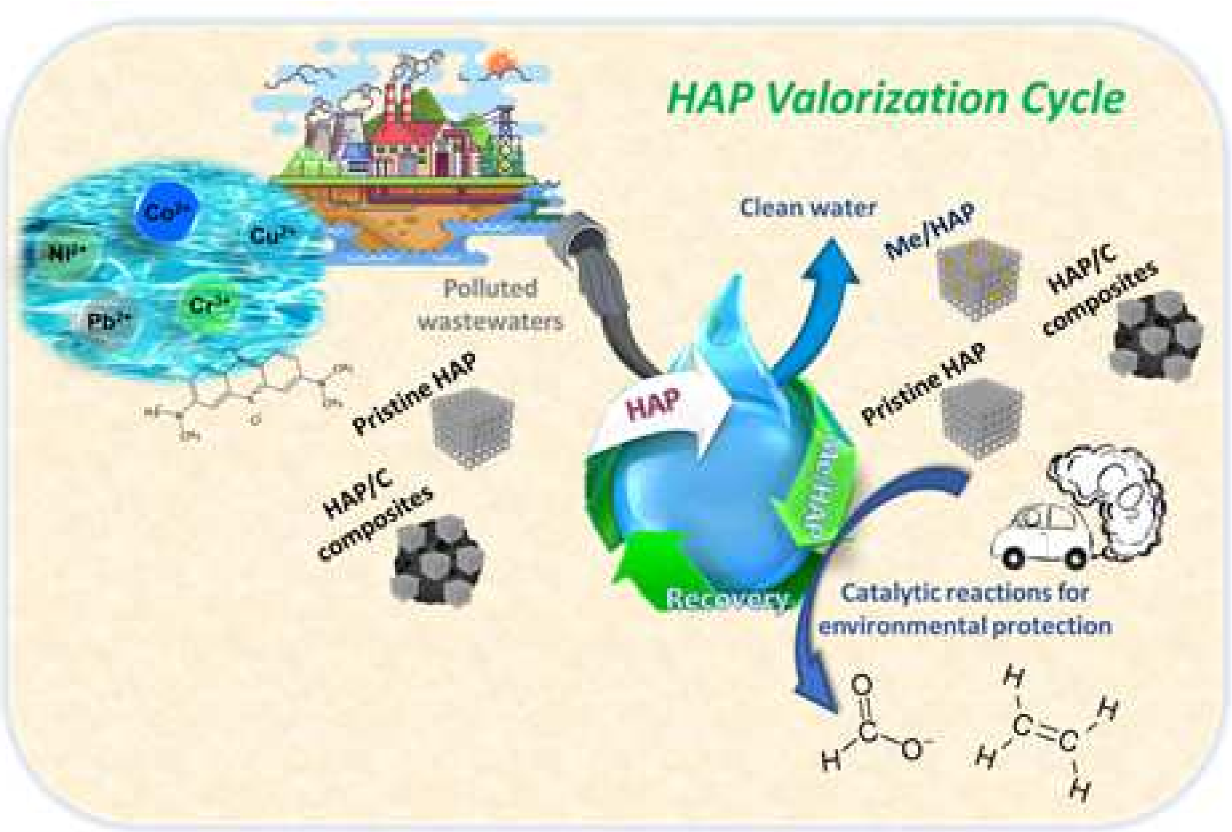

6 Acknowledgements

Finally, I would like to acknowledge all the scientists that joined my efforts in the collection, interpretation and understanding of all the results reported in the present dissertation:

Prof. Antonella Gervasini (UniMi, Dipartimento di Chimica), Prof. Stefano Trasatti (Unimi, Dipartimento di Scienze e Politiche Ambientali) and Dr. Pierangela Cristiani (RSE, Ricerca sul Sistema Energetico), who, as supervisors and co-supervisors, lie faith on me assigning me this doctoral project, while continuously guiding and helping me pursuing meaningful scientific results and deepening my chemical culture.

Prof. Plamen Atanassov and all his group at University of California Irvine (UCI), Department of Biomolecular and Chemical Engineering, for hosting me for 6 months in their labs and allowing me to explore the world of CO_2 electrochemical reduction, sharing with me their vast knowledge in electrochemical science and engineering and giving me the possibility to live a fruitful experience abroad.

A particular acknowledgement for all the people that helped me collecting and interpreting specific data, belonging to their field of research:

Prof. Marco Scavini (UniMi, Dipartimento di Chimica) and Prof. Monica Dapiaggi (UniMi, Dipartimento di Scienze della Terra), for their support in registering and understanding X-ray diffraction data of all the material studied in the present work;
Prof. Aline Auroux (IRCELYON), for gas-phase surface titration of hydroxyapatitic materials and microcalorimetric measurements;
Dr. Guylène Constentin (LRS, Laboratoire de Réactivité de Surface, Sorbonne University), Dr. Claudio Evangelisti (CNR, Consiglio Nazionale delle Ricerche) and Dr. Nadia Santo (UniMi, Dipartimento di Biologia), for TEM imaging.
Prof. Silvia Bruni and PhD student Margherita Longoni (UniMi, Dipartimento di Chimica), for Raman spectra acquisition and results interpretation;
Prof. Daniela Maggioni (UniMi, Dipartimento di Chimica), for the measurement of HAP point of zero charge;
Dr. Marco Schiavoni (UniMi, Dipartimento di Chimica), for the collection of transmittance FT-IR spectra;
Dr. Americo Costantino (UniMi, Dipartimento di Chimica), for ICP and AAS analyses.

Last but not least, all the people that actually shared time working with me, both experimentally and mentally:

The whole Gervasini's research group: Prof. Paolo Carniti, Dr. Sebastiano Campisi, PhD students Melissa Galloni, Mariana Catrinick and Denise Cavuoto, master students Giovanni Paganoni, Riccardo Motta, Ulisse Della Vittoria, Kevin Jaramillo, Mirko Leone, Elisa Longhin and Gloria Salazar Fuentes and bachelor students Elena Cazzulani, Francesco Panico and Elia Cappellini;
The whole Trasatti's research group, in particular Dr. Mirko Magni and master student Davide Sironi;
The whole Atanassov's research group and in particular the CO_2RR subgroup: Dr. Tristan Asset and PhD students Laurent Delafontaine and Shengyuan Gao.

I hopefully didn't forget anybody. However, in the case I unfortunately did, be aware that in a few words it seems impossible to me to thank all of you, as all the people listed here, for the immense support you gave me in these last three years and also the knowledge that you shared with me. You all did an amazing job making me a better science and, I think, a better person.

7 Research achievements

7.1 Research achievements correlated to the present dissertation

7.1.1 Publications

M. Ferri, L. Delafontaine, S. Guo, S. Campisi, A. Gervasini, P. Cristiani, T. Asset, P. Atanassov, "**Rational design of Cu-based hydroxyapatite-doped electrocatalysts for energy efficient and selective CO_2RR**", currently under writing.

M. Ferri, S. Campisi, J. Shen, A. Gervasini, "**Hydroxyapatite/activated carbon composites for the simultaneous removal of organic-inorganic pollutants from wastewater**", currently under writing.

M. Ferri, S. Campisi, P. Carniti, A. Gervasini, J. Shen, "**Tunable acidity in mesoporous carbons for hydrolysis reactions**", New Journal of Chemistry, 2020.
DOI: 10.1039/d0nj00750a

M. Ferri, S. Campisi, A. Gervasini, "**Nickel and copper adsorption on hydroxyapatite: a study for the de-metalation of electronic industrial wastewaters**", Adsorption Journal, 2019.
DOI: 10.1007/s10450-019-00066-w

M. Ferri, S. Campisi, M. Scavini, C. Evangelisti, P. Carniti, A. Gervasini, "**In-depth study of the mechanism of heavy metal trapping on the surface of hydroxyapatite**", Applied Surface Science, 2019.
DOI: 10.1016/j.apsusc.2018.12.264

7.1.2 Oral & Poster Presentations

Rational design of Cu-based hydroxyapatite-doped electrocatalysts for energy efficient and selective CO_2RR, M. Ferri, L. Delafontaine, S. Guo, S. Campisi, A. Gervasini, P. Cristiani, T. Asset, P. Atanassov, **Oral presentation**, ACS Spring 2021, April 5th – 16th, virtual event, attending acceptance.

The "virtuous cycle" of hydroxyapatite: from remediation of heavy metal pollution to catalytic/electrocatalytic applications, M. Ferri, S. Campisi, M.G. Galloni, S. Trasatti, A. Gervasini, **Flash Poster presentation**, ICS2019 (Winter school of catalysis), January 7th-12th, 2019, Bardonecchia (TO), Italy;

Hydroxyapatite materials: from remediation of heavy metal pollution to new catalytic applications, M.Ferri, S. Campisi, A.Gervasini, **Flash Poster presentation**, GIC-DiChIn 2018, September 2nd – 5th, 2018, Milan, Italy;

Structurally and morphologically tailored hydroxyapatite materials for effective immobilization of polluting heavy metal species from wastewaters, M.Ferri, S. Campisi, A.Gervasini, **Oral presentation**, ISSHAC-10, August 27th – 31st, 2018, Lublin, Poland.

7.1.3 Attended congresses/schools

International congress **ACS Spring 2021** – Macromolecular chemistry: the second century, organized by ACS, April 5th – 16th, Virtual event, attending abstract acceptance.

International workshop "**MASTEC: Materials for Today's Energy Challenges**", organized by Dipartimento di Scienze Chimche, Università di Padova, on 3rd - 4th June 2019, Padova, Italy;

Internaltional winter school of catalysis (**ICS2019**), January 7th – 12th, 2019, Bardonecchia (TO), Italy;

Workshop “**Quantitative analysis of crystalline phases : comparison between traditional and chemiometric methods**”, organized by AIC (Associazione Italiana di Cristallografia”, on 6th February 2018, Bologna, Italy.

7.1.4 Funding/Accepted proposals

Funded **beamtime proposal** at Elettra – Sincrotrone Trieste: "Defective structure of hydroxyapatite materials with Ca/P modulation for environmental processes"

Investigators: Prof. Marco Scavini (P.I.), Dr. Sebastiano Campisi, Michele Ferri, Prof. Antonella Gervasini

7.1.5 Awards

Winner of the **Best Poster Award** sponsored by the RSC journal “Sustainable Energy and Fuels" with the contribution: "The "virtuous cycle" of hydroxyapatite: from remediation of heavy metal pollution to catalytic/electrocatalytic applications", ICS2019, Bardonecchia (TO), 2019.

7.1.6 Participation to divulging events

Participation to the Night of the Researchers: MeetMeTonight2018 (live event, Giardini Indro Montanelli, Milano) and MeetMeTonight2020 (virtual event), presenting the “virtuous cycle of hydroxyapatite”.

7.2 Achievements not directly related to the present dissertation

7.2.1 Publications

S. Campisi, M. Ferri, C. E. Chan-Thaw, F. J. Sanchez Trujillo, D. Motta, T. Tabanelli, N. Dimitratos, A. Villa, “**Metal-Support Cooperative Effects in Au/VPO for the Aerobic Oxidation of Benzyl Alcohol to Benzyl Benzoate**”, Nanomaterials, 2019.

DOI: 10.3390/nano9020299

7.2.2 Tutoring activities

Tutoring activity/assistance (frontal lectures) for the course “**General chemistry and elements of physical chemistry**”, held for students of the 1st year of Scienze e Tecnologie Alimentari (Alimentary sciences and technologies). Coordinators : Prof. Fessas and Prof. Molinari. A.Y. 2018/2019.

Chemical laboratory assistant for “**Laboratory of physical chemistry**”, course held for 2nd year students in Industrial Chemistry (Bachelor). Coordinators : Prof. Gervasini and Prof. Chiarello. A.Y. 2017/2018.

Chemical lab assistant for “**Laboratory of general and organic chemistry**”, course held for 1st year students in Biology (Bachelor). Coordinator : Prof. Strumolo. A.Y. 2017/2018.

7.2.3 Participation to divulging events

Organizer, host and speaker of the 2018 and 2019 editions of the UniMi event “**MeetMeOnChem**” (**MMOC**), fostering the research carried ou by PhD students towards undergraduates and local industries. Coordinators of the event: Prof. Licandro and Prof. Roberto.

8 Experimental section

8.1 Synthetic routes to HAP-based and/or doped materials

In the following, all the syntheses of the materials studied in this thesis work are reported.

8.1.1 Synthesis of stoichiometric HAP

Stoichiometric hydroxyapatite ($Ca_{10}(PO_4)_6(OH)_2$, atom/atom Ca/P ratio equal to 1.67) has been synthesized according to an optimized co-precipitation route.

250 mL of a 0.100 M $(NH_4)_2HPO_4$ aqueous solution were placed in a three-necked round flask thus equipped: central neck connected to a mechanical stirrer, side-necks fitted with reflux condenser and adaptor for peristaltic tube connection, respectively. Under mechanical stirring (200 RPM), $(NH_4)_2HPO_4$ solution was heated to 80°C by means of an oil bath. pH was regulated at 9.7 (± 0.2) adding 50 mL of a 28-30 wt.% NH_4OH solution.

Then, 250 mL of a 0.167 M aqueous solution of $Ca(NO_3)_2 \cdot 4H_2O$ were fed to the flask through a peristaltic pump (dropping rate = 1.5 mL min^{-1}). Throughout the addition, solution pH was periodically checked and kept constant at 9.7 (± 0.2) by dosing precise amounts of 28-30 wt.% NH_4OH solution. All solutions were prepared from MilliQ water (15.0 MΩ, Millipore).

Addition of the Ca(II) precursor solution leads to the formation of a milky suspension. HAP precipitates according to the following chemical equation:

$$10\ Ca(NO_3)_2 + 6\ (NH_4)_2HPO_4 + 8\ NH_3 + 2\ H_2O \rightarrow Ca_{10}(PO_4)_6(OH)_{2\downarrow} + 20\ (NH_4)NO_3$$

Equation 4

Once the addition of Ca(II) precursor was finished, the suspension was stirred for 5 minutes, then hot-filtered under vacuum on Buchner funnel. The obtained white solid was washed with hot MilliQ water (*ca*. 1.5 L), until neutrality of the washing water. HAP powders were then dried for 16 h at 50°C under vacuum and then thermally treated for 8 h at 120°C under air.

8.1.2 Synthesis of HAP/C composites for wastewater remediation and sensing applications

Synthesis of HAP/C composites has been carried out according to a co-precipitation route similar to the one presented in paragraph 8.1.1; main differences lie in (*i*) the presence of a carbonaceous scaffold slurry in the reaction vessel, (*ii*) precipitation temperature and (*iii*) volume/concentration of precursors' solutions. Atomic Ca/P ratio of HAP in all composite materials was stoichiometric, i.e. *ca*. 1.67.

Experimentally, *ca*. 300 mg of carbonaceous scaffold were dispersed by ultrasonication (15 minutes) in 10 to 40 mL of MilliQ water, depending on the hydrophobicity of the scaffold itself. This suspension was then introduced in a three necked round flask containing 100 mL of a 0.400 M $(NH_4)_2HPO_4$ solution. Flask was equipped with a mechanical stirrer (central neck) and the resulting slurry was stirred at 200 RPM for 5 minutes. pH of the solution was adjusted to *ca*. 9.7 (± 0.2) by addition of *ca*. 10 mL of a 28-30wt. % NH_4OH solution. Then, 100 mL of a 0.668 M $Ca(NO_3)_2 \cdot 4H_2O$ solution were added dropwise by means of a peristaltic pump (1.65 mL min^{-1}). Precipitation occurred at RT, under mechanical stirring (200 RPM); periodic additions of base were performed, as to keep pH constant at *ca*. 9.7. All solutions were prepared with MilliQ water.

After completing the addition of the Ca(II) precursor's solution, suspension was stirred for 5 minutes and then vacuum filtered on Buchner funnel. Powders were washed with MilliQ water up to neutrality of washing water, then dried for 16 h at 50°C under vacuum and thermally treated for 8 h at 120°C under air.

Carbonaceous scaffolds employed were (*i*) commercial carbon nanofibers (CNFs PR24-HHT, purchased from Pyrograf), (*ii*) biomass-derived mesoporous carbon (CMC, furnished by the group of Prof.

Shen from Nanjing University and synthesized according to [168]) and (*iii*) extra pure granular activated charcoal (purchased from Sigma Aldrich).

Given that HAP precipitation yield is almost quantitatively (> 99%) and considering both the concentration of precursors' solutions and the mass of carbonaceous scaffold used, HAP/C composites obtained have a carbon content equal to *ca*. 4.3wt %. Effect of the HAP:C ratio on the material performance was studied for the most promising samples. HAP/C composites with a carbon content up to *ca*. 20wt. % were synthesized following the above presented route but increasing the amount of carbonaceous scaffold in the slurry. "Bare" HAP (herein referred to as HAP_RT) has been synthesized according to the same route but in absence of the carbonaceous scaffold.

8.1.3 Synthesis of HAP-doped electrocatalysts for CO_2RR

8.1.3.1 HAP-doped Cu/3D-GNS electrocatalysts

Synthesis of 3D-GNS has been performed according to the patented Sacrificial Support Method (SSM) [226] and as reported in the literature [232]. Briefly, graphene oxide (GO), synthesized by a modified Hummers method [233], was exfoliated in aqueous solution by ultrasonication (600 kJ were delivered to 10 g of GO in 1 L of MilliQ water for 2 hours). 20 g of EH-5 fumed silica (Cab-O-Sil, surface area ≈ 400 m^2 g^{-1}) were then added to the mixture. The suspension was sonicated for 1 more hour and then dried at 85°C overnight. Dry powder was ball-milled at 400 RPM for 15 minutes prior to be reduced at 800°C under a 7% H_2 in Ar flux (flowrate = 100 ccm) for 1 hour. The reduced sample now constituted by a graphene nanosheets-silica mixture (GNS-SiO_2) has been ball-milled as previously described. SiO_2 support was leached by acidic etching with 25 wt.% HF (24 hours). Leached sample was filtered and washed with MilliQ water until neutrality of the wash water was reached. The resulting powders where dried at 85°C overnight and then doped with nitrogen by means of a thermal treatment (850°C for 2 hours) in 10% NH_3 in Ar (flowrate = 100 ccm). Such obtained 3D-GNS powders have been stocked and used as support for Cu NP and HAP.

Ca. 85 mg of 3D-GNS were dispersed in *ca*. 40 mL of isopropyl alcohol (IPA). The pH of the suspension was adjusted to 10 by the addition of 0.7 mL of a 0.1 M KOH aqueous solution. Similarly, *ca*. 24 mg of commercial Cu NP (Sigma-Aldrich, CAS 7440-50-8, ø = 25 nm) were dispersed in *ca*. 40 mL of IPA, adjusting the pH as indicated for the 3D-GNS suspension. Both mixtures were sonicated for 30 minutes as to achieve optimal suspension. Then, the Cu NP suspension was added in a single shot to the 3D-GNS one. The resulting mixture was stirred at RT for 48 h. After the immobilization step, the powder was vacuum filtered on 0.45 µm Nylon membrane, washed with MilliQ water and dried at 110°C for 45 minutes. Such obtained sample was labelled Cu/3D-GNS.

Ca. 100 mg of Cu/3D-GNS were suspended in *ca*. 90 mL of MilliQ water. The pH of the suspension was adjusted to 7 adding 42 µL of a 0.1 M KOH aqueous solution. Analogously, *ca*. 12 mg of HAP_RT (synthesis reported in paragraph 8.1.2), were dispersed in *ca*. 20 mL of MilliQ water, adjusting suspension pH at 7 by adding 15 µL of a 0.1 M KOH solution. Both mixtures were sonicated for 45 minutes, to favor samples suspension. Then, the HAP suspension was added to the Cu/3D-GNS suspension in a single shot; the resulting mixture was stirred at RT for 48 h. Finally, the powder was vacuum filtered on 0.45 µm Nylon membrane, washed with MilliQ water and dried at 110°C for 3 hours. Such obtained sample was labelled Cu+HAP/3D-GNS.

By means of the reported procedure, two electrocatalysts have been synthesized: a non-doped Cu/3D-GNS, with a 20 wt.% Cu loading (by design) and a HAP-doped Cu+HAP/3D-GNS, with a 20 wt.% Cu and a 10 wt. % loading of HAP (by design).

8.2 Physical-chemical characterization techniques

8.2.1 General structural and morphological characterization of HAPs materials

Synthetic HAP-based and/or doped samples have been structurally and morphologically characterized through several investigation techniques: nitrogen adsorption-desorption isotherms (N_2 ads/des), scanning transmission electron microscopy (STEM), routine and synchrotron X-ray powder diffraction (XRPD), Fourier Transform Infrared Spectroscopy (FT-IR) and zeta-potential measurements.

N_2 adsorption-desorption isotherms were collected at liquid nitrogen temperature, by means of a Sorptomatic 1990 version instrument from Thermo Scientific (Carlo Erba), that uses a static volumetric technique. The analysis was controlled by computer processing using the MILES-200 program and the MILEADP software for computations. Low-pressure part of the adsorption branch of the isotherm has been modeled by 3-parameter BET equation ($0.05 < p/p^0 < 0.4$) whilst the desorption branch has been interpreted by B.J.H. (Barrett-Joyner-Halenda) model ($0.3 < p/p^0 < 0.95$), as to determine specific surface area (S_a) and pore size distribution (PSD), respectively. Prior to the analysis, dried samples (*ca*. 150 mg) were outgassed for 4 h at 150°C under a residual pressure of 0.1 mbar, in order to ensure the fully removal of water from meso and micropores. Nitrogen used for the analyses was 99.9995% purity. The adsorbed volume, expressed in cm^3(STP) g^{-1}, was converted into pore volume (cm^3 g^{-1}), using N_2density at normal liquid state (0.8081 g cm g^{-1}); molecular area of N_2 was taken as 16.2 $Å^2$.

To determine Ca/P ratio, *ca*. 100 mg of HAP were mineralized in HNO_3 (65wt. %) and diluted; the resulting solution was analyzed by Inductively Coupled Plasma – Atomic Emission Spectroscopy (ICP-AES), using a Perkin Elmer, Optical Emission Spectrofotometer, Model Optima 8000 DV. Calcium and phosphorous standard solutions (1,000 µg/mL, 2% HNO_3 from Perkin Elmer) were used for ICP-AES calibration.

ZEISS LIBRA 200FE microscope with a 200 kV FEG source, in column second-generation omega filter was used for transmission electron microscopy (TEM). Chemical analysis was performed using HAADF-STEM (High Angular Annular Dark Field Scanning Transmission Electron Microscopy) facility and Energy-dispersive X-ray (EDX) probe (Oxford INCA Energy TEM 200). EDX spectra and element maps were collected along with HAADF-STEM micrographs. After grinding in an agate mortar, HAP powders were suspended in isopropanol and sonicated to achieve optimal dispersion. Suspensions were deposited onto a lacey carbon-coated copper grid (300 mesh) and the solvent was allowed to evaporate at RT.

X-ray powder diffraction analyses were performed using a Philips Powder X-ray diffractometer equipped with a PW 1830 generator. Monochromator was made in graphite, operating with Cu Kα ($\lambda = 1.5418$ Å) radiation. The X-ray tube worked at 40 kV×40 mA. The acquisition range 2θ range of the diffraction patterns was from 8° to 60°. Scan rate was fixed at 0.6° min^{-1} with a step size of 0.05°. Phase identification was performed by Match! Software, from Crystal Impact GbR.

High resolution XRPD diffractograms of HAP were collected at the ID22 beamline of the European Synchrotron (ESRF) in Grenoble, France. Patterns have been also registered after the addition of crystalline TiO_2 (≈ 15wt. %, internal standard), as to detect possible amorphous phases. Data were collected at room temperature in high-resolution setup, using an X-ray wavelength of 0.354260(3) Å up to $2\theta = 32°$ ($Q_{max} \approx 10.8$ $Å^{-1}$) for a total counting time of about half an hour per pattern. Rietveld analysis was executed adopting the GSAS suite of programs [234]. In the refinement, scale factors, unit cell parameters, atomic positional degrees of freedom, and atomic isotropic mean square displacements parameters (adp, one for each element) were varied as well as the background and line shape parameters. As to the Pair Distribution Function (PDF) analysis, the same HAP "as prepared" sample was measured at the ID15 beamline of ESRF using a Dectris Pilatus 2M CdTe. The X-ray energy was around 100 keV ($\lambda = 0.123984$ Å). Sample-detector distance (250.9 mm), detector tilt, beam position, and wavelength were calibrated using the diffraction pattern of CeO_2 via the library pyFAI [235]. The images were then radially integrated using pyFAI, the PDF was calculated as the

G(r) described in the literature [236] after background subtraction, suitable corrections and normalization using the program PDFGetx2 [237]. Maximum value of momentum transfer used for PDF calculation was Q_{max}=24 Å^{-1}. The PDF data were refined against structural models using the program PDFGui [238].

Rough preliminary unit cell refinement was performed using CelRef V3 software (developed at Laboratoire des Matériaux et du Génie Physique, Ecole Nationale Supérieure de Physique de Grenoble).

Fourier Transform Infrared (FT-IR) spectra were collected in the wavenumber range from 400 cm^{1} to 4000 cm^{-1}, at RT, using a Perkin-Elmer Spectrum Two Fourier transform infrared spectrometer. Prior to the analysis, samples were dried for 16 h at 120°C under air and then padded in mixture with dried KBr (sample to KBr weight ratio *ca*. 1:30).

Zeta-potential measurements have been carried out in a Malvern dip-cell for laser Doppler electrophoresis (electrophoretic light scattering). Suspensions of HAP were prepared, adjusted at the desired pH by means of HCl and/or NaOH 0.1 M. Then, dip-cells were filled and zeta-potential evaluated by light scattering.

8.2.2 Additional structural and morphological characterization of HAP/C composites for wastewater remediation and sensing applications

In addition to the typical physical-chemical characterization techniques listed and detailed in the previous paragraph (nitrogen adsorption-desorption isotherms (N_2 ads/des), transmission electron microscopy (TEM), X-ray powder diffraction (XRPD), Fourier Transform Infrared Spectroscopy (FT-IR)), HAP/C composites were further characterized by means of: thermogravimetric analyses (TGA), Raman spectroscopy and powder conductivity measurements by linear sweep voltammetry (LSV).

N_2 ads/des analyses, routine XRPD and FT-IR measurements have been carried out according to what reported in paragraph 8.2.1.

To determine the exact carbon wt.% in the composites TGA analyses were carried out on the samples, using a Perkin-Elmer TGA-7. Physical mixtures with precisely known ratio between HAP and carbonaceous scaffolds have been analyzed as well, as to obtain a weight loss vs carbon wt.% calibration line.

Ca. 10 mg of HAP/C composite were weighted in a crucible and pyrolyzed according to the following thermal ramp:

- Heating from RT to 120°C at 10.00 °C min^{-1} under flushing N_2 (20.00 mL min^{-1});
- Isothermal step at 120°C (60 minutes);
- Heating from 120 to 800°C at 5.00°C min^{-1} under flushing air (20 mL min^{-1});
- Cooling down to RT at 20°C min^{-1} under flushing N_2 (20 mL min^{-1}).

TEM observation were performed using an EFTEM Leo912 ab (Zeiss, Oberkochen, Germany) transmission electron microscope equipped with a tungsten filament source operating at 100 kV under vacuum. Regarding samples preparation, *ca*. 7 mg of samples were weighted, dispersed and sonicated in water for 15 minutes. The suspension was further homogenized in a vortex mixer (*ca*. 10 s) and then diluted (dilution factor 1:100). 10 µL of the resulting suspension were dropped on 300 mesh formvar/carbon copper grids (Cu 300 FC); grids were then left to dry for 16 h at RT.

Raman spectra have been collected on a micro-Raman spectrometer equipped with a Jasco RPM-100 probe, provided with a notch filter and an Olympus 50x objective and interfaced to the laser and to a Lot-Oriel MS125 spectrometer. Cooling of the detector (Andor CCD, 1024 × 128 pixels) was was operated by a Peltier device. A frequency-doubled Nd:YAG laser emitting at 532 nm was used as excitation source. Spectra have been collected with an acquisition time of 4 s (100 spectra accumulation, background corrected).

Conductivity of HAP/C composites were measured by LSV. The measurement cell consisted of two PVC plates with plugging channels, to provide an electrical contact with top and bottom gold-plated copper electrodes. Powders were placed in a PTFE cylinder, serving as sample holder, further positioned between the PVC plates. The large PVC cap on top of the upper copper electrode is used as the basement for applying the mass used to press the powder inside the cylinder. Applied pressure ranges from 72 kPa to 5.3 MPa. The thickness of the powder sample was monitored by a laser engraved scale on the contact rod of the upper copper electrode. The resistance/conductivity measured were corrected accordingly to the real powders thickness at each precise applied pressure. LSV measures were carried out with a ModuLab®XM ECS potentiostat/galvanostat system (Solartron Analytical XM PSTAT 1 MS/s). Potential was linearly scanned from 2 to 100 mV at a 10 mV s^{-1} scan rate. The slope of applied potential vs registered current was taken as the material's resistance and further converted in conductivity through Ohm's second law.

8.2.3 Structural and morphological characterization of HAP-doped electrocatalysts for CO_2RR

N_2 adsorption/desorption analyses have been performed using a Micromeritics 3Flex Analyzer, operating under the same conditions previously described for similar analyses in paragraph 8.2.1. Low-pressure part of the adsorption branch of the isotherm has been linearized according to the linear 2-parameter BET equation ($0.01 < p/p^0 < 0.35$) whilst the desorption branch has been interpreted by N_2 – DFT model, as to determine specific surface area (S_a) and pore size distribution (PSD), respectively.

Aberration-corrected scanning transmission electron microscopy (AC-STEM) characterization was performed using a JEOL Grand ARM300F with two spherical aberration correctors at 300 kV for both probe-forming and TEM imaging; the instrument was further equipped with an EDX probe for the collection of elemental maps.

XPS measurements were carried out on an AXIS Supra instrument (Kratos Analytical), equipped with a dual anode Al/Ag monochromatic X-ray source. XPS data treatment was performed using CasaXPS software.

8.2.4 Surface acid/base characterization of HAP

Surface acidity and basicity of HAP samples have been determined by means of liquid-solid acid/base titration. Because of the different nature of "bare" HAP and HAP/CMC composites, different techniques have been applied, namely Liquid Recirculation Chromatographic Method (LRCM, closed-line conditions) and pulsed-injections mode, respectively detailed in the following paragraphs 8.2.4.1 and 8.2.4.2.

8.2.4.1 LRCM liquid-phase acid/base titration of HAP

Quantification of surface acid and basic sites of "bare" HAP was performed by liquid-solid phase titration, using 2-phenylethylamine (PEA) and benzoic acid (BA) as basic and acid probe, respectively. Titrations were carried out in cyclohexane (determination of intrinsic acidity and basicity, I.A. and I.B.) and in water (effective acidity and basicity, E.A and E.B.). A scheme of the modified HPLC line employed for the titrations is reported in Figure 72.

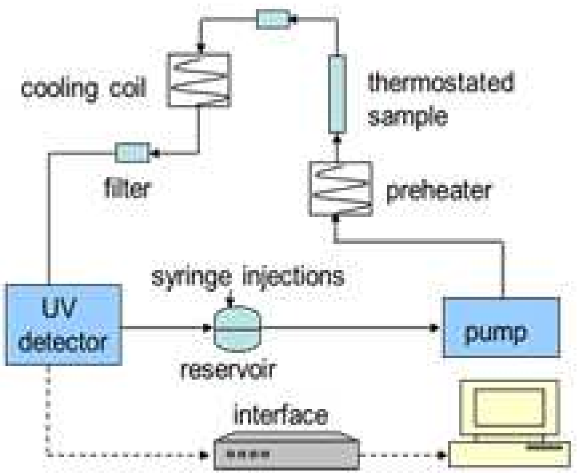

Figure 72: Scheme of the closed modified HPLC line employed for liquid-phase acid/base titrations according to LRCM principles

Dried HAP sample (*ca*. 80 mg, crushed and sieved as 80-200 mesh particles) was placed in a sample holder (stainless steel tube, Ø = 2 mm, h = 12 cm) between two sand pillows. HAP sample was then activated by thermal treatment (150°C in 8 mL min^{-1} air flux for 4 h) and successively vacuum-wetted with the appropriate solvent (water or cyclohexane). The sample holder was then mounted on a recirculation modified chromatographic line (HPLC), equipped with a Waters 515 pump and a monochromatic UV detector (Waters, model 2487, working at fixed $\lambda = 254$ nm). During the analyses, the sample was thermostated at 30.0 ± 0.1°C.

By means of successive injections of known amounts of PEA (50 µL, *ca*. 0.10 M in both solvents) or BA (50 µL, *ca*. 0.05 M in cyclohexane and *ca*. 0.025 M in water) solutions, a characteristic "step chromatogram" was obtained: each step indicates the achieving of adsorption equilibrium.

After the collection of a first adsorption isotherm (I run), pure solvent was flowed through the saturated sample for *ca*. 16 h, thus permitting desorption of the probe molecules adsorbed on weakly interacting sites. Then, a second PEA or BA titration was performed on the same sample (II run), as to discriminate strong and weak adsorption sites.

Details on the numerical treatment of collected data are reported in supplementary material, paragraph 10.1.1.

8.2.4.2 Pulsed-injection mode liquid-phase acid/base titration of HAP/C composites

In the case of HAP/CMC composites, the quantification of surface acid/basic sites has been performed according to a pulsed-injection titration method, a slightly modified procedure in respect with the recirculation mode liquid-phase titration reported in paragraph 8.2.4.1. The modified HPLC line was constituted by a L-6200 A Merck Hitachi pump, a AS-2000A Merck Hitachi autosampler and a UV-Visible L-4250 Merck Hitachi detector operating at 254 nm (Figure 73).

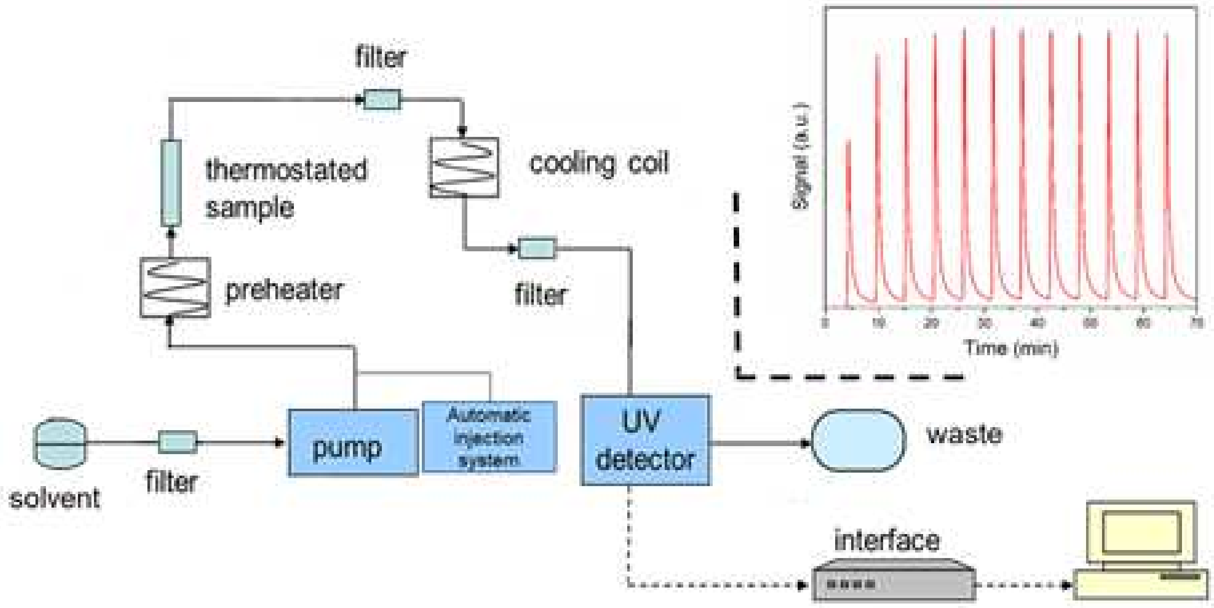

Figure 73: Scheme of the modified HPLC line for pulse liquid-solid titrations (main figure) and a typical chromatogram obtained from an acid/basic titration (inset).

Same acid/basic probes have been used (2-phenylethylamine, PEA, and benzoic acid, BA). Even in this case, titrations were carried out in cyclohexane (determination of intrinsic acidity and basicity, I.A. and I.B.) and in water (effective acidity and basicity, E.A and E.B.).

Previous to the actual experiment, a dried sample mass of *ca*. 20 mg was crushed, sieved as 80-200 mesh particles, and then placed in a sample holder (stainless steel tube, Ø = 2 mm, h = 12 cm) between two sand pillows. The sample was then thermally activated for 3 h at 150°C under flowing air (7 mL min^{-1}) and successively vacuum-wetted with the proper solvent. The filled sample holder was then put mounted on the modified HPLC line and thermostated at 30°C (L-5025 Merck column thermostat).

Analysis was carried out with a liquid flow rate of 5 mL min^{-1} and injections of fixed volume of probe solution were regularly made ($\Delta t_{inj} = 5$ min, 10 µL of *ca*. 0.12 M PEA in both solvents for acid sites titration;

Δt_{inj} = 40 min and 40 µL of *ca*. 0.05 M BA in cyclohexane and *ca*. 0.025 M in water for basic sites titration). A chromatogram, constituted by successive increasing peaks, was obtained. Saturation was considered to be reached when for successive injections constant peaks' height and area were obtained. All details regarding the numerical interpretation of the collected data are reported in paragraph 10.2.2.1.

8.2.4.3 Gas-phase acid/base calorimetric titration of HAP

Adsorption microcalorimetry measurements were performed at 80 °C in a heat flow calorimeter (Calvet C80 from Setaram, Figure 74) fitted with a conventional volumetric line and equipped with a Barocel capacitance manometers for pressure measurements.

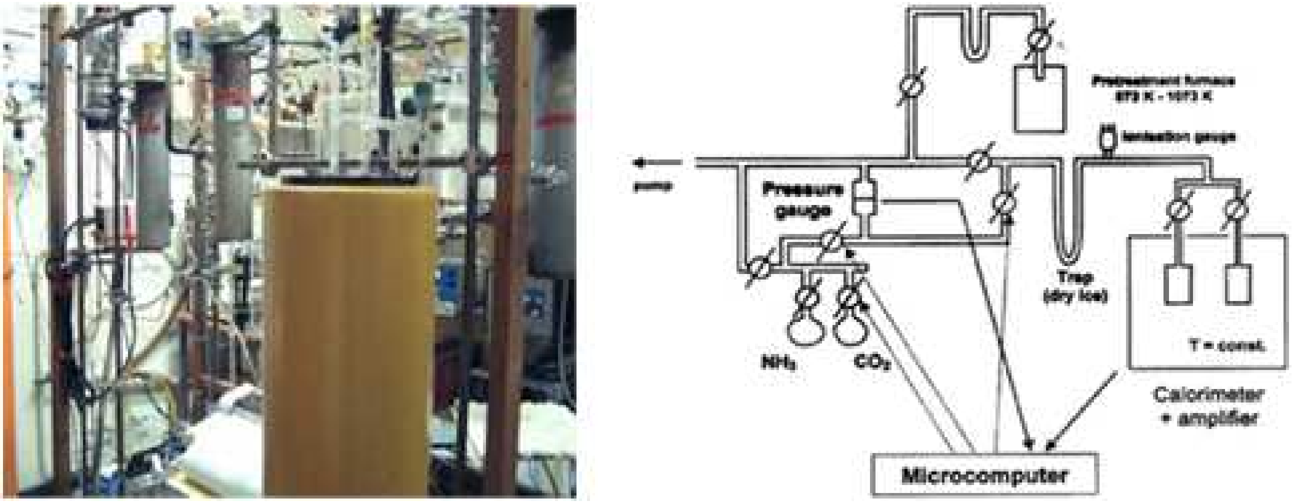

Figure 74: Picture of the differential heat-flow microcalorimeter (left) and related scheme of the volumetric line (right).

C80 calorimeter works in a differential configuration, with two identical calorimetric vessels connected in opposition. During the analysis, one vessel contains the sample under investigation while the other, usually empty, serves as reference. Thanks to the differential assembly of the calorimetric vessels, all parasitic phenomena, such as all thermal effects other than the adsorption onto solid surface of the sample, are compensated. The heat flux derived from the thermopiles was calibrated by Joule effect experiments [239].

During the acid-base titration, volumetric data of adsorption of a chosen acid/basic probes (SO_2 and NH_3) were collected by multi-introduction of dosed amounts of the probe. Adsorbed amount was determined monitoring the decrease of pressure by means of transducer gauges (pressure values are corrected taking into account the gas fall due to the expansion phenomena). Moles of adsorbed ~~gas~~ probe (n_{ads}) were properly expressed per either unit mass ($n_{ads}\ g_{HAP}^{-1}$) or unit surface area ($n_{ads}\ m_{HAP}^{-2}$) of the adsorbent. Once achieved the equilibrium pressure and that corresponding to the heat release during adsorption, successive amount of probe was sent on the sample.

In a typical experiment, *ca*. 100 mg of dried sample were pre-treated in the calorimetric quartz cell for 16 h at 150°C, under a residual pressure of 10^{-2} Pa. NH_3 (Air Liquide, purity > 99.9%) and SO_2 (Air Liquide, purity >99.9%) were used as basic and acid probe, respectively. A high temperature of adsorption (80 °C) was chosen to minimize probes physisorption. The differential heats of adsorption were then measured as a function of coverage/moles of adsorbed probe, introducing by subsequent injections small doses of the adsorbate in the thermostated calorimetric cell. Titrations were considered concluded when an equilibrium pressure of about *ca*. 0.66 mbar was reached (I run). Then, samples were outgassed for 30 min at 80°C, and a second identical titration was performed (up to an equilibrium pressure of *ca*. 0.3 mbar, II run), as to discriminate between reversibly and irreversibly chemisorbed amount of the probe molecules (i.e. distinction between weak and strong adsorption sites towards the probes).

8.3 Pollutants' adsorption tests

8.3.1 Heavy metal cations removal from simulated wastewater by stoichiometric HAP

8.3.1.1 Static batch adsorption tests and adsorption isotherms

HAP adsorption ability towards several metal cations, namely Cu(II), Pb(II), Cr(III), Co(II) and Ni(II) has been evaluated according to a batch method in static condition: this system configuration was employed since similar to industrial remediation procedures in settling/sedimentation tanks.

In a typical experiment, a determined volume of single or multi-metal containing solution was introduced in a test tube containing HAP powders (solid to liquid ratio equal to 10 g_{HAP} L^{-1}) and then placed in a thermostatic bath at 30°C (± 0.1). At given time intervals, the supernatant was collected, diluted as necessary, and analyzed by ICP-AES (Perkin Elmer, Optical Emission Spectrophotometer, Model Optima 8000 DV) or IC-UV/Vis (Dionex DX-120 chromatograph equipped with a derivatization system and a Merck Hitachi L-4200 UV/Vis detector), depending on metal's nature and speciation. Copper, lead, chromium, cobalt and nickel standards (1,000 µg/mL, 2% HNO_3 from Perkin Elmer) were used for both ICP-AES and IC-UV Vis calibrations.

All solutions were prepared using MilliQ water (15.0 MΩ, Millipore) and the corresponding nitrate salts of the above listed metals. Concentration of metal solutions ranged from 15 to 300 ppm. Depending on the test, solution pH has been adjusted at 4, 7 and 9 (± 0.2) by dropwise addition of 0.5 M HNO_3 or NaOH (CyberScan 500 pHmeter equipped with a combined glass electrode).

All adsorption tests were performed in triplicate.

Metal loaded HAP samples (Me-HAP) were separated from liquid by centrifugation/filtration, dried at 120°C for 16 h and then structurally and morphologically characterized according to paragraph 8.2.1. Double check analyses were carried out on selected Me-HAPs: these samples have been mineralized in HNO_3 (65wt. %), diluted and then analyzed by ICP-AES or IC-UV Vis, depending on metal's nature and speciation.

Leaching tests were also performed: *ca.* 0.1 g of metal-loaded HAP were suspended in test tubes containing with 10 mL of deionized water and stirred for 24 h at RT. Metal species content in the supernatants were quantitatively assessed by ICP-AES or IC-UV Vis.

Adsorption isotherms were collected retaining batch adsorption test operative parameters but under vigorous stirring. Initial metal concentration ranges were expanded accordingly to the metal nature and affinity to HAP surface. The time at which the adsorption equilibria was reached depended on metal's nature and was previously assessed by literature checking and explorative tests. Analytical techniques for determination of residual metal concentration and Me-HAP samples characterization are the same presented above.

Equilibrium data gathered from the experiments were then fitted according to the most appropriate theoretical model isotherms. Equations applied in the present study are presented in the 10.1.3.

8.3.1.2 Microcalorimetric study of metal species adsorption onto HAP surface

Thermochemical effects of selected metal cations adsorption onto HAP surface were by means of microcalorimetric titration. Experiments were carried out on a titration heat flow calorimeter with differential configuration (Titrys, from Setaram, Figure 75), fitted with stirred stainless-steel calorimetric cells (h = 80 mm; Ø = 17 mm). The calorimeter was connected to a syringe pump (Figure 75) for a dosed introduction of given amounts of a solution containing known concentration of metal cations.

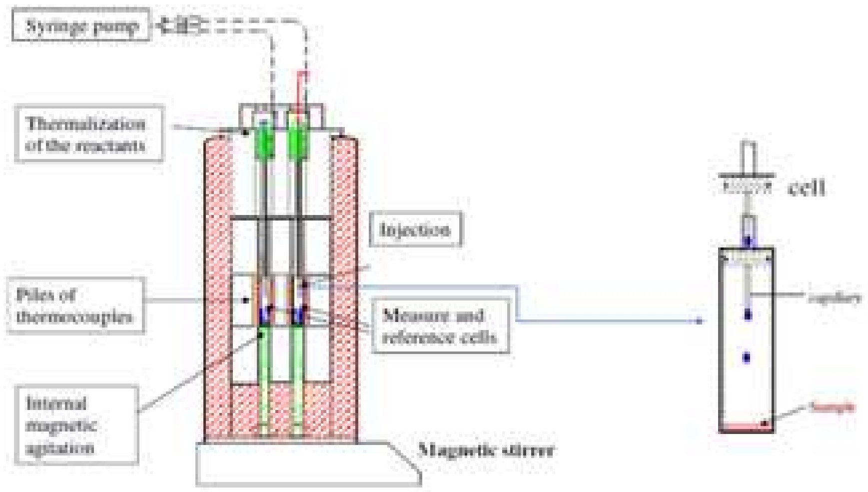

Figure 75: Depiction of the differential microcalorimeter (left) and measurement cell details (right).

On a typical experiment, the reference cell was filled with 1.5 ml N_2 degassed HPLC water while a slurry *ca*. 100 mg of HAP in the same volume of degassed HPLC water was put in the measurement cell. HAP samples were activated ex-situ, by outgassing for 2 h at 150°C. Cells were then thermostated at 30°C. *Ca*. 3 h were needed to ensure a stable heat flux signal.

By means of a programmable syringe pump (PH 2000, Harvard Apparatus), connected to the calorimeter by capillary tubes, successive pulsed injection of known amounts of metal solutions were fed to both reference and measurement cells. A preheating furnace allowed to inject probe solutions at exactly 30°C, thus minimizing the thermal noise of the injection itself. All metal solutions were prepared using degassed HPLC water and the corresponding nitrate salts of the studied metal cations.

Titration conditions has been optimized as a function of the adsorption thermal effect of each metal species, modifying interval time, number and volume of injections. Concentration of metal solutions ranged from 0.05 to 0.3 M and were case by case optimized, considering both the solubility of the metal salts and the experimental thermal response.

8.3.2 Remediation of simultaneous organic and inorganic pollution of simulated wastewater by HAP/C composites

HAP/C composites adsorption ability towards a benchmark inorganic pollutant, namely Cu(II) and Ni(II), has been evaluated according to a batch method in static condition, as reported in paragraph 8.3.1.1. Sorption experiments have been conducted in test tubes, contacting HAP/C composites (solid to liquid ratio equal to 10 $g_{HAP/C}$ L^{-1}) with metal containing solutions (concentration ranging from 300 to 15 ppm) for 2 h at 30°C (thermostatic bath). At the end of the test, the supernatant was collected, diluted as necessary, and analyzed by IC-UV/Vis (Dionex DX-120 chromatograph equipped with a derivatization system and a Merck Hitachi L-4200 UV/Vis detector). Copper and nickel standards (1,000 µg/mL, 2% HNO_3 from Perkin Elmer) were used for both ICP-AES and IC-UV Vis calibrations. All solutions were prepared using MilliQ water (15.0 MΩ, Millipore) and the corresponding nitrate salts of the above listed metals. pH of the solutions was checked before and after the adsorption test.

Ability of HAP/C composite to remove organic pollutants have been tested as well, applying the same experimental procedure reported for inorganic pollutants in paragraph 8.3.1.1. Methylene blue (MB) has been selected as benchmark organic pollutant. The initial concentration of MB in the simulated wastewater was ranging from 250 to 500 ppm. The initial and final MB concentrations were determined by UV-visible spectrophotometry, by measuring the absorbance at the maximum absorption wavelength (λ_{max} = 662 nm) using a Shimadzu UV–3600 spectrophotometer.

Finally, the sorption ability of HAP/CMC materials towards co-present organic and inorganic pollutants has been tested by contacting ternary solutions (300 ppm Cu(II) + 300 ppm Ni(II) + 250 ppm MB) with HAP/CMC composites according same experimental setup detailed in paragraph 8.3.1.1.

After the adsorption tests, pollutant-loaded HAP/C samples were separated from liquid by centrifugation/filtration, dried at 120°C for 16 h. Selected samples underwent leaching tests according to the same experimental procedure reported in paragraph 8.3.1.1.

8.4 Sensing of heavy metal cations in aqueous solution

8.4.1 Crafting of free-standing HAP/C based electrodes

Free-standing HAP/C based electrodes has been crafted in form of sheets by means of a rolling, cutting and shaping procedure of HAP/C pastes containing 8 wt.% of PTFE.

Ca. 155 mg of HAP/C composite have been grinded in an agate mortar and then dispersed in 8-10 mL of absolute ethanol by ultrasonication (2 minutes), as to obtain a homogeneous suspension. 15 µL of PTFE (chemical binder) has been added by a micropipette and the mixture has been ultrasonicated for other 15 minutes. The suspension was then placed on a heating plate and the solvent slowly evaporated. The obtained paste was recovered, rolled, cut and shaped in *ca*. 2x3 cm HAP/C sheets.

A layered electrode was then assembled (Figure 76), composed (bottom to top) by a graphite foil (current collector), conductive glue (E-dug) and HAP/C sheet. Kapton has been used to wrap the final electrode and to preferentially expose a normalized area of *ca*. 0.5x0.5 cm.

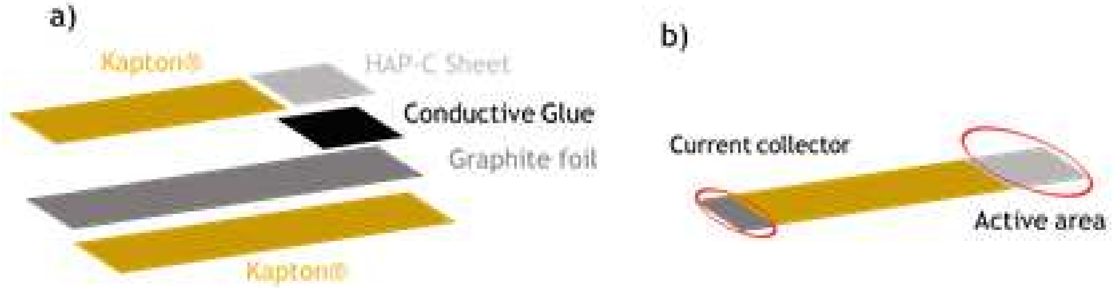

Figure 76: Exploded view of a) the layered HAP/C based electrode and b) final assembled electrode.

Electrodes underwent a final curing process (necessary for conductive glue polymerization) for 30 minutes at 80°C under air and with a 5 kg weight on top.

8.4.2 Cell setup and applied electrochemical techniques

All electrochemical tests aimed to the identification and quantification of metal species in simulated polluted wastewater have been conducted in a 5 mL three-electrode cell. HAP/C based electrodes have been used as working electrodes (WE), a Pt wire has been used as counter electrode (CE) while a saturated calomel electrode (SCE) has been used as reference electrode (RE). Electrochemical data were collected by means of a Gamry Interface 1000 potentiostat/galvanostat. Simulated polluted wastewaters were produced by adding known amounts of metal containing solution (taken from stock standard solutions of corresponding nitrate salts) to a 0.1 M KNO_3 solution. The concentration of metal species in solution varied from *ca*. 10^{-4} to *ca*. 10^{-7} M, depending on the electrochemical response of the metal/HAP/C composite system. When needed, pH was regulated by small additions of 0.5 M HNO_3 or NH_4OH. All solutions were prepared in MilliQ water.

Cyclic voltammetry (CV) has been the electrochemical technique applied for a preliminary system evaluation (response of different HAP/C composite-based electrodes to different metal species, at variable concentration and pH). Analyses were conducted at different potential scan rates (ranging from 10 to 50 mV s^{-1}) in the potential window amid -1.5 and 1.5 V vs SCE.

Square wave anodic stripping voltammetry (SWASV) experiments were performed in order to asses quality and quantity (after adequate calibration) of metal species traces in simulated polluted wastewater. After a variable open-circuit potential period (OCP), dependent on the nature of both the tested HAP/C composite and metal species, cations were accumulated by reduction (reductive pre-concentration step) at the electrode surface by apply for 1 minute a potential of -1.0 V vs SCE. Then, potential has been scanned in the anodic sense (anodic stripping) with a scan rate of 50 mV s^{-1}. Oxidation of reductively pre-concentrated metal species at electrode surface resulted in peculiar peaks: associated potential (i.e. peak position) and current density (i.e. peak height) pertained to metal nature and concentration, respectively.

8.5 Electrocatalytic CO_2RR

The electrocatalytic activity of Cu-based HAP-doped materials has been evaluated in an ad-hoc designed electrochemical flow-cell. The catalysts have been dispersed by spraying on a carbon-based gas diffusion layer (GDL), thus obtaining gas diffusion electrodes (GDEs).

Such GDEs have been assembled in the flow-cell, using Cu-based GDEs as cathodes and commercial Pt/C-based GDE as anodes. Catalysts have been studied under flowing conditions by means of different electrochemical techniques, such as linear sweep voltammetry and chronoamperometry. The products of CO_2RR (and eventual parasite reactions, like HER) at different applied potentials have been collected and further analyzed. Gas phase products have been identified and quantified by GC-TCD analyses whilst liquid phase products were analyzed by ^{1}H NMR.

GDE preparation, cell design and assembly, applied electrochemical techniques and the analytical methods for the determination and quantification of reaction products are detailed in the following paragraphs.

8.5.1 Electrochemical cell setup

8.5.1.1 Preparation of a gas diffusion electrode (GDE)

A proper gas diffusion layer (GDL) was crafted by hot pressing for 10 minutes (210°F, applied pressure *ca*. 6-7 tons m^{-2}) a 5 cm^2 square of Sigracet BC29 carbon paper to a STERLITECH laminated PTFE 1.0 μm pore size membrane filter. Such obtained GDL has been used as physical support for spraying the studied electrocatalysts.

Inks of electrocatalysts have been prepared mixing a precise amount of catalyst (Cu-based for the cathode, commercial Pt/C for the anode) and Nafion solution (5 wt.%) in IPA and sonicating for *ca*. 30 minutes. As rule of thumb, the Nafion/C content of catalyst ratio of the cathode's ink has been set at *ca*. 0.3 and the overall Cu loading on the GDE set at *ca*. 5 mg cm^{-2}. On the other hand, Pt/C based ink (for anodes) have been according to what reported in literature by Sasikumar [240]. The following table summarizes all the details for ink preparation.

Table 30: Desired active phase loading on GDEs and related quantities for ink preparation.

	Electrodic material	**Desired loading**	**$m_{Electrodic\ material}$**	**$V_{Nafion\ solution\ (5\ wt\%)}$**	**V_{IPA}**
	-	*mg cm^{-2}*	*mg*	*μL*	*mL*
Anode	Commercial Pt/C	5.00 (Pt/C)	85.0	60	5-6
Cathode	Synthetic Cu(+HAP)/3D-GNS	0.75 (Cu)	70.0	380	5-7

Once a completely homogeneous ink was obtained, catalyst deposition onto GDE was carried out. GDEs were placed on a heating plate at 135°F, as to guarantee the fast evaporation of the solvent and a regular deposition of the catalyst itself. The top reservoir of a clean spraying gun, connected to an air compressor, was filled up with the electrocatalyst's ink. GDEs were then sprayed in a rastering fashion, homogeneously and letting a few seconds to let the ink dry before each pass. Periodical weighting of the GDEs ensured to reach the desired catalyst loading (Table 30). Once completely dried, electrical connections to GDEs were realized by means of copper tape prior to assembling the electrochemical cell.

8.5.1.2 *Flow-cell assembly and operativity*

The ad-hoc designed electrochemical cell is composed of three pieces, which are assembled as depicted in Figure 77a. Such flow-cell mimics (at lab scale) a CO_2RR electrolyzer, where CO_2 is directly fed to the surface of the electrocatalyst through a GDE-like setup, thus allowing a proper evaluation of the catalyst's performances under industrially relevant conditions.

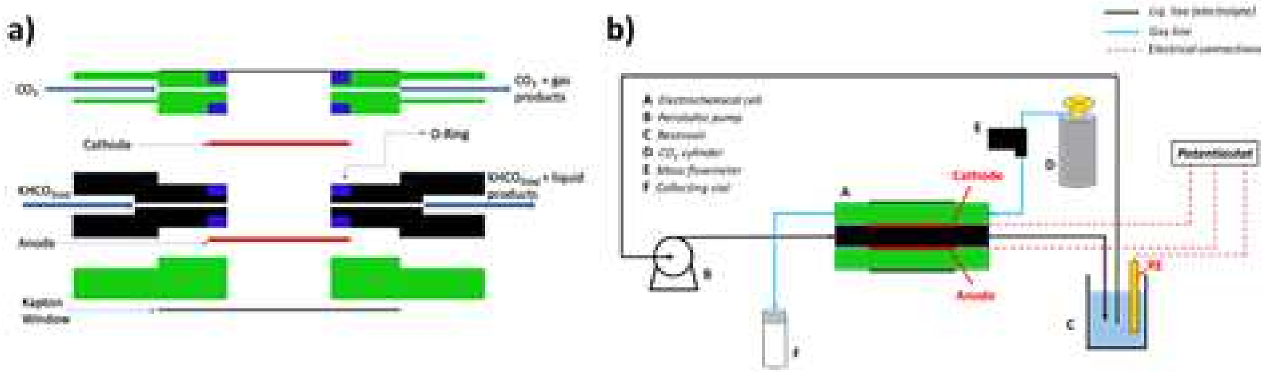

Figure 77: a) Exploded view of the electrochemical flow-cell and b) complete flowsheet of the electrochemical system used to perform CO_2RR tests.

After assembling the cell as reported in Figure 77a, external connections were made as to flow both electrolyte (central part of the cell) and CO_2 (gas chamber on the cathodic compartment of the cell) in the cell. A schematized flowsheet of the system is reported in Figure 77b.

35 mL of a 0.5 $KHCO_3$ aqueous solution (pH *ca*. 8.1), used as electrolyte, was continuously flowed through the central compartment of the cell (Figure 77a) by means of a Masterflex L/S® peristaltic pump, at a flowrate of *ca*. 1 mL min^{-1}. After passing through the cell, the electrolyte was conveyed to a 50 mL beaker, which acted as reservoir. The reference electrode (standard Ag/AgCl) was placed in the beaker and held in place by a ring stand; all electrodes were connected to a BioLogic - SAS, model VSP300 potentiostat, controlled using the EC Lab software interface.

CO_2 was continuously delivered to the cathodic GDE from a CO_2 cylinder (99.99% pure, Matheson) at a constant flowrate of 10.00 sccm by means of an Alicat MC series mass flowmeter. Gases leaving the cell (i.e. unreacted CO_2 and gas phase CO_2RR and HER products) were flushed through the sampling vial.

Electrochemical tests performed on each electrocatalyst followed the scheme reported in Table 31 and were aimed to characterize the system and, in combination with gas and liquid phase sampling, to assess the products distribution in function of the applied potential.

Table 31: Electrochemical techniques applied to the study of CO_2RR electrocatalysts and their derived outcomes

Technique	Outcomes	Parameters
PEIS (*Potentiostatic Electrochemical Impedance Spectroscopy*)	Resistance of the system; Correction of applied potential	Initial E = 0 vs E_{OC} Range: from 200 kHz to 100 mHz N_d = 7 (per decade) Sinus amplitude V_a = 10 mV N_a = 2 (measures per frequency)
CV (*Cyclic Voltammetry*)	Conditioning of the GDE surface	Initial E = -0.5 V vs Ref dE/dt = 500 mV s^{-1} Vertex E = -0.5 V vs Ref Reverse E = -2.4 V vs Ref n = 50 cycles
LSV (*Linear Sweep Voltammetry*)	Evaluation of onset potential of the reaction; Comparison of delivered *i* in the presence and absence of the reactant	Initial E = -0.5 V vs Ref Final E = -2.4 V vs Ref dE/dt = 20 mV s-1 Gas feed: N_2 (blank) or CO_2
CA (*Chronoamperometry*)	Evaluation, together with gas and liquid phase sampling, of products distribution and faradic efficiency at different applied potentials	Potentiostatic scan E range: from -0.9 to -2.0 V vs Ref t = 30 minutes

Knowing the pH of the electrolyte, the applied potential has been first converted from E vs Ag/AgCl to E vs RHE; then calculating the actual resistance of the overall system from PEIS tests, IR-correction of E vs RHE have been performed. All the electrochemical data are indeed reported as E vs RHE – IR Corrected, in terms of potentials.

Both gas and liquid phase were sampled at the end of each chronoamperometric scan, as to determine the nature and quantity of CO_2RR and thus, the related faradic efficiency.

Gas phase sampling was allowed by the presence of a sampling vial on the outlet of the cathodic gas chamber, as depicted in Figure 77b. The continuous flow of the exiting gas mixture guaranteed a complete purging of the vial from air; sampling was carried out by contemporary pulling out the secondary exit needle and the outlet tube from the septum *ca.* 30 seconds before the end of the chronoamperometric step.

Liquid phase was instead sampled, at the end of each chronoamperometric scan, withdrawing precise and known amounts of electrolyte from the reservoir with a micropipette and then refilling with the same amount of fresh electrolyte.

Both liquid and gas phase samples were stocked and further analyzed as detailed in the next paragraph to detect and quantify CO_2RR products.

8.5.2 Analysis of gas and liquid phase products

Gas phase products have been separated and identified by means of gas chromatography coupled with a thermal conductivity detector (GC/TCD). Experimentally, 200 µL were withdrawn from the vial using a 500 µL Vici® gas-tight syringe and injected in an Agilent 7890 gas chromatograph mounting a 19095P-MS6 HP MOLSIEVE Column (Ø = 530 µm length = 30m). Different gas carriers, oven temperatures and flowrates have been used for the determination of different gas phase products.

H_2 has been separated by the columns at 40°C using N_2 as gas carrier (flowrate = 27.7 mL min^{-1}) while CO and CH_4 separation method involved the same parameters but He as carrier (flowrate = 57.7 mL min^{-1}).

Peaks were previously assigned to specific molecules performing injections of the above-mentioned gases; calibration lines (peak area vs. V/V% or μmol) were obtained too, injecting the same gases at different concentration (dilution performed with N_2). The last of expected products, ethylene, was not directly detected; it concentration, and thus faradic efficiency, was calculated by difference from the total charged passed through the system during the CA scan (Q_{tot}) and the sum of all partial charges obtained from all the other detected products (ΣQ_i) applying Faraday's second law of electrolysis.

Calibration of N_2 and O_2 signals were as well performed through injection of different volumes of atmospheric air; the knowledge of the relation between N_2 and O_2 peak area vs $V_{air\ injected}$ allowed an accurate evaluation of air contamination in the samples and thus the calculation of their real concentration.

All peaks integrations have been performed manually using the dedicated tool in Agilent Clarity interface.

Liquid phase products were detected and quantified by quantitative ^{1}H NMR, applying the internal standard method. Briefly, 0.1 mL of D_2O and 0.1 mL of 6 mM DSS (2,2-Dimethyl-2-silapentane-5-sulfonate, internal standard) were added to 0.5 mL of the sample in an NMR tube. ^{1}H NMR spectra of the samples were then acquired using a Bruker CRYO500 MHz NMR spectrometer with a 6 sec pre-scan delay, an acquisition time of 106 s for a total number of 16 scans. The free induction decays (FIDs) were weighted by a 90-degree phase-shifted sine-bell function before Fourier transformation. The signal of water, standing around at 4.78 ppm, have been systematically suppressed using pulsed field gradients method. NMR peaks have been assigned to each CO_2RR product by comparison with NMR spectra collected on standard solution. Quantitative evaluation of such products has been carried out using the internal standard method and the peak area ratio, also taking into account the multiplicity (i.e. number of protons) of the signals themselves. The applied formula was:

$$C_x = \frac{A_x}{A_{Cal}} \times \frac{N_{Cal}}{N_x} \times C_{Cal}$$

where C is the molar concentration, A the peak area and N the multiplicity associated with the peak, with subscripts x and Cal indicating the compound under study and the internal standard, DSS, respectively.

The DSS peak selected for the formula application was the singlet positioned at chemical shift 0 ppm, with multiplicity equal to 9.

9 References

[1] E.M. Rivera-Munoz, Hydroxyapatite-Based Materials: Synthesis and Characterization, in: Biomed. Eng. - Front. Challenges, InTech, 2011: pp. 75–98. doi:10.5772/19123.

[2] H.B. Lu, C.T. Campbell, D.J. Graham, B.D. Ratner, Surface characterization of hydroxyapatite and related calcium phosphates by XPS and TOF-SIMS, Anal. Chem. 72 (2000) 2886–2894. doi:10.1021/ac990812h.

[3] P.N. Kumta, C. Sfeir, D.H. Lee, D. Olton, D. Choi, Nanostructured calcium phosphates for biomedical applications: Novel synthesis and characterization, Acta Biomater. 1 (2005) 65–83. doi:10.1016/j.actbio.2004.09.008.

[4] M. Mucalo, Hydroxyapatite (Hap) for Biomedical Applications, Elsevier, 2015. doi:10.1016/C2013-0-16440-9.

[5] N. Ramesh, S.C. Moratti, G.J. Dias, Hydroxyapatite–polymer biocomposites for bone regeneration: A review of current trends, J. Biomed. Mater. Res. - Part B Appl. Biomater. 106 (2018) 2046–2057. doi:10.1002/jbm.b.33950.

[6] W.S.W. Harun, R.I.M. Asri, J. Alias, F.H. Zulkifli, K. Kadirgama, S.A.C. Ghani, J.H.M. Shariffuddin, A comprehensive review of hydroxyapatite-based coatings adhesion on metallic biomaterials, Ceram. Int. 44 (2018) 1250–1268. doi:10.1016/j.ceramint.2017.10.162.

[7] H. Tounsi, S. Djemal, C. Petitto, G. Delahay, Copper loaded hydroxyapatite catalyst for selective catalytic reduction of nitric oxide with ammonia, Appl. Catal. B Environ. 107 (2011) 158–163. doi:10.1016/j.apcatb.2011.07.009.

[8] A. Fihri, C. Len, R.S. Varma, A. Solhy, Hydroxyapatite: A review of syntheses, structure and applications in heterogeneous catalysis, Coord. Chem. Rev. 347 (2017) 48–76. doi:10.1016/j.ccr.2017.06.009.

[9] S. Campisi, M.G. Galloni, F. Bossola, A. Gervasini, Comparative performance of copper and iron functionalized hydroxyapatite catalysts in NH 3 -SCR, Catal. Commun. 123 (2019) 79–85. doi:10.1016/j.catcom.2019.02.008.

[10] M. Schiavoni, S. Campisi, P. Carniti, A. Gervasini, T. Delplanche, Focus on the catalytic performances of Cu-functionalized hydroxyapatites in NH3-SCR reaction, Appl. Catal. A Gen. 563 (2018) 43–53. doi:10.1016/j.apcata.2018.06.020.

[11] M. Ibrahim, M. Labaki, J.M. Giraudon, J.F. Lamonier, Hydroxyapatite, a multifunctional material for air, water and soil pollution control: A review, J. Hazard. Mater. 383 (2020) 121139. doi:10.1016/j.jhazmat.2019.121139.

[12] A. Corami, S. Mignardi, V. Ferrini, Copper and zinc decontamination from single- and binary-metal solutions using hydroxyapatite, J. Hazard. Mater. 146 (2007) 164–170. doi:10.1016/j.jhazmat.2006.12.003.

[13] Y. Feng, J.L. Gong, G.M. Zeng, Q.Y. Niu, H.Y. Zhang, C.G. Niu, J.H. Deng, M. Yan, Adsorption of Cd (II) and Zn (II) from aqueous solutions using magnetic hydroxyapatite nanoparticles as adsorbents, Chem. Eng. J. 162 (2010) 487–494. doi:10.1016/j.cej.2010.05.049.

[14] I. Smičiklas, S. Dimović, I. Plećaš, M. Mitrić, Removal of Co2+from aqueous solutions by hydroxyapatite, Water Res. 40 (2006) 2267–2274. doi:10.1016/j.watres.2006.04.031.

[15] S. Campisi, C. Castellano, A. Gervasini, Tailoring the structural and morphological properties of

hydroxyapatite materials to enhance the capture efficiency towards copper(II) and lead(II) ions, New J. Chem. 42 (2018) 4520–4530. doi:10.1039/C8NJ00468D.

[16] I. Mobasherpour, E. Salahi, M. Pazouki, Comparative of the removal of Pb2+, Cd2+and Ni2+by nano crystallite hydroxyapatite from aqueous solutions: Adsorption isotherm study, Arab. J. Chem. 5 (2012) 439–446. doi:10.1016/j.arabjc.2010.12.022.

[17] M. Ferri, S. Campisi, M. Scavini, C. Evangelisti, P. Carniti, A. Gervasini, In-depth study of the mechanism of heavy metal trapping on the surface of hydroxyapatite, Appl. Surf. Sci. 475 (2019) 397–409. doi:10.1016/j.apsusc.2018.12.264.

[18] M.P. Mahabole, R.U. Mene, R.S. Khairnar, Gas sensing and dielectric studies on cobalt doped hydroxyapatite thick films, Adv. Mater. Lett. 4 (2013) 46–52. doi:10.5185/amlett.2013.icnano.146.

[19] M. Nagai, T. Saeki, T. Nishino, Carbon Dioxide Sensor Mechanism of Porous Hydroxyapatite Ceramics, J. Am. Ceram. Soc. 73 (1990) 1456–1460. doi:10.1111/j.1151-2916.1990.tb05228.x.

[20] R.U. Mene, M.P. Mahabole, R.S. Khairnar, Surface modified hydroxyapatite thick films for CO2 gas sensing application: Effect of swift heavy ion irradiation, Radiat. Phys. Chem. 80 (2011) 682–687. doi:10.1016/j.radphyschem.2011.02.002.

[21] M.P. Mahabole, R.C. Aiyer, C. V. Ramakrishna, B. Sreedhar, R.S. Khairnar, Synthesis, characterization and gas sensing property of hydroxyapatite ceramic, Bull. Mater. Sci. 28 (2005) 535–545. doi:10.1007/BF02706339.

[22] L.J. Cummings, M.A. Snyder, K. Brisack, Chapter 24 Protein Chromatography on Hydroxyapatite Columns, Methods Enzymol. 463 (2009) 387–404. doi:10.1016/S0076-6879(09)63024-X.

[23] S.K. Swain, D. Sarkar, Study of BSA protein adsorption/release on hydroxyapatite nanoparticles, Appl. Surf. Sci. 286 (2013) 99–103. doi:10.1016/j.apsusc.2013.09.027.

[24] D.R.K. Weerasuriya, W.P.S.L. Wijesinghe, R.M.G. Rajapakse, Encapsulation of anticancer drug copper bis(8-hydroxyquinoline) in hydroxyapatite for pH-sensitive targeted delivery and slow release, Mater. Sci. Eng. C. 71 (2017) 206–213. doi:10.1016/j.msec.2016.10.010.

[25] A. Haider, S. Haider, S.S. Han, I.K. Kang, Recent advances in the synthesis, functionalization and biomedical applications of hydroxyapatite: a review, RSC Adv. 7 (2017) 7442–7458. doi:10.1039/c6ra26124h.

[26] S.M. Mousa, N.S. Ammar, H.A. Ibrahim, Removal of lead ions using hydroxyapatite nano-material prepared from phosphogypsum waste, J. Saudi Chem. Soc. 20 (2016) 357–365. doi:10.1016/j.jscs.2014.12.006.

[27] M. Ozawa, K. Satake, S. Suzuki, Removal of aqueous manganese using fish bone hydroxyapatite, J. Mater. Sci. Lett. 22 (2003) 1363–1364. doi:10.1023/A:1025795529901.

[28] G.S. Kumar, E.K. Girija, Flower-like hydroxyapatite nanostructure obtained from eggshell: A candidate for biomedical applications, Ceram. Int. 39 (2013) 8293–8299. doi:10.1016/j.ceramint.2013.03.099.

[29] P. Perrin, O.J. Bodson, T. Delplanche, D. Breugelmans, PROCESS FOR PRODUCING A CALCIUM PHOSPHATE REACTANT, REACTANT OBTAINED AND USE THEREOF IN THE PURIFICATION OF LIQUID EFFLUENTS, 2015. doi:PCT/EP2015/060923.

[30] S.J. Joris, C.H. Amberg, The nature of deficiency in nonstoichiometric hydroxyapatites. II. Spectroscopic studies of calcium and strontium hydroxyapatites, J. Phys. Chem. 75 (1971) 3172–

3178. doi:10.1021/j100689a025.

[31] S. Raynaud, E. Champion, D. Bernache-Assollant, P. Thomas, Calcium phosphate apatites with variable Ca/P atomic ratio I. Synthesis, characterisation and thermal stability of powders, Biomaterials. 23 (2002) 1065–1072. doi:10.1016/S0142-9612(01)00218-6.

[32] T. Tsuchida, J. Kubo, T. Yoshioka, S. Sakuma, T. Takeguchi, W. Ueda, Reaction of ethanol over hydroxyapatite affected by Ca/P ratio of catalyst, J. Catal. 259 (2008) 183–189. doi:10.1016/j.jcat.2008.08.005.

[33] L. Silvester, J.F. Lamonier, R.N. Vannier, C. Lamonier, M. Capron, A.S. Mamede, F. Pourpoint, A. Gervasini, F. Dumeignil, Structural, textural and acid-base properties of carbonate-containing hydroxyapatites, J. Mater. Chem. A. 2 (2014) 11073–11090. doi:10.1039/c4ta01628a.

[34] T. Tsuchida, J. Kubo, T. Yoshioka, S. Sakuma, T. Takeguchi, W. Ueda, Reaction of ethanol over hydroxyapatite affected by Ca/P ratio of catalyst, J. Catal. 259 (2008) 183–189. doi:10.1016/j.jcat.2008.08.005.

[35] M.I. Kay, A.S. Young, R.A. Posner, Crystal Structure of Hydroxyapatite, Nat. Chem. 204 (1964) 1050–1052. doi:https://doi.org/10.1038/2041050a0.

[36] A.S. Posner, A. Perloff, A.F. Diorio, Refinement of the hydroxyapatite structure, Acta Crystallogr. 11 (1958) 308–309. doi:10.1107/s0365110x58000815.

[37] P.A. Brunton, R.P.W. Davies, J.L. Burke, A. Smith, A. Aggeli, S.J. Brookes, J. Kirkham, Treatment of early caries lesions using biomimetic self-assembling peptides-A clinical safety trial, Br. Dent. J. 215 (2013) 1–6. doi:10.1038/sj.bdj.2013.741.

[38] A. Fihri, C. Len, R.S. Varma, A. Solhy, Hydroxyapatite: A review of syntheses, structure and applications in heterogeneous catalysis, Coord. Chem. Rev. 347 (2017) 48–76. doi:10.1016/j.ccr.2017.06.009.

[39] S.D. Jiang, Q.Z. Yao, G.T. Zhou, S.Q. Fu, Fabrication of hydroxyapatite hierarchical hollow microspheres and potential application in water treatment, J. Phys. Chem. C. 116 (2012) 4484–4492. doi:10.1021/jp211648x.

[40] S.K. Saha, A. Banerjee, S. Banerjee, S. Bose, Synthesis of nanocrystalline hydroxyapatite using surfactant template systems: Role of templates in controlling morphology, Mater. Sci. Eng. C. 29 (2009) 2294–2301. doi:10.1016/j.msec.2009.05.019.

[41] and T.T. Pierre Layrolle, Atsuo Ito, Sol – Gel Synthesis of Amorphous Calcium Phosphate and Sintering into Bioceramics, Microporous Hydroxyapatite, J. Am. Ceram. Soc. 28 (1998).

[42] S. Recillas, V. Rodríguez-Lugo, M.L. Montero, S. Viquez-Cano, L. Hernandez, V.M. Castaño, Studies on the precipitation behavior of calcium phosphate solutions, J. Ceram. Process. Res. 13 (2012) 5–10.

[43] J.C. Elliott, Structure and chemistry of the apatites and other calcium orthophosphates, Elsevier, 2013.

[44] L.C. Bell, A.M. Posner, J.P. Quirk, The Point of Zero Charge of Hydroxyapatite and Fluoropatite in Aqueous Solutions, J. Colloid. Inter. Sci. 42 (1973) 250–261.

[45] K. Skartsila, N. Spanos, Surface characterization of hydroxyapatite: Potentiometric titrations coupled with solubility measurements, J. Colloid Interface Sci. 308 (2007) 405–412. doi:10.1016/j.jcis.2006.12.049.

[46] I.D. Smičiklas, S.K. Milonjić, P. Pfendt, S. Raičević, The point of zero charge and sorption of cadmium

(II) and strontium (II) ions on synthetic hydroxyapatite, Sep. Purif. Technol. 18 (2000) 185–194. doi:10.1016/S1383-5866(99)00066-0.

[47] V.P. Orlovskii, V.S. Komlev, S.M. Barinov, Hydroxyapatite and hydroxyapatite-based ceramics, Inorg. Mater. 38 (2002) 973–984. doi:10.1023/A:1020585800572.

[48] S. Raynaud, E. Champion, D. Bernache-assollant, J. Laval, Determination of Calcium / Phosphorus Atomic Ratio of, J. Am. Ceram. Soc. 84 (2001) 359–366.

[49] K. Haberko, M.M. Bućko, J. Brzezińska-Miecznik, M. Haberko, W. Mozgawa, T. Panz, A. Pyda, J. Zarebski, Natural hydroxyapatite - Its behaviour during heat treatment, J. Eur. Ceram. Soc. 26 (2006) 537–542. doi:10.1016/j.jeurceramsoc.2005.07.033.

[50] Q. Liu, J.P. Matinlinna, Z. Chen, C. Ning, G. Ni, H. Pan, B.W. Darvell, Effect of thermal treatment on carbonated hydroxyapatite: Morphology, composition, crystal characteristics and solubility, Ceram. Int. 41 (2015) 6149–6157. doi:10.1016/j.ceramint.2014.11.062.

[51] J. Gupta, M. Agarwal, Biodiesel production from a mixture of vegetable oils using marble slurry derived heterogeneous catalyst, Curr. Trends Biomed. Eng. Biosci. 5 (2017) 1–5.

[52] B. Yan, Y. Zhang, G. Chen, R. Shan, W. Ma, C. Liu, The utilization of hydroxyapatite-supported CaO-CeO2catalyst for biodiesel production, Energy Convers. Manag. 130 (2016) 156–164. doi:10.1016/j.enconman.2016.10.052.

[53] Y. Sun, Z. Qu, D. Chen, H. Wang, F. Zhang, Q. Fu, Formaldehyde catalytic oxidation over hydroxyapatite modified with various organic molecules, Chinese J. Catal. 35 (2014) 1927–1936. doi:10.1016/S1872-2067(14)60129-7.

[54] H. Nishikawa, T. Oka, N. Asai, H. Simomichi, T. Shirai, M. Fuji, Oxidative decomposition of volatile organic compounds using thermally-excited activity of hydroxyapatite, Appl. Surf. Sci. 258 (2012) 5370–5374. doi:10.1016/j.apsusc.2012.02.011.

[55] A. Rapacz-Kmita, A. Ślósarczyk, Z. Paszkiewicz, Mechanical properties of HAp-ZrO2 composites, J. Eur. Ceram. Soc. 26 (2006) 1481–1488. doi:10.1016/j.jeurceramsoc.2005.01.059.

[56] G. Tripathi, B. Basu, A porous hydroxyapatite scaffold for bone tissue engineering: Physico-mechanical and biological evaluations, Ceram. Int. 38 (2012) 341–349. doi:10.1016/j.ceramint.2011.07.012.

[57] J.P. Gittings, C.R. Bowen, A.C.E. Dent, I.G. Turner, F.R. Baxter, J.B. Chaudhuri, Electrical characterization of hydroxyapatite-based bioceramics, Acta Biomater. 5 (2009) 743–754. doi:10.1016/j.actbio.2008.08.012.

[58] Y. Tanaka, M. Kikuchi, K. Tanaka, K. Hashimoto, J. Hojo, M. Nakamura, A. Nagai, T. Sugiyama, F. Munakata, K. Yamashita, Fast oxide ion conduction due to carbonate substitution in hydroxyapatite, J. Am. Ceram. Soc. 93 (2010) 3577–3579. doi:10.1111/j.1551-2916.2010.04105.x.

[59] X. Wei, M.Z. Yates, Yttrium-doped hydroxyapatite membranes with high proton conductivity, Chem. Mater. 24 (2012) 1738–1743. doi:10.1021/cm203355h.

[60] K. Yamashita, K. Kitagaki, T. Umegaki, Thermal Instability and Proton Conductivity of Ceramic Hydroxyapatite at High Temperatures, J. Am. Ceram. Soc. 78 (1995) 1191–1197. doi:10.1111/j.1151-2916.1995.tb08468.x.

[61] K. Yamashita, H. Owada, T. Umegaki, T. Kanazawa, K. Katayama, Protonic conduction in yttrium-substituted hydroxyapatite ceramics and their applicability to H2-O2 fuel cell, Solid State Ionics. 40–

41 (1990) 918–921. doi:10.1016/0167-2738(90)90153-I.

[62] X. Wang, X. Feng, J. Shang, Y. Jin, C. Zhang, Photocatalytic Reduction of CO2 Using Titanium-Substituted and Fluorine-Doped Titanium-Substituted Hydroxyapatite as Photocatalysts, Catal. Letters. 147 (2017) 2706–2713. doi:10.1007/s10562-017-2175-5.

[63] R. Chong, Y. Fan, Y. Du, L. Liu, Z. Chang, D. Li, Hydroxyapatite decorated TiO2 as efficient photocatalyst for selective reduction of CO2 with H2O into CH4, Int. J. Hydrogen Energy. 3 (2018) 22329–22339. doi:10.1016/j.ijhydene.2018.10.045.

[64] F. Kim, W., Zhang, Q. & Saito, Mechanochemical synthesis of hydroxyapatite from Ca(OH)2-P2O5 and CaO-Ca(OH)2-P2O5 mixtures, J. Mater. Sci. 35 (2000) 5401–5405. doi:https://doi.org/10.1023/A:1004859231795.

[65] M.H. Fathi, E. Mohammadi Zahrani, Mechanical alloying synthesis and bioactivity evaluation of nanocrystalline fluoridated hydroxyapatite, J. Cryst. Growth. 311 (2009) 1392–1403. doi:10.1016/j.jcrysgro.2008.11.100.

[66] P. Honarmandi, P. Honarmandi, A. Shokuhfar, B. Nasiri-Tabrizi, R. Ebrahimi-Kahrizsangi, Milling media effects on synthesis, morphology and structural characteristics of single crystal hydroxyapatite nanoparticles, Adv. Appl. Ceram. 109 (2010) 117–122. doi:10.1179/174367509X12447975734230.

[67] B. Yeong, X. Junmin, J. Wang, Mechanochemical Synthesis of Hydroxyapatite from Calcium Oxide and Brushite, J. Am. Ceram. Soc. 84 (2004) 465–67. doi:10.1111/j.1151-2916.2001.tb00681.x.

[68] C.C. Silva, A.G. Pinheiro, R.S. de Oliveira, J.C. Góes, N. Aranha, L.R. de Oliveira, A.S.B. Sombra, Properties and in vivo investigation of nanocrystalline hydroxyapatite obtained by mechanical alloying, Mater. Sci. Eng. C. 24 (2004) 549–554. doi:10.1016/j.msec.2004.02.004.

[69] M.-F. Hsieh, L.-H. Perng, T.-S. Chin, H.-G. Perng, Phase purity of sol–gel-derived hydroxyapatite ceramic, Biomaterials. 22 (2001) 2601–2607. doi:10.1016/S0142-9612(00)00448-8.

[70] W. Feng, L. Mu-Sen, L. Yu-Peng, Q. Yong-Xin, A simple sol-gel technique for preparing hydroxyapatite nanopowders, Mater. Lett. 59 (2005) 916–919. doi:10.1016/j.matlet.2004.08.041.

[71] G. Velu, B. Gopal, Preparation of nanohydroxyapatite by a Sol-Gel method using alginic acid as a complexing agent, J. Am. Ceram. Soc. 92 (2009) 2207–2211. doi:10.1111/j.1551-2916.2009.03221.x.

[72] A.H. Rajabi-Zamani, A. Behnamghader, A. Kazemzadeh, Synthesis of nanocrystalline carbonated hydroxyapatite powder via nonalkoxide sol-gel method, Mater. Sci. Eng. C. 28 (2008) 1326–1329. doi:10.1016/j.msec.2008.02.001.

[73] I.S. Kim, P.N. Kumta, Sol-gel synthesis and characterization of nanostructured hydroxyapatite powder, Mater. Sci. Eng. B Solid-State Mater. Adv. Technol. 111 (2004) 232–236. doi:10.1016/j.mseb.2004.04.011.

[74] H. Eshtiagh-Hosseini, M.R. Housaindokht, M. Chahkandi, Effects of parameters of sol-gel process on the phase evolution of sol-gel-derived hydroxyapatite, Mater. Chem. Phys. 106 (2007) 310–316. doi:10.1016/j.matchemphys.2007.06.002.

[75] J. Chen, Y. Wang, X. Chen, L. Ren, C. Lai, W. He, Q. Zhang, A simple sol-gel technique for synthesis of nanostructured hydroxyapatite, tricalcium phosphate and biphasic powders, Mater. Lett. 65 (2011) 1923–1926. doi:10.1016/j.matlet.2011.03.076.

[76] K. Sakamoto, S. Yamaguchi, A. Nakahira, M. Kaneno, M. Okazaki, J. Ichihara, Y. Tsunawaki, J.C. Elliott,

Shape-controlled synthesis of hydroxyapatite from α-tricalcium bis(orthophosphate) in organic-aqueous binary systems, J. Mater. Sci. 37 (2002) 1033–1041. doi:10.1023/A:1014316401945.

[77] H.C. Park, D.J. Baek, Y.M. Park, S.Y. Yoon, R. Stevens, Thermal stability of hydroxyapatite whiskers derived from the hydrolysis of α-TCP, J. Mater. Sci. 39 (2004) 2531–2534. doi:10.1023/B:JMSC.0000020021.82216.6b.

[78] C. Durucan, P.W. Brown, A-Tricalcium Phosphate Hydrolysis To Hydroxyapatite At and Near Physiological Temperature, J. Mater. Sci. Mater. Med. 11 (2000) 365–371. doi:10.1023/A:1008934024440.

[79] J. Reichert, J.G.P. Binner, An evaluation of hydroxyapatite-based filters for removal of heavy metal ions from aqueous solutions, J. Mater. Sci. 31 (1996) 1231–1241. doi:10.1007/BF00353102.

[80] A. Corami, S. Mignardi, V. Ferrini, Cadmium removal from single- and multi-metal (Cd + Pb + Zn + Cu) solutions by sorption on hydroxyapatite, J. Colloid Interface Sci. 317 (2008) 402–408. doi:10.1016/j.jcis.2007.09.075.

[81] C. Lamonier, J.F. Lamonier, B. Aellach, A. Ezzamarty, J. Leglise, Specific tuning of acid/base sites in apatite materials to enhance their methanol thiolation catalytic performances, Catal. Today. 164 (2011) 124–130. doi:10.1016/j.cattod.2010.10.035.

[82] W. Janusz, E. Skwarek, The study of the properties of the hydroxyapatite/electrolyte interface, Ann. UMCS, Chem. 64 (2009). doi:10.2478/v10063-008-0003-x.

[83] S. Diallo-Garcia, M. Ben Osman, J.M. Krafft, S. Casale, C. Thomas, J. Kubo, G. Costentin, Identification of surface basic sites and acid-base pairs of hydroxyapatite, J. Phys. Chem. C. 118 (2014) 12744–12757. doi:10.1021/jp500469x.

[84] X. Chen, J. V Wright, J.L. Conca, L.M. Peurrung, EVALUATION OF HEAVY METAL REMEDIATION USING MINERAL APATITE The United States Environmental Protection Agency (US EPA) Land Disposal Restrictions (LDR) Program sets treatment standards for the wastes banned from land disposal (US EPA , 1990). The tr, (2000) 57–78.

[85] I. Mobasherpour, E. Salahi, M. Pazouki, Removal of nickel (II) from aqueous solutions by using nano-crystalline calcium hydroxyapatite, J. Saudi Chem. Soc. 15 (2011) 105–112. doi:10.1016/j.jscs.2010.06.003.

[86] C. Stötzel, F.A. Müller, F. Reinert, F. Niederdraenk, J.E. Barralet, U. Gbureck, Ion adsorption behaviour of hydroxyapatite with different crystallinities, Colloids Surfaces B Biointerfaces. 74 (2009) 91–95. doi:10.1016/j.colsurfb.2009.06.031.

[87] S.B. Chen, Y.B. Ma, L. Chen, K. Xian, Adsorption of aqueous Cd2+, Pb2+, Cu2+ ions by nano-hydroxyapatite: Single-and multi-metal competitive adsorption study, Geochem. J. 44 (2010) 233–239. doi:10.2343/geochemj.1.0065.

[88] A.I. Adeogun, E.A. Ofudje, M.A. Idowu, S.O. Kareem, S. Vahidhabanu, B. Ramesh Babu, Biowaste-Derived Hydroxyapatite for Effective Removal of Reactive Yellow 4 Dye: Equilibrium, Kinetic, and Thermodynamic Studies, ACS Omega. 3 (2018) 1991–2000. doi:10.1021/acsomega.7b01768.

[89] W. Wei, R. Sun, J. Cui, Z. Wei, Removal of nitrobenzene from aqueous solution by adsorption on nanocrystalline hydroxyapatite, Desalination. 263 (2010) 89–96. doi:10.1016/j.desal.2010.06.043.

[90] K. Lin, J. Pan, Y. Chen, R. Cheng, X. Xu, Study the adsorption of phenol from aqueous solution on hydroxyapatite nanopowders, J. Hazard. Mater. 161 (2009) 231–240. doi:10.1016/j.jhazmat.2008.03.076.

[91] S.J.T. Pollard, G.D. Fowler, C.J. Sollars, R. Perry, Low-cost adsorbents for waste and wastewater treatment: a review, Sci. Total Environ. 116 (1992) 31–52. doi:10.1016/0048-9697(92)90363-W.

[92] M. Olivares-Marín, M.M. Maroto-Valer, Development of adsorbents for CO2 capture from waste materials: a review, Greenh. Gases Sci. Technol. 2 (2012) 20–35. doi:10.1002/ghg.45.

[93] F.S. Souza, M.J.S. Matos, B.R.L. Galvão, A.F.C. Arapiraca, S.N. Silva, I.P. Pinheiro, Adsorption of CO 2 on biphasic and amorphous calcium phosphates : An experimental and theoretical analysis, Chem. Phys. Lett. 714 (2019) 143–148. doi:10.1016/j.cplett.2018.10.080.

[94] Z.H. Cheng, A. Yasukawa, K. Kandori, T. Ishikawa, FTIR Study of Adsorption of CO 2 on Nonstoichiometric Calcium Hydroxyapatite, Langmuir. (1998) 6681–6686. doi:10.1021/la980339n.

[95] S. Diallo-Garcia, M. Ben Osman, J.M. Krafft, S. Casale, C. Thomas, J. Kubo, G. Costentin, Identification of surface basic sites and acid-base pairs of hydroxyapatite, J. Phys. Chem. C. 118 (2014) 12744–12757. doi:10.1021/jp500469x.

[96] F. Marken, D. Fermin, Electrochemical reduction of carbon dioxide: Overcoming the limitations of photosynthesis, Royal Society of Chemistry, 2018.

[97] J.E. Andrews, P. Brimblecombe, T.D. Jickells, P.S. Liss, An introduction to environmental chemistry, 1996. doi:10.2134/jeq1998.00472425002700020031x.

[98] J.P. Vareda, A.J.M. Valente, L. Durães, Assessment of heavy metal pollution from anthropogenic activities and remediation strategies: A review, J. Environ. Manage. 246 (2019) 101–118. doi:10.1016/j.jenvman.2019.05.126.

[99] G.K. Sarma, S. Sen Gupta, K.G. Bhattacharyya, Nanomaterials as versatile adsorbents for heavy metal ions in water: a review, Environ. Sci. Pollut. Res. 26 (2019) 6245–6278. doi:10.1007/s11356-018-04093-y.

[100] J.H. Duffus, "heavy metals" - A meaningless term? (IUPAC technical report), Pure Appl. Chem. 74 (2002) 793–807. doi:10.1351/pac200274050793.

[101] K.H. Vardhan, P.S. Kumar, R.C. Panda, A review on heavy metal pollution, toxicity and remedial measures: Current trends and future perspectives, J. Mol. Liq. 290 (2019) 111197. doi:10.1016/j.molliq.2019.111197.

[102] N.S. Bolan, G. Choppala, A. Kunhikrishnan, J. Park, R. Naidu, Microbial Transformation of Trace Elements in Soils in Relation to Bioavailability and Remediation, in: D.M. Whitacre (Ed.), Rev. Environ. Contam. Toxicol., Springer New York, New York, NY, 2013: pp. 1–56. doi:10.1007/978-1-4614-6470-9_1.

[103] D.C. Adriano, W.W. Wenzel, J. Vangronsveld, N.S. Bolan, Role of assisted natural remediation in environmental cleanup, Geoderma. 122 (2004) 121–142. doi:10.1016/j.geoderma.2004.01.003.

[104] W.H. Organization, Guidelines for drinking-water quality, World Health Organization, 1993.

[105] M.B. Pescod, Wastewater treatment and use in agriculture, (1992).

[106] W.H. Organization, Evaluations of the Joint FAO/WHO Expert Committee on Food Additives (JECFA). 2017, (2017).

[107] C.H. Chen, J. Liu, M.E. Stoll, G. Henriksen, D.R. Vissers, K. Amine, Aluminum-doped lithium nickel cobalt oxide electrodes for high-power lithium-ion batteries, J. Power Sources. 128 (2004) 278–285. doi:10.1016/j.jpowsour.2003.10.009.

[108] B. Scrosati, J. Garche, Lithium batteries: Status, prospects and future, J. Power Sources. 195 (2010) 2419–2430. doi:10.1016/j.jpowsour.2009.11.048.

[109] M.A. Islam, D.W. Morton, B.B. Johnson, B.K. Pramanik, B. Mainali, M.J. Angove, Opportunities and constraints of using the innovative adsorbents for the removal of cobalt(II) from wastewater: A review, Environ. Nanotechnology, Monit. Manag. 10 (2018) 435–456. doi:10.1016/j.enmm.2018.10.003.

[110] A.E. Burakov, E. V. Galunin, I. V. Burakova, A.E. Kucherova, S. Agarwal, A.G. Tkachev, V.K. Gupta, Adsorption of heavy metals on conventional and nanostructured materials for wastewater treatment purposes: A review, Ecotoxicol. Environ. Saf. 148 (2018) 702–712. doi:10.1016/j.ecoenv.2017.11.034.

[111] S. Wadhawan, A. Jain, J. Nayyar, S.K. Mehta, Role of nanomaterials as adsorbents in heavy metal ion removal from waste water: A review, J. Water Process Eng. 33 (2020). doi:10.1016/j.jwpe.2019.101038.

[112] P. Carniti, A. Gervasini, Liquid-Solid Adsorption Properties: Measurement of the Effective Surface Acidity of Solid Catalysts BT - Calorimetry and Thermal Methods in Catalysis, in: A. Auroux (Ed.), Springer Berlin Heidelberg, Berlin, Heidelberg, 2013: pp. 543–551. doi:10.1007/978-3-642-11954-5_17.

[113] K.S.W. Sing, D.H. Everett, R.A.W. Haul, L. Moscou, R.A. Pierotti, J. Rouquerol, T. Siemieniewska, Reporting Physisorption Data for Gas/Solid Systems with Special Reference to the Determination of Surface Area and Porosity, Pure Appl. Chem. 57 (1985) 603–619. doi:10.1351/pac198557040603.

[114] M. Scavini, M. Coduri, M. Allieta, P. Masala, S. Cappelli, C. Oliva, M. Brunelli, F. Orsini, C. Ferrero, Percolating hierarchical defect structures drive phase transformation in Ce1-xGdxO2-x/2: A total scattering study, IUCrJ. 2 (2015) 511–522. doi:10.1107/S2052252515011641.

[115] X. Xiao, M. Widenmeyer, W. Xie, T. Zou, S. Yoon, M. Scavini, S. Checchia, Z. Zhong, P. Hansmann, S. Kilper, A. Kovalevsky, A. Weidenkaff, Tailoring the structure and thermoelectric properties of BaTiO3: Via Eu2+ substitution, Phys. Chem. Chem. Phys. 19 (2017) 13469–13480. doi:10.1039/c7cp00020k.

[116] A. Minguzzi, C. Locatelli, O. Lugaresi, E. Achilli, G. Cappelletti, M. Scavini, M. Coduri, P. Masala, B. Sacchi, A. Vertova, P. Ghigna, S. Rondinini, Easy Accommodation of Different Oxidation States in Iridium Oxide Nanoparticles with Different Hydration Degree as Water Oxidation Electrocatalysts, ACS Catal. 5 (2015) 5104–5115. doi:10.1021/acscatal.5b01281.

[117] J.R. Di Iorio, S.A. Bates, A.A. Verma, W.N. Delgass, F.H. Ribeiro, J.T. Miller, R. Gounder, The Dynamic Nature of Brønsted Acid Sites in Cu-Zeolites During NOx Selective Catalytic Reduction: Quantification by Gas-Phase Ammonia Titration, Top. Catal. 58 (2015) 424–434. doi:10.1007/s11244-015-0387-8.

[118] A.M. Mohammad, T.A. Salah Eldin, M.A. Hassan, B.E. El-Anadouli, Efficient treatment of lead-containing wastewater by hydroxyapatite/chitosan nanostructures, Arab. J. Chem. 10 (2017) 683–690. doi:10.1016/j.arabjc.2014.12.016.

[119] M. Sprynskyy, B. Buszewski, A.P. Terzyk, J. Namieśnik, Study of the selection mechanism of heavy metal (Pb2+, Cu2+, Ni2+, and Cd2+) adsorption on clinoptilolite, J. Colloid Interface Sci. 304 (2006) 21–28. doi:10.1016/j.jcis.2006.07.068.

[120] N. Gupta, A.K. Kushwaha, M.C. Chattopadhyaya, Adsorptive removal of Pb2+, Co2+and Ni2+by hydroxyapatite/chitosan composite from aqueous solution, J. Taiwan Inst. Chem. Eng. 43 (2012) 125–131. doi:10.1016/j.jtice.2011.07.009.

[121] A. Bonilla-Petriciolet, D.I. Mendoza-Castillo, H.E. Reynel-Ávila, Adsorption processes for water treatment and purification, 2017. doi:10.1007/978-3-319-58136-1.

[122] A.H.M.G. Hyder, S.A. Begum, N.O. Egiebor, Adsorption isotherm and kinetic studies of hexavalent chromium removal from aqueous solution onto bone char, J. Environ. Chem. Eng. 3 (2015) 1329–1336. doi:10.1016/j.jece.2014.12.005.

[123] R. Zhu, R. Yu, J. Yao, D. Mao, C. Xing, D. Wang, Removal of Cd2+from aqueous solutions by hydroxyapatite, Catal. Today. 139 (2008) 94–99. doi:10.1016/j.cattod.2008.08.011.

[124] S. Babel, T.A. Kurniawan, Low-cost adsorbents for heavy metals uptake from contaminated water: A review, J. Hazard. Mater. 97 (2003) 219–243. doi:10.1016/S0304-3894(02)00263-7.

[125] A. Demirbas, Heavy metal adsorption onto agro-based waste materials: A review, J. Hazard. Mater. 157 (2008) 220–229. doi:10.1016/j.jhazmat.2008.01.024.

[126] J.V. Flores-Cano, R. Leyva-Ramos, F. Carrasco-Marin, A. Aragòn-Pina, J.J. Salazar-Rabago, S. Leyva-Ramos, Adsorption mechanism of Chromium(III) from water solution on bone char: effect of operating conditions, Adsorption. 22 (2016) 297–308. doi:10.1007/s10450-016-9771-3.

[127] O. Rosskopfová, M. Galamboš, L. Pivarčiová, M. Čaplovičová, P. Rajec, Adsorption of nickel on synthetic hydroxyapatite from aqueous solutions, J. Radioanal. Nucl. Chem. 295 (2013) 459–465. doi:10.1007/s10967-012-1799-6.

[128] A. Martell, Critical Stability Constants: Inorganic Complexes, Springer US, 2013. https://books.google.it/books?id=tIfjBwAAQBAJ.

[129] D. Rai, D.A. Moore, N.J. Hess, K.M. Rosso, L. Rao, S.M. Heald, Chromium(III) hydroxide solubility in the aqueous K+-H +-OH--CO2-HCO 3- -CO 32- -H2O system: A thermodynamic model, J. Solution Chem. 36 (2007) 1261–1285. doi:10.1007/s10953-007-9179-5.

[130] Y. Nishiyama, T. Hanafusa, J. Yamashita, Y. Yamamoto, T. Ono, Adsorption and removal of strontium in aqueous solution by synthetic hydroxyapatite, J. Radioanal. Nucl. Chem. 307 (2016) 1279–1285. doi:10.1007/s10967-015-4228-9.

[131] X. Xia, J. Shen, F. Cao, C. Wang, M. Tang, Q. Zhang, S. Wei, A facile synthesis of hydroxyapatite for effective removal strontium ion, J. Hazard. Mater. 368 (2019) 326–335. doi:10.1016/j.jhazmat.2019.01.040.

[132] J.K. Fawell, U. Lund, B. Mintz, Chromium in Drinking-water, Heal. Criteria Other Support. Information, World Heal. Organ. 2 (1996) 1–13. http://www.who.int/water_sanitation_health/dwq/chemicals/chromium.pdf.

[133] S. Campisi, C. Castellano, A. Gervasini, Tailoring the structural and morphological properties of hydroxyapatite materials to enhance the capture efficiency towards copper(II) and lead(II) ions, New J. Chem. 42 (2018) 4520–4530. doi:10.1039/C8NJ00468D.

[134] M. Kwaśniak-Kominek, M. Manecki, J. Matusik, M. Lempart, Carbonate substitution in lead hydroxyapatite Pb5(PO4)3OH, J. Mol. Struct. 1147 (2017) 594–602. doi:10.1016/j.molstruc.2017.06.111.

[135] M.A. Fetcenko, S.R. Ovshinsky, B. Reichman, K. Young, C. Fierro, J. Koch, A. Zallen, W. Mays, T. Ouchi, Recent advances in NiMH battery technology, J. Power Sources. 165 (2007) 544–551. doi:10.1016/j.jpowsour.2006.10.036.

[136] M. Zackrisson, L. Avellán, J. Orlenius, Life cycle assessment of lithium-ion batteries for plug-in hybrid

electric vehicles – Critical issues, J. Clean. Prod. 18 (2010) 1519–1529. doi:10.1016/j.jclepro.2010.06.004.

[137] G. Gollavelli, C.C. Chang, Y.C. Ling, Facile synthesis of smart magnetic graphene for safe drinking water: Heavy metal removal and disinfection control, ACS Sustain. Chem. Eng. 1 (2013) 462–472. doi:10.1021/sc300112z.

[138] T. Bora, J. Dutta, Applications of nanotechnology in wastewater treatment-A review, J. Nanosci. Nanotechnol. 14 (2014) 613–626. doi:10.1166/jnn.2014.8898.

[139] S. Wong, N. Ngadi, I.M. Inuwa, O. Hassan, Recent advances in applications of activated carbon from biowaste for wastewater treatment: A short review, J. Clean. Prod. 175 (2018) 361–375. doi:10.1016/j.jclepro.2017.12.059.

[140] S. Kalita, M. Pathak, G. Devi, H.P. Sarma, K.G. Bhattacharyya, A. Sarma, A. Devi, Utilization of: Euryale ferox Salisbury seed shell for removal of basic fuchsin dye from water: Equilibrium and kinetics investigation, RSC Adv. 7 (2017) 27248–27259. doi:10.1039/c7ra03014b.

[141] G.N. Hlongwane, P.T. Sekoai, M. Meyyappan, K. Moothi, Simultaneous removal of pollutants from water using nanoparticles: A shift from single pollutant control to multiple pollutant control, Sci. Total Environ. 656 (2019) 808–833. doi:10.1016/j.scitotenv.2018.11.257.

[142] A. Dąbrowski, P. Podkościelny, Z. Hubicki, M. Barczak, Adsorption of phenolic compounds by activated carbon - A critical review, Chemosphere. 58 (2005) 1049–1070. doi:10.1016/j.chemosphere.2004.09.067.

[143] Y. Dai, N. Zhang, C. Xing, Q. Cui, Q. Sun, The adsorption, regeneration and engineering applications of biochar for removal organic pollutants: A review, Chemosphere. 223 (2019) 12–27. doi:10.1016/j.chemosphere.2019.01.161.

[144] A. Sigdel, W. Jung, B. Min, M. Lee, U. Choi, T. Timmes, S.J. Kim, C.U. Kang, R. Kumar, B.H. Jeon, Concurrent removal of cadmium and benzene from aqueous solution by powdered activated carbon impregnated alginate beads, Catena. 148 (2017) 101–107. doi:10.1016/j.catena.2016.06.029.

[145] M.S. Fernando, R.M. De Silva, K.M.N. De Silva, Synthesis, characterization, and application of nano hydroxyapatite and nanocomposite of hydroxyapatite with granular activated carbon for the removal of Pb 2+ from aqueous solutions, Appl. Surf. Sci. 351 (2015) 95–103. doi:10.1016/j.apsusc.2015.05.092.

[146] Y. Long, J. Jiang, J. Hu, X. Hu, Q. Yang, S. Zhou, Removal of Pb(Ⅱ) from aqueous solution by hydroxyapatite/carbon composite: Preparation and adsorption behavior, Colloids Surfaces A Physicochem. Eng. Asp. 577 (2019) 471–479. doi:10.1016/j.colsurfa.2019.06.011.

[147] K.W. Jung, S.Y. Lee, J.W. Choi, Y.J. Lee, A facile one-pot hydrothermal synthesis of hydroxyapatite/biochar nanocomposites: Adsorption behavior and mechanisms for the removal of copper(II) from aqueous media, Chem. Eng. J. 369 (2019) 529–541. doi:10.1016/j.cej.2019.03.102.

[148] Z. Ruan, Y. Tian, J. Ruan, G. Cui, K. Iqbal, A. Iqbal, H. Ye, Z. Yang, S. Yan, Synthesis of hydroxyapatite/multi-walled carbon nanotubes for the removal of fluoride ions from solution, Appl. Surf. Sci. 412 (2017) 578–590. doi:10.1016/j.apsusc.2017.03.215.

[149] Y. Wang, L. Hu, G. Zhang, T. Yan, L. Yan, Q. Wei, B. Du, Removal of Pb(II) and methylene blue from aqueous solution by magnetic hydroxyapatite-immobilized oxidized multi-walled carbon nanotubes, J. Colloid Interface Sci. 494 (2017) 380–388. doi:10.1016/j.jcis.2017.01.105.

[150] Y. Zhu, Y. Jiang, Z. Zhu, H. Deng, H. Ding, Y. Li, L. Zhang, J. Lin, Preparation of a porous

hydroxyapatite-carbon composite with the bio-template of sugarcane top stems and its use for the Pb(II) removal, J. Clean. Prod. 187 (2018) 650–661. doi:10.1016/j.jclepro.2018.03.275.

[151] A. Waheed, M. Mansha, N. Ullah, Nanomaterials-based electrochemical detection of heavy metals in water: Current status, challenges and future direction, TrAC - Trends Anal. Chem. 105 (2018) 37–51. doi:10.1016/j.trac.2018.04.012.

[152] Y. Lu, X. Liang, C. Niyungeko, J. Zhou, J. Xu, G. Tian, A review of the identification and detection of heavy metal ions in the environment by voltammetry, Talanta. 178 (2018) 324–338. doi:10.1016/j.talanta.2017.08.033.

[153] B.K. Bansod, T. Kumar, R. Thakur, S. Rana, I. Singh, A review on various electrochemical techniques for heavy metal ions detection with different sensing platforms, Biosens. Bioelectron. 94 (2017) 443–455. doi:10.1016/j.bios.2017.03.031.

[154] L. Cui, J. Wu, H. Ju, Electrochemical sensing of heavy metal ions with inorganic, organic and bio-materials, Biosens. Bioelectron. 63 (2015) 276–286. doi:10.1016/j.bios.2014.07.052.

[155] L. Fan, J. Chen, S. Zhu, M. Wang, G. Xu, Determination of Cd2+ and Pb2+ on glassy carbon electrode modified by electrochemical reduction of aromatic diazonium salts, Electrochem. Commun. 11 (2009) 1823–1825. doi:10.1016/j.elecom.2009.07.026.

[156] P. Kissinger, W.R. Heineman, Laboratory Techniques in Electroanalytical Chemistry, revised and expanded, CRC press, 2018.

[157] A. Krolicka, A. Bobrowski, K. Kalcher, J. Mocak, I. Svancara, K. Vytras, Study on Catalytic Adsorptive Stripping Voltammetry of Trace Cobalt at Bismuth Film Electrodes, Electroanalysis. 15 (2003) 1859–1863. doi:10.1002/elan.200302763.

[158] C. Ariño, N. Serrano, J.M. Díaz-Cruz, M. Esteban, Voltammetric determination of metal ions beyond mercury electrodes. A review, Anal. Chim. Acta. 990 (2017) 11–53. doi:10.1016/j.aca.2017.07.069.

[159] M.A. El Mhammedi, M. Bakasse, A. Chtainia, Square-wave voltammetric determination of paraquat at carbon paste electrode modified with hydroxyapatite, Electroanalysis. 19 (2007) 1727–1733. doi:10.1002/elan.200703927.

[160] D. Pan, Y. Wang, Z. Chen, T. Yin, W. Qin, Fabrication and characterization of carbon nanotube-hydroxyapatite nanocomposite: Application to anodic stripping yoltammetric determination of cadmium, Electroanalysis. 21 (2009) 944–952. doi:10.1002/elan.200804492.

[161] Y. Li, X. Liu, X. Zeng, Y. Liu, X. Liu, W. Wei, S. Luo, Simultaneous determination of ultra-trace lead and cadmium at a hydroxyapatite-modified carbon ionic liquid electrode by square-wave stripping voltammetry, Sensors Actuators, B Chem. 139 (2009) 604–610. doi:10.1016/j.snb.2009.03.045.

[162] Y. Zhang, Y. Liu, X. Ji, C.E. Banks, W. Zhang, Flower-like hydroxyapatite modified carbon paste electrodes applicable for highly sensitive detection of heavy metal ions, J. Mater. Chem. 21 (2011) 7552–7554. doi:10.1039/c1jm10949a.

[163] A.A.A. Khan, M.A. Abdullah, Bismuth-modified hydroxyapatite carbon electrode for simultaneous in-situ cadmium and lead analysis, Int. J. Electrochem. Sci. 8 (2013) 195–203.

[164] P. Kanchana, N. Sudhan, S. Anandhakumar, J. Mathiyarasu, P. Manisankar, C. Sekar, Electrochemical detection of mercury using biosynthesized hydroxyapatite nanoparticles modified glassy carbon electrodes without preconcentration, RSC Adv. 5 (2015) 68587–68594. doi:10.1039/c5ra11424a.

[165] F. Gao, N. Gao, A. Nishitani, H. Tanaka, Rod-like hydroxyapatite and Nafion nanocomposite as an

electrochemical matrix for simultaneous and sensitive detection of Hg2 +, Cu2 +, Pb2 + and Cd2 +, J. Electroanal. Chem. 775 (2016) 212–218. doi:10.1016/j.jelechem.2016.05.032.

[166] H. Ajab, A.A. Ali Khan, M.S. Nazir, A. Yaqub, M.A. Abdullah, Cellulose-hydroxyapatite carbon electrode composite for trace plumbum ions detection in aqueous and palm oil mill effluent: Interference, optimization and validation studies, Environ. Res. 176 (2019) 108563. doi:10.1016/j.envres.2019.108563.

[167] B. Kaur, R. Srivastava, B. Satpati, Ultratrace detection of toxic heavy metal ions found in water bodies using hydroxyapatite supported nanocrystalline ZSM-5 modified electrodes, New J. Chem. 39 (2015) 5137–5149. doi:10.1039/c4nj02369b.

[168] Y. Huang, S. Hu, S. Zuo, Z. Xu, C. Han, J. Shen, Mesoporous carbon materials prepared from carbohydrates with a metal chloride template, J. Mater. Chem. 19 (2009) 7759–7764. doi:10.1039/b911011a.

[169] M. Ferri, S. Campisi, P. Carniti, A. Gervasini, J. Shen, Tunable acidity in mesoporous carbons for hydrolysis reactions, New J. Chem. 44 (2020) 5873–5883. doi:10.1039/d0nj00750a.

[170] Z.Q. Li, C.J. Lu, Z.P. Xia, Y. Zhou, Z. Luo, X-ray diffraction patterns of graphite and turbostratic carbon, Carbon N. Y. 45 (2007) 1686–1695. doi:10.1016/j.carbon.2007.03.038.

[171] Tuinstra F, Koenig JL, Raman Spectrum of Graphite, J. Chem. Phys. 53 (1970) 1126–1130. doi:10.1063/1.1674108.

[172] D. Yamini, G. Devanand Venkatasubbu, J. Kumar, V. Ramakrishnan, Raman scattering studies on PEG functionalized hydroxyapatite nanoparticles, Spectrochim. Acta - Part A Mol. Biomol. Spectrosc. 117 (2014) 299–303. doi:10.1016/j.saa.2013.07.064.

[173] M.O. Corapcioglu, C.P. Huang, The surface acidity and characterization of some commercial activated carbons, Carbon N. Y. 25 (1987) 569–578. doi:10.1016/0008-6223(87)90200-4.

[174] K. Kadirvelu, K. Thamaraiselvi, C. Namasivayam, Adsorption of nickel(II) from aqueous solution onto activated carbon prepared from coirpith, Sep. Purif. Technol. 24 (2001) 497–505. doi:10.1016/S1383-5866(01)00149-6.

[175] Y. Li, X. Liu, X. Zeng, Y. Liu, X. Liu, W. Wei, S. Luo, Simultaneous determination of ultra-trace lead and cadmium at a hydroxyapatite-modified carbon ionic liquid electrode by square-wave stripping voltammetry, Sensors Actuators, B Chem. 139 (2009) 604–610. doi:10.1016/j.snb.2009.03.045.

[176] N. Brandon, O.B.E. Freng, I.C. London, Electrochemical Reduction of Carbon Dioxide, Royal Society of Chemistry, Cambridge, 2018. doi:10.1039/9781782623809.

[177] J. Qiao, Y. Liu, J. Zhang, Electrochemical Reduction of Carbon Dioxide, CRC Press, 2016. doi:10.1201/b20177.

[178] H. Xie, T. Wang, J. Liang, Q. Li, S. Sun, Cu-based nanocatalysts for electrochemical reduction of CO2, Nano Today. 21 (2018) 41–54. doi:10.1016/j.nantod.2018.05.001.

[179] J. Artz, T.E. Müller, K. Thenert, J. Kleinekorte, R. Meys, A. Sternberg, A. Bardow, W. Leitner, Sustainable Conversion of Carbon Dioxide: An Integrated Review of Catalysis and Life Cycle Assessment, Chem. Rev. 118 (2018) 434–504. doi:10.1021/acs.chemrev.7b00435.

[180] Q. Lu, F. Jiao, Electrochemical CO2 reduction: Electrocatalyst, reaction mechanism, and process engineering, Nano Energy. 29 (2016) 439–456. doi:10.1016/j.nanoen.2016.04.009.

[181] Y. Hori, A. Murata, R. Takahashi, Formation of hydrocarbons in the electrochemical reduction of

carbon dioxide at a copper electrode in aqueous solution, J. Chem. Soc. Faraday Trans. 1 Phys. Chem. Condens. Phases. 85 (1989) 2309–2326. doi:10.1039/F19898502309.

[182] K. Ito, S. Ikeda, N. Yamauchi, T. Iida, T. Takagi, Electrochemical Reduction Products of Carbon Dioxide at Some Metallic Electrodes in Nonaqueous Electrolytes, Bull. Chem. Soc. Jpn. 58 (1985) 3027–3028. doi:10.1246/bcsj.58.3027.

[183] L. Zhang, Z.J. Zhao, J. Gong, Nanostructured Materials for Heterogeneous Electrocatalytic CO 2 Reduction and their Related Reaction Mechanisms, Angew. Chemie - Int. Ed. 56 (2017) 11326–11353. doi:10.1002/anie.201612214.

[184] C. Xie, Z. Niu, D. Kim, M. Li, P. Yang, Surface and Interface Control in Nanoparticle Catalysis, Chem. Rev. 120 (2020) 1184–1249. doi:10.1021/acs.chemrev.9b00220.

[185] A. Rendón-Calle, S. Builes, F. Calle-Vallejo, A brief review of the computational modeling of CO2 electroreduction on Cu electrodes, Curr. Opin. Electrochem. 9 (2018) 158–165. doi:10.1016/j.coelec.2018.03.012.

[186] A. Mohammad, K. Kibum, L. Cong, A. Aditya Venkata, A. Pedram, Poya Yasaei, P. Patrick, B. Amirhossein, J.M. Cerrato, R. Haasch, P. Zapol, K. Bijandra, Nanostructured transition metal dichalcogenide electrocatalysts for CO2 reduction in ionic liquid, Science (80-.). 353 (2016) 464–467. doi:10.1126/science.aaf8533.

[187] S. Gao, X. Jiao, Z. Sun, W. Zhang, Y. Sun, C. Wang, Q. Hu, X. Zu, F. Yang, S. Yang, L. Liang, J. Wu, Y. Xie, Ultrathin Co3O4 Layers Realizing Optimized CO2 Electroreduction to Formate, Angew. Chemie - Int. Ed. 55 (2016) 698–702. doi:10.1002/anie.201509800.

[188] M. Fields, X. Hong, J.K. Nørskov, K. Chan, Role of Subsurface Oxygen on Cu Surfaces for CO2 Electrochemical Reduction, J. Phys. Chem. C. 122 (2018) 16209–16215. doi:10.1021/acs.jpcc.8b04983.

[189] A. Eilert, F. Cavalca, F.S. Roberts, J. Osterwalder, C. Liu, M. Favaro, E.J. Crumlin, H. Ogasawara, D. Friebel, L.G.M. Pettersson, A. Nilsson, Subsurface Oxygen in Oxide-Derived Copper Electrocatalysts for Carbon Dioxide Reduction, J. Phys. Chem. Lett. 8 (2017) 285–290. doi:10.1021/acs.jpclett.6b02273.

[190] A. Eilert, F.S. Roberts, D. Friebel, A. Nilsson, Formation of Copper Catalysts for CO2 Reduction with High Ethylene/Methane Product Ratio Investigated with In Situ X-ray Absorption Spectroscopy., J. Phys. Chem. Lett. 7 (2016) 1466–1470. doi:10.1021/acs.jpclett.6b00367.

[191] R. Jern, M. Xie, M. Alam, J. Lee, A. Fisher, X. Wang, K. Hwa, A review on the electrochemical reduction of CO 2 in fuel cells , metal electrodes and molecular catalysts, Catal. Today. 233 (2014) 169–180. doi:http://dx.doi.org/10.1016/j.cattod.2013.11.037.

[192] S. Zhao, D.W. Wang, R. Amal, L. Dai, Carbon-Based Metal-Free Catalysts for Key Reactions Involved in Energy Conversion and Storage, Adv. Mater. 31 (2019) 1–22. doi:10.1002/adma.201801526.

[193] K. Gong, F. Du, Z. Xia, M. Durstock, L. Dai, Nitrogen-doped carbon nanotube arrays with high electrocatalytic activity for oxygen reduction, Science (80-.). 323 (2009) 760–764. doi:10.1126/science.1168049.

[194] A. Wuttig, Y. Yoon, J. Ryu, Y. Surendranath, Bicarbonate Is Not a General Acid in Au-Catalyzed CO2 Electroreduction, J. Am. Chem. Soc. 139 (2017) 17109–17113. doi:10.1021/jacs.7b08345.

[195] L.C. Weng, A.T. Bell, A.Z. Weber, Modeling gas-diffusion electrodes for CO2 reduction, Phys. Chem. Chem. Phys. 20 (2018) 16973–16984. doi:10.1039/c8cp01319e.

[196] T. Burdyny, W.A. Smith, CO2 reduction on gas-diffusion electrodes and why catalytic performance must be assessed at commercially-relevant conditions, Energy Environ. Sci. 12 (2019) 1442–1453. doi:10.1039/c8ee03134g.

[197] C. Delacourt, P.L. Ridgway, J.B. Kerr, J. Newman, Design of an Electrochemical Cell Making Syngas (CO+H2) from CO2 and H2O Reduction at Room Temperature, J. Electrochem. Soc. 155 (2007) B42. doi:10.1149/1.2801871.

[198] N. Theaker, J.M. Strain, B. Kumar, J.P. Brian, S. Kumari, J.M. Spurgeon, Heterogeneously catalyzed two-step cascade electrochemical reduction of CO2 to ethanol, Electrochim. Acta. 274 (2018) 1–8. doi:10.1016/j.electacta.2018.04.072.

[199] Y. Hori, Electrochemical CO2 Reduction on Metal Electrodes, 42 (2008) 89–189. doi:10.1007/978-0-387-49489-0_3.

[200] X. Wang, X. Feng, J. Shang, Y. Jin, C. Zhang, Photocatalytic Reduction of - CO 2 Using Titanium-Substituted and Fluorine-Doped Titanium-Substituted Hydroxyapatite as Photocatalysts, Catal. Letters. 147 (2017) 2706–2713. doi:10.1007/s10562-017-2175-5.

[201] K.P. Kuhl, E.R. Cave, D.N. Abram, T.F. Jaramillo, New insights into the electrochemical reduction of carbon dioxide on metallic copper surfaces, Energy Environ. Sci. 5 (2012) 7050–7059. doi:10.1039/c2ee21234j.

[202] O.A. Baturina, Q. Lu, M.A. Padilla, L. Xin, W. Li, A. Serov, K. Artyushkova, P. Atanassov, F. Xu, A. Epshteyn, T. Brintlinger, M. Schuette, G.E. Collins, CO2 electroreduction to hydrocarbons on carbon-supported Cu nanoparticles, ACS Catal. 4 (2014) 3682–3695. doi:10.1021/cs500537y.

[203] M. Padilla, O. Baturina, J.P. Gordon, K. Artyushkova, P. Atanassov, A. Serov, Selective CO2 electroreduction to C2H4 on porous Cu films synthesized by sacrificial support method, J. CO2 Util. 19 (2017) 137–145. doi:10.1016/j.jcou.2017.03.006.

[204] R. Reske, H. Mistry, F. Behafarid, B. Roldan Cuenya, P. Strasser, Particle size effects in the catalytic electroreduction of CO2 on Cu nanoparticles, J. Am. Chem. Soc. 136 (2014) 6978–6986. doi:10.1021/ja500328k.

[205] A. Loiudice, P. Lobaccaro, E.A. Kamali, T. Thao, B.H. Huang, J.W. Ager, R. Buonsanti, Tailoring Copper Nanocrystals towards C2 Products in Electrochemical CO2 Reduction, Angew. Chemie - Int. Ed. 55 (2016) 5789–5792. doi:10.1002/anie.201601582.

[206] K.J.P. Schouten, Y. Kwon, C.J.M. Van Der Ham, Z. Qin, M.T.M. Koper, A new mechanism for the selectivity to C1 and C2 species in the electrochemical reduction of carbon dioxide on copper electrodes, Chem. Sci. 2 (2011) 1902–1909. doi:10.1039/c1sc00277e.

[207] X. Nie, M.R. Esopi, M.J. Janik, A. Asthagiri, Selectivity of CO2 reduction on copper electrodes: The role of the kinetics of elementary steps, Angew. Chemie - Int. Ed. 52 (2013) 2459–2462. doi:10.1002/anie.201208320.

[208] Y. Hori, H. Wakebe, T. Tsukamoto, O. Koga, Adsorption of CO accompanied with simultaneous charge transfer on copper single crystal electrodes related with electrochemical reduction of CO2 to hydrocarbons, Surf. Sci. 335 (1995) 258–263. doi:10.1016/0039-6028(95)00441-6.

[209] Y. Hori, I. Takahashi, O. Koga, N. Hoshi, Selective formation of C2 compounds from electrochemical reduction of CO2 at a series of copper single crystal electrodes, J. Phys. Chem. B. 106 (2002) 15–17. doi:10.1021/jp013478d.

[210] E. Pérez-Gallent, M.C. Figueiredo, F. Calle-Vallejo, M.T.M. Koper, Spectroscopic Observation of a

Hydrogenated CO Dimer Intermediate During CO Reduction on Cu(100) Electrodes, Angew. Chemie - Int. Ed. 56 (2017) 3621–3624. doi:10.1002/anie.201700580.

[211] S. Sen, D. Liu, G.T.R. Palmore, Electrochemical reduction of CO2 at copper nanofoams, ACS Catal. 4 (2014) 3091–3095. doi:10.1021/cs500522g.

[212] R. Kas, K.K. Hummadi, R. Kortlever, P. De Wit, A. Milbrat, M.W.J. Luiten-Olieman, N.E. Benes, M.T.M. Koper, G. Mul, Three-dimensional porous hollow fibre copper electrodes for efficient and high-rate electrochemical carbon dioxide reduction, Nat. Commun. 7 (2016) 1–7. doi:10.1038/ncomms10748.

[213] J.J. Lv, M. Jouny, W. Luc, W. Zhu, J.J. Zhu, F. Jiao, A Highly Porous Copper Electrocatalyst for Carbon Dioxide Reduction, Adv. Mater. 30 (2018) 1–8. doi:10.1002/adma.201803111.

[214] Q. Li, W. Zhu, J. Fu, H. Zhang, G. Wu, S. Sun, Controlled assembly of Cu nanoparticles on pyridinic-N rich graphene for electrochemical reduction of CO2 to ethylene, Nano Energy. 24 (2016) 1–9. doi:10.1016/j.nanoen.2016.03.024.

[215] Y. Song, R. Peng, D.K. Hensley, P. V. Bonnesen, L. Liang, Z. Wu, H.M. Meyer, M. Chi, C. Ma, B.G. Sumpter, A.J. Rondinone, High-Selectivity Electrochemical Conversion of CO2 to Ethanol using a Copper Nanoparticle/N-Doped Graphene Electrode, ChemistrySelect. 1 (2016) 6055–6061. doi:10.1002/slct.201601169.

[216] R. Shibuya, T. Kondo, J. Nakamura, Active sites in nitrogen-doped carbon materials for oxygen reduction reaction, Carbon-Based Met. Catal. Des. Appl. 1–2 (2018) 227–249. doi:10.1002/9783527811458.vol1-ch8.

[217] S. Kabir, K. Artyushkova, A. Serov, P. Atanassov, Role of Nitrogen Moieties in N-Doped 3D-Graphene Nanosheets for Oxygen Electroreduction in Acidic and Alkaline Media, ACS Appl. Mater. Interfaces. 10 (2018) 11623–11632. doi:10.1021/acsami.7b18651.

[218] F. Adib, A. Bagreev, T.J. Bandosz, Adsorption/oxidation of hydrogen sulfide on nitrogen-containing activated carbons, Langmuir. 16 (2000) 1980–1986. doi:10.1021/la990926o.

[219] T.J. Bandosz, Chapter 5 Desulfurization on activated carbons, in: 2006: pp. 231–292. doi:10.1016/S1573-4285(06)80014-1.

[220] G.P. Hao, W.C. Li, D. Qian, A.H. Lu, Rapid synthesis of nitrogen-doped porous carbon monolith for CO2 capture, Adv. Mater. 22 (2010) 853–857. doi:10.1002/adma.200903765.

[221] H. Kiuchi, R. Shibuya, T. Kondo, J. Nakamura, H. Niwa, J. Miyawaki, M. Kawai, M. Oshima, Y. Harada, Lewis Basicity of Nitrogen-Doped Graphite Observed by CO2 Chemisorption, Nanoscale Res. Lett. 11 (2016) 0–6. doi:10.1186/s11671-016-1344-6.

[222] H. Wang, J. Jia, P. Song, Q. Wang, D. Li, S. Min, C. Qian, L. Wang, Y.F. Li, C. Ma, T. Wu, J. Yuan, M. Antonietti, G.A. Ozin, Efficient Electrocatalytic Reduction of CO2 by Nitrogen-Doped Nanoporous Carbon/Carbon Nanotube Membranes: A Step Towards the Electrochemical CO2 Refinery, Angew. Chemie - Int. Ed. 56 (2017) 7847–7852. doi:10.1002/anie.201703720.

[223] P.P. Sharma, J. Wu, R.M. Yadav, M. Liu, C.J. Wright, C.S. Tiwary, B.I. Yakobson, J. Lou, P.M. Ajayan, X.D. Zhou, Nitrogen-Doped Carbon Nanotube Arrays for High-Efficiency Electrochemical Reduction of CO2: On the Understanding of Defects, Defect Density, and Selectivity, Angew. Chemie - Int. Ed. 54 (2015) 13701–13705. doi:10.1002/anie.201506062.

[224] J. Wu, S. Ma, J. Sun, J.I. Gold, C. Tiwary, B. Kim, L. Zhu, N. Chopra, I.N. Odeh, R. Vajtai, A.Z. Yu, R. Luo, J. Lou, G. Ding, P.J.A. Kenis, P.M. Ajayan, A metal-free electrocatalyst for carbon dioxide reduction to multi-carbon hydrocarbons and oxygenates, Nat. Commun. 7 (2016) 1–6.

doi:10.1038/ncomms13869.

[225] Y. Song, W. Chen, C. Zhao, S. Li, W. Wei, Y. Sun, Metal-Free Nitrogen-Doped Mesoporous Carbon for Electroreduction of CO 2 to Ethanol, Angew. Chemie Int. Ed. 56 (2017) 10840–10844. doi:10.1002/anie.201706777.

[226] A. Serov, P. Atanassov, US Patent n° 9,673.456 B2, 2017. https://patents.google.com/patent/US9673456B2/en.

[227] S. Kabir, A. Serov, K. Artyushkova, P. Atanassov, Design of Novel Graphene Materials as a Support for Palladium Nanoparticles: Highly Active Catalysts towards Ethanol Electrooxidation, Electrochim. Acta. 203 (2016) 144–153. doi:10.1016/j.electacta.2016.04.026.

[228] A. Serov, N.I. Andersen, S.A. Kabir, A. Roy, T. Asset, M. Chatenet, F. Maillard, P. Atanassov, Palladium Supported on 3D Graphene as an Active Catalyst for Alcohols Electrooxidation, J. Electrochem. Soc. 162 (2015) F1305–F1309. doi:10.1149/2.0301512jes.

[229] R. Gokhale, Y. Chen, A. Serov, K. Artyushkova, P. Atanassov, Novel dual templating approach for preparation of highly active Fe-N-C electrocatalyst for oxygen reduction, Electrochim. Acta. 224 (2017) 49–55. doi:10.1016/j.electacta.2016.12.052.

[230] M.C. Biesinger, Advanced analysis of copper X-ray photoelectron spectra, Surf. Interface Anal. 49 (2017) 1325–1334. doi:10.1002/sia.6239.

[231] S. Sen, D. Liu, G.T.R. Palmore, Electrochemical reduction of CO2 at copper nanofoams, ACS Catal. 4 (2014) 3091–3095. doi:10.1021/cs500522g.

[232] A. Serov, N.I. Andersen, S.A. Kabir, A. Roy, T. Asset, M. Chatenet, F. Maillard, P. Atanassova, Palladium supported on 3D Graphene as an active catalyst for alcohols electrooxidation, J. Electrochem. Soc. 162 (2015) F1305–F1309. doi:10.1149/2.0301512jes.

[233] W.S. Hummers, R.E. Offeman, Preparation of Graphitic Oxide, J. Am. Chem. Soc. 80 (1958) 1339. doi:10.1021/ja01539a017.

[234] B.H. Toby, EXPGUI, a graphical user interface for GSAS, J. Appl. Crystallogr. 34 (2001) 210–213. doi:10.1107/S0021889801002242.

[235] G. Ashiotis, A. Deschildre, Z. Nawaz, J.P. Wright, D. Karkoulis, F.E. Picca, J. Kieffer, The fast azimuthal integration Python library: PyFAI, J. Appl. Crystallogr. 48 (2015) 510–519. doi:10.1107/S1600576715004306.

[236] D.A. Keen, A comparison of various commonly used correlation functions for describing total scattering, J. Appl. Crystallogr. 34 (2001) 172–177. doi:10.1107/S0021889800019993.

[237] X. Qiu, J.W. Thompson, S.J.L. Billinge, PDFgetX2: A GUI-driven program to obtain the pair distribution function from X-ray powder diffraction data, J. Appl. Crystallogr. 37 (2004) 678. doi:10.1107/S0021889804011744.

[238] C.L. Farrow, P. Juhas, J.W. Liu, D. Bryndin, E.S. Boin, J. Bloch, T. Proffen, S.J.L. Billinge, PDFfit2 and PDFgui: Computer programs for studying nanostructure in crystals, J. Phys. Condens. Matter. 19 (2007). doi:10.1088/0953-8984/19/33/335219.

[239] Auroux, H. Gervasini, Principal Adsorption Mechanisms of NH3 and COz on the Different Types of Adsorption Sites in Metal Oxides, J. Phys. Chem. 94 (1990) 6371–6379.

[240] G. Sasikumar, J.W. Ihm, H. Ryu, Dependence of optimum Nafion content in catalyst layer on platinum loading, J. Power Sources. 132 (2004) 11–17. doi:10.1016/j.jpowsour.2003.12.060.

10 Supplementary material

10.1 Chapter 1

10.1.1 Physical-chemical characterization of synthetic hydroxyapatite

Numerical treatment of acid/base recirculation mode liquid-phase titration data

The isotherms of PEA and BA adsorption on HAP collected in I and II runs have been modeled according to Langmuir model equation.

From the linearized equation, the relevant parameters n_{max}, and b_{ads} can be obtained:

$$\frac{C_e}{q_e} = \frac{1}{n_{max}\, b_{ads}} + \frac{C_e}{n_{max}}$$

Equation 5

in which, Ce is the PEA or BA probe concentration in solution (M); n_{max} is the maximum amount of absorbed probe ($mol_{Probe}\, g_{HAP}^{-1}$); and b_{ads} is the adsorption constant (M^{-1}).

I run isotherm can be associated with probe adsorption on both strong and weak acid/basic sites of the sample surface: so, its linear regression gives back the total number of surface acid/basic sites. Conversely, II run adsorption accounts only for probe adsorption on weak acid/basic sites, since strongly interacting ones will not be freed by the mild desorption step occurred between the two titrations.

Due to the presence of different nature of acid/basic sites on HAP surface, it was not possible to obtain a satisfying fitting of I run isotherm straightforwardly applying Langmuir model equation. This limitation originates from the physical-chemical underpinning of Langmuir equation, that postulates homogeneity of sorbent sites toward adsorbate species (see paragraph 10.1.3.1). However, such a constrain has been overcome through mathematical data treatment.

At first, the adsorption isotherm of the II run was linearly regressed according to Equation 5, to obtain n_{max} and b_{ads}, parameters, both referring to weak adsorption sites. Then, at given probe concentrations, subtraction of the amount of probe adsorbed in II run from that adsorbed in I run was made. The so computed amount of probe adsorbed gave a new series of data, associated with the amount of probe adsorbed on strong acid/base sites. Even for this calculated isotherm, Langmuir parameters (n_{max} and b_{ads}, related to strong adsorption sites) were regressed according to Equation 5. Finally, by summing up the Langmuir isotherm modeled on II run experimental data and that pertaining to strong acid/base sites, a Langmuir isotherm able to effectively describe I adsorption run was obtained, together with the relevant parameters (n_{max}, and b_{ads}, related to total acid/basic sites).

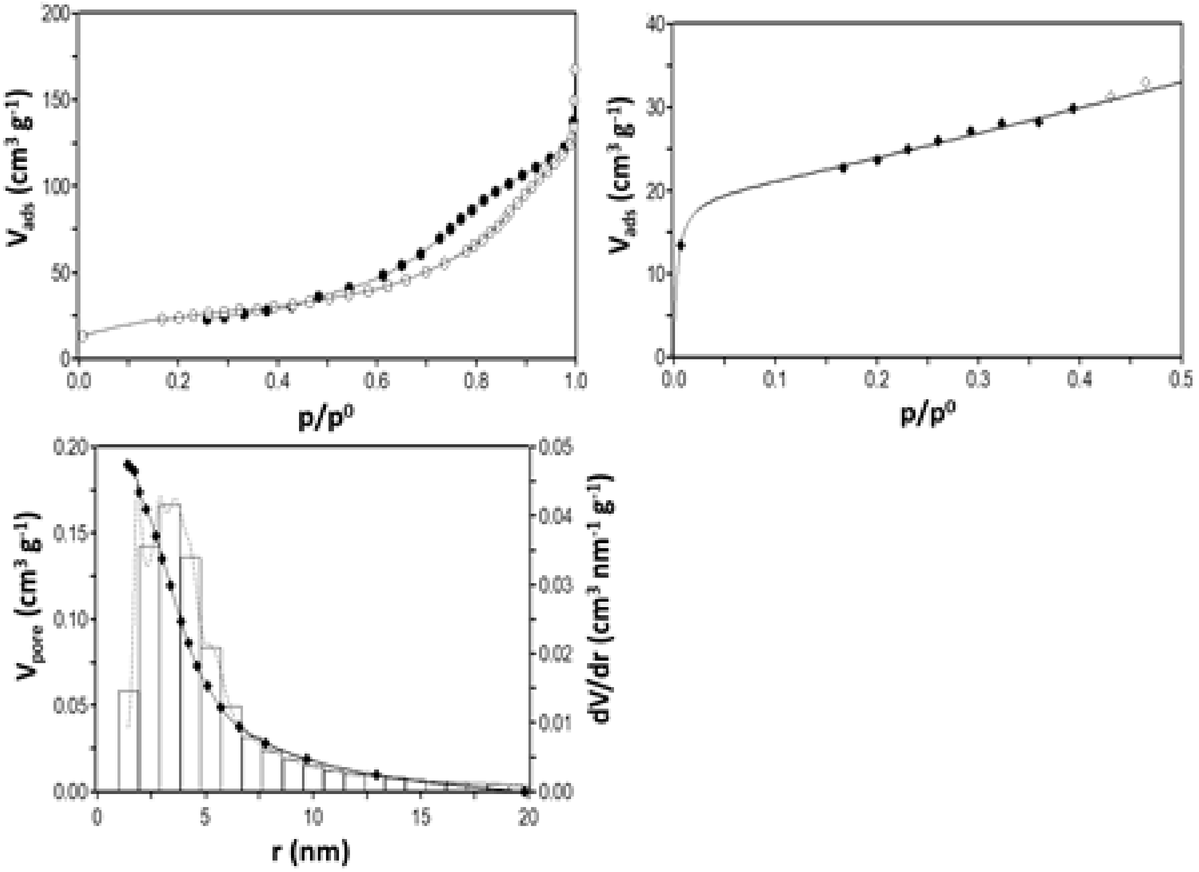

Figure 78: N_2 adsorption/desorption analysis results for HAP after exposure to an acidic aqueous solution. a) Adsorption and desorption isotherms; b) fitting of the low-pressure portion isotherm by 3-parameters B.E.T. equation ($0.05 < p/p^0 < 0.4$); c) total pore volume (full markers) and pore volume distribution, according to B.J.H. model.

Table 32: Refined unit cell parameters for pristine and acid-exposed HAP.

Sample	**a**	**b**	**c**	**Volume**
	Å	*Å*	*Å*	*Å*^{3}
Theoretical HAP[a]	9.4338 -	9.4338 -	6.8853 -	530.7
Pristine HAP	9.4119 ± 0.0226	9.4119 -	6.8642 ± 0.0012	526.6
Post acid exposure HAP	9.4364 ± 0.0117	9.4364 -	6.8789 ± 0.0003	530.6

[a] *Calculated from data reported in reference* [35].

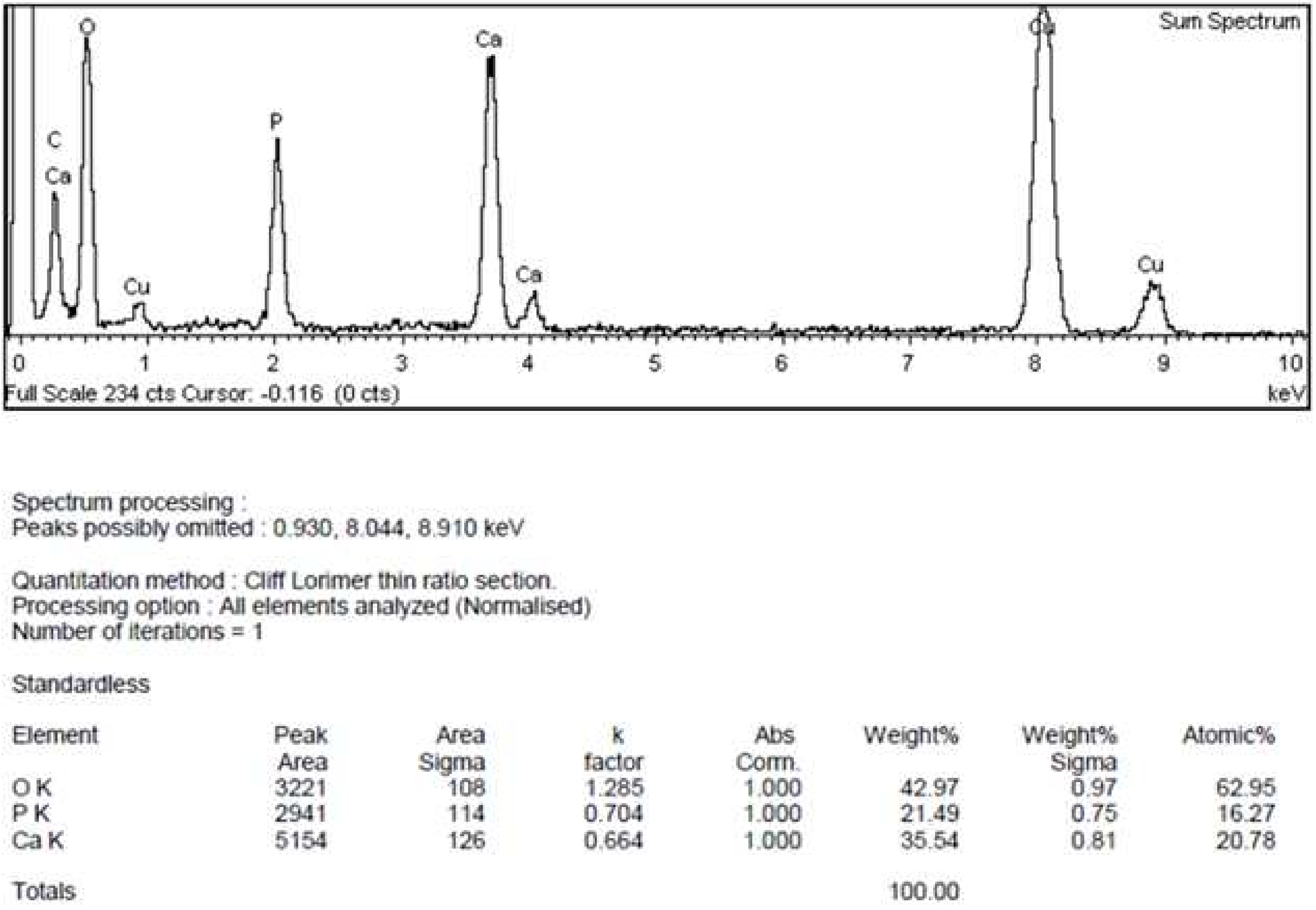

Spectrum processing :
Peaks possibly omitted : 0.930, 8.044, 8.910 keV

Quantitation method : Cliff Lorimer thin ratio section.
Processing option : All elements analyzed (Normalised)
Number of iterations = 1

Standardless

Element	Peak Area	Area Sigma	k factor	Abs Corrn.	Weight%	Weight% Sigma	Atomic%
O K	3221	108	1.285	1.000	42.97	0.97	62.95
P K	2941	114	0.704	1.000	21.49	0.75	16.27
Ca K	5154	126	0.664	1.000	35.54	0.81	20.78
Totals					100.00		

Figure 79: EDX spectrum of synthetic HAP from coupled TEM/EDX imaging and related elements quantification.

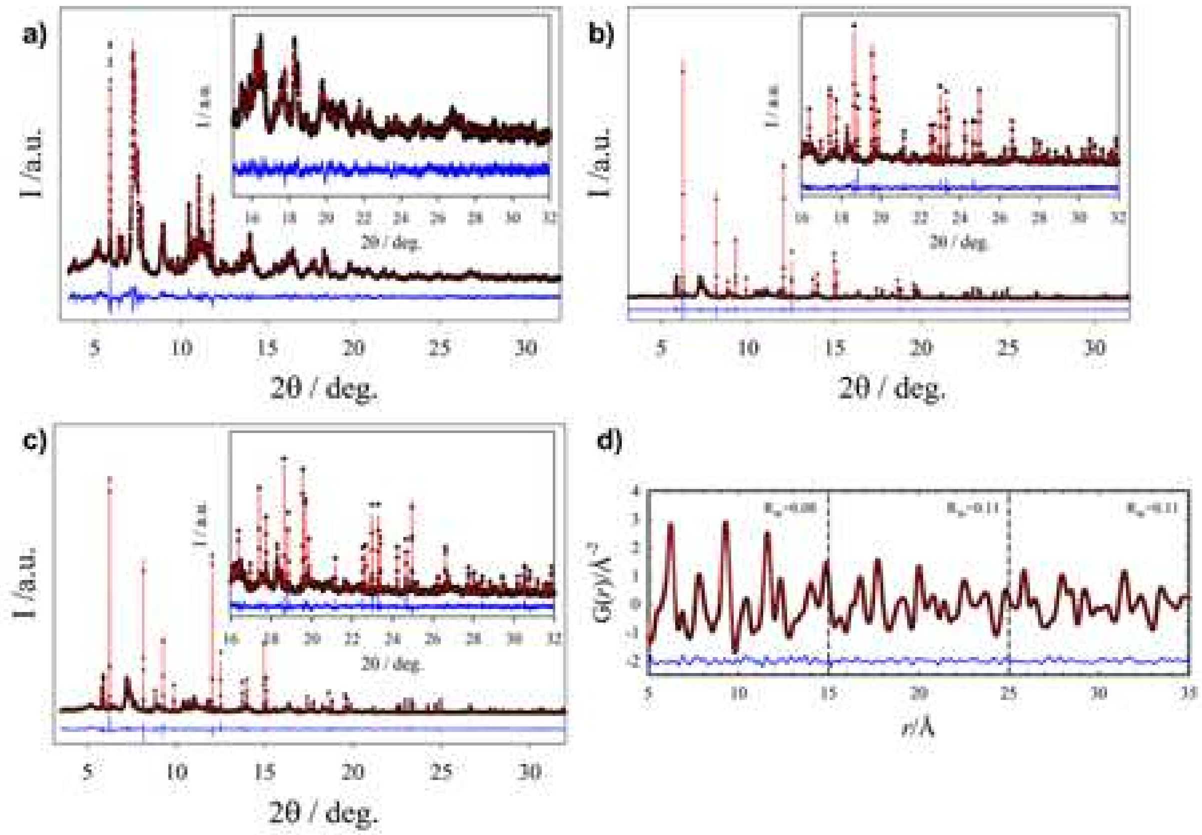

Figure 80: a) XRPD patterns of HAP sample after treatment in water at pH 3 for 24 h; b) synthetic HAP+TiO₂ sample; c) HAP+TiO₂ sample after treatment in water at pH 3 for 24 h; d) G(r) refinements in the 5-15, 15-25 and 25-35 Å r intervals using the real space Rietveld method for the as prepared HAP sample. Vertical dashed lines delimitate different fitting ranges.

Table 33: Regressed Langmuir parameters for PEA and BA adsorption isotherms collected at 30°C in cyclohexane (intrinsic acidity/basicity) and water (effective acidity/basicity).

	Intrinsic Acidity			**Intrinsic Basicity**		
	n_{max} *meq g⁻¹*	b_{ads} *L mol⁻¹*	R^2	n_{max} *meq g⁻¹*	b_{ads} *L mol⁻¹*	R^2
I Run[a]	0.159	9554	0.988	0.196	137488	0.999
II Run	0.121	8345	0.983	0.115	133654	0.999
Strong Sites	0.0378	11860	0.906	0.0845	80342	0.974
Langmuiran Sum	0.159	9085	1	0.199	105111	1
	Effective Acidity			**Effective Basicity**		
	n_{max} *meq g⁻¹*	b_{ads} *L mol⁻¹*	R^2	n_{max} *meq g⁻¹*	b_{ads} *L mol⁻¹*	R^2
I Run[a]	0.0333	7189	0.968	-	-	-
II Run	0.0189	12679	0.984	-	-	-
Strong Sites	0.0108	9230	0.955	-	-	-
Langmuiran Sum	0.0297	11298	1	-	-	-

[a] *Isotherm computed for I adsorption run, not shown in Figure 14.*

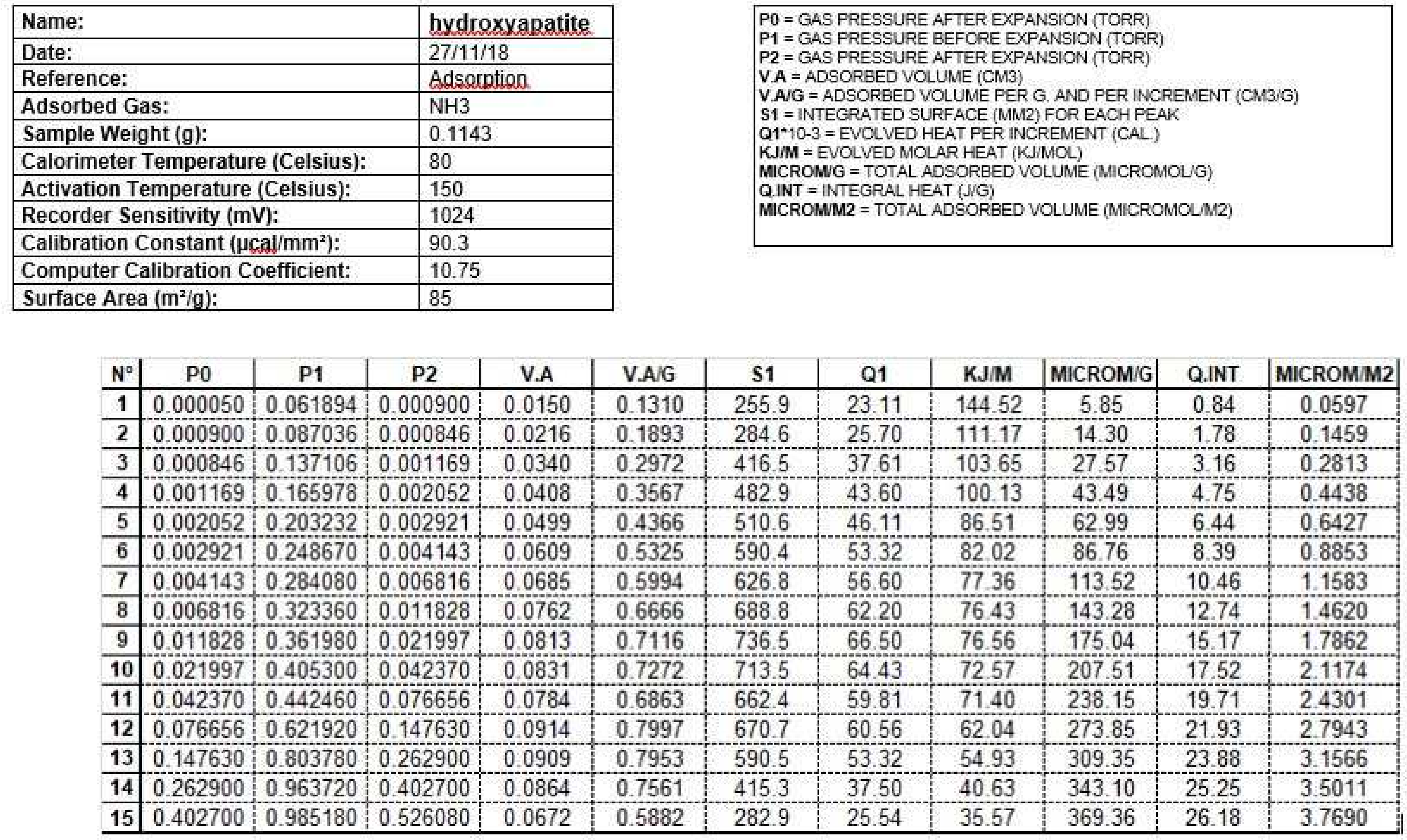

Name:	hydroxyapatite
Date:	27/11/18
Reference:	Adsorption
Adsorbed Gas:	NH3
Sample Weight (g):	0.1143
Calorimeter Temperature (Celsius):	80
Activation Temperature (Celsius):	150
Recorder Sensitivity (mV):	1024
Calibration Constant (µcal/mm²):	90.3
Computer Calibration Coefficient:	10.75
Surface Area (m²/g):	85

P0 = GAS PRESSURE AFTER EXPANSION (TORR)
P1 = GAS PRESSURE BEFORE EXPANSION (TORR)
P2 = GAS PRESSURE AFTER EXPANSION (TORR)
V.A = ADSORBED VOLUME (CM3)
V.A/G = ADSORBED VOLUME PER G. AND PER INCREMENT (CM3/G)
S1 = INTEGRATED SURFACE (MM2) FOR EACH PEAK
Q1*10-3 = EVOLVED HEAT PER INCREMENT (CAL.)
KJ/M = EVOLVED MOLAR HEAT (KJ/MOL)
MICROM/G = TOTAL ADSORBED VOLUME (MICROMOL/G)
Q.INT = INTEGRAL HEAT (J/G)
MICROM/M2 = TOTAL ADSORBED VOLUME (MICROMOL/M2)

N°	P0	P1	P2	V.A	V.A/G	S1	Q1	KJ/M	MICROM/G	Q.INT	MICROM/M2
1	0.000050	0.061894	0.000900	0.0150	0.1310	255.9	23.11	144.52	5.85	0.84	0.0597
2	0.000900	0.087036	0.000846	0.0216	0.1893	284.6	25.70	111.17	14.30	1.78	0.1459
3	0.000846	0.137106	0.001169	0.0340	0.2972	416.5	37.61	103.65	27.57	3.16	0.2813
4	0.001169	0.165978	0.002052	0.0408	0.3567	482.9	43.60	100.13	43.49	4.75	0.4438
5	0.002052	0.203232	0.002921	0.0499	0.4366	510.6	46.11	86.51	62.99	6.44	0.6427
6	0.002921	0.248670	0.004143	0.0609	0.5325	590.4	53.32	82.02	86.76	8.39	0.8853
7	0.004143	0.284080	0.006816	0.0685	0.5994	626.8	56.60	77.36	113.52	10.46	1.1583
8	0.006816	0.323360	0.011828	0.0762	0.6666	688.8	62.20	76.43	143.28	12.74	1.4620
9	0.011828	0.361980	0.021997	0.0813	0.7116	736.5	66.50	76.56	175.04	15.17	1.7862
10	0.021997	0.405300	0.042370	0.0831	0.7272	713.5	64.43	72.57	207.51	17.52	2.1174
11	0.042370	0.442460	0.076656	0.0784	0.6863	662.4	59.81	71.40	238.15	19.71	2.4301
12	0.076656	0.621920	0.147630	0.0914	0.7997	670.7	60.56	62.04	273.85	21.93	2.7943
13	0.147630	0.803780	0.262900	0.0909	0.7953	590.5	53.32	54.93	309.35	23.88	3.1566
14	0.262900	0.963720	0.402700	0.0864	0.7561	415.3	37.50	40.63	343.10	25.25	3.5011
15	0.402700	0.985180	0.526080	0.0672	0.5882	282.9	25.54	35.57	369.36	26.18	3.7690

Figure 81: Experimental data collected for NH_3 isothermal calorimetric titration of HAP.

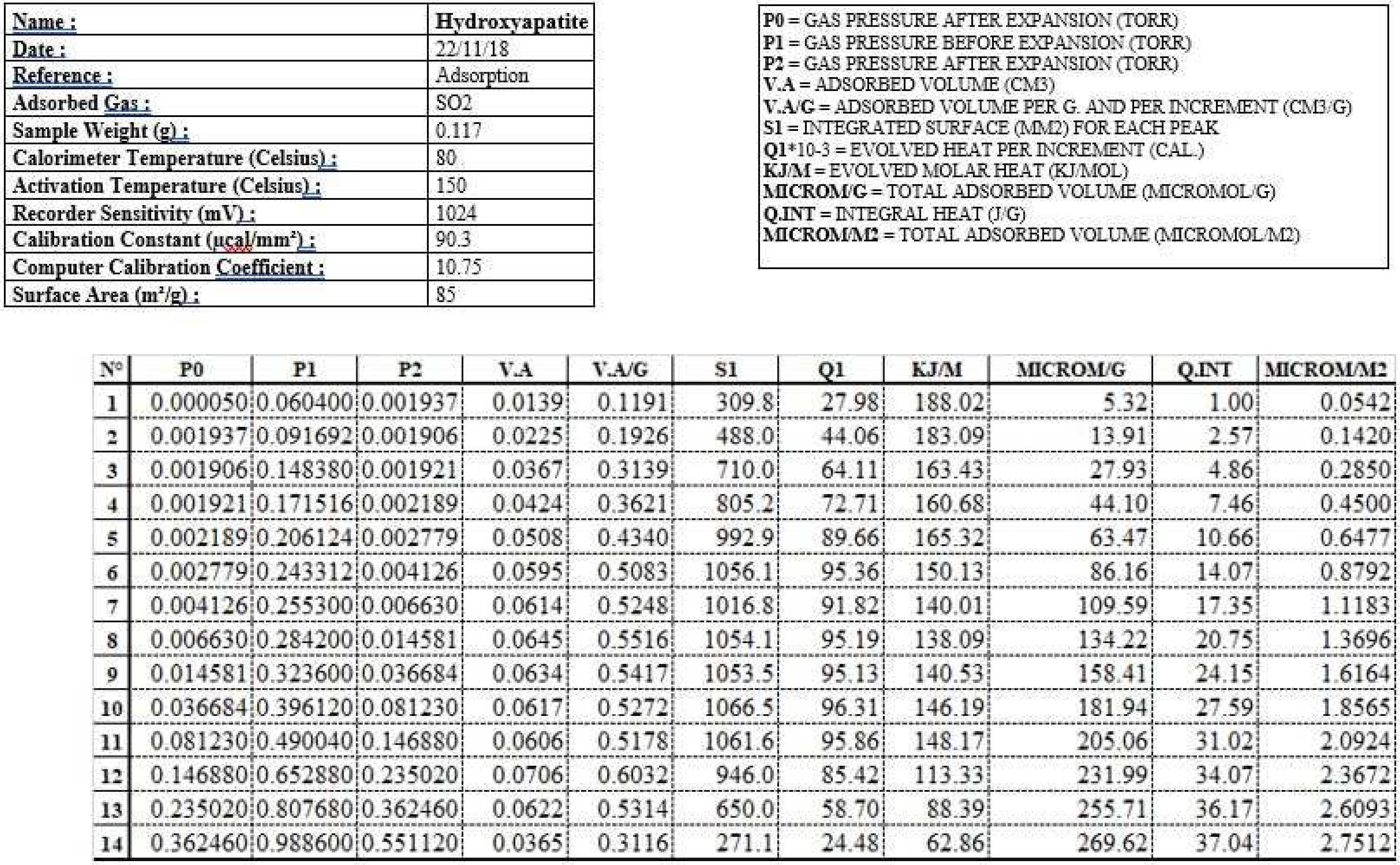

Name :	**Hydroxyapatite**
Date :	22/11/18
Reference :	Adsorption
Adsorbed Gas :	SO2
Sample Weight (g) :	0.117
Calorimeter Temperature (Celsius) :	80
Activation Temperature (Celsius) :	150
Recorder Sensitivity (mV) :	1024
Calibration Constant (µcal/mm^2) :	90.3
Computer Calibration Coefficient :	10.75
Surface Area (m^2/g) :	85

P0 = GAS PRESSURE AFTER EXPANSION (TORR)
P1 = GAS PRESSURE BEFORE EXPANSION (TORR)
P2 = GAS PRESSURE AFTER EXPANSION (TORR)
V.A = ADSORBED VOLUME (CM3)
V.A/G = ADSORBED VOLUME PER G. AND PER INCREMENT (CM3/G)
S1 = INTEGRATED SURFACE (MM2) FOR EACH PEAK
Q1*10-3 = EVOLVED HEAT PER INCREMENT (CAL.)
KJ/M = EVOLVED MOLAR HEAT (KJ/MOL)
MICROM/G = TOTAL ADSORBED VOLUME (MICROMOL/G)
Q.INT = INTEGRAL HEAT (J/G)
MICROM/M2 = TOTAL ADSORBED VOLUME (MICROMOL/M2)

N°	P0	P1	P2	V.A	V.A/G	S1	Q1	KJ/M	MICROM/G	Q.INT	MICROM/M2
1	0.000050	0.060400	0.001937	0.0139	0.1191	309.8	27.98	188.02	5.32	1.00	0.0542
2	0.001937	0.091692	0.001906	0.0225	0.1926	488.0	44.06	183.09	13.91	2.57	0.1420
3	0.001906	0.148380	0.001921	0.0367	0.3139	710.0	64.11	163.43	27.93	4.86	0.2850
4	0.001921	0.171516	0.002189	0.0424	0.3621	805.2	72.71	160.68	44.10	7.46	0.4500
5	0.002189	0.206124	0.002779	0.0508	0.4340	992.9	89.66	165.32	63.47	10.66	0.6477
6	0.002779	0.243312	0.004126	0.0595	0.5083	1056.1	95.36	150.13	86.16	14.07	0.8792
7	0.004126	0.255300	0.006630	0.0614	0.5248	1016.8	91.82	140.01	109.59	17.35	1.1183
8	0.006630	0.284200	0.014581	0.0645	0.5516	1054.1	95.19	138.09	134.22	20.75	1.3696
9	0.014581	0.323600	0.036684	0.0634	0.5417	1053.5	95.13	140.53	158.41	24.15	1.6164
10	0.036684	0.396120	0.081230	0.0617	0.5272	1066.5	96.31	146.19	181.94	27.59	1.8565
11	0.081230	0.490040	0.146880	0.0606	0.5178	1061.6	95.86	148.17	205.06	31.02	2.0924
12	0.146880	0.652880	0.235020	0.0706	0.6032	946.0	85.42	113.33	231.99	34.07	2.3672
13	0.235020	0.807680	0.362460	0.0622	0.5314	650.0	58.70	88.39	255.71	36.17	2.6093
14	0.362460	0.988600	0.551120	0.0365	0.3116	271.1	24.48	62.86	269.62	37.04	2.7512

Figure 82: Experimental data collected for SO_2 isothermal calorimetric titration of HAP.

10.1.2 Remediation of simulated polluted wastewaters by HAP: removal efficiencies and mechanisms

Table 34: Efficiencies of metal species removal (%) by stoichiometric synthetic HAP in static batch adsorption tests under acidic (pH 4) and alkaline (pH 9) conditions. $t_{contact}$ *= 24 h, T = 30°C, solution volume to solid ratio ca. 100 mL* g_{HAP}^{-1}*, initial* Me^{n+} *conc. = 300 ppm.*

pH	**Removal efficiencies (%)**				
	Cu(II)	*Pb(II)*	*Cr(III)*	*Ni(II)*	*Co(II)*
4	74	99	58	34	40
9	100	100	99	98	96

Table 35: Refined unit cell parameters for pristine and metal-loaded HAPs.

Sample	**a**	**b**	**c**	**Volume**
	Å	*Å*	*Å*	*Å*^{3}
Pristine HAP	9.4119 ± 0.0226	9.4119 -	6.8642 ± 0.0012	526.6
Ni-HAP	9.4295 ± 0.0393	9.4295 -	6.8576 ± 0.0032	528.1
Co-HAP	9.4278 ± 0.0289	9.4278 -	6.8617 ± 0.0013	528.2
Cu-HAP	9.4299 ± 0.0094	9.4299 -	6.8896 ± 0.0003	530.6
Cr-HAP	9.4292 ± 0.0095	9.4292 -	6.8856 ± 0.0003	530.2
Pb-HAP	9.4377 ± 0.0107	9.4377 -	6.8834 ± 0.0003	531

Table 36: Refined unit cell parameters for hydroxyl pyromorphite (theoretical calculation from literature data) and Pb(II)-loaded HAP.

Sample	**a**	**b**	**c**	**Volume**
	Å	*Å*	*Å*	*Å*^{3}
Theoretical Pyromorphite	9.7871 -	9.7871 -	7.307 -	606.1
Pb-HAP	9.7952 ± 0.0256	9.7952	7.2931 ± 0.0030	606.0

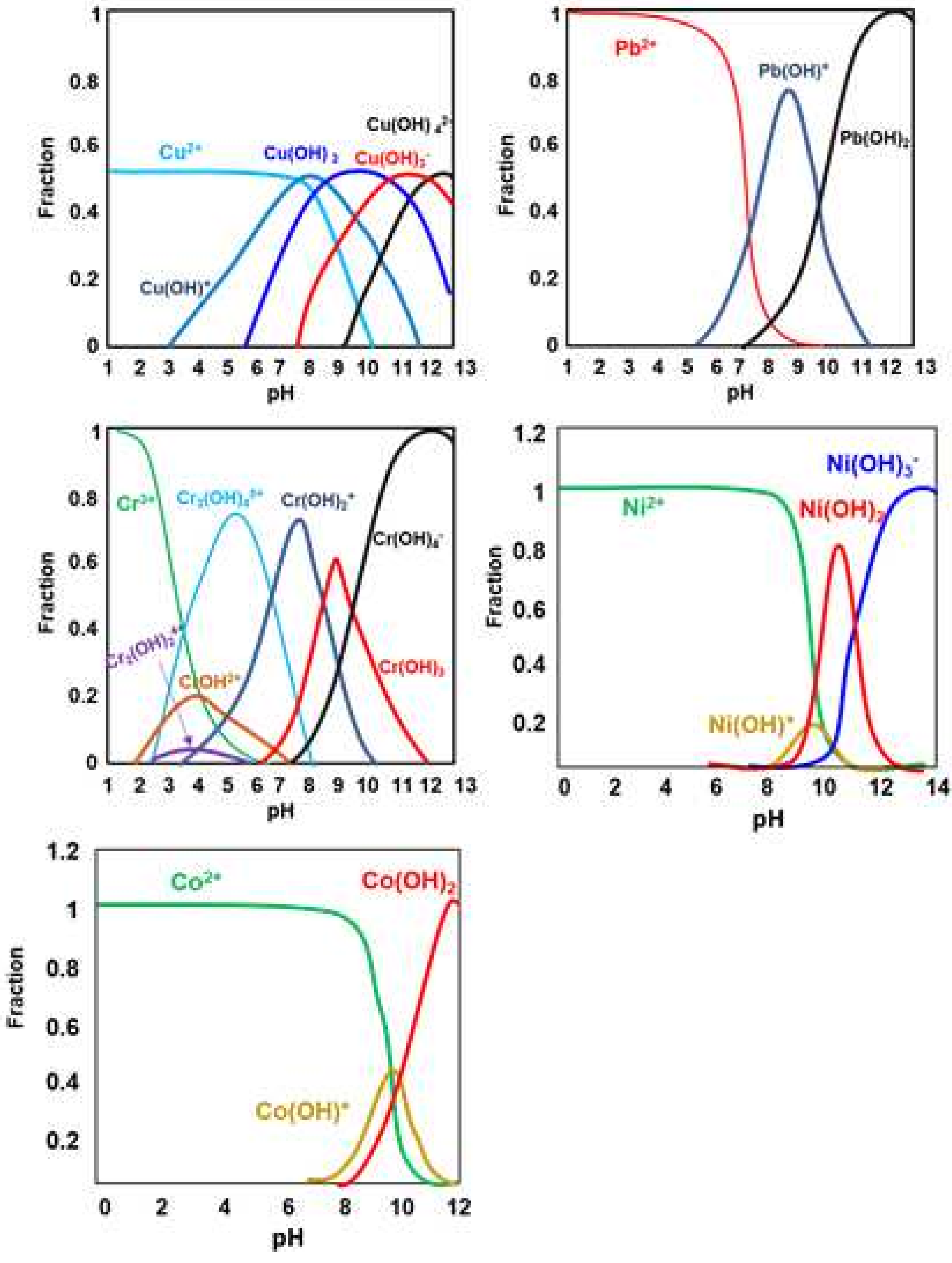

Figure 83: Speciation of the target heavy metals in aqueous solution.

Table 37: Model equations' parameters and correlation coefficients obtained from regression of Cu(II) experimental data according to the reported isotherm models.

Isotherm Model	Parameter	Value			R^2
Langmuir	n_{max} *(mmol g_{HAP}^{-1})*	1.25	±	0.02	0.997
	b *(L $mmol^{-1}$)*	0.369	±	0.169	
Freundlich	n_F	6.05	±	1.20	0.660
	K_F *(mmol g_{HAP}^{-1})*	0.599	±	0.128	
Temkin	B *(J $mmol^{-1}$)*	0.109	±	0.010	0.892
	A_T *(L $mmol^{-1}$)*	667	±	72	
Toth	n_{max} *(mmol g_{HAP}^{-1})*	1.31			0.128[a]
	b *(L $mmol^{-1}$)*	53.0			
	n	0.371			
Fowler-Guggenheim	*w (KJ mol^{-1})*	-0.824	±	-2.77	0.0423
	K_{FG} *(L $mmol^{-1}$)*	2.32	±	2.84	
Flory-Huggins	n	0.745	±	0.092	0.867
	K_{FH} *(L $mmol^{-1}$)*	0.0634	±	0.0034	
	ΔG *(J $mmol^{-1}$)*	-6.95	±	0.14	

[a] Sum of residual squares from non-linear regression

Table 38: Model equations' parameters and correlation coefficients obtained from regression of Pb(II) experimental data according to the reported isotherm models.

Isotherm Model	Parameter	Value			R^2
Langmuir	n_{max} *(mmol g_{HAP}^{-1})*	2.42	±	0.03	0.999
	b *(L $mmol^{-1}$)*	2.75	±	0.96	
Freundlich	n_F	3.18	±	0.27	0.927
	K_F *(mmol g_{HAP}^{-1})*	1.10	±	1.11	
Temkin	B *(J $mmol^{-1}$)*	0.261	±	0.022	0.930
	A_T *(L $mmol^{-1}$)*	341	±	33	
Toth	n_{max} *(mmol g_{HAP}^{-1})*	3.54			0.412[a]
	b *(L $mmol^{-1}$)*	35.6			
	n	0.312			
Fowler-Guggenheim	*w (KJ mol^{-1})*	6.88	±	2.51	0.556
	K_{FG} *(L $mmol^{-1}$)*	21.5	±	3.80	
Flory-Huggins	n	0.0868	±	0.0094	0.887
	K_{FH} *(L $mmol^{-1}$)*	0.0207	±	0.0001	
	ΔG *(J $mmol^{-1}$)*	-9.77	±	0.01	

[a] Sum of residual squares from non-linear regression

Table 39: Model equations' parameters and correlation coefficients obtained from regression of Cr(III) experimental data according to the reported isotherm models.

	Isotherm Model	Parameter	Value			R^2
First branch	Langmuir	n_{max} $(mmol\ g_{HAP}^{-1})$	0.631	±	0.007	0.999
		b $(L\ mmol^{-1})$	38.1	±	35.6	
	Freundlich	n_F	5.00	±	0.81	0.864
		K_F $(mmol\ g_{HAP}^{-1})$	0.577	±	0.160	
	Temkin	B $(J\ mmol^{-1})$	5.64E-02	±	4.76E-03	0.959
		A_T $(L\ mmol^{-1})$	23428	±	2184	
	Toth	n_{max} $(mmol\ g_{HAP}^{-1})$	0.660			8.91E-03[a]
		b $(L\ mmol^{-1})$	1434			
		n	0.433			
	Fowler-Guggenheim	w $(KJ\ mol^{-1})$	3.57	±	2.56	0.493
		K_{FG} $(L\ mmol^{-1})$	621	±	78	
	Flory-Huggins	n	0.133	±	0.015	0.939
		K_{FH} $(L\ mmol^{-1})$	0.168	±	0.003	
		ΔG $(J\ mmol^{-1})$	-4.50	±	0.05	
Second branch	Langmuir	n_{max} $(mmol\ g_{HAP}^{-1})$	1.69	±	0.76	0.713
		b $(L\ mmol^{-1})$	0.171	±	0.167	
	Freundlich	n_F	2.45	±	2.18	0.389
		K_F $(mmol\ g_{HAP}^{-1})$	0.417	±	0.406	
	Temkin	B $(J\ mmol^{-1})$	0.400	±	0.358	0.384
		A_T $(L\ mmol^{-1})$	1.49	±	7.98	
	Polynomial fit (DoseResp)[b]	A1	0.625		N.D.	N.D.
		A2	1.2			
		log(x0)	7.85			
		p	5.22			

[a] Sum of residual squares from non-linear regression

[b] Fit performed according to the mathematical DoseResp logarithmic model.
Model equation: q_e = A1 + (A2-A1)/(1+10^((log(x0)-C_e)·p))

Table 40: Model equations' parameters and correlation coefficients obtained from regression of Ni(II) experimental data according to the reported isotherm models.

Isotherm Model	**Parameter**	**Value**			**R^2**
Langmuir	n_{max} *(mmol g_{HAP}^{-1})*	0.317	±	0.004	0.998
	b *(L $mmol^{-1}$)*	2.88	±	0.59	
Freundlich	n_F	3.02	±	0.42	0.838
	K_F *(mmol g_{HAP}^{-1})*	0.174	±	0.011	
Temkin	B *(J $mmol^{-1}$)*	0.0426	±	0.0038	0.925
	A_T *(L $mmol^{-1}$)*	140	±	14	
Toth	n_{max} *(mmol g_{HAP}^{-1})*	0.371			7.20E-03[a]
	b *(L $mmol^{-1}$)*	11.8			
	n	0.492			
Fowler-Guggenheim	*w (KJ mol^{-1})*	0.336	±	2.590	0.004
	K_{FG} *(L $mmol^{-1}$)*	4.92	±	2.26	
Flory-Huggins	n	0.406	±	0.031	0.945
	K_{FH} *(L $mmol^{-1}$)*	0.327	±	0.019	
	ΔG *(J $mmol^{-1}$)*	-2.82	±	0.14	

[a] Sum of residual squares from non-linear regression

Table 41: Model equations' parameters and correlation coefficients obtained from regression of Co(II) experimental data according to the reported isotherm models.

Isotherm Model	**Parameter**	**Value**			**R^2**
Langmuir	n_{max} *(mmol g_{HAP}^{-1})*	0.382	±	0.009	0.994
	b *(L $mmol^{-1}$)*	3.70	±	1.66	
Freundlich	n_F	3.70	±	0.25	0.951
	K_F *(mmol g_{HAP}^{-1})*	0.228	±	0.009	
Temkin	B *(J $mmol^{-1}$)*	0.0398	±	0.0032	0.934
	A_T *(L $mmol^{-1}$)*	850	±	75	
Toth	n_{max} *(mmol g_{HAP}^{-1})*	1.77			6.05E-03[a]
	b *(L $mmol^{-1}$)*	2.74E+04			
	n	0.125			
Fowler-Guggenheim	*w (KJ mol^{-1})*	10.8	±	1.1	0.953
	K_{FG} *(L $mmol^{-1}$)*	156	±	9	
Flory-Huggins	n	0.318	±	0.040	0.863
	K_{FH} *(L $mmol^{-1}$)*	0.259	±	0.016	
	ΔG *(J $mmol^{-1}$)*	-3.40	±	0.16	

[a] Sum of residual squares from non-linear regression

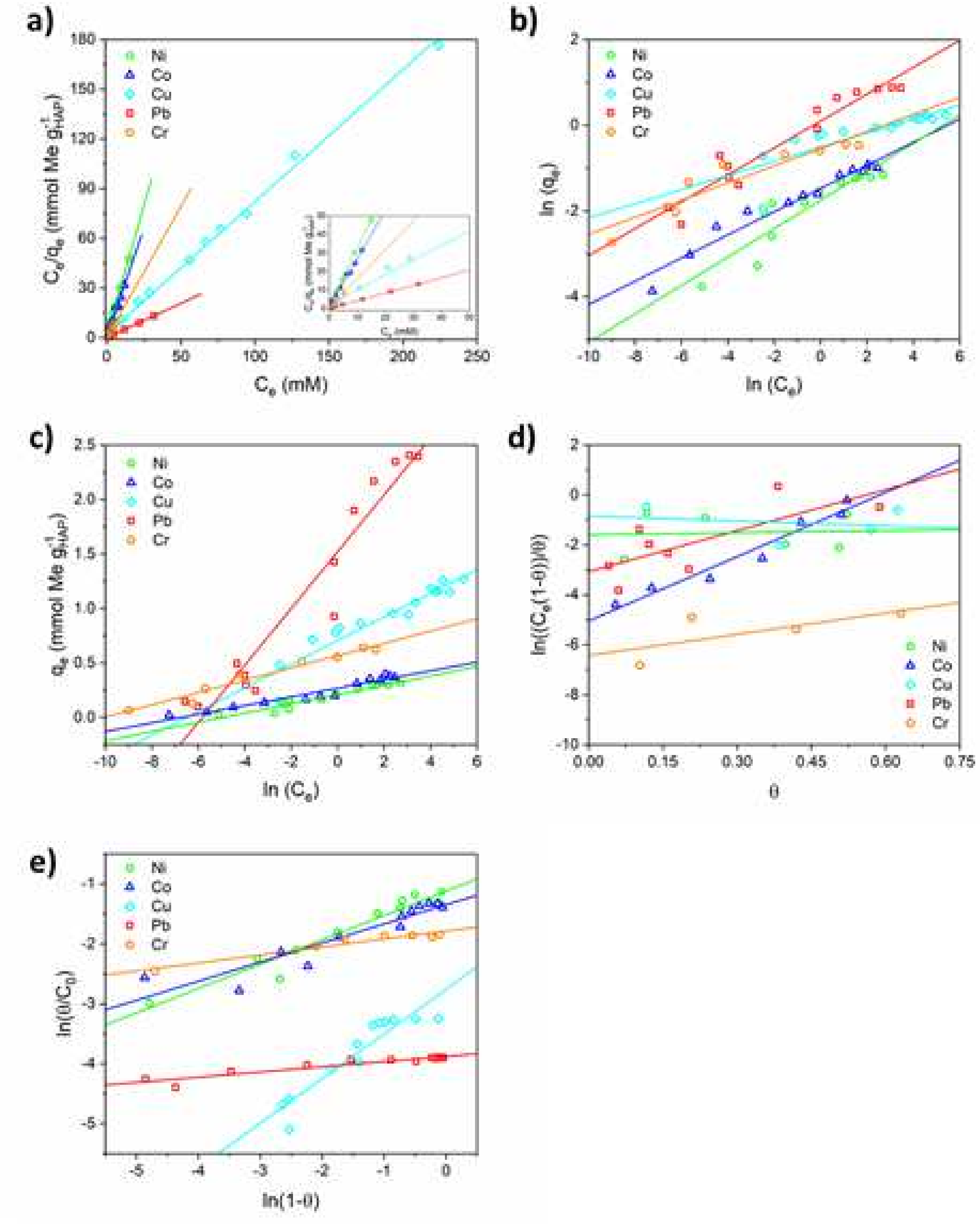

Figure 84: Linear regression of experimental data for all metal species according to a) Langmuir, b) Freundlich, c) Temkin, d) Fowler-Guggenheim and e) Flory-Huggins isotherm model equations. Regressions of Cr(III) data were performed only on the first branch of the isotherm since the second one is supposed to be related to an immobilization phenomenon that does not strictly correlate to adsorption onto HAP surface.

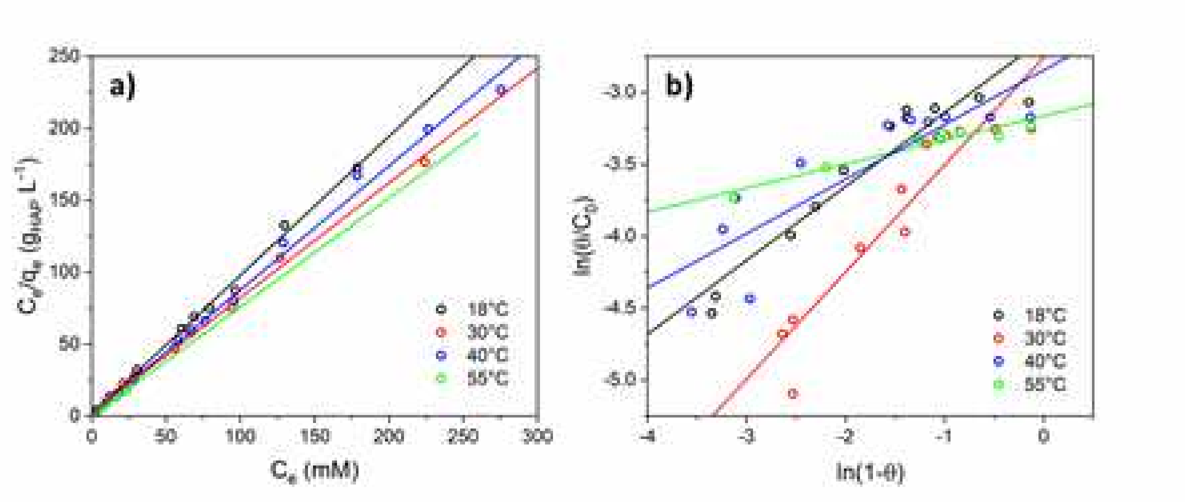

Figure 85: Linear regression of experimental data for Cu(II) according to Langmuir isotherm model equation.

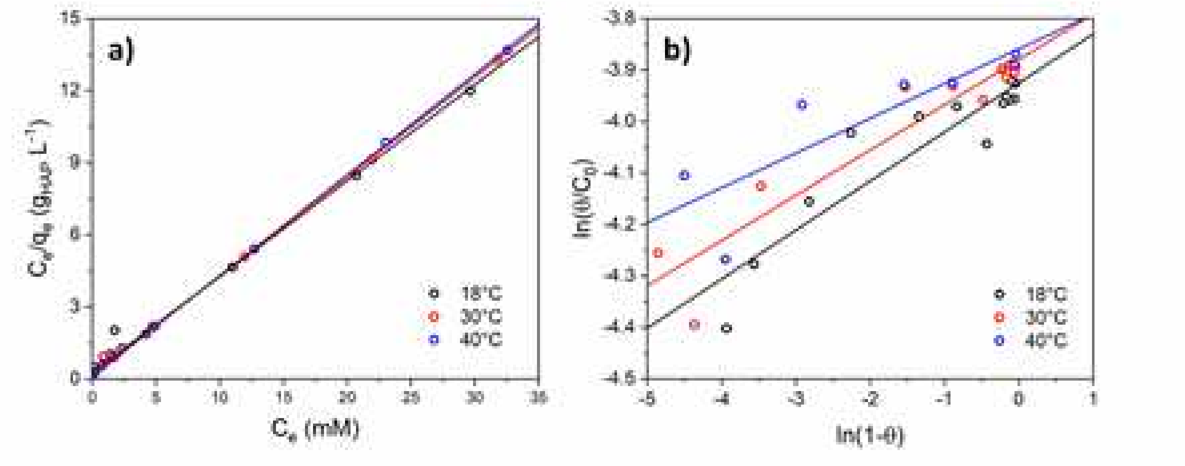

Figure 86: Linear regression of experimental data for Pb(II) according to Langmuir isotherm model equation.

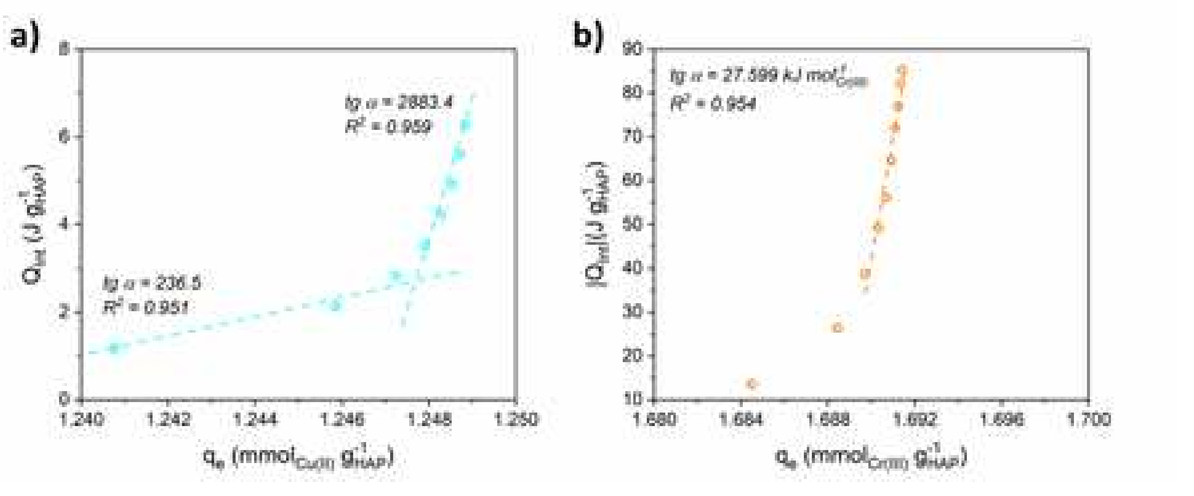

Figure 87: Calorimetric isotherms of a) Cu(II) and b) Cr(III) adsorption onto HAP surface. As stated in the main text, collection of experimental points in a narrow qe range, too close to nmax, preclude a reliable analysis of slopes and thus the calculation of correct $\Delta_{abs}H$.

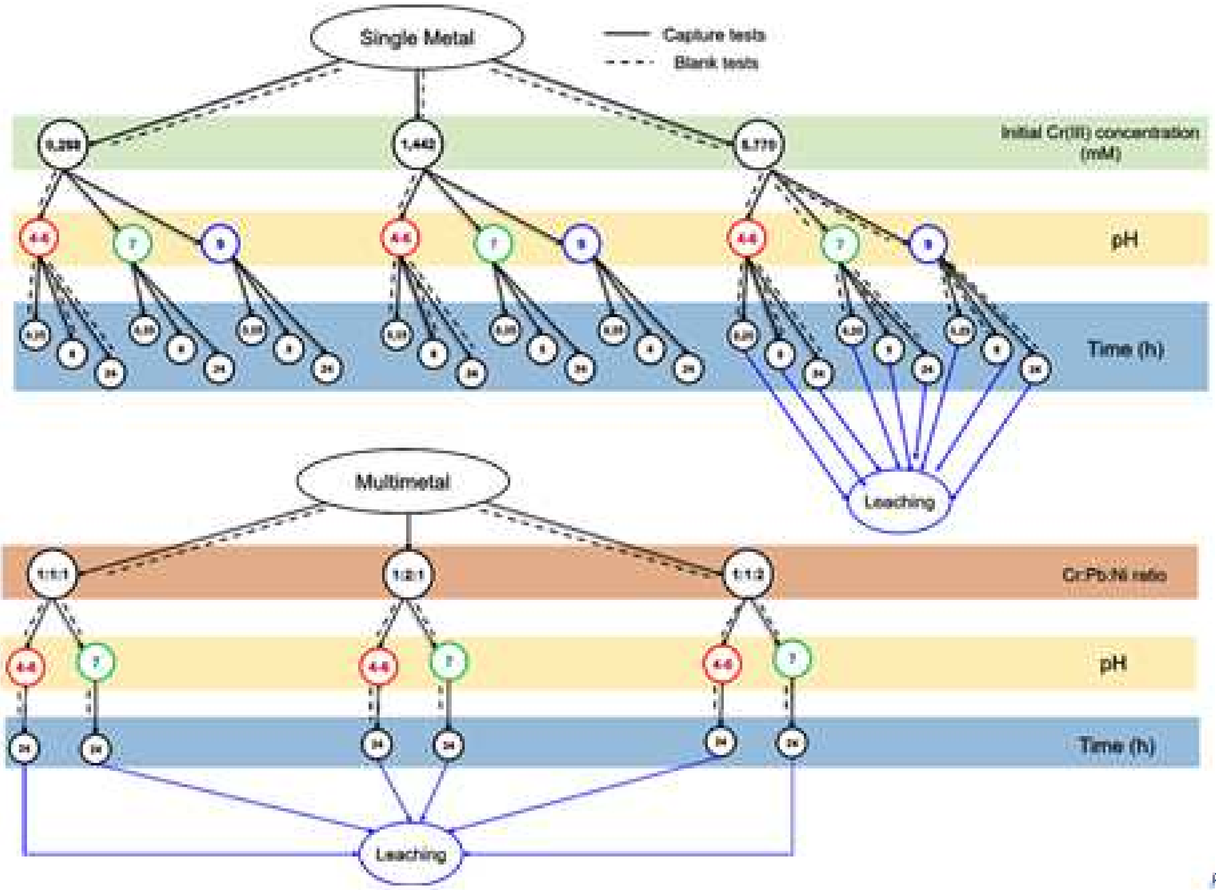

Figure 88: Summary view of all the experiments of metal uptake performed by using synthetic HAP sample, of all the blank tests (using silica as sorbent) and of all the leaching tests from Cr/HAP samples, and from Cr-Pb-Ni/HAP samples (molar ratio of the Cr(III):Pb(II):Ni(II) solution at fixed total molar concentration of ca. 6 mM). From reference (Ferri et al. 2019).

Table 42: Amounts of nickel and cobalt uptake on HAP measured from static batch single metal adsorption tests at 30°C, solution volume to solid ratio ca. 100 mL g_{HAP}^{-1}, at different pH, initial metal concentration and contact time.

Contact time (h)	***Ni(II) adsorbed (mmol g_{HAP}^{-1})***					
	pH 4			*pH 9*		
	Initial Ni(II) Concentration					
	0.221 mM	*1.141 mM*	*4.174 mM*	*0.221 mM*	*1.141 mM*	*4.174 mM*
0.25	0.00336	0.0185	0	0.0234	0.0788	0.337
8	0.00822	0.0350	0.0907	0.0226	0.105	0.362
24	0.00889	0.0475	0.132	0.0231	0.104	0.368

Contact time (h)	***Co(II) adsorbed (mmol g_{HAP}^{-1})***					
	pH 4			*pH 9*		
	Initial Co(II) Concentration					
	0.240 mM	*1.205 mM*	*4.327 mM*	*0.240 mM*	*1.205 mM*	*4.327 mM*
0.25	0.0097	0.0357	0.0289	0.0252	0.104	0.418
8	0.0100	0.0556	0.0980	0.0237	0.114	0.453
24	0.0145	0.0642	0.165	0.0234	0.112	0.442

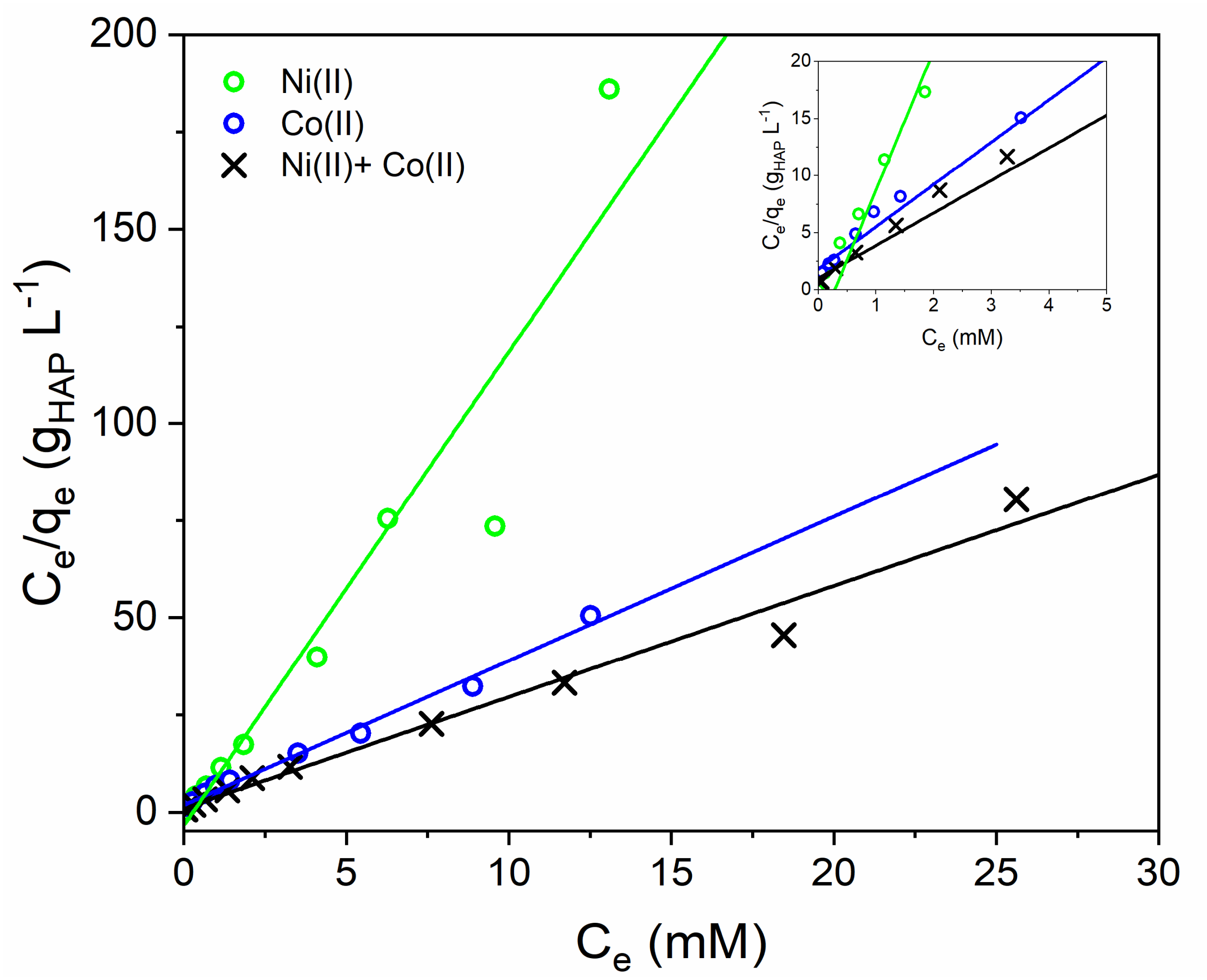

Figure 89: Linear regression of experimental data for Ni(II), Co(II) and Ni(II) + Co(II) according to Langmuir isotherm model equation.

10.1.3 Adsorption Isotherms

10.1.3.1 Langmuir isotherm

Langmuir adsorption isotherm is principally used to describe gas-solid adsorption phenomena. Adsorption of different species can be quantitatively compared by means of this model. Postulates of the model are the homogeneity of the sorbent sites toward the target species, the absence of interaction between adsorbate species on the surface, mono-layer coverage of the surface and constant heat of adsorption.

The linear form of Langmuir adsorption isotherm is the following:

$$\frac{C_e}{q_e} = \frac{1}{n_{max}\, b_{ads}} + \frac{C_e}{n_{max}}$$

Equation 6

where:

- C_e is the equilibrium concentration in the bulk phase (mmol L^{-1});
- q_e is the concentration of the adsorbate on the sorbent (mmol g^{-1});
- n_{max} is the maximum monolayer coverage of the adsorbate on the sorbent (mmol g^{-1});
- b_{ads} is the Langmuir constant (L $mmol^{-1}$), indicative of the adsorbate-sorbent interaction strength.

10.1.3.2 Freundlich isotherm

Freundlich adsorption isotherm is an empirical relation applicable to adsorption processes occurring on heterogenous surfaces, postulating an exponential energy distribution of the surface-active sites. Thus, the isotherm parameters describe surface heterogeneity and the distribution and energy of surface sites of the sorbent.

Linear form of the Freundlich isotherm is the following:

$$log\ q_e = log\ K_F + \frac{1}{n} log\ C_e$$

Equation 7

where:

- K_F is the sorbent adsorption capacity (mmol g^{-1});
- 1/n is indicative of the adsorption intensity.

10.1.3.3 Temkin isotherm

Temkin isotherm model is commonly used for systems in which the effects of indirect adsorbate/adsorbate interactions on the adsorption process are not negligible. Temkin isotherm is applicable for intermediate concentration of adsorbate, since it unrealistically derives for low and high adsorbate concentrations. Assumption of the model is the linear decrease of the heat of adsorption of the adsorbate when surface coverage increases.

Linearization of Temkin isotherm model is the following:

$$q_e = B\ lnA_T + B\ lnC_e\ with\ B = \frac{RT}{b_T}$$

Equation 8

where:

- b_T is a Temkin isotherm constant (adimensional);
- B is a constant related to heat of sorption (J mmol^{-1});
- A_T is the Temkin isotherm equilibrium binding constant (L g^{-1}).

10.1.3.4 Toth isotherm

Toth isotherm is an empirical modification of the Langmuir equation, introducing an exponential n factor, useful to describe heterogeneous adsorption systems. When n=1, the equation reduces to the classical Langmuir isotherm, while deviates from 1 in correlation with the increased heterogeneity of the sorbent surface.

Linearization of Toth isotherm could be expressed as follows:

$$ln \frac{q_e^n}{n_{max}^n - q_e^n} = n \; ln(b_{ads}) + n \; ln(C_e)$$

Equation 9

where:

- n is the Toth isotherm constant (adimensional);
- n_{max} and b_{ads} have the same meaning they have in Langmuir isotherm.

The values of parameters of the Toth model can be evaluated by nonlinear curve fitting method.

10.1.3.5 Fowler-Guggenheim isotherm

Fowler-Guggenheim isotherm is a modification of the Langmuir model equation that takes into consideration the lateral interaction between adsorbed species. Also, it postulates a linear correlation between heat of adsorption and adsorbate loading onto the surface.

Linearization of Fowler-Guggenheim equation can be expressed as:

$$\ln \frac{C_e(1-\theta)}{\theta} = -\ln K_{FG} + \frac{2w\theta}{RT}$$

where:

- K_{FG} is the Fowler-Guggenheim equilibrium constant (L mg^{-1}):
- θ is fractional coverage;
- w represents the interaction energy between adsorbed molecules (kJ mol^{-1}).

Since the adsorbate species could interact both attractively and repulsively, w parameter can take positive or negative values (in case of attraction and repulsion, respectively), indicating a linear increasing or decreasing heat of adsorption as surface coverage increases. The model stands up to $\theta = 0.6$, then deviations could occur because of the high surface coverage degree. In case lateral interaction are negligible, w reduces to zero and Fowler-Guggenheim equation to the Langmuir one.

10.1.3.6 Flory-Huggins isotherm

Flory-Huggins isotherm can express the feasibility and spontaneity of an adsorption process, since from its parameters it is possible to calculate the standard Gibbs' free energy variation related to the adsorption process. The equation describes the degree of surface coverage characteristics of the adsorbate-sorbent system.

Linearization of Flory-Huggins isotherm is commonly expressed as the following:

$$ln\left(\frac{\theta}{C_0}\right) = lnK_{FH} + n\ ln(1-\theta)$$

Equation 10

where:

- C_0 is the initial adsorbate concentration in bulk solution (mmol L^{-1});
- θ is degree of surface coverage;
- n is number of occupied adsorption sites;
- K_{FH} is Flory-Huggins equilibrium constant (L $mmol^{-1}$).

As previously written, it is possible to calculate the standard Gibbs' free energy variation of the adsorption process (ΔG^0) from K_{FH}, correlating the parameters by the following equation:

$$\Delta G^0 = RTln(K_{FH})$$

Equation 11

10.2 Chapter 2

10.2.1 Preliminary screening of different carbonaceous scaffold

14.5

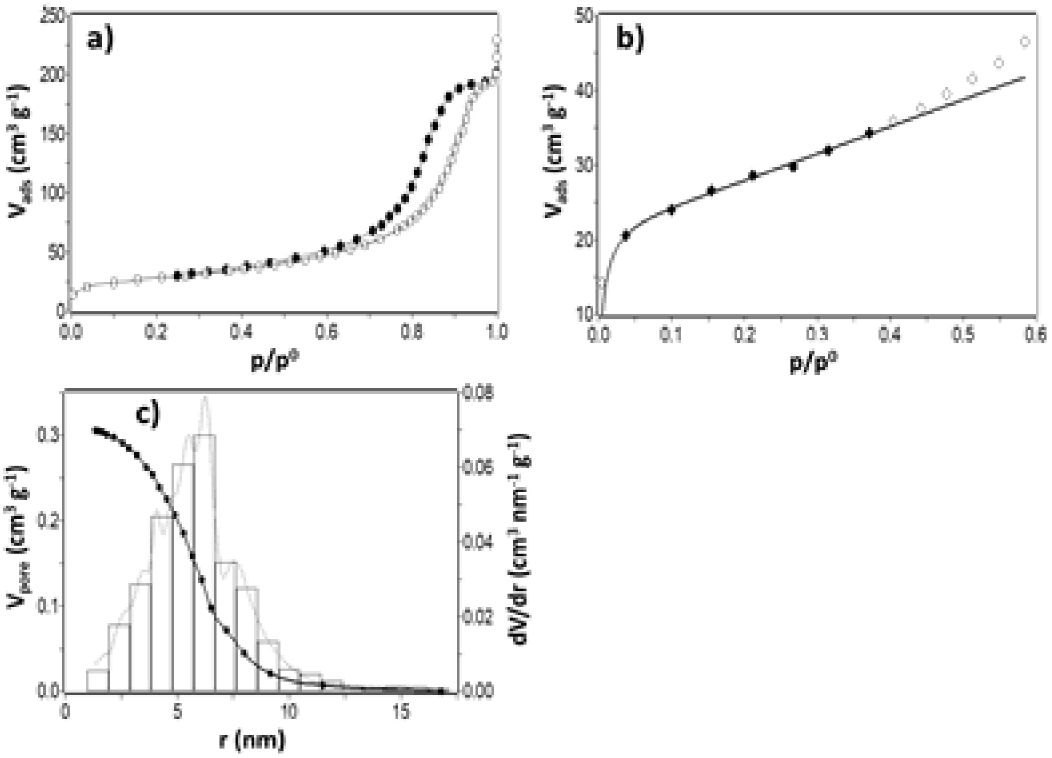

Figure 90: N_2 adsorption/desorption analysis results for HAP_RT. a) Adsorption and desorption isotherms; b) fitting of the low-pressure portion isotherm by 3-parameters B.E.T. equation ($0.05 < p/p^0 < 0.4$); c) total pore volume (full markers) and pore volume distribution, according to B.J.H. model.

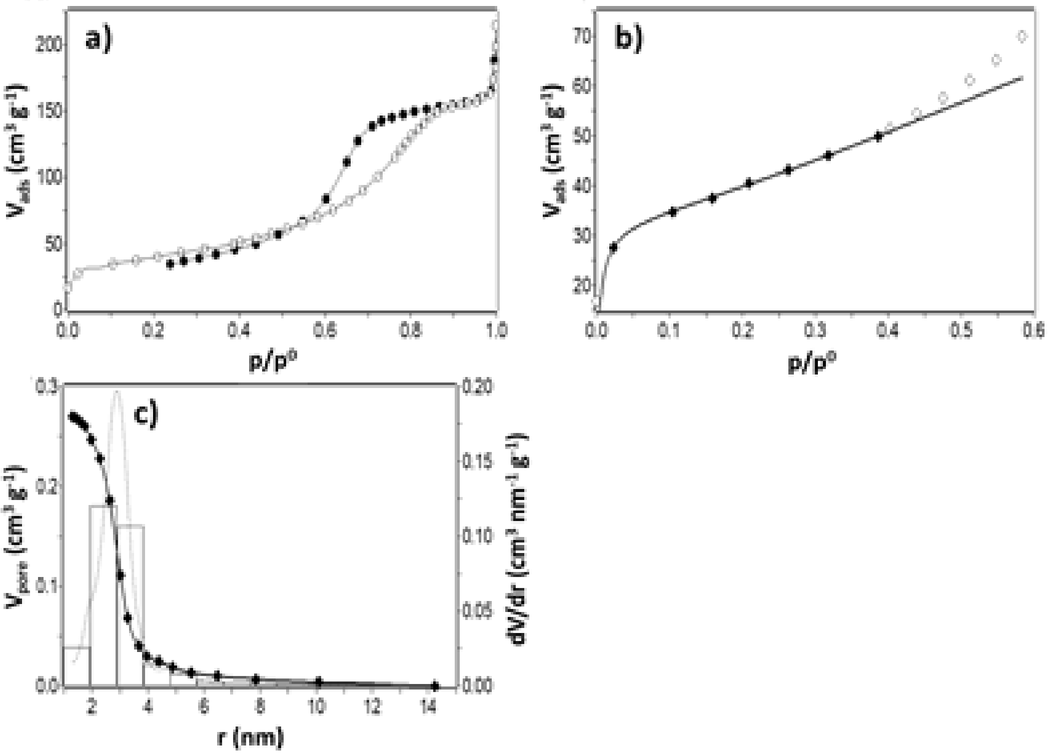

Figure 91: N_2 adsorption/desorption analysis results for HAP/CNF composite. a) Adsorption and desorption isotherms; b) fitting of the low-pressure portion isotherm by 3-parameters B.E.T. equation ($0.05 < p/p^0 < 0.4$); c) total pore volume (full markers) and pore volume distribution, according to B.J.H. model.

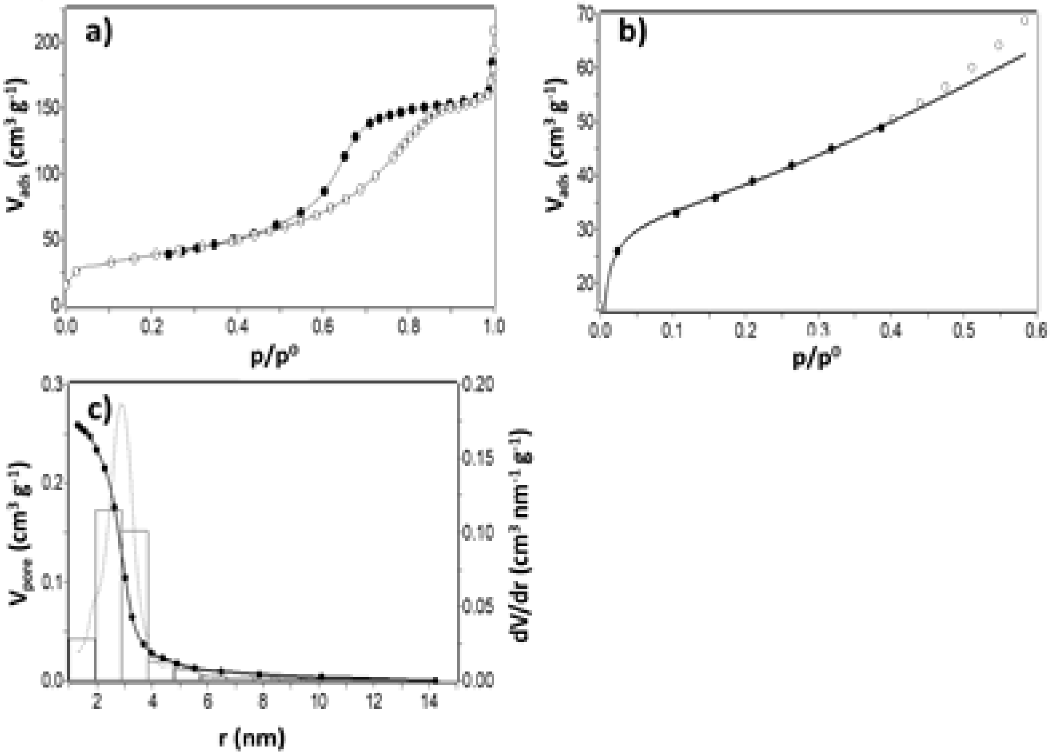

Figure 92: N_2 adsorption/desorption analysis results for HAP/CMC composite. a) Adsorption and desorption isotherms; b) fitting of the low-pressure portion isotherm by 3-parameters B.E.T. equation ($0.05 < p/p^0 < 0.4$); c) total pore volume (full markers) and pore volume distribution, according to B.J.H. model.

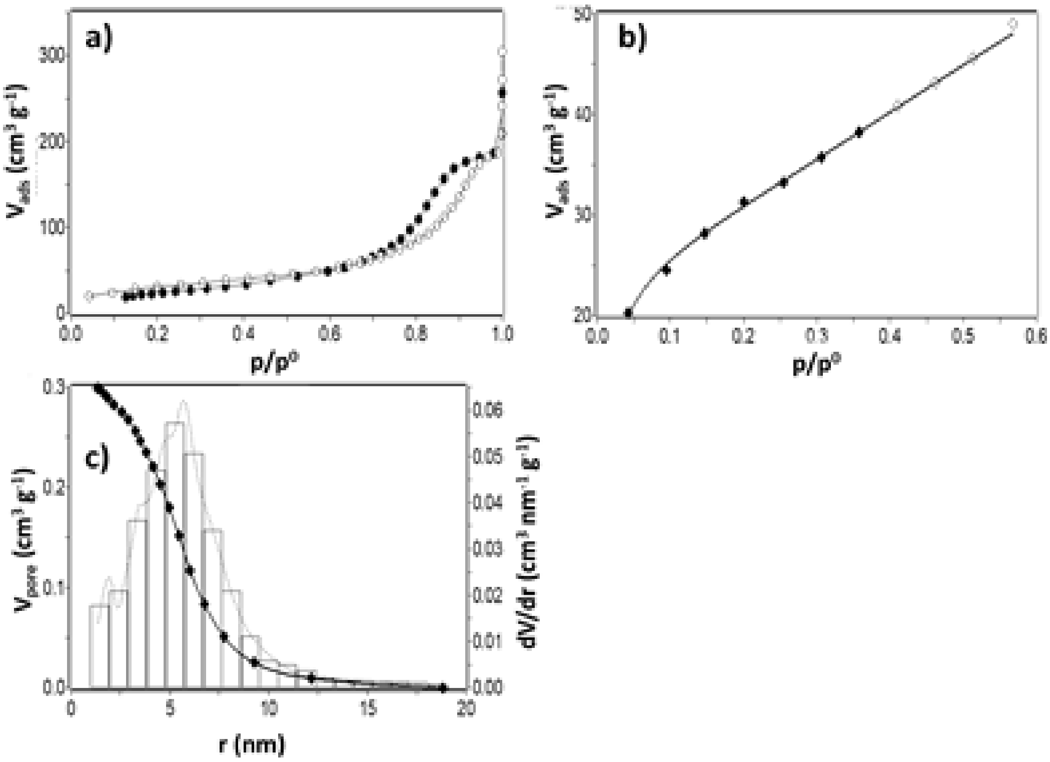

Figure 93: N_2 adsorption/desorption analysis results for HAP/AC composite. a) Adsorption and desorption isotherms; b) fitting of the low-pressure portion isotherm by 3-parameters B.E.T. equation ($0.05 < p/p^0 < 0.4$); c) total pore volume (full markers) and pore volume distribution, according to B.J.H. model.

10.2.2 HAP/C composite materials for efficient wastewater remediation

Table 43: Weighted masses of CMC and HAP and related CMC wt. % in HAP_CMC physical mixtures.

Sample - Physical mixture	**m CMC**	**m HAP**	**CMC wt. %**
	mg	*mg*	*%*
MIX_HAP_CMC_4	4.9	104.3	4.49
MIX_HAP_CMC_8	9.0	92.4	8.88
MIX_HAP_CMC_12	13.9	89.6	13.43
MIX_HAP_CMC_16	17.9	81.0	18.10

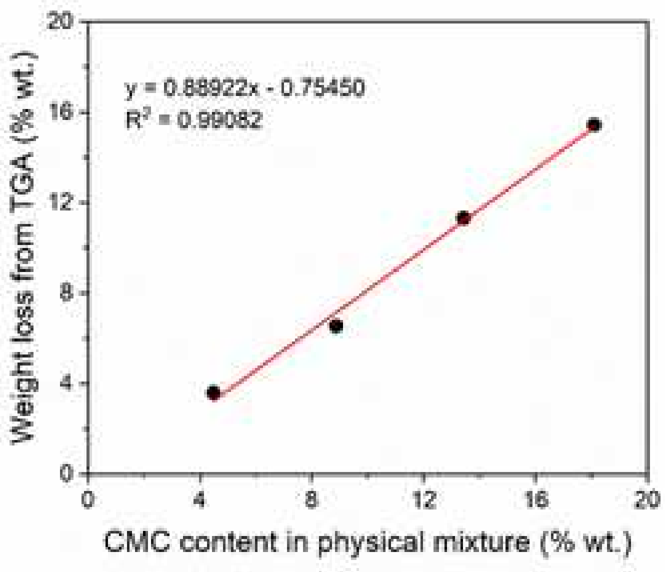

Figure 94: Calibration line of thermogravimetric weight loss versus CMC wt. % content obtained from TG analyses on physical mixtures.

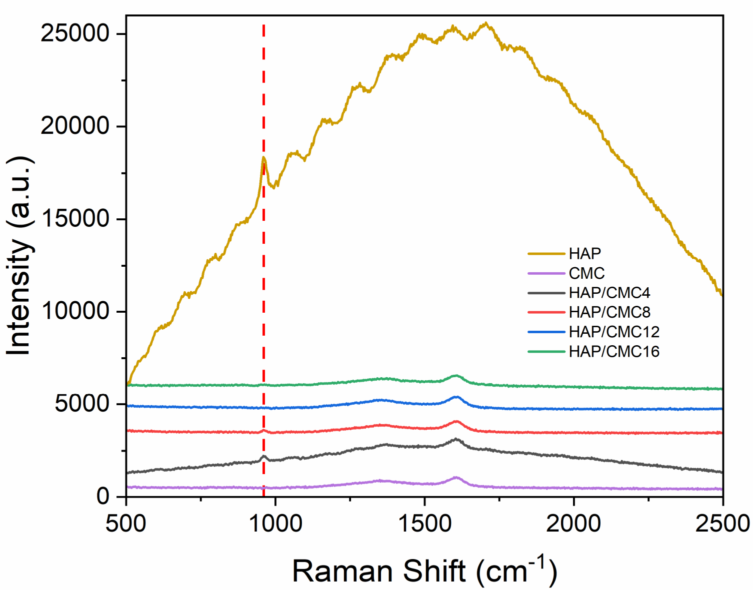

Figure 95: Comparison of the Raman intensities of pristine HAP_RT (yellow line) versus HAP/CMC composites and pristine CMC.

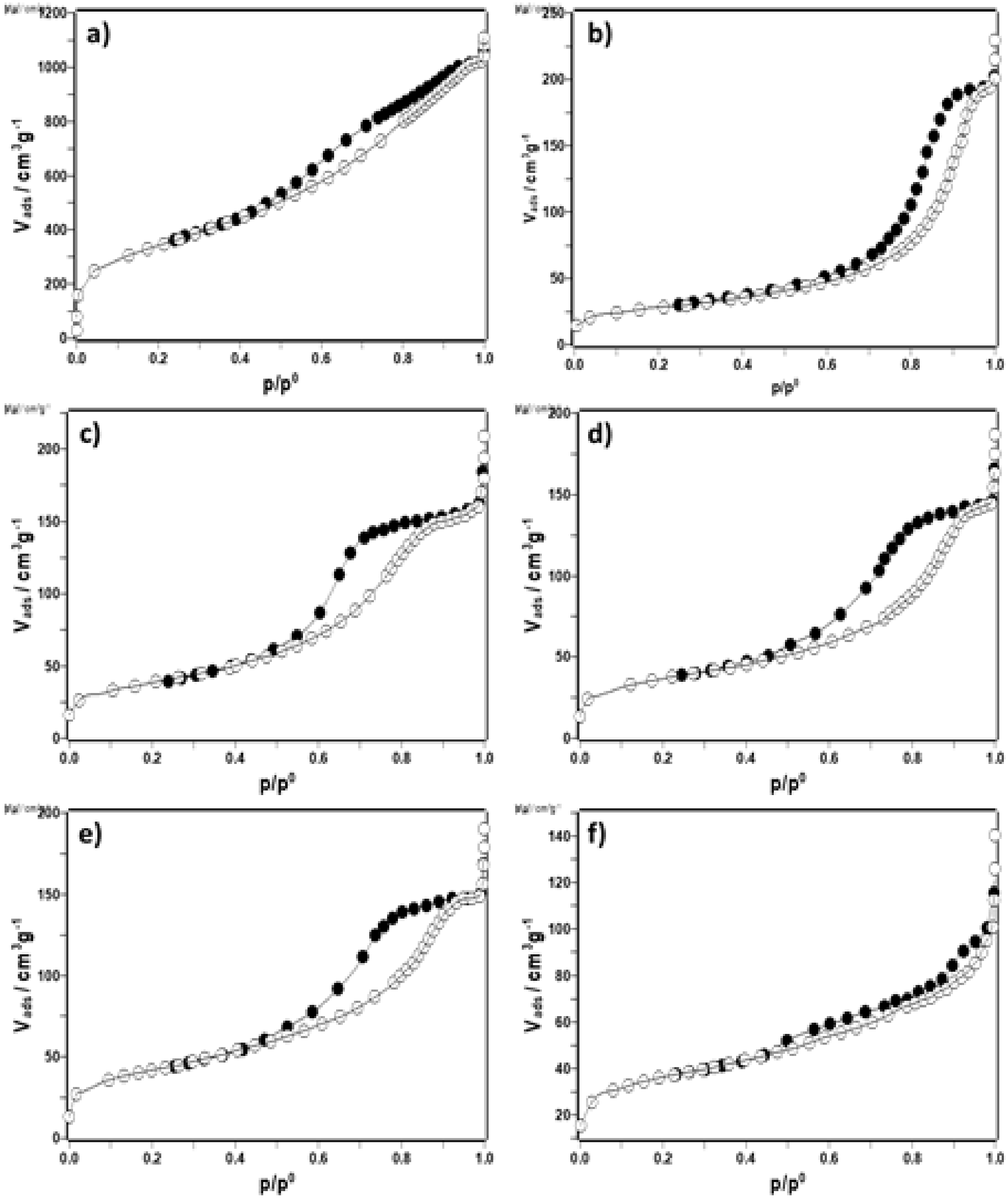

Figure 96: N$_2$ adsorption/desorption isotherms for a) pristine CMC ; b) pristine HAP_RT; c) HAP/CMC4; d) HAP/CMC8; e) HAP/CMC12 and f) HAP/CMC16.

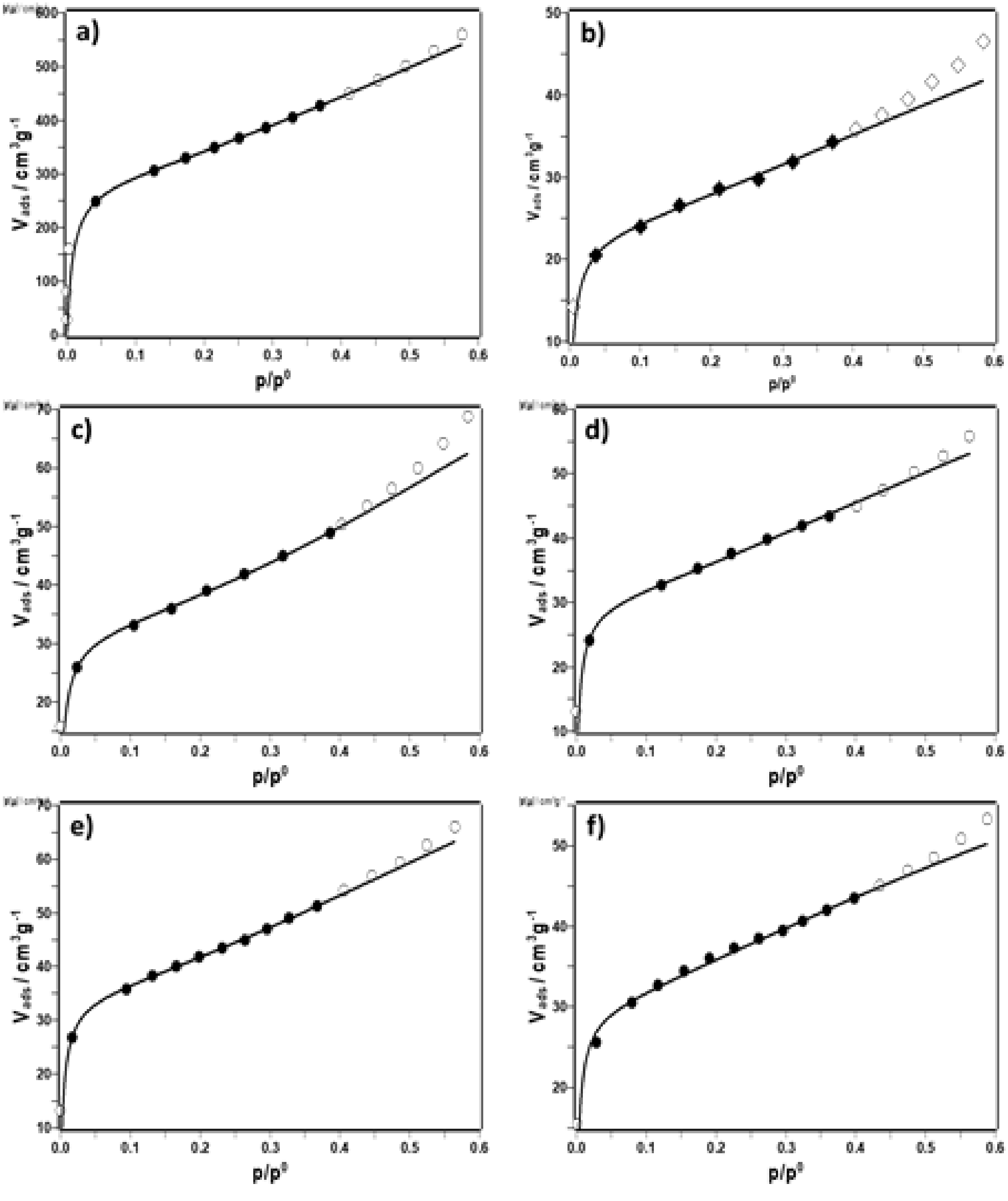

Figure 97: 3-parameters BET linearization for a) pristine CMC ; b) pristine HAP_RT; c) HAP/CMC4; d) HAP/CMC8; e) HAP/CMC12 and f) HAP/CMC16.

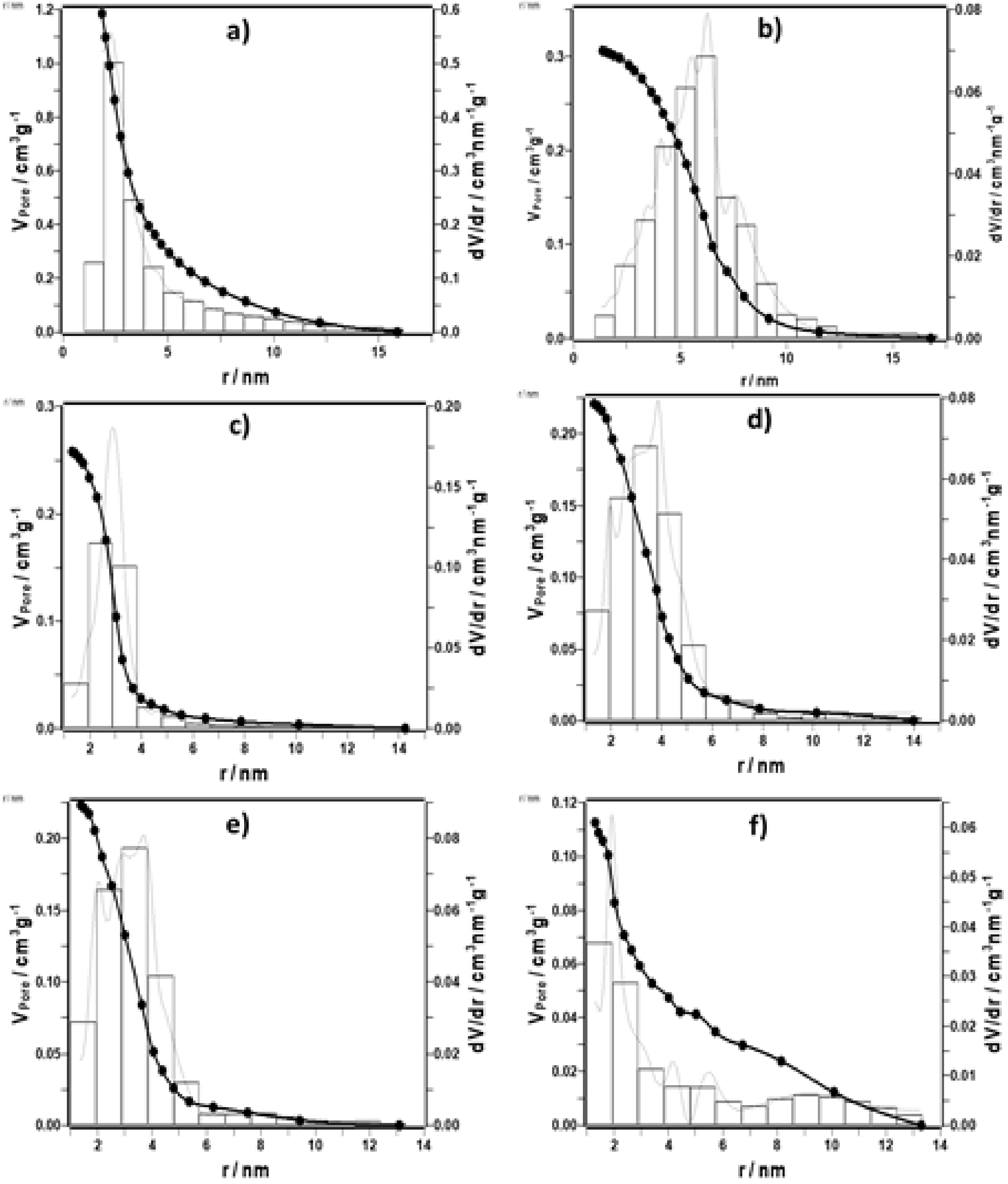

Figure 98: Pore size distribution, calculated according to the BJH model, for a) pristine CMC ; b) pristine HAP_RT; c) HAP/CMC4; d) HAP/CMC8; e) HAP/CMC12 and f) HAP/CMC16.

Table 44: Number of intrinsic and effective surface acid and basic sites of pristine moieties (HAP_RT and CMC) and HAP/CMC composites. Value normalized by the surface area are reported in µeq m^{-2} for the sake of clarity (i.e.to avoid the use of the scientific numeric format).

Sample	**Total acid sites**			**Total basic sites**		
	Intrinsic (Cy)		Effective (H_2O)	Intrinsic (Cy)		Effective (H_2O)
	meq g^{-1}	*µeq m^{-2}*	*meq g^{-1}*	*meq g^{-1}*	*µeq m^{-2}*	*meq g^{-1}*
HAP_RT	0.221	2.197	0	0.016	0.156	0
HAP/CMC4	0.156	1.139	0	0.004	0.030	0
HAP/CMC8	0.089	0.687	0	0.006	0.048	0
HAP/CMC12	0.091	0.613	0	0.020	0.137	0
HAP/CMC16	0.021	0.174	0	0.003	0.024	0
Pristine CMC	0.251	0.203	N.D.	0	0	N.D.

10.2.2.1 Numerical treatment of acid/base liquid-phase pulsed titration data

In a pulsed titration, the non-adsorbed probe is revealed by the UV-vis detector as a peak whose area can be directly correlated to the quantity of probe itself (by a previous calibration of the system). Thus, by difference with the amount of injected probe, it is possible to obtain the quantity of adsorbed probe molecules. Because of increasing surface saturation, the peaks area tends to increase with the number of injections, as the quantity of probe adsorbed by the sample tends to diminish. Once saturation is attained, the peak areas have constant value, identifying the end point of the titration.

It is possible to quantify the number of surface acid/base sites by computing the amount of probe adsorbed and assuming a given stoichiometry between the probe and the surface acid/base site:

$$\text{probe adsorbed}_i = \frac{[probe] \cdot V_{Inj}}{m_{cat}} \cdot \frac{A_{sat} - A_i}{A_{sat}}$$

Equation 12

where:

- probe adsorbed (mmol g^{-1}) = quantity of probe molecule adsorbed on the sample during the i^{th} injection;
- [probe] (mol L^{-1}) = concentration of the injected probe (PEA or BA) solution;
- V_{Inj} (mL) = volume of the single i^{th} injection;
- m_{cat} (g) = mass of sample put in the sample holder;
- A_{sat} = average chromatographic area of the peaks at saturation (when constant area value is attained);
- A_i = chromatographic area of the i^{th} peak.

When a 1:1 stoichiometry between the probe and the site is assumed, the number of acidic/basic sites of the analyzed sample corresponds to the total amount of probe molecule adsorbed. It is then possible to draw isotherm-like plots (Figure 43a), where the actual amount of adsorbed probe is plotted against the injected amount, and to express the total number of surface acid/base sites of the sample as meq g^{-1} or meq m^{-2}.

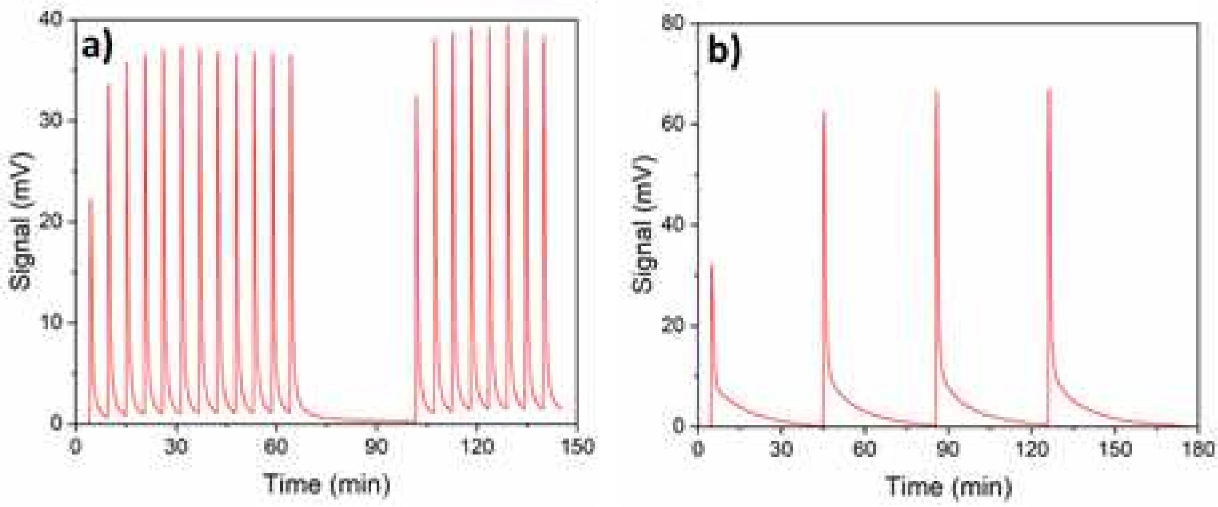

Figure 99: Typical chromatograms registered on HAP/CMC composites under the operative conditions detailed in paragraph 8.2.4.2. a) Surface acidity liquid-solid pulsed injection titration (probe molecule: PEA); b) Surface basicity liquid-solid pulsed injection titration (probe molecule: BA).

10.2.2.2 Simultaneous removal of organic and inorganic pollutant in simulated wastewater by HAP/CMC composites

Table 45: Percentage (left entries) and mass on mass ($mg_{Cu(II)}\,g^{-1}_{Sorbent}$) removal of Cu(II) by pristine moieties and different composites. Sorption tests performed according to a stirred batch method, T = 30°C, contact time = 2 h, natural pH (ca. 6).

Sample	**Adsorbed Cu(II)**					
	% Removal			Mass on mass removal ($mg_{Cu(II)}\,g^{-1}_{Sorbent}$)		
	C_0 ≈ 15 ppm	C_0 ≈ 75 ppm	C_0 ≈ 300 ppm	C_0 ≈ 15 ppm	C_0 ≈ 75 ppm	C_0 ≈ 300 ppm
HAP_RT	98.18	99.63	99.80	1.53	7.93	32.02
HAP/CMC4	98.73	99.73	98.63	1.55	8.01	26.66
HAP/CMC8	99.60	99.82	98.39	1.59	7.87	30.43
HAP/CMC12	99.68	99.80	98.53	1.39	6.33	30.23
HAP/CMC_16	99.53	99.59	96.44	1.56	5.99	29.23
CMC	100.00	85.50	39.43	1.52	6.48	12.21

Table 46: Percentage (left entries) and mass on mass ($mg_{Ni(II)}\,g^{-1}_{Sorbent}$) removal of Ni(II) by pristine moieties and different composites. Sorption tests performed according to a stirred batch method, T = 30°C, contact time = 2 h, natural pH (ca. 6).

Sample	**Adsorbed Ni(II)**					
	% Removal			Mass on mass removal ($mg_{Ni(II)}\,g^{-1}_{Sorbent}$)		
	C_0 ≈ 15 ppm	C_0 ≈ 75 ppm	C_0 ≈ 300 ppm	C_0 ≈ 15 ppm	C_0 ≈ 75 ppm	C_0 ≈ 300 ppm
HAP_RT	88.49	69.91	42.32	1.45	5.85	10.53
HAP/CMC4	88.24	76.08	44.66	1.34	6.34	14.36
HAP/CMC8	89.76	76.42	37.21	1.40	6.18	11.42
HAP/CMC12	89.57	80.10	39.94	1.45	6.50	13.13
HAP/CMC_16	90.78	78.43	29.05	1.37	5.55	9.74
CMC	100.00	65.09	20.14	1.67	5.00	6.49

Table 47: Percentage (left entries) and mass on mass ($mg_{MB}\,g^{-1}_{Sorbent}$) removal of MB by pristine moieties and different composites. Sorption tests performed according to a stirred batch method, T = 30°C, contact time = 2 h, natural pH (ca. 6).

Sample	**Adsorbed MB**				**Removal Projections**
	% Removal		Mass on mass removal ($mg_{MB}\,g^{-1}_{Sorbent}$)		$mg_{MB}\,g^{-1}_{Sorbent}$
	C_0 ≈ 250 ppm	C_0 ≈ 500 ppm	C_0 ≈ 250 ppm	C_0 ≈ 500 ppm	C_0 ≈ 500 ppm
HAP_RT	16.87	13.46	3.91	6.44	-
HAP/CMC4	80.82	52.76	20.09	25.59	18.25
HAP/CMC8	99.99	78.55	24.83	37.95	30.31
HAP/CMC12	99.97	88.86	24.58	40.95	42.37
HAP/CMC_16	99.99	99.74	25.06	47.36	54.43
CMC	99.95	99.98	25.06	48.78	-

Table 48: Consecutive MB adsorption tests on CMC, carried out to determine the $q_{max\ MB}$ on the sorbent (bold value on the last row, on the right). Operative conditions are the same as other stirred batch adsorption tests.

Run	**Initial MB Conc.**	**Removed MB**	$q_{Single\ Run}$	$q_{Cumulative}$
n°	*ppm*	*%*	$mg_{MB}\ g^{-1}_{CMC}$	$mg_{MB}\ g^{-1}_{CMC}$
1	610	100.00	60.3	60.3
2	305	100.00	30.2	90.5
3	305	100.00	30.2	120.7
4	305	100.00	30.2	150.8
5	305	100.00	30.2	181.0
6	305	100.00	30.2	211.2
7	305	100.00	30.2	241.3
8	305	100.00	30.2	271.5
9	305	99.46	30.0	**301.5**

Table 49: Percentage (left entries) and mass on mass ($mg_{Pollutant}\ g^{-1}_{Sorbent}$) removal of Cu(II), Ni(II) and MB (in ternary mixtures) by pristine moieties and different composites. Sorption tests performed according to a stirred batch method, T = 30°C, contact time = 2 h, Cu(II) & Ni(II) initial concentration ca. 300 ppm and MB initial concentration ca. 250 ppm, natural pH (ca. 6).

Sample	**Cu(II)**	**Ni(II)**	**MB**	**Cu(II)**	**Ni(II)**	**MB**
	% Removal			*Mass on mass removal ($mg_{Pollutant}\ g^{-1}_{Sorbent}$)*		
HAP_RT	98.56	26.95	2.76	29.76	7.34	0.64
HAP/CMC4	95.43	28.78	93.71	28.55	7.77	21.62
HAP/CMC8	86.65	25.96	99.39	27.25	7.37	24.10
HAP/CMC12	96.29	17.20	99.94	30.13	4.72	24.12
HAP/CMC_16	91.52	14.09	99.75	28.75	3.78	24.17
CMC	46.86	9.09	99.93	15.33	2.68	25.21

10.2.2.3 Development of HAP/C based electrodes for electrochemical sensing of heavy metal cations' traces in waterbodies

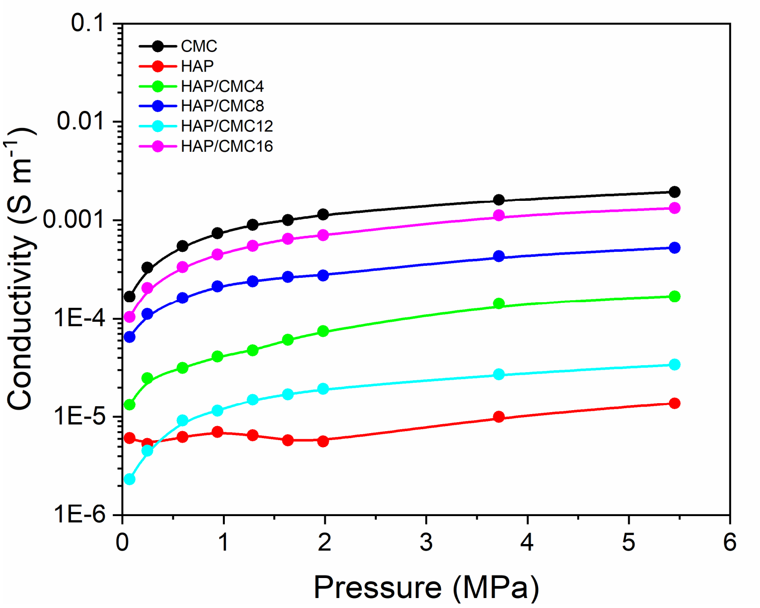

Sample	Conductivity $S\ m^{-1}$
HAP_RT	$1.37 \cdot 10^{-5}$
HAP/CMC4	$1.70 \cdot 10^{-4}$
HAP/CMC8	$5.27 \cdot 10^{-4}$
HAP/CMC16	$1.33 \cdot 10^{-3}$
Pristine CMC	$1.95 \cdot 10^{-3}$

Figure 100: Conductivity versus applied pressure of HAP/CMC composites powders and related values extrapolated from the plateau.

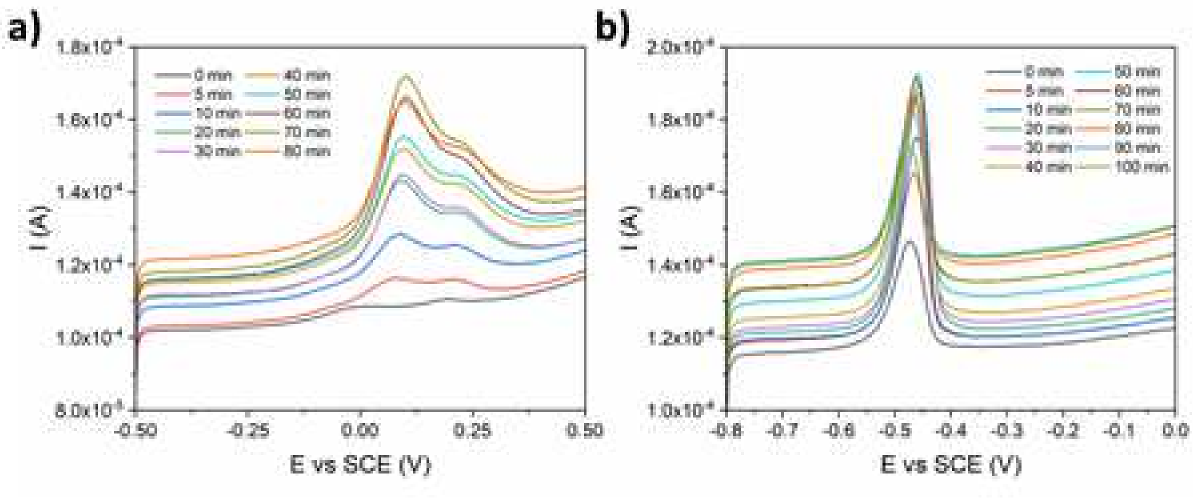

Figure 101: Stripping voltammograms envelopes registered on HAP/CMC8 in the presence of a) Cu(II) 10^{-5} M and b) Pb(II) 10^{6} M at different OCP preconcentration times.

Table 50: Regression parameters for HAP/CMC8-based electrodes' calibrations. Experimental data and regression line are graphically reported in Figure 52.

		Slope	**Intercept**	**R^2**
Cu(II)	Sequential	23033.4	-0.0372	0.910
	Timely	29367.1	-0.0714	0.812
Pb(II)	Sequential	40245.1	-0.0580	0.966
	Timely	56973.4	-0.127	0.819

Table 51: Initial, final and percentage variation of electrical conductivity of HAP/CMC8-based electrodes immerged in Pb(II) or Cu(II) containing solutions.

Solution	**Immersion time**	**[Me(II)]**	**Electrode conductivity (σ)** μS m^{-1}		
	min	*µM*	*Pristine*	*Post-immersion*	$\Delta\sigma$ (%)
MilliQ H_2O	50	-	0.66	0.57	-14
Pb(II) in MilliQ H_2O	50	1	0.66	0.45	-32
		10		0.23	-65
		100		0.13	-80
Cu(II) in MilliQ H_2O	60	1	0.66	0.20	-70
		10		0.11	-84
		100		0.086	-87

10.3 Chapter 3

10.3.1 Characterization of HAP-doped electrocatalysts for CO_2RR

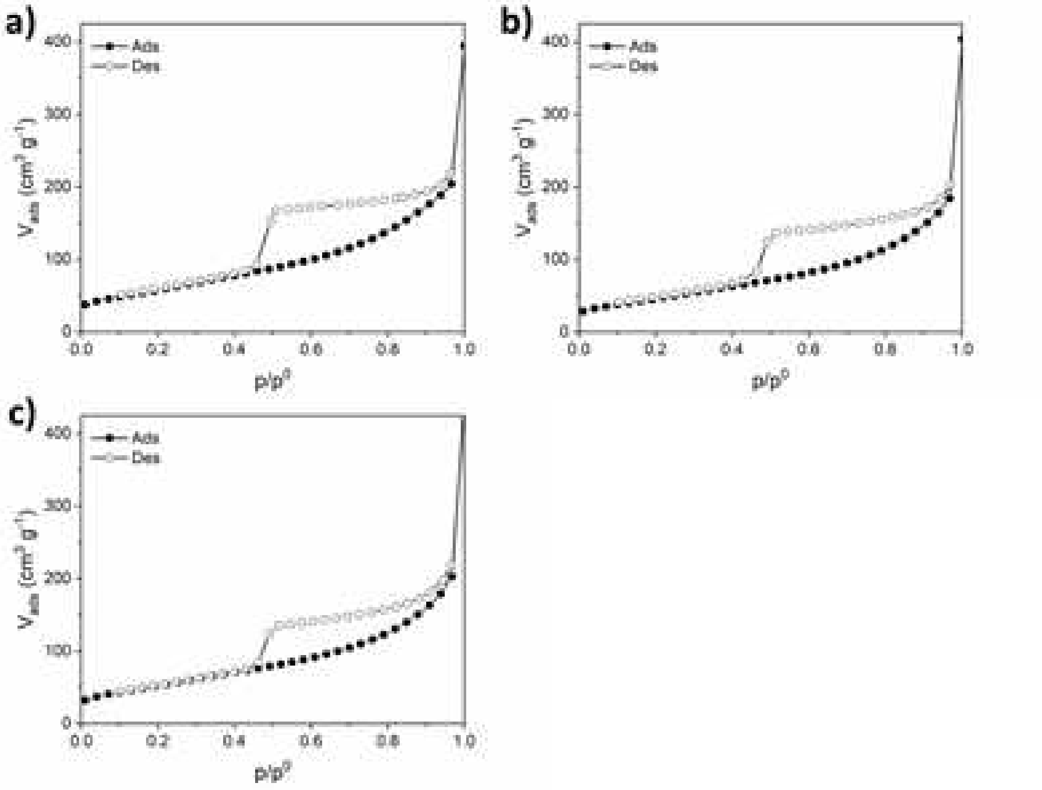

Figure 102: N_2 ads/des isotherms of a) 3D-GNS; b) Cu/3D-GNS and c) Cu+HAP/3D-GNS.

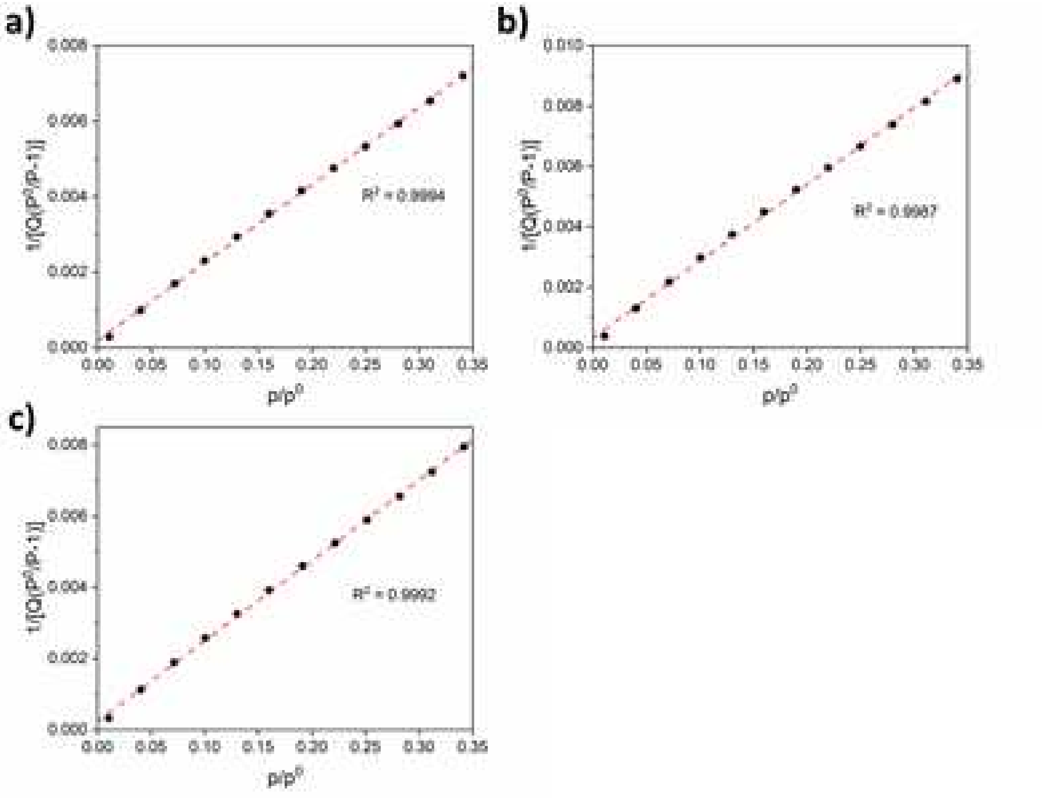

Figure 103: BET linearizations (2-parameters), performed on the adsorption branch of the N_2 ads/des isotherms ($0.01 < p/p^0 < 0.35$), of a) 3D-GNS; b) Cu/3D-GNS and c) Cu+HAP/3D-GNS.

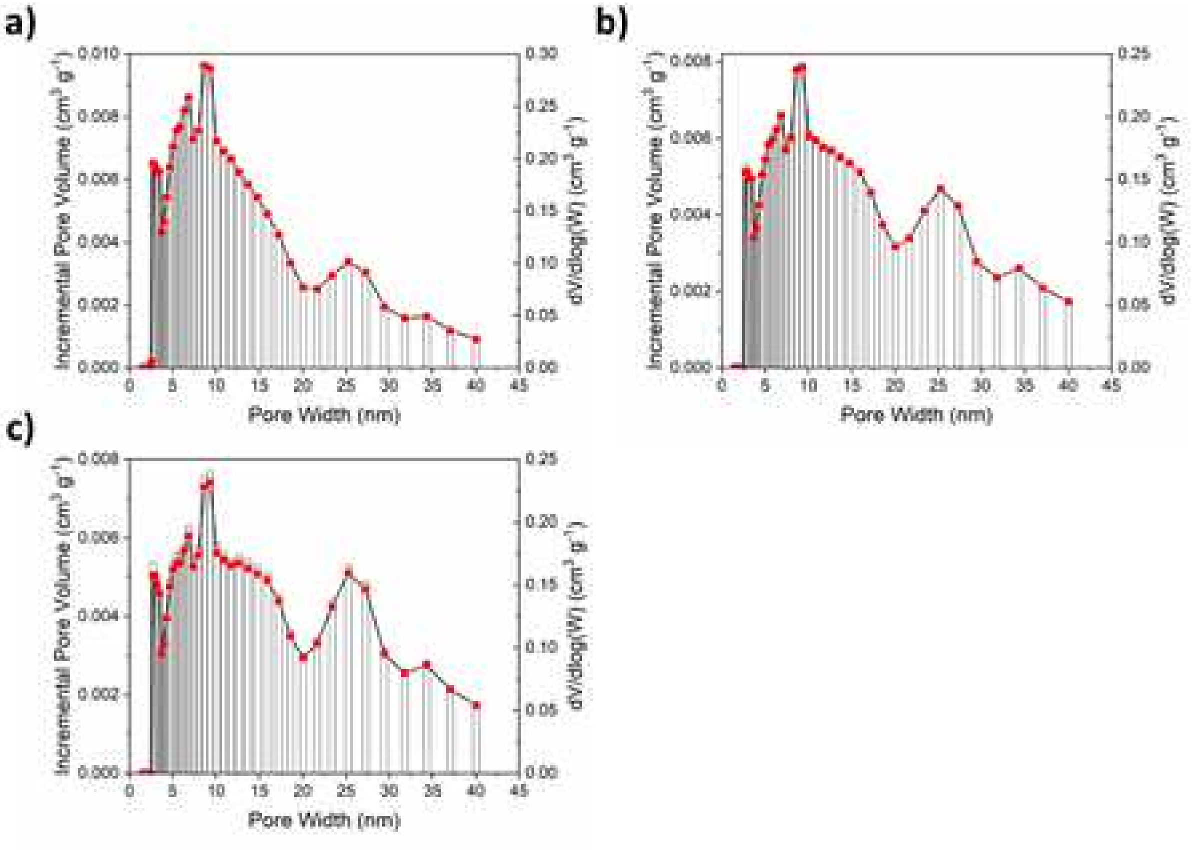

Figure 104: Pore size distribution of a) 3D-GNS; b) Cu/3D-GNS and c) Cu+HAP/3D-GNS, calculated according to the N_2 – DFT model.

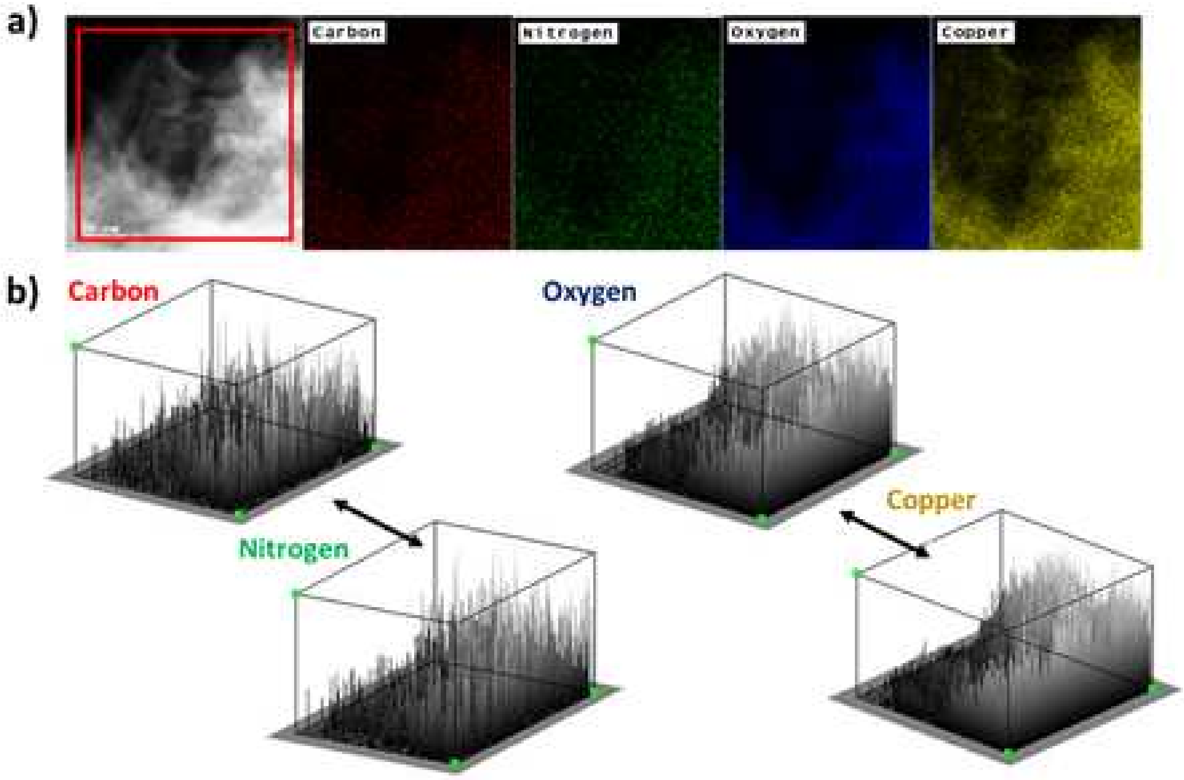

Figure 105: Elemental surface plots in counts vs. spatial coordinate (b) related to STEM/EDX elemental maps of Cu/3D-GNS (a, herein reported from Figure 65 for the sake of clarity)

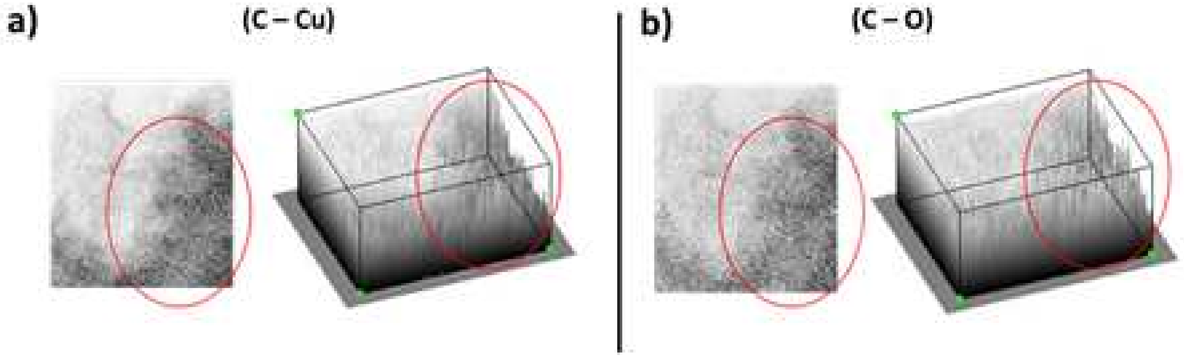

Figure 106: EDX maps (left side in each box) and counts vs. spatial coordinate surface plots (right side in each box) obtained by subtraction of pristine elemental EDX maps of Cu/3D-GNS. Reported maps and plots are the result of a) C with Cu and b) C with O subtraction.

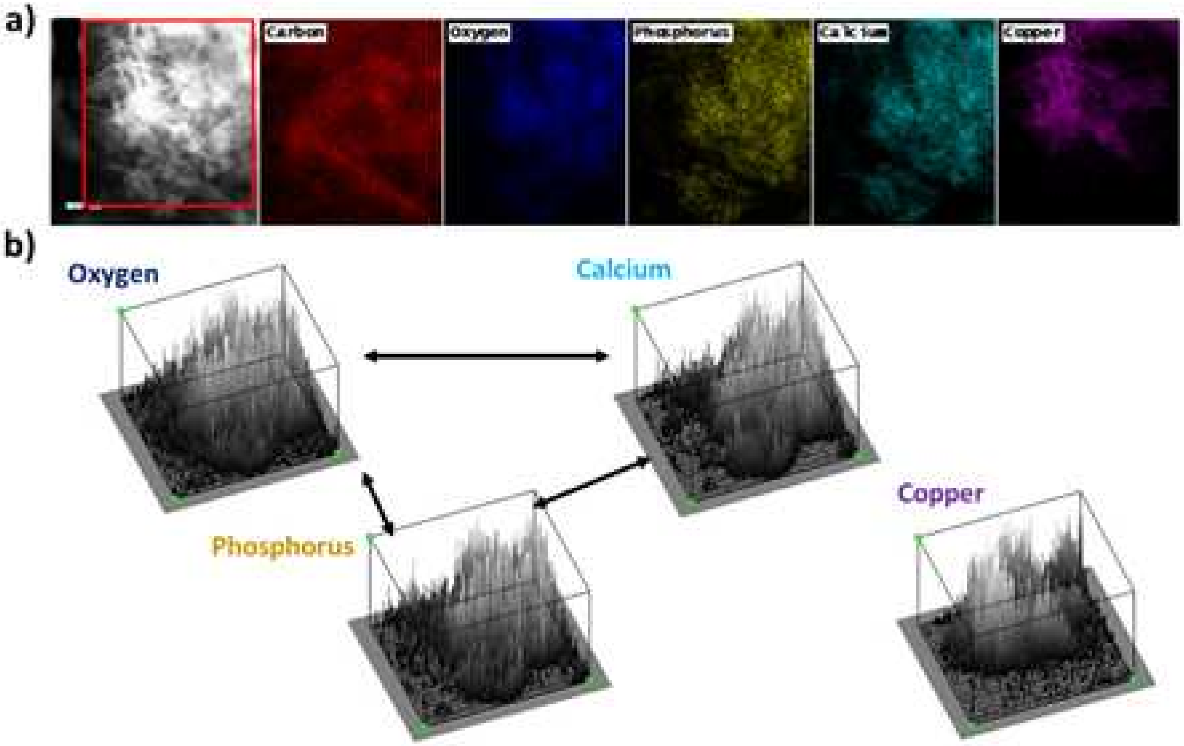

Figure 107: Elemental surface plots in counts vs. spatial coordinate (b) related to STEM/EDX elemental maps of Cu+HAP/3D-GNS (a, herein reported from Figure 66 for the sake of clarity)

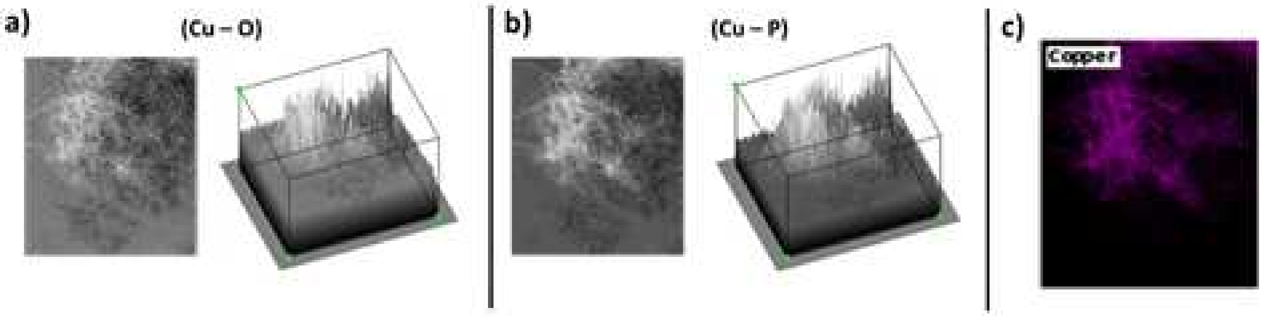

Figure 108: EDX maps (left side in each box) and counts vs. spatial coordinate surface plots (right side in each box) obtained by subtraction of pristine elemental EDX maps of Cu+HAP/3D-GNS. Reported maps and plots are the result of a) Cu with O and b) Cu with P subtraction. Pristine Cu EDX map has been reported as well (c) for the sake of clarity.

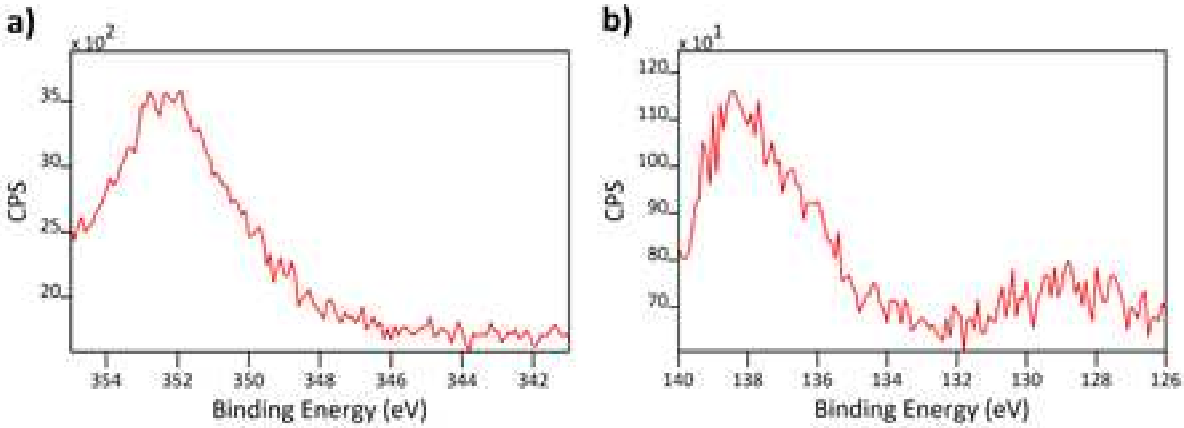

Figure 109: HR XPS spectra collected in the a) Ca 2p and b) P 2p regions for doped Cu+HAP/3D-GNS electrocatalysts.

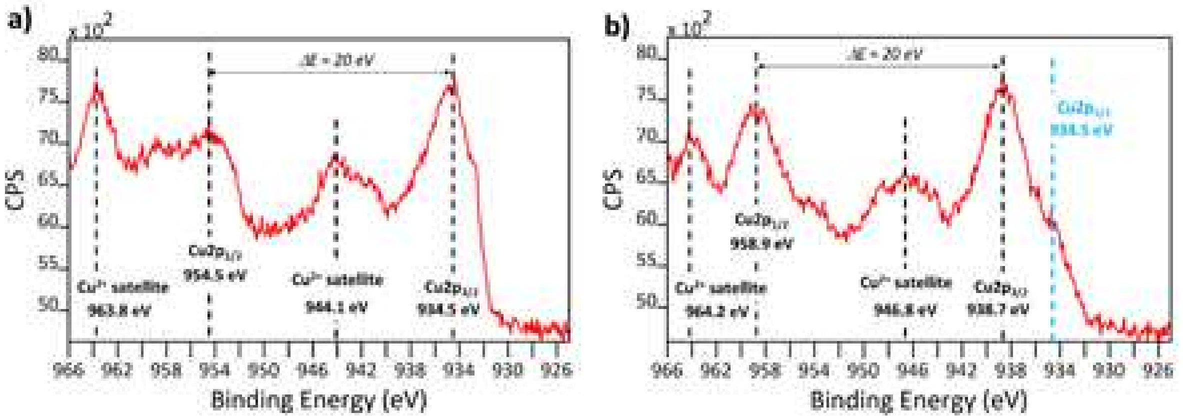

Figure 110: HR XPS spectra collected in the Cu 2p region for a) undoped Cu/3D-GNS and b) doped Cu+HAP/3D-GNS electrocatalysts.

10.3.2 Electrochemical CO_2RR: performances of HAP-doped electrocatalysts

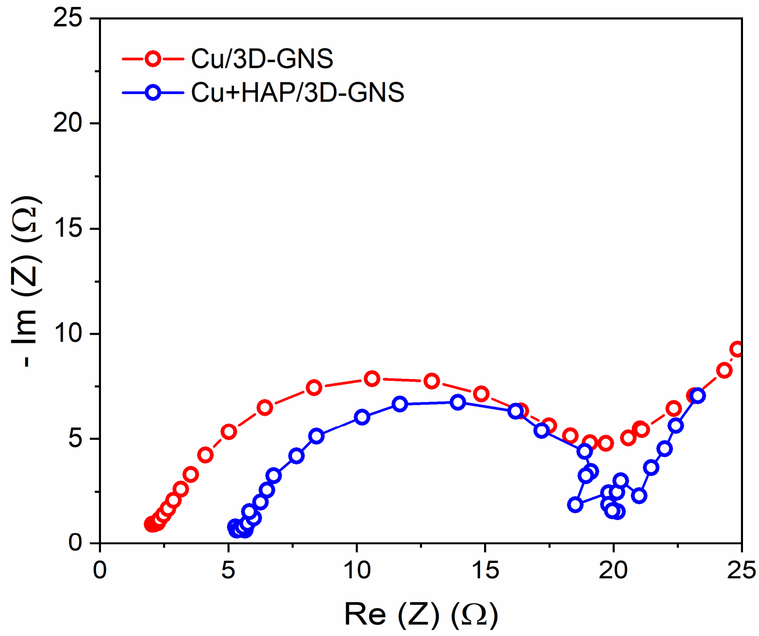

Figure 111: Nyquist plot obtained by EIS onto Cu/3D-GNS (red data) and Cu+HAP/3D-GNS (blue data) modified GDEs.

11 Permissions

In the following, the permissions to reproduce partial contents of published articles are gathered.

Portion	Authors	License	Reference
Fig. 1	Brunton et al.	Open access	[37]
Fig. 2	Silvester et al.	See following attachments	[33]
Figs. 3 and 4	Campisi et al.	See following attachments	[133]
Fig. 6	Cheng et al.	See following attachments	[94]
Figs. 7 and 8	Diallo-Garcia et al.	See following attachments	[95]
Figs. 26 to 30	Ferri et al.	Author of the publication	[17]
Fig. 35	Waheed et al.	See following attachments	[151]
Figs. 54, 56 and 57	Yang et al.,	See following attachments	[184]
Fig. 55	Rendòn-Calle et al.	See following attachments	[185]
Fig. 58	a) Buonsanti et al. b) Strasser et al.	See following attachments See following attachments	[205] [204]
Fig. 59	Atanassov et al.	See following attachments	[217]
Fig. 60	Harada et al.	Open access	[221]
Fig. 61	a) Ozin et al. b) Sun et al.	See following attachments See following attachments	[222] [225]
Figs. 62 and 63	Li et al.	See following attachments	[63]

Copyright
Clearance
Center
Marketplace™

Order Number: 1093031
Order Date: 26 Jan 2021

Payment Information

Michele Ferri
michele.ferri@unimi.it
Payment method: Invoice

Billing Address:
Mr. Michele Ferri
Università degli Studi di Milano
Via Golgi 19
Milan, 20133
Italy

+39 3331412545
michele.ferri@unimi.it

Customer Location:
Mr. Michele Ferri
Università degli Studi di Milano
Via Golgi 19
Milan, 20133
Italy

Order Details

1. Journal of materials chemistry. A, Materials for energy and sustainability

Billing Status:
Open

Order license ID	1093031-1
Order detail status	Completed
ISSN	2050-7496
Type of use	Republish in a thesis/dissertation
Publisher	Royal Society of Chemistry
Portion	Cartoon

0,00 EUR
Republication Permission

LICENSED CONTENT

Publication Title	Journal of materials chemistry. A, Materials for energy and sustainability	**Country**	United Kingdom of Great Britain and Northern Ireland
Author/Editor	Royal Society of Chemistry (Great Britain)	**Rightsholder**	Royal Society of Chemistry
		Publication Type	e-Journal
Date	01/01/2013	**URL**	http://pubs.rsc.org/en/journals/journalissues/ta
Language	English		

REQUEST DETAILS

Portion Type	Cartoon	**Distribution**	Worldwide
Number of cartoons	1	**Translation**	Original language of publication
Format (select all that apply)	Print,Electronic	**Copies for the disabled?**	No
Who will republish the content?	Academic institution	**Minor editing privileges?**	No

Duration of Use	Life of current edition	**Incidental promotional use?**	No
Lifetime Unit Quantity	Up to 499	**Currency**	EUR
Rights Requested	Main product		

NEW WORK DETAILS

Title	Hydroxyapatite-based materials for environmental processes	**Institution name**	Università degli Studi di Milano
		Expected presentation date	2021-03-31
Instructor name	Michele Ferri		

ADDITIONAL DETAILS

The requesting person / organization to appear on the license	Michele Ferri

REUSE CONTENT DETAILS

Title, description or numeric reference of the portion(s)	Figure 13	**Title of the article/chapter the portion is from**	N/A
Editor of portion(s)	N/A	**Author of portion(s)**	Royal Society of Chemistry (Great Britain)
Volume of serial or monograph	N/A		
Page or page range of portion	16	**Publication date of portion**	2013-01-01

Total Items: 1

Subtotal: 0,00 EUR

Order Total: 0,00 EUR

Copyright Clearance Center Marketplace™

Order Number: 1093030
Order Date: 26 Jan 2021

Payment Information

Michele Ferri
michele.ferri@unimi.it
Payment method: Invoice

Billing Address:
Mr. Michele Ferri
Università degli Studi di Milano
Via Golgi 19
Milan, 20133
Italy

+39 3331412545
michele.ferri@unimi.it

Customer Location:
Mr. Michele Ferri
Università degli Studi di Milano
Via Golgi 19
Milan, 20133
Italy

Order Details

1. New journal of chemistry

Billing Status:
Open

Order license ID	1093030-1
Order detail status	Completed
ISSN	1369-9261
Type of use	Republish in a thesis/dissertation
Publisher	ROYAL SOCIETY OF CHEMISTRY
Portion	Cartoon

0,00 EUR
Republication Permission

LICENSED CONTENT

Publication Title	New journal of chemistry	**Country**	United Kingdom of Great Britain and Northern Ireland
Author/Editor	Centre national de la recherche scientifique (France),Royal Society of Chemistry (Great Britain)	**Rightsholder**	Royal Society of Chemistry
		Publication Type	e-Journal
		URL	http://www.rsc.org/njc
Date	01/01/1987		
Language	English		

REQUEST DETAILS

Portion Type	Cartoon	**Distribution**	Worldwide
Number of cartoons	1	**Translation**	Original language of publication
Format (select all that apply)	Print,Electronic	**Copies for the disabled?**	No
Who will republish the content?	Academic institution	**Minor editing privileges?**	No

Duration of Use	Life of current edition	**Incidental promotional use?**	No
Lifetime Unit Quantity	Up to 499	**Currency**	EUR
Rights Requested	Main product		

NEW WORK DETAILS

Title	Hydroxyapatite-based materials for environmental processes	**Institution name**	Università degli Studi di Milano
		Expected presentation date	2021-03-31
Instructor name	Michele Ferri		

ADDITIONAL DETAILS

The requesting person / organization to appear on the license	Michele Ferri

REUSE CONTENT DETAILS

Title, description or numeric reference of the portion(s)	Graphical Abstract	**Title of the article/chapter the portion is from**	N/A
Editor of portion(s)	N/A	**Author of portion(s)**	Centre national de la recherche scientifique (France); Royal Society of Chemistry (Great Britain)
Volume of serial or monograph	N/A		
Page or page range of portion	1	**Publication date of portion**	2021-03-31

Total Items: 1

Subtotal: 0,00 EUR

Order Total: 0,00 EUR

Copyright Clearance Center RightsLink®

Home | Help | Email Support | Michele Ferri

FTIR Study of Adsorption of CO2 on Nonstoichiometric Calcium Hydroxyapatite

Author: Zhi Hua Cheng, Akemi Yasukawa, Kazuhiko Kandori, et al

Publication: Langmuir

Publisher: American Chemical Society

Date: Nov 1, 1998

Copyright © 1998, American Chemical Society

PERMISSION/LICENSE IS GRANTED FOR YOUR ORDER AT NO CHARGE

This type of permission/license, instead of the standard Terms & Conditions, is sent to you because no fee is being charged for your order. Please note the following:

- Permission is granted for your request in both print and electronic formats, and translations.
- If figures and/or tables were requested, they may be adapted or used in part.
- Please print this page for your records and send a copy of it to your publisher/graduate school.
- Appropriate credit for the requested material should be given as follows: "Reprinted (adapted) with permission from (COMPLETE REFERENCE CITATION). Copyright (YEAR) American Chemical Society." Insert appropriate information in place of the capitalized words.
- One-time permission is granted only for the use specified in your request. No additional uses are granted (such as derivative works or other editions). For any other uses, please submit a new request.

If credit is given to another source for the material you requested, permission must be obtained from that source.

BACK CLOSE WINDOW

© 2021 Copyright - All Rights Reserved | Copyright Clearance Center, Inc. | Privacy statement | Terms and Conditions
Comments? We would like to hear from you. E-mail us at customercare@copyright.com

Copyright Clearance Center RightsLink®

Home | Help | Email Support | Michele Ferri

Identification of Surface Basic Sites and Acid–Base Pairs of Hydroxyapatite

Author: Sarah Diallo-Garcia, Manel Ben Osman, Jean-Marc Krafft, et al

Publication: The Journal of Physical Chemistry C

Publisher: American Chemical Society

Date: Jun 1, 2014

Copyright © 2014, American Chemical Society

PERMISSION/LICENSE IS GRANTED FOR YOUR ORDER AT NO CHARGE

This type of permission/license, instead of the standard Terms & Conditions, is sent to you because no fee is being charged for your order. Please note the following:

- Permission is granted for your request in both print and electronic formats, and translations.
- If figures and/or tables were requested, they may be adapted or used in part.
- Please print this page for your records and send a copy of it to your publisher/graduate school.
- Appropriate credit for the requested material should be given as follows: "Reprinted (adapted) with permission from (COMPLETE REFERENCE CITATION). Copyright (YEAR) American Chemical Society." Insert appropriate information in place of the capitalized words.
- One-time permission is granted only for the use specified in your request. No additional uses are granted (such as derivative works or other editions). For any other uses, please submit a new request.

If credit is given to another source for the material you requested, permission must be obtained from that source.

BACK CLOSE WINDOW

© 2021 Copyright - All Rights Reserved | Copyright Clearance Center, Inc. | Privacy statement | Terms and Conditions
Comments? We would like to hear from you. E-mail us at customercare@copyright.com

ELSEVIER LICENSE
TERMS AND CONDITIONS

Jan 26, 2021

This Agreement between Università degli Studi di Milano -- Michele Ferri ("You") and Elsevier ("Elsevier") consists of your license details and the terms and conditions provided by Elsevier and Copyright Clearance Center.

License Number	4996430366746
License date	Jan 26, 2021
Licensed Content Publisher	Elsevier
Licensed Content Publication	TrAC Trends in Analytical Chemistry
Licensed Content Title	Nanomaterials-based electrochemical detection of heavy metals in water: Current status, challenges and future direction
Licensed Content Author	Abdul Waheed,Muhammad Mansha,Nisar Ullah
Licensed Content Date	Aug 1, 2018
Licensed Content Volume	105
Licensed Content Issue	n/a
Licensed Content Pages	15
Start Page	37
End Page	51
Type of Use	reuse in a thesis/dissertation

Portion	figures/tables/illustrations
Number of figures/tables /illustrations	1
Format	both print and electronic
Are you the author of this Elsevier article?	No
Will you be translating?	No
Title	Hydroxyapatite-based materials for environmental processes
Institution name	Università degli Studi di Milano
Expected presentation date	Mar 2021
Portions	Figure 1
Requestor Location	Università degli Studi di Milano Via Golgi 19 Milan, 20133 Italy Attn: Università degli Studi di Milano
Publisher Tax ID	GB 494 6272 12
Total	0.00 EUR

Terms and Conditions

INTRODUCTION

1. The publisher for this copyrighted material is Elsevier. By clicking "accept" in connection with completing this licensing transaction, you agree that the following terms and conditions apply to this transaction (along with the Billing and Payment terms and conditions established by Copyright Clearance Center, Inc. ("CCC"), at the time that you opened your Rightslink account and that are available at any time at http://myaccount.copyright.com).

Copyright Clearance Center RightsLink®

Home | Help | Email Support | Michele Ferri

Surface and Interface Control in Nanoparticle Catalysis

Author: Chenlu Xie, Zhiqiang Niu, Dohyung Kim, et al
Publication: Chemical Reviews
Publisher: American Chemical Society
Date: Jan 1, 2020

Copyright © 2020, American Chemical Society

PERMISSION/LICENSE IS GRANTED FOR YOUR ORDER AT NO CHARGE

This type of permission/license, instead of the standard Terms & Conditions, is sent to you because no fee is being charged for your order. Please note the following:

- Permission is granted for your request in both print and electronic formats, and translations.
- If figures and/or tables were requested, they may be adapted or used in part.
- Please print this page for your records and send a copy of it to your publisher/graduate school.
- Appropriate credit for the requested material should be given as follows: "Reprinted (adapted) with permission from (COMPLETE REFERENCE CITATION). Copyright (YEAR) American Chemical Society." Insert appropriate information in place of the capitalized words.
- One-time permission is granted only for the use specified in your request. No additional uses are granted (such as derivative works or other editions). For any other uses, please submit a new request.

If credit is given to another source for the material you requested, permission must be obtained from that source.

BACK CLOSE WINDOW

© 2021 Copyright - All Rights Reserved | Copyright Clearance Center, Inc. | Privacy statement | Terms and Conditions
Comments? We would like to hear from you. E-mail us at customercare@copyright.com

ELSEVIER LICENSE
TERMS AND CONDITIONS

Jan 26, 2021

This Agreement between Università degli Studi di Milano -- Michele Ferri ("You") and Elsevier ("Elsevier") consists of your license details and the terms and conditions provided by Elsevier and Copyright Clearance Center.

License Number	4996431068474
License date	Jan 26, 2021
Licensed Content Publisher	Elsevier
Licensed Content Publication	Current Opinion in Electrochemistry
Licensed Content Title	A brief review of the computational modeling of CO2 electroreduction on Cu electrodes
Licensed Content Author	Alejandra Rendón-Calle,Santiago Builes,Federico Calle-Vallejo
Licensed Content Date	Jun 1, 2018
Licensed Content Volume	9
Licensed Content Issue	n/a
Licensed Content Pages	8
Start Page	158
End Page	165
Type of Use	reuse in a thesis/dissertation

Portion	figures/tables/illustrations
Number of figures/tables /illustrations	1
Format	both print and electronic
Are you the author of this Elsevier article?	No
Will you be translating?	No
Title	Hydroxyapatite-based materials for environmental processes
Institution name	Università degli Studi di Milano
Expected presentation date	Mar 2021
Portions	Figure 4b
Requestor Location	Università degli Studi di Milano Via Golgi 19 Milan, 20133 Italy Attn: Università degli Studi di Milano
Publisher Tax ID	GB 494 6272 12
Total	0.00 EUR

Terms and Conditions

INTRODUCTION

1. The publisher for this copyrighted material is Elsevier. By clicking "accept" in connection with completing this licensing transaction, you agree that the following terms and conditions apply to this transaction (along with the Billing and Payment terms and conditions established by Copyright Clearance Center, Inc. ("CCC"), at the time that you opened your Rightslink account and that are available at any time at

JOHN WILEY AND SONS LICENSE
TERMS AND CONDITIONS

Jan 26, 2021

This Agreement between Università degli Studi di Milano -- Michele Ferri ("You") and John Wiley and Sons ("John Wiley and Sons") consists of your license details and the terms and conditions provided by John Wiley and Sons and Copyright Clearance Center.

License Number	4996440362065
License date	Jan 26, 2021
Licensed Content Publisher	John Wiley and Sons
Licensed Content Publication	Angewandte Chemie International Edition
Licensed Content Title	Tailoring Copper Nanocrystals towards C2 Products in Electrochemical CO2 Reduction
Licensed Content Author	Anna Loiudice, Peter Lobaccaro, Esmail A. Kamali, et al
Licensed Content Date	Apr 5, 2016
Licensed Content Volume	55
Licensed Content Issue	19
Licensed Content Pages	4
Type of use	Dissertation/Thesis
Requestor type	University/Academic
Format	Print and electronic

Portion	Figure/table
Number of figures/tables	1
Will you be translating?	No
Title	Hydroxyapatite-based materials for environmental processes
Institution name	Università degli Studi di Milano
Expected presentation date	Mar 2021
Portions	Figure 4
Requestor Location	Università degli Studi di Milano Via Golgi 19 Milan, 20133 Italy Attn: Università degli Studi di Milano
Publisher Tax ID	EU826007151
Total	0.00 EUR
Terms and Conditions	

TERMS AND CONDITIONS

This copyrighted material is owned by or exclusively licensed to John Wiley & Sons, Inc. or one of its group companies (each a"Wiley Company") or handled on behalf of a society with which a Wiley Company has exclusive publishing rights in relation to a particular work (collectively "WILEY"). By clicking "accept" in connection with completing this licensing transaction, you agree that the following terms and conditions apply to this transaction (along with the billing and payment terms and conditions established by the Copyright Clearance Center Inc., ("CCC's Billing and Payment terms and conditions"), at the time that you opened your RightsLink account (these are available at any time at http://myaccount.copyright.com).

Terms and Conditions

- The materials you have requested permission to reproduce or reuse (the "Wiley

Particle Size Effects in the Catalytic Electroreduction of CO2 on Cu Nanoparticles

Author: Rulle Reske, Hemma Mistry, Farzad Behafarid, et al
Publication: Journal of the American Chemical Society
Publisher: American Chemical Society
Date: May 1, 2014

Copyright © 2014, American Chemical Society

PERMISSION/LICENSE IS GRANTED FOR YOUR ORDER AT NO CHARGE

This type of permission/license, instead of the standard Terms & Conditions, is sent to you because no fee is being charged for your order. Please note the following:

- Permission is granted for your request in both print and electronic formats, and translations.
- If figures and/or tables were requested, they may be adapted or used in part.
- Please print this page for your records and send a copy of it to your publisher/graduate school.
- Appropriate credit for the requested material should be given as follows: "Reprinted (adapted) with permission from (COMPLETE REFERENCE CITATION). Copyright (YEAR) American Chemical Society." Insert appropriate information in place of the capitalized words.
- One-time permission is granted only for the use specified in your request. No additional uses are granted (such as derivative works or other editions). For any other uses, please submit a new request.

If credit is given to another source for the material you requested, permission must be obtained from that source.

BACK CLOSE WINDOW

© 2021 Copyright - All Rights Reserved | Copyright Clearance Center, Inc. | Privacy statement | Terms and Conditions
Comments? We would like to hear from you. E-mail us at customercare@copyright.com

Home | Help | Email Support | Michele Ferri

Role of Nitrogen Moieties in N-Doped 3D-Graphene Nanosheets for Oxygen Electroreduction in Acidic and Alkaline Media

Author: Sadia Kabir, Kateryna Artyushkova, Alexey Serov, et al

Publication: Applied Materials

Publisher: American Chemical Society

Date: Apr 1, 2018

Copyright © 2018, American Chemical Society

PERMISSION/LICENSE IS GRANTED FOR YOUR ORDER AT NO CHARGE

This type of permission/license, instead of the standard Terms & Conditions, is sent to you because no fee is being charged for your order. Please note the following:

- Permission is granted for your request in both print and electronic formats, and translations.
- If figures and/or tables were requested, they may be adapted or used in part.
- Please print this page for your records and send a copy of it to your publisher/graduate school.
- Appropriate credit for the requested material should be given as follows: "Reprinted (adapted) with permission from (COMPLETE REFERENCE CITATION). Copyright (YEAR) American Chemical Society." Insert appropriate information in place of the capitalized words.
- One-time permission is granted only for the use specified in your request. No additional uses are granted (such as derivative works or other editions). For any other uses, please submit a new request.

If credit is given to another source for the material you requested, permission must be obtained from that source.

BACK CLOSE WINDOW

© 2021 Copyright - All Rights Reserved | Copyright Clearance Center, Inc. | Privacy statement | Terms and Conditions
Comments? We would like to hear from you. E-mail us at customercare@copyright.com

JOHN WILEY AND SONS LICENSE
TERMS AND CONDITIONS

Jan 26, 2021

This Agreement between Università degli Studi di Milano -- Michele Ferri ("You") and John Wiley and Sons ("John Wiley and Sons") consists of your license details and the terms and conditions provided by John Wiley and Sons and Copyright Clearance Center.

License Number	4996441501848
License date	Jan 26, 2021
Licensed Content Publisher	John Wiley and Sons
Licensed Content Publication	Angewandte Chemie International Edition
Licensed Content Title	Efficient Electrocatalytic Reduction of CO2 by Nitrogen-Doped Nanoporous Carbon/Carbon Nanotube Membranes: A Step Towards the Electrochemical CO2 Refinery
Licensed Content Author	Geoffrey A. Ozin, Markus Antonietti, Jiayin Yuan, et al
Licensed Content Date	Jun 1, 2017
Licensed Content Volume	56
Licensed Content Issue	27
Licensed Content Pages	6

Type of use	Dissertation/Thesis
Requestor type	University/Academic
Format	Print and electronic
Portion	Figure/table
Number of figures/tables	1
Will you be translating?	No
Title	Hydroxyapatite-based materials for environmental processes
Institution name	Università degli Studi di Milano
Expected presentation date	Mar 2021
Portions	Figure 5
Requestor Location	Università degli Studi di Milano Via Golgi 19 Milan, 20133 Italy Attn: Università degli Studi di Milano
Publisher Tax ID	EU826007151
Total	0.00 EUR

Terms and Conditions

TERMS AND CONDITIONS

This copyrighted material is owned by or exclusively licensed to John Wiley & Sons, Inc. or one of its group companies (each a"Wiley Company") or handled on behalf of a society with

JOHN WILEY AND SONS LICENSE
TERMS AND CONDITIONS

Jan 26, 2021

This Agreement between Università degli Studi di Milano -- Michele Ferri ("You") and John Wiley and Sons ("John Wiley and Sons") consists of your license details and the terms and conditions provided by John Wiley and Sons and Copyright Clearance Center.

License Number	4996450221348
License date	Jan 26, 2021
Licensed Content Publisher	John Wiley and Sons
Licensed Content Publication	Angewandte Chemie International Edition
Licensed Content Title	Metal-Free Nitrogen-Doped Mesoporous Carbon for Electroreduction of CO2 to Ethanol
Licensed Content Author	Yuhan Sun, Wei Wei, Shenggang Li, et al
Licensed Content Date	Jul 28, 2017
Licensed Content Volume	56
Licensed Content Issue	36
Licensed Content Pages	5
Type of use	Dissertation/Thesis
Requestor type	University/Academic
Format	Print and electronic

Portion	Figure/table
Number of figures/tables	1
Will you be translating?	No
Title	Hydroxyapatite-based materials for environmental processes
Institution name	Università degli Studi di Milano
Expected presentation date	Mar 2021
Portions	Figure 3
Requestor Location	Università degli Studi di Milano Via Golgi 19 Milan, 20133 Italy Attn: Università degli Studi di Milano
Publisher Tax ID	EU826007151
Total	0.00 EUR

Terms and Conditions

TERMS AND CONDITIONS

This copyrighted material is owned by or exclusively licensed to John Wiley & Sons, Inc. or one of its group companies (each a"Wiley Company") or handled on behalf of a society with which a Wiley Company has exclusive publishing rights in relation to a particular work (collectively "WILEY"). By clicking "accept" in connection with completing this licensing transaction, you agree that the following terms and conditions apply to this transaction (along with the billing and payment terms and conditions established by the Copyright Clearance Center Inc., ("CCC's Billing and Payment terms and conditions"), at the time that you opened your RightsLink account (these are available at any time at http://myaccount.copyright.com).

Terms and Conditions

- The materials you have requested permission to reproduce or reuse (the "Wiley

ELSEVIER LICENSE
TERMS AND CONDITIONS

Jan 26, 2021

This Agreement between Università degli Studi di Milano -- Michele Ferri ("You") and Elsevier ("Elsevier") consists of your license details and the terms and conditions provided by Elsevier and Copyright Clearance Center.

License Number	4996450510705
License date	Jan 26, 2021
Licensed Content Publisher	Elsevier
Licensed Content Publication	International Journal of Hydrogen Energy
Licensed Content Title	Hydroxyapatite decorated TiO2 as efficient photocatalyst for selective reduction of CO2 with H2O into CH4
Licensed Content Author	Ruifeng Chong,Yangyang Fan,Yuqing Du,Ling Liu,Zhixian Chang,Deliang Li
Licensed Content Date	Dec 6, 2018
Licensed Content Volume	43
Licensed Content Issue	49
Licensed Content Pages	11
Start Page	22329
End Page	22339
Type of Use	reuse in a thesis/dissertation

Portion	figures/tables/illustrations
Number of figures/tables /illustrations	3
Format	both print and electronic
Are you the author of this Elsevier article?	No
Will you be translating?	No
Title	Hydroxyapatite-based materials for environmental processes
Institution name	Università degli Studi di Milano
Expected presentation date	Mar 2021
Portions	Figure 5a,b - Figure 6 - Scheme 1
Requestor Location	Università degli Studi di Milano Via Golgi 19 Milan, 20133 Italy Attn: Università degli Studi di Milano
Publisher Tax ID	GB 494 6272 12
Total	0.00 EUR

Terms and Conditions

INTRODUCTION

1. The publisher for this copyrighted material is Elsevier. By clicking "accept" in connection with completing this licensing transaction, you agree that the following terms and conditions apply to this transaction (along with the Billing and Payment terms and conditions established by Copyright Clearance Center, Inc. ("CCC"), at the time that you opened your Rightslink account and that are available at any time at http://myaccount.copyright.com).